Mesoporous bioactive glasses as smart platform to stimulate bone regeneration

Carlotta Pontremoli

* * * * * *

Supervisors
Prof. Sonia L. Fiorilli
Prof. Chiara Vitale Brovarone, Co-Supervisor

Doctoral Examination Committee:
Prof. Gloria Berlier, Referee, University of Torino
Prof. Maria Chatzinikolaidou, Referee, University of Crete

I hereby declare that, the contents and organisation of this dissertation constitute my own original work and does not compromise in any way the rights of third parties, including those relating to the security of personal data.

………………………………....

Carlotta Pontremoli

Turin, January 26, 2021

Summary

In the field of bone regeneration, considerable attention has been addressed towards the use of mesoporous bioactive glasses (MBGs), as multifunctional therapeutic platforms for advanced medical devices. Their extremely high exposed surface area and pore volume allow to store and release functional molecules (such as anti-inflammatory, antimicrobial agents, growth factors) and, additionally, their composition can be enriched through the incorporation of specific elements (*i.e.* Sr, Cu) with the aim to combine in a single biomaterial several therapeutic abilities, such as pro-osteogenic, pro-angiogenic and antibacterial properties.

The goal of this PhD research work was to design and develop a multifunctional platform based on Mesoporous Bioactive Glasses, to be used as therapeutic delivery system for biomedical application, in particular to treat compromised tissue healing and stimulate bone regeneration. To this purpose, two synthesis procedures were selected to produce the MBGs with a binary composition based on SiO_2 and CaO (ratio 85/15) enriched with different therapeutic ions, the base-catalysed sol-gel procedure and the aerosol assisted spray-drying method. These two different approaches allowed to produce nano-sized particles and micro-sized particles, respectively, with different peculiar features. Different Active Pharmaceutical Ingredients (APIs) were identified and selected to exert a specific therapeutic effect. Specifically, the amount and the type of therapeutic ions added during the synthesis were selected by following the idea to exert peculiar outcomes, in particular copper was added to provide an antibacterial and pro-angiogenic effect, while strontium ions were selected thanks to their well-known pro-osteogenic properties. In a second step, the therapeutic potential of the MBGs has been further enriched by loading ibuprofen and N-acetylcysteine, in order to develop a drug delivery system, able to co-release both the ions and the drugs at the pathological site. Ibuprofen was employed in combination with Cu-containing MBGs, aiming to design a

multifunctional platform with anti-microbic/pro-angiogenic effects associated to the copper and anti-inflammatory potential exerted by ibuprofen to be used *in situ* for delayed bone healing applications. On the other hands, N-Acetylcysteine (NAC) was loaded into the Sr-containing MBGs to be used as osteogenesis-enhancing platform, able to deliver into the bony defect both strontium ions and NAC, thus improving bone regeneration and promote bone defect healing. Two different loading procedures have been investigated, the adsorption and the incipient wetness methods, to identify the most suitable loading procedure in terms of yields and required time.

Furthermore, different surface modification approaches were investigated, with the aim to provide the final device with anti-adhesive properties and to obtain a prolonged and sustained release of the cargo. In details, the *zwitterionization* procedure has been selected to impart anti-adhesive properties to the MBGs, allowing to repel the protein adhesion and thus to prevent the biofilm formation. *Zwitterionic* surfaces are characterized by an equal number of both positive and negative charges in order to preserve the overall electrical neutrality and the related anti-adhesive properties are imparted by a strongly bonded water molecule layer which acts as a barrier against the adsorption of both proteins and bacteria. The resulting multifunctional device is supposed to target simultaneously all the causes, often mutually interlocked, of the pathologies related to compromised bone tissue healing. On the other hands, the Layer by Layer deposition has been chosen as promising strategy to modulate the cargo release rate. Two different routes were investigated: in the first strategy, chitosan, alginate and chitosan were assembled by forming the multi-layered surface and, successively, ibuprofen was loaded by incipient wetness impregnation. In the second one, alginate was replaced by the ibuprofen, by exploiting the ibuprofen negative charge (COO-), able to electrostatically interact with the chitosan positive charge.

Finally, to make MBGs suitable as long-term therapeutics delivery systems for bone healing, a hybrid formulation based on the conjugation of MBGs with an injectable thermosensitive hydrogel, acting as a vehicle phase, has been investigated in order to develop a multifunctional platform to be injected directly at the pathological site for the sustained delivery of therapeutic agent.

Acknowledgments

Solo ciò che appare nel mondo come qualcosa di poco conto potrà un giorno diventare una cosa.

Table of contents

List of tables

List of figures

Thesis goals

Under normal healing conditions bone fully regenerates in 6-8 weeks after fractures [1], but despite this excellent regenerative capability, still up to 10–15% of the fractures show unsuccessful healing outcomes, resulting in delayed healing conditions or even, in the worst scenario case, to non-union fractures [2]. Aging and related pathologies are risk factors, therefore, due to the increase of elderly population, the total number of patients suffering from delayed bone healing or non-unions is expected to dramatically increase in the next future. Although the recent and remarkable advancements in terms of biomaterials and surgical strategies to treat bone fractures and support bone regeneration in compromised clinical situations, impaired healing outcomes are still a relevant and challenging clinical issue [3]. The primary causes for an ineffective healing are various and depend among others on the fracture site and seriousness, the patient clinical situation (age, osteoporosis, chronic or autoimmune diseases) and concomitant complications, such as bacterial infections.

In the last decades, a plethora of nano-biomaterials has been offered by the scientific community in order to replace or repair damaged tissues and to overcome the clinical challenges associated to compromised bone regeneration. Among the others, bioactive bioceramics stand out thanks to their excellent biocompatibility associated to the ability to induce the formation of a hydroxyapatite layer, similar to the natural component of bone [2]. The term bioactivity, as proposed for the first time in 1969 by Professor Hench, refers to the formation of a chemical bonding between biological tissues and bone biomaterials [47,48]. Over the years, the morphological and textural features of bioactive glasses have been modified in order to improve their biological performances. In fact, along with the bioactive behaviour, an ideal biomaterial should also provide the delivery of active agents, with the final aim to address all the causes leading to the delayed healing of bone [1].

The idea of combining in a single biomaterial the bioactivity typical of bioactive glasses with the ability to load and release active agents able to provide specific biological effects would be one of the greatest achievements of biomaterial development [4]. In this scenario, mesoporous bioactive glasses (MBGs) have received considerable attention as multifunctional biomedical devices since their first appearance [5], when for the first time, Prof. DY Zhao (2004) [6] and Prof. M. Vallet-Regí (2006) [7] proposed nano-structured bioceramics, based on SiO_2- CaO-P_2O_5 composition (similarly to the conventional bioactive sol-gel glasses) and characterized by the textural properties, in term of surface area and regular porosity, typical of the silica based mesoporous materials. Their extremely high exposed surface area and pore volume allow to load and release functional molecules of different size, spanning from anti-inflammatory or antimicrobial agents to growth factors. Moreover, the composition of MBGs can be enriched through the incorporation of specific therapeutic elements (i.e. Sr, Cu) with the aim to combine in a single biomaterial several therapeutic functions, such as pro-osteogenic, pro-angiogenic and antibacterial properties. Due their attractive features MBGs have been used to develop a great variety of devices for tissue engineering, among which hierarchical porous scaffolds with enhanced biocompatibility and osteoconductivity for bone regeneration applications [8] and nanocarriers for drug release thanks to their accessible mesoporous structure and unique surface properties. Particularly, in the field of bone tissue regeneration, the need to develop advanced drug delivery systems is due to several factors, including poor blood circulation and inadequate tissue penetration of bone tissue. Furthermore, conventional administration routes, such as oral administration and injection, present low therapeutic tissue levels and often various side effects since the therapeutic agents may not be delivered efficiently and adequately to the pathological site [9]. The sustained drug release from biomaterials, at variance with systemic administration, allows to enhance the delivery efficiency, maintaining an effective therapeutic dose over time at the pathological site and, concurrently, reducing the side effects. In addition, conventional drug administration routes still exhibits some drawbacks in particular for unstable or very poorly soluble drugs, proteins or nucleic acids [10]. Based on these considerations, the design of new drug delivery systems able to release multiple therapeutic agents to target simultaneously different causes of compromised healing processes [13] is prominently needed, as extensively described in chapter 1.

Despite the promising MBG features described up to now, to date, some drawbacks have greatly limited their practical applications and their true clinical translation, among which the strong burst release of incorporated drug once contacted with body fluids, and the difficulties related to their administration at the pathological site (*i.e.* bone fracture cavity) in the form of powder. Since MBGs alone are not exploitable as long-term drug delivery systems for orthopaedic applications, their combination with polymers able to modulate the release kinetics and/or to act as a vehicle phase to the pathological site would greatly enlarge the clinical potential of these nanocarriers. To this purpose, the MOZART project

(Mesoporous matrices for localized pH-triggered release of therapeutic ions and drugs) funded by the European Community (programme Horizon 2020) and coordinated by Politecnico di Torino (Prof. C. Vitale-Brovarone), aimed to develop a library of mesoporous inorganic nanomatrices (MBGs and ordered mesoporous carbons, OMCs) containing therapeutic ions and loaded with specific drugs to be used as multifunctional platform in the treatment of delayed bone healing and non-healing skin wounds. In MOZART, the incorporation into a thermosensitive hydrogel allows to introduce and maintain the particles in the site of interest.

In this scenario, the present PhD thesis was focused on the design and development of a multifunctional platform based on Mesoporous Bioactive Glasses (MBGs), to be used as therapeutic delivery system for biomedical application, in particular for bone regeneration, capable to target different therapeutic effects and to overcome the drawbacks of the traditional treatments.

In particular, the first aim of this PhD thesis was to produce MBG particles with a binary composition based on SiO_2 and CaO enriched with therapeutic ions and loaded with selected drugs. To this purpose, the amount and the type of therapeutic ions added during the synthesis were selected by following the idea to exert peculiar outcomes, in particular copper were added to provide an antibacterial and pro-angiogenic effect, while strontium ions were selected thanks to their well-known pro-osteogenic properties. In a second step, the therapeutic potential of the MBGs has been enriched by loading ibuprofen and N-acetylcysteine (NAC). Specifically, Ibuprofen was employed in combination with Cu-containing MBGs (results reported in chapter 3), aiming to design a multifunctional platform with anti-microbic/pro-angiogenic effects associated to the copper and anti-inflammatory potential exerted by ibuprofen to be used *in situ* for delayed bone healing applications. On the other hands, N-Acetylcysteine was loaded into the Sr-containing MBGs (results reported in chapter 4) to be used as osteogenesis-enhancing platform, able to deliver into the bony defect both strontium ions and NAC, thus improving bone regeneration and promote bone defect healing.

The second aim was to investigate different surface modification approaches able to impart to MBGs further peculiar features. To this purpose, the Layer by Layer deposition has been evaluated as suitable non-covalent approach to modulate the release rate of the incorporated active agents, hence avoiding the burst release of both the ions and drugs. More in details, multi-layered copper-containing MBGs have been developed, by following two different routes with the final aim to obtain two different multifunctional platforms showing a sustained release profile of both the ions and drug. The first strategy involved the use of the natural biodegradable and biocompatible polyelectrolytes chitosan and alginate, alternatively deposited by exploiting their opposite positive and negative charges, respectively. Once obtained the desired multi-layered surface in term of layer number, ibuprofen was loaded into the multi-layered MBGs. In the second approach, the alginate layer was replaced by the ibuprofen, thus introduced as polyelectrolyte layer, by exploiting

the ibuprofen negative charge (COO⁻), able to electrostatically interact with the chitosan positive charge. The related results are reported in chapter 3.

On the other hands, *zwitterionization* has been identified as functionalization approach to further enrich the therapeutic potential of the MBGs, imparting anti-adhesive/anti-fouling features. In fact, thanks to the high number of terminal hydroxyl groups, the MBG surface can be easily functionalized by grafting alkoxysilane moieties with the aim to achieve several targets. In this PhD project, following the general idea of the ZODIAC project, in order to design anti-adhesive/anti-fouling surfaces [16,17], *zwitterionization* has been selected as one of the most promising approach to obtain a material surface with hydrophilic behaviour and electrically neutral charges. In fact, *zwitterionic* surfaces are characterized by an equal number of both positive and negative charges which preserve the overall electrical neutrality.

In this context, during this PhD work, an advanced biomaterial based on strontium containing MBGs were designed with the idea to synergistically combine the effects of therapeutic ions with anti-adhesive properties. In fact, the antiadhesive surface can avoid the formation of a protein layer on the material surface once in contact with biological fluids, which is responsible of the reduction of the material performance, due to the inhibition of the effect exerted by the drug/ion release and of the formation of a hydroxyapatite layer [18], essential for the strong bond with living bone tissue and the promotion of osteogenesis. A preliminary biological evaluation was carried out during the period that I spent in Madrid in collaboration with the group of *Prof. Maria Vallet-Regì*'at *Departamento de Química Inorgánica y Bioinorgánica, Universidad Complutense de Madrid (UCM), CIBER de Bioingeniería, Biomateriales y Nanomedicina (CIBER-BBN),* a partner involved in the ZODIAC project. In particular, at UCM the in *vitro* biocompatibility assays in the presence of a mouse pre-osteoblastic cell line MC3T3-E1 were performed to evaluate the effect of *zwitterionic* Sr-MBGs on the osteoblastic cell growth and differentiation. Moreover, to assess the anti-adhesive ability imparted by the surface *zwitterionization*, a reduced protein adsorption of serum proteins was evaluated by gel electrophoresis (SDS-PAGE) experiments using bovine serum albumin (BSA) and fibrinogen (Fib), respectively. The related results are reported in chapter 4.

The third aim was to identify a strategy to overcome the drawbacks which limits the MBG practical applications and clinical translation. In fact, the developed MBGs are not exploitable alone in form of powders as long-term therapeutics delivery systems for bone healing. Thus, the conjugation with a thermosensitive polymer able to both modulate the release kinetics and act as a vehicle phase to deliver the therapeutic agent directly at the pathological site was investigated. In particular, MBGs have been incorporated into an injectable Poly(ether urethane) (PEU) based thermosensitive hydrogel developed by Professor Ciardelli's group (DIMEAS, Politecnico di Torino, Italy). The high versatility of the resulting hybrid formulation can find widespread application in the biomedical field for the localized and sustained co-delivery of therapeutic ions and drugs in the treatment of a variety

of pathological conditions of soft (e.g., non-healing wounds) and hard (e.g., delayed bone healing) tissues. In fact, by tailoring the composition and the cargo of MBGs, different ions and drugs can be co-released based on the therapeutic effects required by the final application.

During this PhD project, by following MOZART project requirements, two different hybrid formulations based on Cu-containing MBGs loaded with ibuprofen (reported in chapter 3) and Sr-containing MBGs loaded with NAC (reported in chapter 4) embedded into the thermosensitive hydrogel were developed with the aim to validate *in vivo* an injectable platform for the prolonged and sustained release of therapeutic concentrations ions and drugs.

Finally, the therapeutic potential of the different developed systems through different *in vitro* and *in vivo* biological assessments was evaluated. Specifically, the *in vitro* biological response of the strontium-containing MBGs were carried out in collaboration with *Nobil Bio Ricerche Srl* and the related results are reported in chapter 4. The *in vivo* biological response to evaluate the safety and efficacy of the hybrid formulation based on Sr-containing MBGs loaded with NAC were carried out during the three months that I spent in Berlin at *Charitè – Universitätsmedizin Berlin* in collaboration with the group of *Dr. rer. Nat. Katharina Schmidt-Bleek* at the *Research Group "Bone healing" of the Julius Wolff Institute,* the MOZART partners involved in the *in vivo* experiments to confirm the safety and the efficacy of the device developed within the MOZART project. The related results are reported in chapter 4.

References

[1]   T. Winkler, F.A. Sass, G.N. Duda, K. Schmidt-Bleek, A review of biomaterials in bone defect healing, remaining shortcomings and future opportunities for bone tissue engineering, Bone Joint Res. 7 (2018) 232–243. doi:10.1302/2046-3758.73.BJR-2017-0270.R1.

[2]   N.P. Haas, Callusmodulation Fiktion oder Realität?, Chirurg. 71 (2000) 987–988.

[3]   C. Schlundt, C.H. Bucher, S. Tsitsilonis, H. Schell, G.N. Duda, K. Schmidt-Bleek, Clinical and Research Approaches to Treat Non-union Fracture, Curr. Osteoporos. Rep. 16 (2018) 155–168. doi:10.1007/s11914-018-0432-1.

[4]   M. Vallet-Regí, Evolution of bioceramics within the field of biomaterials, Comptes Rendus Chim. 13 (2010) 174–185. doi:10.1016/j.crci.2009.03.004.

[5]   X. Yan, C. Yu, X. Zhou, J. Tang, D. Zhao, Highly ordered mesoporous bioactive glasses with superior in vitro bone-forming bioactivities, Angew. Chemie - Int. Ed. 43 (2004) 5980–5984. doi:10.1002/anie.200460598.

[6]   X. Yan, C. Yu, X. Zhou, J. Tang, D. Zhao, Highly ordered mesoporous bioactive glasses with superior in vitro bone-forming bioactivities, Angew. Chemie - Int. Ed. 43 (2004) 5980–5984. doi:10.1002/anie.200460598.

[7]   A. López-Noriega, D. Arcos, I. Izquierdo-Barba, Y. Sakamoto, O. Terasaki, M. Vallet-Regí, Ordered mesoporous bioactive glasses for bone tissue regeneration, Chem. Mater. 18 (2006) 3137–3144. doi:10.1021/cm060488o.

[8]   F. Baino, S. Fiorilli, C. Vitale-Brovarone, Bioactive glass-based materials with hierarchical porosity for medical applications: Review of recent advances, Acta Biomater. 42 (2016) 18–32. doi:10.1016/j.actbio.2016.06.033.

[9]   Y. Li, Y.-Z. Liu, T. Long, X.-B. Yu, T. Tang, K.-R. Dai, B. Tian, Y.-P. Guo, Z.-A. Zhu, Mesoporous bioactive glass as a drug delivery system: fabrication, bactericidal properties and biocompatibility, J. Mater. Sci. Mater. Med. 24 (2013) 1951–1961. doi:10.1007/s10856-013-4960-z.

[10]   M. Vallet-Regí, Ordered mesoporous materials in the context of drug delivery systems and bone tissue engineering, Chem. - A Eur. J. 12 (2006) 5934–5943. doi:10.1002/chem.200600226.

[11]   A. Alenezi, Y. Naito, T. Terukina, W. Prananingrum, Y. Jinno, T. Tagami, T. Ozeki, S. Galli, R. Jimbo, Controlled release of clarithromycin from PLGA microspheres enhances bone regeneration in rabbit calvaria defects, J. Biomed. Mater. Res. Part B Appl. Biomater. 106 (2018) 201–208. doi:10.1002/jbm.b.33844.

[12]   J. Wu, G. Miao, Z. Zheng, Z. Li, W. Ren, C. Wu, Y. Li, Z. Huang, L. Yang, L. Guo, 3D printing mesoporous bioactive glass/sodium alginate/gelatin sustained release scaffolds for bone repair, J. Biomater. Appl. 33 (2019) 755–765.

doi:10.1177/0885328218810269.

[13] A. Anand, P. Das, S.K. Nandi, B. Kundu, Development of antibiotic loaded mesoporous bioactive glass and its drug release kinetics, Ceram. Int. 46 (2020) 5477–5483. doi:10.1016/j.ceramint.2019.10.264.

[14] C. Wu, J. Chang, Mesoporous bioactive glasses: structure characteristics, drug/growth factor delivery and bone regeneration application, Interface Focus. 2 (2012) 292–306. doi:10.1098/rsfs.2011.0121.

[15] J.H. Lee, A. El-Fiqi, N. Mandakhbayar, H.H. Lee, H.W. Kim, Drug/ion co-delivery multi-functional nanocarrier to regenerate infected tissue defect, Biomaterials. 142 (2017) 62–76. doi:10.1016/j.biomaterials.2017.07.014.

[16] W.H. Kuo, M.J. Wang, H.W. Chien, T.C. Wei, C. Lee, W.B. Tsai, Surface modification with poly(sulfobetaine methacrylate-co-acrylic acid) to reduce fibrinogen adsorption, platelet adhesion, and plasma coagulation, Biomacromolecules. (2011). doi:10.1021/bm2013185.

[17] A.J. Keefe, N.D. Brault, S. Jiang, Suppressing surface reconstruction of superhydrophobic PDMS using a superhydrophilic zwitterionic polymer, Biomacromolecules. (2012). doi:10.1021/bm300399s.

[18] S. Lin, J.R. Jones, The effect of serum proteins on apatite growth for 45S5 Bioglass and common sol-gel derived glass in SBF, (2018) 13–20.

CHAPTER 1

State of the Art

1.1 Introduction

The goal of this research work was to design and develop a multifunctional platform based on Mesoporous Bioactive Glasses (MBGs), to be used as therapeutic delivery system for biomedical application, in particular for bone regeneration. Different Active Pharmaceutical Ingredients (APIs) were identified and selected to exert a specific therapeutic effect, spanning from the pro-angiogenic properties to the anti-inflammatory and pro-osteogenic potential. Furthermore, different surface modification procedures were investigated, in order to both increase the therapeutic potential of the final device and to obtain a prolonged and sustained release of incorporated APIs. Finally, the developed MBGs, not exploitable alone as long-term therapeutics delivery systems for bone healing, were conjugated with a polymer phase able to both modulate the release kinetics and act as a vehicle phase to deliver the therapeutic agent directly at the pathological site.

In this chapter, an overview of the biomaterials used in biomedical fields for bone regeneration and the strategies adopted to develop the multifunctional platform will be described. In particular, after a general overview of the biological events involved in the bone healing process, in the section 1.3 a general description of the biomaterials designed for bone healing application will be described.

The section 1.4 is focused on Mesoporous Bioactive Glasses, which represent one of the most appealing biomaterials to be used as multifunctional devices for the delivery of APIs in the field of bone tissue regeneration. Since the MBG composition can be easily enriched with therapeutic ions selected depending on the

final target, the section 1.4.1 describes the biological effects of the most commonly employed therapeutic ions.

Moreover, by tailoring the MBG mesopore size, several therapeutic molecules, from small drug to large protein or growth factors, can be load with the idea to boost the therapeutic MBG potential. To this purpose, section 1.5 will extensively describe the different approaches to effectively load APIs into the MBGs mesopores.

Section 1.7 will focus on the strategies to functionalise MBG surface exploiting the high number of terminal hydroxyl groups with the aim to achieve several targets (*e.g.,* increased drug loading ability, API release modulation, anti-adhesive surfaces). Among the different strategies, particular attention was given to the *zwitterionization* procedure and the Layer by Layer deposition, investigated during this research work.

Finally, in the section 1.8, several strategies to design a hybrid functional formulation to be used as drug delivery systems will be described and discussed, with particular focus on injectable systems for bone regeneration and the adopted approaches to modulate the release kinetics of therapeutic agents at the pathological site.

1.2 Bone fracture healing process

Bone is one of the few tissues able to completely heal without the formation of a fibrous scar [1]. In fact, the bone fracture healing process recapitulates the pathway of embryonic bone development [2,3], and thus can be considered a kind of tissue regeneration. Despite this great regenerative potential, in 5-10% of the individuals [4], the fracture healing process fails under the conventional treatments, leading to a delay healing or, in the worst case, to a non-union [5]. These conditions can cause prolonged pain, disability, and long-term hospitalization, leading to deeply negative consequences in many aspects of life. Moreover, many factors of risk, such as the age or concomitant other pathologies, could further increase this number, also increasing the socio-economic impact. To date, the bone fragility due to the age causes around 9 million fractures [6]; with the continuous increasing of the population age, the pathologies which can further compromise the bone healing process, *e.g* the diabetes, are also expected to increase, causing a rose number of fractures and consequently a burden for the socio-economic and health care systems [7]. Based on these considerations, a thorough comprehension of the molecular and cellular mechanisms which take place during the fracture healing process is the essential prerequisite to identify the suitable strategy for the patient benefit.

Bone healing process is characterized by a finely orchestrated sequence of consecutive, but also overlapped, mechanisms able to completely regenerate the
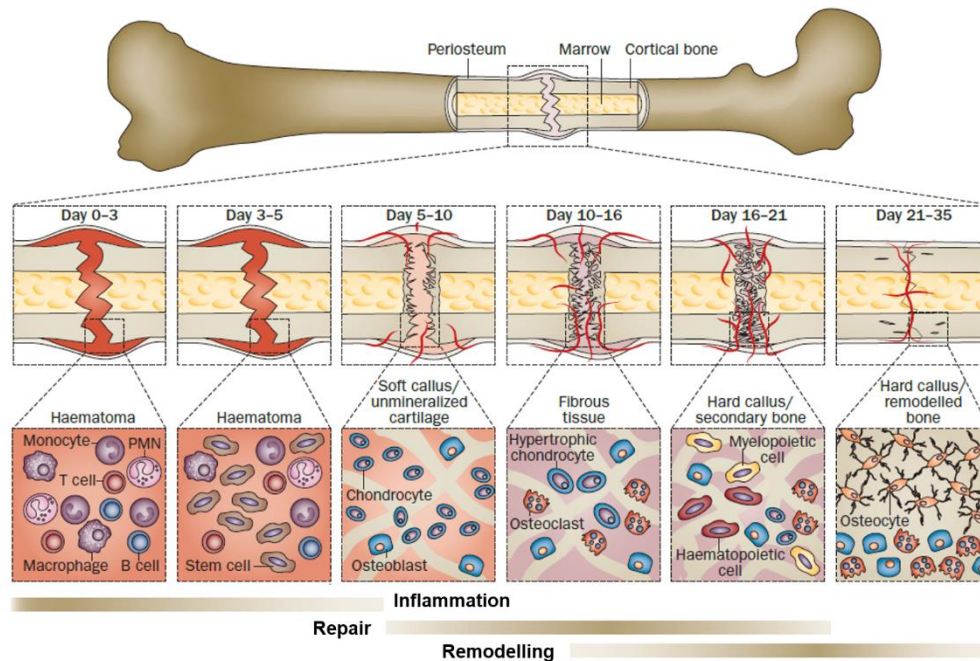
Figure 1.1 Bone fracture healing process.

original bone (*restitutio ad integrum*) [8]. As showed in figure 1.1, the bone fracture healing follows three overlapped steps: inflammation, repair and remodelling.

Inflammatory phase

The blood vessel rupture inside the bone and in the bordering soft tissue due to the fracture, promotes the beginning of the inflammatory phase and fracture healing [9,10]. This means that without inflammation, the bone is not able to heal. The inflammatory response allows the hematoma formation, which starts to coagulate into and around the fracture borders, generating a template for the callus development [1,11] and acting as a scaffold for the recruitment of additional inflammatory cells. The first cells involved at this stage are the polymorphonuclear neutrophils (PMNs), which secrete several chemokines such as the tumour necrosis factor-α (TNF-α) or the interleukin-1, able to engage longer-lived macrophages and promote angiogenesis [12].

Among the different interleukins, IL-1 and IL-6 can be considered the most important for fracture healing. In fact, IL-1, produced by macrophages during the acute phase of inflammation, stimulates the IL-6 in osteoblasts, promoting the formation of the primary cartilaginous callus, as well as the angiogenesis. On the other hands, IL-6 is involved in the angiogenesis process, by stimulating the vascular endothelial growth factor (VEGF) production, and the osteoblasts and osteoclasts differentiation [1,12,13]. The recruitment of these cells will play a crucial role during the repair stage.

At the same time, the migration of endothelial cells and fibroblasts occurs into the hematoma, leading to the formation of new blood vessels and the production of new collagen, respectively.

As specified above, the inflammation phase allows to prepare the tissue for the repair and healing; in fact, the secretion of TNF and IL- 6 is essential for the recruitment of the cells responsible of the tissue regeneration. The depletion of this phase can delay the mesenchymal stem cell differentiation and thus, the bone repair [4,14–16]. On the other hand, if the inflammation remains unsolved, complications such as a bacterial infection can occur, leading to a tissue damage and healing failure [8].

Repair phase

Gradually, a granulation tissue rich in cells, new vessels and collagen fibres replaces the hematoma [10,17]. Since this region is mechanically less stable, a soft callus is generated by the cartilaginous tissue to give the fracture a stable structure, followed secondarily by the generation of a hard callus [3,18]. The formation of these callus structures is strictly correlated to the recruitment of the Mesenchymal Stem Cells (MSCs). In fact, after the recruitment, MSCs activate a molecular cascade, which allows the production of collagen I and collagen II matrix as well as the induction of different peptide signalling molecules. Among them, the transforming growth factor-beta (TGF-β) superfamily members induce ossification [1], while the Bone Morphogenetic Proteins (BMPs) superfamily are involved in the bone repair process by recruiting the progenitor cells [19]. More in details, after approximately 10–14 days of proliferation, chondrocytes become hypertrophic, start to release calcium [10], which is transported into the extracellular matrix, where precipitates with phosphate to form apatite crystals [20]. After calcification, the cartilage is replaced by woven bone, and the structure results more solid and mechanically rigid [18]. Simultaneously, the blood vessels invade the calcified cartilage, allowing the recruitment of monocytes, which differentiate into osteoclast-like cells, enable to resorb the calcified cartilage, and MSCs which differentiate into osteoblasts able to fill the resorption lacunae with new bone [10,21]. At the end of this process, new bone tissue with a trabecular structure is obtained.

Remodelling phase

At this phase, the biomechanical properties of healthy bone are not completely restored. To reach the biomechanical stability, a second resorptive process with the replacement of the hard callus with a lamellar bone structure is necessary. To this purpose, the remodelling phase is orchestrated by a balance between osteoclasts, which resorb the hard callus resorption and osteoblasts which deposit lamellar bone. The remodelling process can take years in humans to fully regenerate the bone structure. During this time, the external callus is gradually replaced by a lamellar bone in order to re-establish a medullar cavity, typical of a diaphyseal bone [1,10,22].

After a gradually understanding of the molecular and cellular events occurring during the bone fracture healing process, several therapeutic approaches have been investigated, spanning from the use of biological strategies (*e.g* the employment of

MSCs, BMPs, platelet-rich plasma) to immunotherapy and mechanotherapy, with the aim to promote or facilitate the healing process. A well-designed therapeutic plan is expected to guide the physiological process of fracture healing to reach the union and thus increase the efficacy of orthopaedic surgical treatments [23–25]. To this purpose, the bone tissue engineering could represent an appealing alternative, by combining the use or stimulation of progenitor cells, such as MSCs, to induce osteogenesis, with osteoconductive biomaterials, in order to support the different stages of the bone healing process.

Over the recent years, a plethora of biomaterials gained the attention of the scientific community as alternative therapeutic treatments for bone regeneration and a detailed overview will be discussed in the following section.

1.3 Biomaterials for bone healing applications

Despite the fascinating bone ability to heal, regenerate and self-repair, bone defects especially those caused by trauma, cancer or concomitant diseases, can fail to heal and, thus, need a therapeutic approach for bone reconstruction [26,27]. Since non-healing bone defects are continuous growing, becoming a serious clinical issue, over the last decades, great efforts have been devoted to design and develop new bone biomaterials for bone repair [27–31]. To this purpose, the structure of the natural bone, reported in fig. 1.2, needs to be considered.
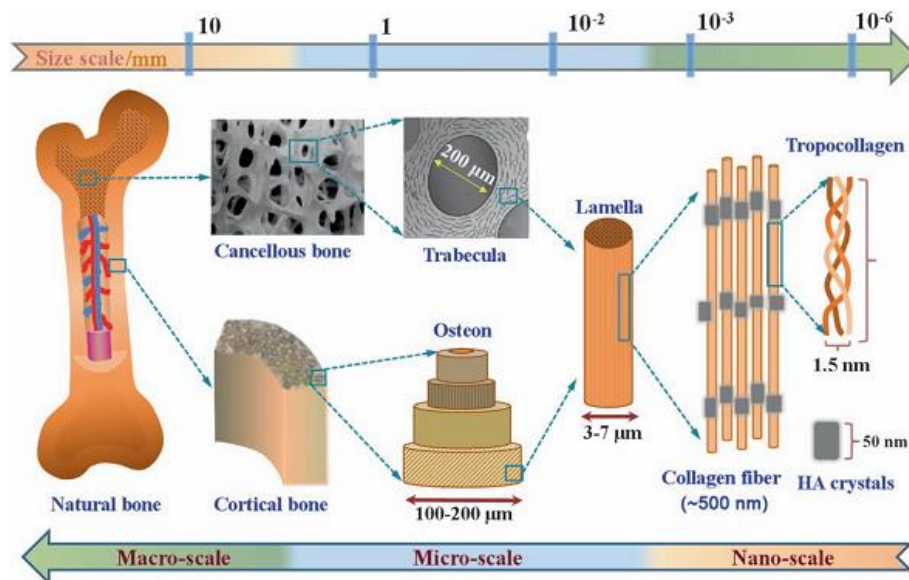
Figure 1.2 The chemical composition and multi-scale structure of natural bone.

Natural bone can be considered a composite material, with a remarkable and specific hierarchical architecture, constituted by organic and inorganic materials [27,32,33]. At the macroscale level, a cortical bone and a cancellous bone can be distinguished. The cortical bone represents the outer surface of the bone and is

composed by calcium (99%) and phosphate (90%), which make the bone relatively dense and strong. On the other hands, the cancellous bone, located inside the bone, results spongy, due to the presence of intertwining lamellar trabeculae [27]. Collagen fibres are the mainly component of the organic matrix, and contain tropocollagen, which provides the bone with a peculiar structure [27,34], due to the presence of the collagen, which is soft, and hydroxyapatite mineral, which is stiffer. On contrary, a specific strength is provided by the inorganic component, mainly made up of calcium (Ca) and phosphorus (P) in the form of hydroxyapatite (HA) crystals, sodium (Na), potassium (K), magnesium (Mg), fluoride (F), chlorine (Cl), carbonate (CO_3^{2-}), and some trace of silicon (Si), strontium (Sr), iron (Fe), zinc (Zn), and copper (Cu) [27,35].

However, this specific composition and structure can vary depending on the site of the defect, the patient age and living conditions, leading to different requirements for bone repair materials [36].

Based on these considerations, to date, the development of the ideal bone biomaterial, able to satisfy all the requirements for bone repair, is still a great challenge.

Nowadays, autologous bone grafting is still considered the "gold standard" for repairing bone defect in orthopaedic procedures [29,33,37].

The autologous bone graft is "*an osseous graft harvested from an anatomic site and transplanted to another site within the same individuals*"[33,38,39]. Thanks to the innate osteoconductive (the ability to support the attachment of osteoblast and osteo-progenitor cells), osteoinductive (the ability to induce differentiation) and osteogenic (osteo-differentiation and new bone formation) properties, the autologous bone graft is able to rapidly and completely integrate into the host bone [38,40], excluding any disease transmission or immunogenicity [26]. Despite the overmentioned promising features, some important drawbacks limit their application in clinical settings, such as donor site complication and pain, increased operative time, potential for donor site morbidity, limitation of special shape available and additional costs [30,33,41,42].

The use of bone allografts can be considered an alternative to overcome the limitations of autologous bone grafts.

Allografts refer to "*bony tissue harvested from one individual and transplanted to a genetically different individual of the same species*"[38,39], which can substitute the use of autografts when poor healing potential or non-union situations are observed [33]. Nevertheless, allografts can present immunogenic reactions, risk of viral transmission as well as higher risk of failure due to the activation of major histocompatibility complex (MHC) antigens [43].

To face these limitations, the interest in the discipline of bone substitutes and tissue engineering started to grow, making the biomaterial development a promising approach for repairing bone defects. The term "tissue engineering" can be defined as "*the utilization of a combination of multidisciplinary approaches to improve or*

Bone Tissue Engineering (BTE)

Scaffolds

Cells
Stem cells

Biomaterials

Biological features
Biocompatibility
Bioresorbability
Non immunogenic
Bioactive

Signals

Biophysical and chemical factors
Growth factors or other biomolecules
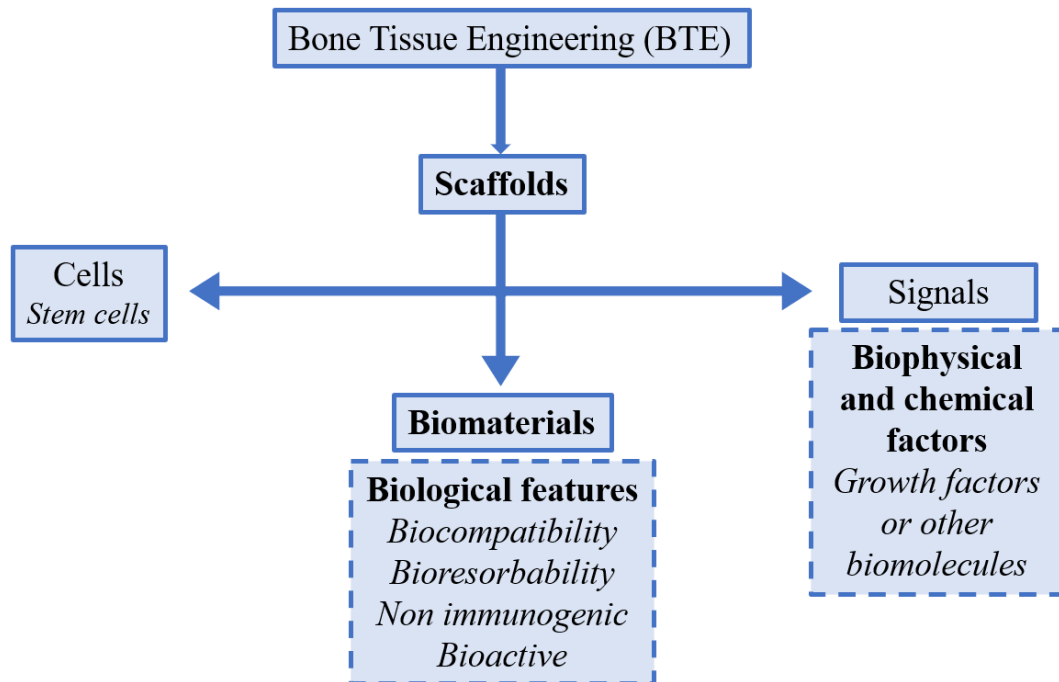
Figure 1.3 Strategies for bone tissue engineering.

replace biological tissues"[29,44]. Bone tissue engineering (BTE) aims to develop a bone scaffold, able to simultaneously induce the bone formation and act as a carrier for cells or other active agents. To this purpose, the biomaterial, a fundamental component of scaffolds, plays a crucial role in bone tissue engineering, as reported in figure 1.3. In fact, the use of a specific biomaterial could help to guide and control the structure and function of the regenerated tissue. Biomaterials can be defined as "*synthetic or natural materials to be used in medicine for therapeutic purposes and placed within the human body, in contact with the patient tissue*"[45]. Once in contact with the tissues, the biomaterials interact chemically, biologically and physically with the biological targets.

The first generation of biomaterials, appeared in the 1960s [46], were bioinert, with a minimal interaction with the surrounding tissues and aimed to replace the tissue, with no toxic reaction to the host. This category includes metals (titanium or titanium alloys), synthetic polymers (such as polymethyl methacrylate PMMA) and ceramics (alumina and zirconia).

The second generation of biomaterials, such as polymers (*e.g.,* collagen), calcium phosphates, calcium carbonate, calcium sulphates, and bioactive glasses, introduced some important features, among which the bioactivity, and the biodegradation in *vivo.*

Based on these fundamental characteristics, the third generation of biomaterials aimed to exert specific beneficial biological responses, through the combination with active substances, such as functional biomolecules or ions able to act as chemical or biological cues.

Since the biomaterials are supposed to remain in the body, the safety requirements such as biocompatibility and non-toxicity need to be satisfied. Moreover, the biomaterials must not be associated to inflammatory or immune responses, while need to induce an appropriate biological response. The controllable biodegradation, as well as an excellent bioactive behaviour are further fundamental prerequisites. The term bioactivity, as proposed for the first time in 1969 by Professor Hench, refers to the formation of a chemical bonding between biological tissues and bone biomaterials [47,48].

In order to maintain the function and the structure of woven bone, the biomaterial should not only fill the bone defect, but also degrade matching the growth rate of new bone. Moreover, since the biomaterial needs to provide structural support, mechanical properties and appropriate stability are required.

More importantly, the ideal biomaterial should exhibit osteoconduction, osteoinduction and osteogenesis. In fact, a good osteoinductivity allows to induce the differentiation of stem cells increasing the formation of new bone tissue; osteoconductivity provides a compatible interface between the biomaterial and the native tissue, allowing the attachment of osteoblasts and osteo-progenitor cells; osteogenesis refers to osteo-differentiation and formation of new bone integrated with the bone biomaterial [27,33,49–51].

Commonly, the evaluated bone biomaterials can be divided in three main categories: bioceramics, polymers, and biomedical metals [27,52]. As mentioned above, two of the fundamental criteria for a bone biomaterial are the biodegradation and the bioactivity and some polymers and metals resulted bio inert and not biodegradable. Furthermore, most of polymers and metals lack bioactivity and requires of mechanical interlocking to bind bone tissue. Based on these considerations, bioactive and biodegradable bioceramics gained particular attention for the regeneration and the replace of damaged bones. Some representatives of this category of bioactive biomaterial are Ca–P ceramics, Ca–Si ceramics and bioactive glasses.

Ca–P ceramics, which include hydroxyapatite HA [$Ca_{10}(PO_4)_6(OH)_2$] and tricalcium phosphate TCP [$Ca_3(PO_4)_2$], show a composition comparable to the inorganic phase of the natural bone [53,54], as well as a good biocompatibility, osteoconductivity and osteointegration features [31,55]. Furthermore, the released ions and degradation products have been demonstrated to enhance the bone healing process, by creating an alkaline environment which increases the cell activity [27,56]. Despite these undeniable features, the use of CaP in clinical application is still limited, due to the high fragility and unpredictable degradation rate; in fact, the resorption rate can be delayed due to the high crystallinity and Ca/P ratio and part of material can remain for years in the pathological site [31,57,58]. Since calcium plays a key role in the bone and blood vessel growth [59] while

silicon has been demonstrated to be beneficial to improve bone density [60], over the recent years, Ca-Si ceramics have been designed and developed. During the osteogenesis process, Si ions can enhance the degree of calcification, induce the collagen production and stimulate the differentiation and proliferation of osteoblasts [61,62]. Moreover, Ca-Si ceramics demonstrated higher mechanical properties, compared to the Ca-P ceramics [63,64], making them an efficient alternative for applications in bone repair.

At the beginning of 70s, Larry Hench discovered that certain compositions of Na_2O–CaO–P_2O_5–SiO_2 glasses were able to strongly bond the bone [65]. Since then, these glasses become known as "*bioactive glasses*" defined as "*biomaterials able to interact with the living tissue*". The first bioactive glass, denoted as Bioglass® 45S5, was obtained by a melt-quenching technique with a final composition of 45% SiO_2, 24.5% CaO, 24.5% Na_2O and 6% P_2O_5 (in wt. %)[66]. After soaking in a solution deprived of calcium or phosphates, Bioglass® 45S5 was able to create a hydroxyapatite layer on the glass surface, comparable to the interfacial hydroxyapatite crystals observed *in vivo* in the rat model [48]. The discovery of this HA formation paved the way to a several experiments aimed to understand the mechanisms of this surface reaction.

The mechanism of bioactivity is described as the series of reactions involved on the material surface in contact with body fluids [67,68] and is summarized in figure 1.4.
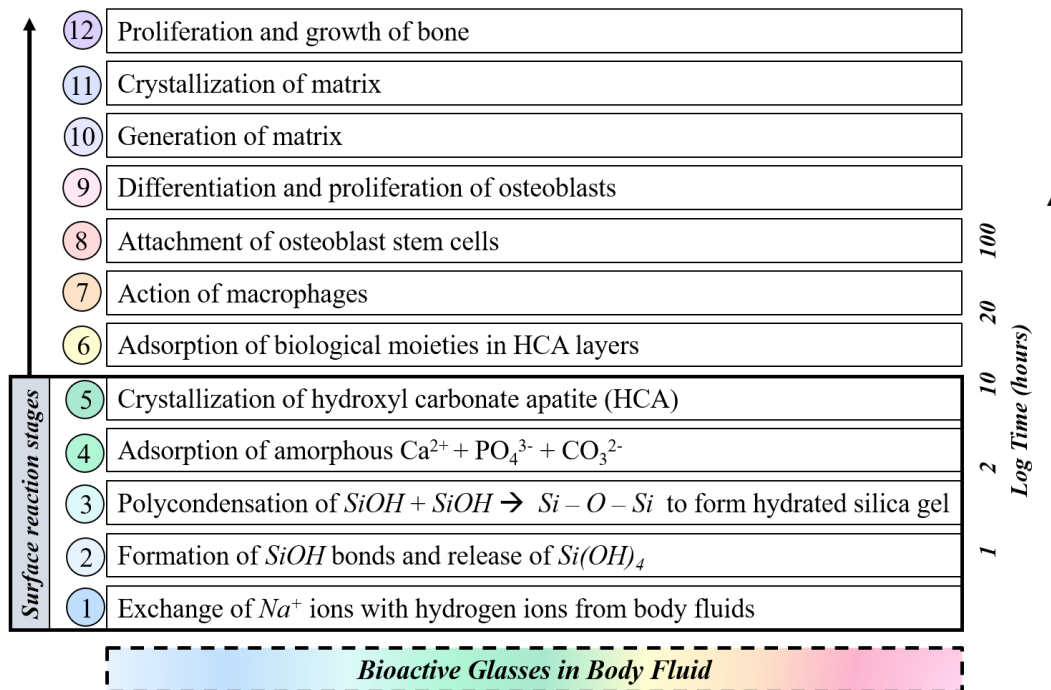
Figure 1.4 Reaction involved at the interface of a bioactive material and body fluid.

The first five reaction steps occur at the interface with the fluid which contain H^+ and H_3O^+ ions; the following seven reaction steps, on contrary, consist in cellular-dependent reactions which stimulate the proliferation and differentiation of osteoblasts and induce the new bone formation. More in details, a rapid exchange reaction involves Na^+ and Ca^{2+} from the glass surface with H^+ and H_3O^+ ions in solution, causing the hydrolysis of the silica groups and the formation of silanol (Si–OH) groups on the glass surface:

$$Si - O - Na^+ + H^+ \rightarrow Si - OH^+ + Na^+ \ (aq) \qquad (1)$$
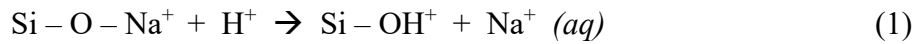
Since H^+ ions are consumed, the pH increases, leading to the dissolution of silica in form of silicic acid into the solution, and thus Si-OH groups continue to create on the glass surface:

$$Si - O - Si + H_2O \rightarrow Si\text{-}OH + OH\text{-}Si \qquad (2)$$
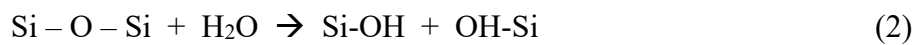
The polycondensation of an amorphous SiO_2-rich layer depleted in Na^+ and Ca^{2+} occurs on the surface. At this stage, Ca^{2+} ions and PO_4^{3-} groups migrate from the glass through the SiO_2-rich layer and from the solution, causing the deposition of an amorphous calcium phosphate layer on the top of the SiO_2-rich layer. The dissolution of the glass continues, the OH^- and $(CO_3)^{2-}$ groups from the solution are incorporated into the calcium-phosphate layer, which grows in size and starts to crystallize forming the hydroxyl carbonate apatite (HCA).
The stages from 6 to 12 involve the biological processes, in which the osteoprogenitor cells start to proliferate and differentiate. Simultaneously to the degradation of the bioactive glass, osteoblasts induce the extracellular matrix (collagen) formation and mineralization, forming a layer of nanocrystals and collagen on the surface of the material [67,68].

Among the different technique to prepare bioactive glasses, the most common investigated are the melt-quenching route and the sol-gel route.
The melt-quenching route allows to obtain glass by the fusion of a stoichiometric amounts of the different precursor oxides (*e.g.,* SiO_2, P_2O_5, Na_2CO_3, $CaCO_3$). These constituents are then mixed and melted. In order to obtain homogenous and uniform particle size, and thus facilitate the mixture of the precursors, the use of a ball mill for some hours is necessary. The obtained mixture is then transferred in a platinum or alumina crucible and melted in a high resistance furnace at high temperature (between 1100 and 1650 °C, up to 3 hours, depending on the composition of the glass).
After the glass melting, the material is poured into moulds which allow to select the desired shape or can be quenched in air, producing the so-called "frits" which are easily powdered.
Finally, the annealing step at 500 °C is required, in order to remove internal stresses from the glass. One of the drawbacks in the use of this technique is the difficult to melt glass which contain less than 10% of alkali oxide, due to the high viscosity [69,70].

Sol-gel route refers to the transformation of a colloidal suspension which contains the glass precursors into a solid network, involving several reaction steps, specifically hydrolysis, polycondensation, gelation, drying and dehydration.
Hydrolysis and polycondensation reactions allow to obtain a gel (a network composed by interconnected pores and polymeric chains), from a sol (dispersion of colloidal particles with a diameter ranging between 1 and 100 nm in a liquid). The gel is then aged, dried and dehydrated.

In details, the process starts with the preparation of the sol, usually by using a mixture of the desired alkoxide or usually obtained through the hydrolysis of the alkoxide precursors by using a catalyst which could be an acid or a base. The most commonly used silica-based network forming is the tetraethyl orthosilicate (TEOS). The hydrolysis of the TEOS usually by water induces the formation of silanol groups ($Si(OH)_4$), which in a second step start to interact, forming Si-O-Si bonds. Hydrolysis can be described as a nucleophilic attack in which the $O - R$ groups are substituted by the OH groups.
The polycondensation process leads to the formation of the silica network (SiO_2).
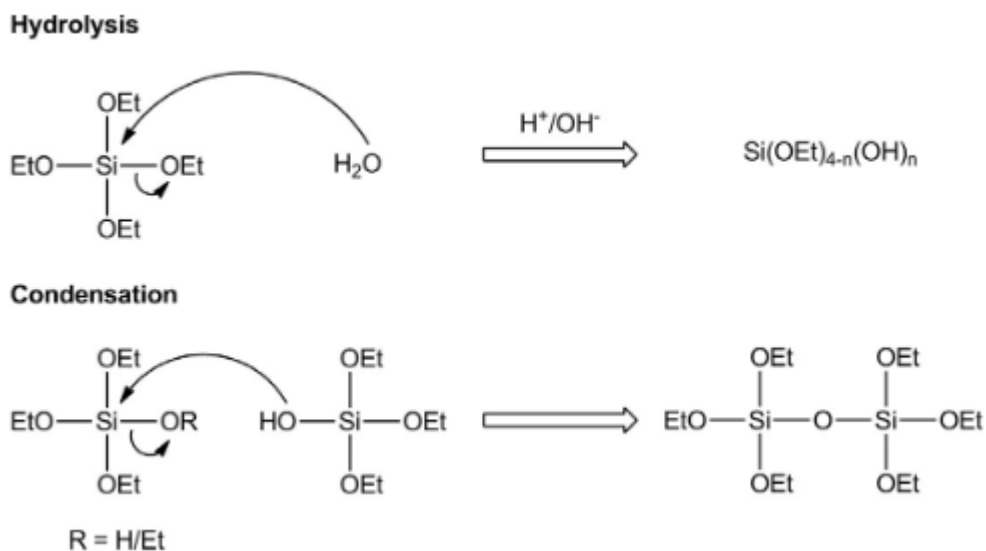
Figure 1.5 Formation of silica sol-gel from TEOS.

Hydrolysis and condensation reactions, reported in figure 1.5 [69,71], occur simultaneously, in fact condensation starts before complete hydrolysis is reached. Their kinetics depend on several factors such as the pH, composition, concentration of the species, temperature, precursor, pressure and the ratio between the mol of solvent and the mol of TEOS.
The gelation process follows the sol formation and is characterized by the creation of a three-dimensional network characterized with a pronounced increase of viscosity due to the cross-linking of silica particles.

The next step is the gel aging, during which a decrease in porosity and an increase in strength is observed due to the continued polycondensation and reprecipitation process of the gel. This phase could cause changes in the gel physical properties like pore volume, surface area and density, which will result hence in the final glass. The following drying step allows to remove the pore liquid from the formed 3D network. At the end, the resulting gel is heated at high temperatures, to ensure the complete elimination of pores, which results in the densification of the network [69,72].

Compared to the conventional melt-quenching route, the sol-gel technique presents several advantages, among which the possibility to produce glasses with high specific surface area and a nano-porous structure. These features lead to a faster degradation and thus to a faster conversion in HA, compared to the melt-derived glasses with the same final composition. Moreover, this route provides material with a less amount of contaminants, by also using a lower processing temperature. One of the most important advantages offered by the sol-gel approach is the possibility to tune forms and shapes, obtaining for examples fibres, foams and, more importantly, nano/micro sized particles [73,74]. In fact, the possibility to produce particles with nano and micro size becomes very appealing in the medical field application, since the first interaction between cells and biomaterials takes place in the nanoscale [75]. Moreover, the nano size of a material is directly correlated to the higher specific surface area and thus, to the bioactive behaviour. In fact, bioactive glasses in form of nanoparticles show a higher ion release rates, which induce a faster solubility, thus increasing the bioactivity [73,75].

To summarize, bioactive glasses have been demonstrated to be biocompatible, providing appropriate structural compatibility without any detrimental effects on living tissues. By tailoring the composition, the shape and the size several targets can be reached, allowing their exploitation in different applications. In fact, their ability to increase vascularization, osteoblast adhesion, and differentiation of mesenchymal stem cells enables their employment in bone tissue engineering as promising filler materials/coatings for bone scaffolds [70,76,77]. Despite all the described approaches to develop a material able to increase bone healing, current bone graft materials show several lacks, and the need to develop a "smarter" material is still an open issue [31]. In fact, an ideal biomaterial should also provide the delivery of active agents, with the final aim to address all the causes involved in the delay healing of bone [45].

The idea of combining in a single biomaterial the bioactivity typical of bioactive glasses with the loading and release of active agents able to provide specific biological effects would be one of the greatest achievements of biomaterial development [78].

To this purpose, silica-based mesoporous materials have been designed as multifunctional device, playing the double function of bioactive material and of release system for biologically active molecules able to improve bone regeneration [78]. Among them, over the recent years, Mesoporous Bioactive Glasses (MBGs)

continued to gain increasing attention and their production and their use in bone regeneration will be extensively discussed in the next section.

1.4 Mesoporous bioactive glasses

According to IUPAC (International Union of Pure and Applied Chemistry) classification, porous materials can be divided into 3 categories depending on their pore size [79].

- Microporous materials: pore size up to 2 nm
- Mesoporous materials: pore size between 2 and 50 nm
- Macroporous materials: pore size greater than 50 nm.

Mesoporous silica-based materials were firstly investigated in the 1990s, when Japanese academic investigators (Kuroda's group at Waseda University [80]) and Mobil Oil Corporation researchers (Kresge's group [81]) started to experiment new materials with pore size larger compared to the zeolites to increase their potential applications as adsorbents, catalysts and catalysts supports. The mechanism to obtain a mesoporous structure is based on the combination of supramolecular chemistry with the sol-gel process. A surfactant acts as template agent for the assembly, followed by the condensation of inorganic silica precursors [82]. A surfactant is an amphiphilic molecule, presenting both polar and nonpolar domains, which confers both hydrophilic and hydrophobic properties. Depending on their head group chemistry and charge, three types of surfactants can be distinguished: (i) cationic, if the hydrophilic group carries a positive charge; (ii) anionic, if the head group carries a negative charge, (iii) nonionic, if the hydrophilic group is not charged [83]. When placed in aqueous solutions, the surfactants are able to spontaneously assemble into micelles, with the hydrophilic head groups forming the outer surface and the hydrophobic tails pointing toward the centre [83]. After the removal of the template agent by calcination or solvent extraction, a mesoporous material presenting peculiar features (high surface area, large pore volume and abundance of silanol groups on the surface) is obtained.

Initially, these types of materials were supposed to be used for catalytic applications. In the 2001, Prof. Maria Vallet-Regì paved the way for a new application in the biomedical field, proposing the mesoporous silica as drug delivery systems. In fact, biological active molecules can be easily loaded into the mesoporous structure, as well as grafted on the silanol-rich surface exploiting the alkoxysylane chemistry, and thus released by diffusion-controlled way [82].

In the 2006, the bioactive behaviour of the mesoporous silica was demonstrated, by soaking the materials in simulated body fluid (SBF), although the kinetics formation of the hydroxyapatite layers appeared too slow compared to the conventional sol-gel glasses. This is the reason why mesoporous silica materials were not considered as innovative materials for bone healing applications [82,84].

An important step forward was achieved by the development of a material which combined the same composition of conventional sol-gel glasses and the structural features of the mesoporous silica, the Mesoporous Bioactive Glasses (MBGs). The MBGs, synthesized for the first time by Prof. DY Zhao (2004) [85] and Prof. M. Vallet-Regí (2006) [86], were nano-structured bioceramics, presenting a composition SiO_2- CaO-P_2O_5 similar to the conventional sol-gel glasses, combined with the structural and textural properties typical of the silica based mesoporous materials. MBGs were firstly synthesized by using an evaporation-induced self-assembly (EISA) process, described for the first time by Brinker *et al.* [87] in 1999. Compared to the conventional sol-gel route, which requires temperatures around 100 °C for the gel aging and dried stages, not compatible with the formation of an ordered micellar phase, the EISA process involves the use of volatile solvent, able to evaporate at room temperature, reaching the *cmc* (critical micellar concentration), and thus leading to self-assembly of the micelles [82,88]. Moreover, by following the typical hydrothermal preparation of silica-based materials, the presence of CaO acting as network modifier could interfere with the interactions between silica and surfactant [82].

Self-assembly, defined as the spontaneous organization of materials through noncovalent interactions, such as hydrogen bonding, Van der Waals forces, etc., is reached by using asymmetric molecules, able to organize into well-defined supra-molecular assemblies. As schematically reported in fig. 1.6, the self-assembly of an amphiphilic surfactant molecule begins with a homogeneous ethanol/water solution of soluble glass precursors and surfactant with a starting concentration $c_0 << cmc$. The solution becomes even more concentrated, due to the progressive evaporation of ethanol, driving the self-assembly of inorganic-surfactant micelles, resulting in the self-organization of micelles into liquid crystalline mesophase [82,83,87].
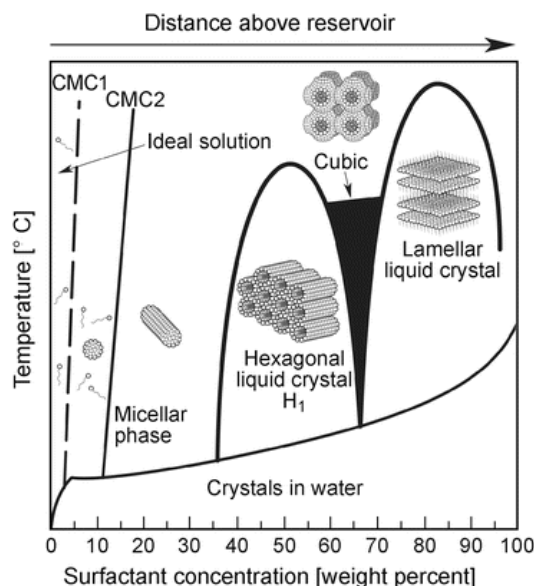
Figure 1.6 Schematic phase diagram of the CTAB (hexadecyltrimethylammonium bromide) surfactant in water.

In this strategy, schematically reported in fig.1.7, the starting solution is composed by the template agent (cationic or nonionic) such as cetyltrimethyl ammonium bromide (CTAB), P123 and F127, inorganic specie precursors (*e.g.,* TEOS, Ca $(NO_3)_2$, TEP), the volatile solvent (usually ethanol) and a catalyst (usually HCl). The reaction mixture is then transferred in a Petri dish and undergoes an evaporation-induced self-assembly (EISA) process. Once the mixture in the form of gel is dried, the surfactant is removed by calcination and a well-ordered mesoporous structure is obtained, exhibiting high surface area and porosity [89,90].
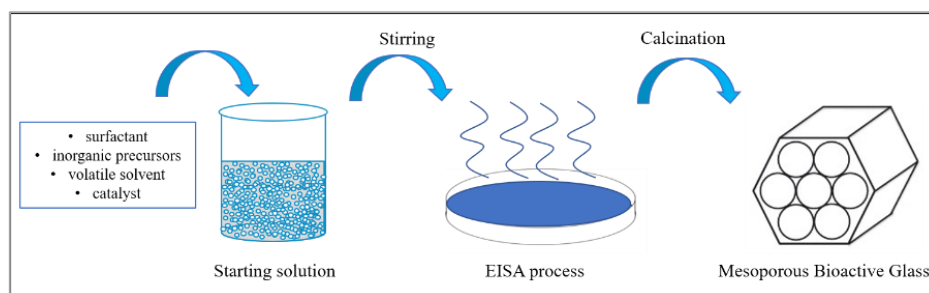
Figure 1.7 MBG synthesis through EISA process.

Despite the efficacy of the process, the EISA shows an important drawback, the impossibility to produce spherical homogeneous particles, due to the final glass grinding phase. In fact, a reliable and reproducible control over both the external morphology and the mesostructure of the material can be considered fundamental requirements to design a bone repair material or a drug delivery system [91].

To this purpose, during this PhD work, two different strategies have been investigated, in order to control the morphology of the produced MBGs.
The first approach consists in a conventional base-catalysed sol-gel process, which allows to produce spherical particles with size in the range of 100-200 nm.
The second approach refers to an aerosol assisted spray drying procedure, in which a solution similar to that used as starting solution in EISA approach, is sprayed by a heated gas carrier, producing micrometric particles in form of dried powders. The spray-drying technique allows, therefore, to decrease the evaporation time usually required by the EISA process and to increase the control and the repeatability of the final morphology of the particles, thanks to the automatic process which allows to avoid any variables induced by external parameters (*e.g.,* temperature and humidity) or by the operator. The use of these synthesis strategies allows to obtain mesoporous materials with different structural features and textural characteristics, by tailoring some parameters, such as surfactant nature and concentration, precursors, solvent or pH.
In particular, the introduction of the surfactant plays an important role in the biological response of the MBGs. In fact, Arcos *et al.* [91] demonstrated that the final pore size and volume can be tailored based on the surfactant chain length. Moreover, compared to the materials produced by using a nonionic surfactant, the

use of cationic surfactant led to a more ordered structure with smaller pore size and higher surface area [91,92]. The higher surface area and pore volume can be considered the main factors for the higher *in vitro* bioactivity of the MBGs, compared to traditional sol-gel and melt bioactive glasses with the same composition.

This effect is also extremely composition dependent, in fact the pure mesoporous silica are usually classified as nonbioactive materials [93]. The introduction of calcium in the MBGs framework, associated with the high surface area induces a faster and larger ion exchange when in contact with SBF, provoking the deposition of HA only after 4 hours [82]. Furthermore, the process is accelerated by the decrease of the pH, due to the calcium release, which induces the formation of octacalcium phosphate, a precursor of hydroxyapatite [92,94]. The composition of MBGs can be further enriched through the incorporation of specific elements (*i.e.,* Sr, Cu) with the aim to widen the well-known bioactive properties, combining in a single biomaterial several therapeutic abilities, such as pro-osteogenic, pro-angiogenic and antibacterial properties [95,96]. Thanks to the possibility to tailor the pore volume, several active agents can be hosted, thus, as mentioned before, the mesoporous bioactive glasses can be exploited and employed as drug-delivery systems for bone tissue regeneration. In addition, the high amount of silanol groups on the MBG surface allows the functionalization with different organic moieties (*i.e.,* alkoxylanes) leading to a tailorable drug loading and release [84].

All of the above-mentioned aspects will be discussed in detail in the following sections.

1.4.1 Ion-containing Mesoporous Bioactive Glasses

Over the recent years, many efforts have been devoted to increase the biological performance of the MBGs, by incorporating into the silica framework, metallic ions which were proved to exert specific biological functions (such as antibacterial effect, pro-angiogenic potential, pro- osteogenic potential).

Compared to the use of growth factor, recombinant proteins or other genetic engineering approaches, which can result expensive, associated to a higher risk and short shelf life, the introduction of metallic ions presents several advantages [62,97]. Therapeutic ions are more stable and not susceptible to the high temperatures, solvent or pressure usually involved in the synthesis process, which can on contrary, damage the degradation of biological molecules. Moreover, several inorganic ions are involved in several cellular functions, inducing secondary signals by activating ion channels or interacting with other ions or with macromolecules [98].

In the schematic illustration reported in fig.1.8, different therapeutic effects exerted by some metallic ions are summarized, highlighting their beneficial role in the production of multifunctional platform to be used in several applications.
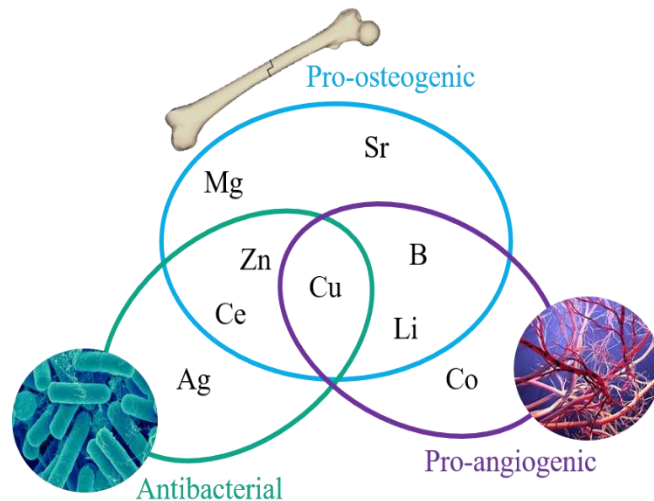
Figure 1.8 Therapeutic effects of the most used metallic ions.

Despite the promising therapeutic potential, during the design of a biomaterial based on ion-containing mesoporous bioactive glasses, the possible cytotoxic effects are important parameters to take into account. In fact, the uncontrolled release, in terms of concentration and release kinetics, could cause side and undesired reactions. Since "*everything is poisonous and nothing is non-toxic, only the dose makes something not poisonous*" [99], the challenge in using inorganic ions for bone healing applications is to identify their correct therapeutic window.

Biological response to copper

Copper is a metal ion present in trace in adult (~100 mg) which has been proved to play an important role in the angiogenesis process [100,101]. A significant distribution of cellular copper has been demonstrated in human endothelial cells, where the ion is able to induce the angiogenic process [102], by coupling with angiogenesis growth factor FGF-2 *in vitro* [101] and by stimulating the proliferation of human endothelial cells [100]. The effect of this ion, when released by a biomaterial, has been investigated in the literature by several studies. Lin and co-workers [103] investigated the effect of copper ions released from a scaffold containing 2% molar of the ion, confirming its ability to promote the growth of new vessel in the fibrous tissue of rat calvarial defects. Moreover, the number of new capillaries was proved to increase with the increasing of copper concentration. More recently, Romero-Sanchez *et al.* [104] investigated the effect of copper-containing MBGs (5%mol of copper) on zebrafish model, showing the increasing in cell proliferation as well as the increasing of the sub-intestinal vessel thickness after the exposure to the ionic products of degradation of copper-containing sample. In addition, Dziadek *et al.* [105] demonstrated the increase in VEGF secretion induced by the copper released by bioactive glasses doped with 1%mol of copper.

Along with the pro-angiogenic effect, the osteogenesis response of the copper has been evaluated. In fact, several studies demonstrated that copper can induce an increase of the differentiation of mesenchymal stem cells (MSC) towards the osteogenic lineage [100,106] as well as the inhibition of the osteoclast activity [107]. The release of copper ions from a titanium implant has been proved to induce differentiation of human bone marrow derived mesenchymal stem cells to osteoblasts, resulting in the expression of collagen type I and the complete mineralization [108]. Despite this evidence, the mechanism behind the possible positive effect of Cu on bone metabolism is still mostly unclear. In fact, several authors reported that copper supplements do not exhibit any effect on biochemical markers of bone formation or bone resorption [109]. On contrary, copper can in some cases decrease the rat bone tissue in *vivo* and in *vitro* [110].

On the contrary, the well know anti-bacterial potential of copper was already clear since ancient Egyptian. Over the years, the number of studies conducted in order to understand the antibacterial mechanism and to exploit this beneficial effect has grown considerably [111], also promoted by the need to find effective solutions able to contrast the antibiotic resistance [112]. Copper, has been used in the past for treating drinking water, wounds, healing ulcers and skin [113,114]. Surprisingly, during the cholera epidemic of the 1800s copper workers have been affected less compared to others, suggesting that copper may be a bacterial fighting element [115].

The antibacterial mechanism which explains how copper may fight bacteria refers to several hypothesis, spanning from the damage of the bacterial cell wall [116] to the formation of reactive oxygen species (ROS) able to damage the bacterial DNA [117]. Figure 1.9 shows the mechanism of action of copper ions: copper causes the rupture of the membrane and consequently the loss of cytoplasmic content (step 1); moreover, the generation of ROS (step 2) causes stress and a further cell damage leading to the degradation of DNA (step 3).
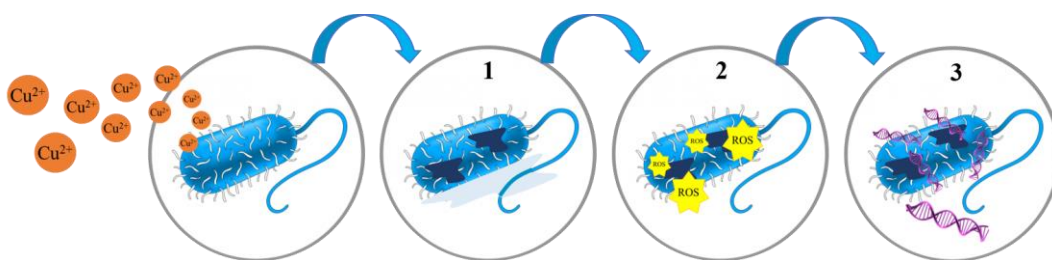
Figure 1.9 Mechanism of action of copper ion released.

The antibacterial property of copper-containing MBG scaffold was tested by Wu *et al.* [118] which demonstrated the reduction of bacteria after 7 days of incubation ascribable to the potential of copper to cause ROS formation.
The antibacterial property of copper-containing MBG has been evaluated also by

Bari *et al.* [119], who analyzed both the synthesized nanoparticles and their extracts. The final results report a bacterial viability reduction for both *E. Coli* and *S. Aureus* (70-75%) and for *S. epidermidis* (50%).

Despite the evident potential of copper as pro-angiogenic and anti-bacterial agent, copper shows a very narrow therapeutic window and the minimal dosage able to exert the therapeutic effect without causing cytotoxicity needs to be carefully investigated.

Wang et. al reported that the antibacterial and pro-angiogenic effects of released copper ions from biocomposites of copper-containing MBG and nanofibrillated cellulose are evident at higher released Cu^{2+} concentration, but this beneficial role of copper is also associated to a higher level of cytotoxicity [120]. Similarly, Rath and co-workers reported that the osteogenic genes are multi-fold expressed only by using high Cu^{2+} concentrations, highlighting that the same effect is not revealed by using low concentration. However, at the same time, highest Cu^{2+} concentration were found to increase cytotoxicity and hence decrease cell viability [121]. Based on these considerations, the correct copper dosage could be considered a critical issue and caution in the use of Cu-containing products needs to be observed, underling the importance of finding the range of doses able to produce therapeutic response without causing any cytotoxicity.

Biological response to strontium

Strontium is an alkaline earth element present in trace in bone [122]. Due to the size and behaviour similar to calcium, the mechanism of action in bone metabolism is ascribable to the affinity between calcium and strontium, allowing Sr to share some osteoblast-mediated processes usually induced by calcium. Considering its effect on osteoclastogenesis, osteoblastogenesis and adipogenesis, Sr is considered as an alternative strategy to treat osteoporosis disease. As reported in figure 1.10, strontium is able to activate the calcium sensing receptor (CaSR), in both osteoblasts and osteoclasts, causing an opposite effect: promotion of the osteoblast activity and inhibition of the osteoclast activity. Briefly, the induction of bone
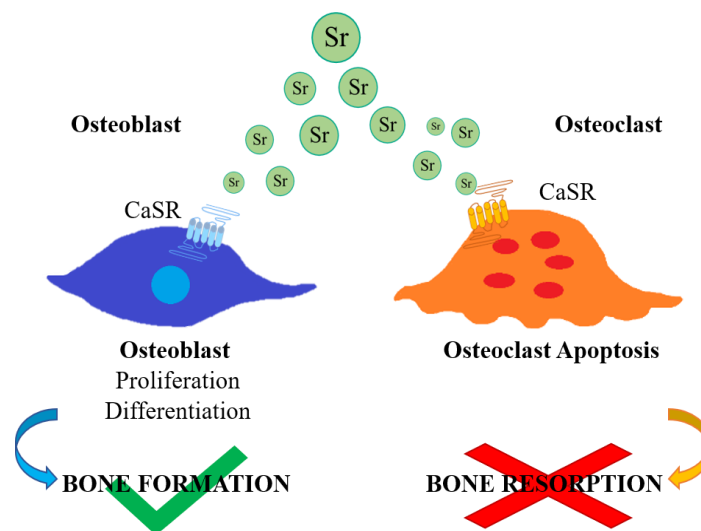
Figure 1.10 Role of strontium on the calcium sensing receptor.

formation is due to the stimulation of different signaling pathways which promote the osteoblast proliferation and differentiation. On the other hands, the activation of the CaSR leads to the osteoclast apoptosis, inhibiting thus their resorbing activity.

Strontium plays an important role also in the osteoclast differentiation by modulating the RANK/RANKL/osteoprotegerin (OPG) pathway. RANKL (receptor activator of nuclear factor-kappaB ligand) induces osteoclastogenesis and bone resorption when binds RANK (receptor activator of nuclear factor-kappaB), an important factor for osteoclast differentiation. OPG is a molecule involved in bone density and mass regulation and results overexpressed by the strontium stimulation. The overexpression of OPG induces the inhibition of the RANKL expression, thus inhibiting the RANKL-induced osteocalstogenesis [123–126]. The role of strontium released by bioactive glasses in the regulation of the osteoclast and osteoblast activity has been investigated by Gentleman *et al.* [127], who replaced part of the calcium with strontium into BG framework. This study evidenced the inhibition of osteoclast differentiation, confirmed by the reducing of erosion pit area (indicator of osteoclast activity). Moreover, the increasing of the osteoblast proliferation and ALP activity further confirms the in *vitro* ability of strontium to stimulate osteoblastogenesis.
Based on these considerations and the well consolidated role of strontium on bone formation, the strontium ranelate, a strontium salt, has been clinically prescribed in Europe as treatment for postmenopausal women with osteoporosis [33], also if the drug has not yet been approved by the FDA so far. Despite the beneficial effect, several side effects referring to cardiovascular risks have been encountered, leading to the suspension of this drug in 2013 [128].

During this PhD thesis, the biological response of Sr-containing mesoporous bioactive glasses was evaluated in terms of cell viability, inflammatory response and anti-osteoclastogenesis activity. By monitoring the RANKL and OPG pathways, an inhibition of osteoclast activity with a RANKL/OPG ratio in favor of OPG induced by the released strontium ions has been observed [95], thus proving the beneficial role of this ion for bone regenerative applications.

Biological response to boron

Boron is present in human body, and beyond the involvement in embryo genesis, inflammatory and immune response [129,130] seems to exert a positive effect on bone and brain health. The effect of the released boron from boron-containing MBG scaffold was evaluated by Wu and co-workers [131], which demonstrated the increasing in osteoblasts proliferation in *vitro*. Gorustovich *et al.* [132] reported the in *vivo* evaluation of B-modified bioactive glass particles, in which part of silicon has been replaced by boron. After 15 days of implantation in rat tibia bone marrow, new bone tissue formation have been observed, characterized by Ca/P ratio close to the hydroxyapatite one [133].
Along with the pro-osteogenic effect, the pro-angiogenic potential induced by

boron gained interest and has been investigated [134], by evaluating in particular the boron effect on the VEGF secretion from bone marrow stromal cells. In fact, the released boron has been proved to be beneficial in the promotion of the cell mitochondrial activity as well as in the enhancement of the VEGF release, strictly connected to the angiogenic processes.

In addition, Haro Duran *et al.* [135] evaluated the boron pro-angiogenic ability by studying the vasculature of the embryonic quail chorioallantoic membrane (CAM assay), after the contact with the dissolution products produced by 45S5 bioglass doped with 2% of boron (in wt.). Several integrins, cytokines and/or growth factors involved in the pro-angiogenic process have been secreted highlighting the pro-angiogenic potential of boron correlated to the proliferation of endothelial cells of the vessel.

Biological response to lithium

Lithium (Li) has been widely employed as treatment of bipolar disease and recently gained further consideration due to its role in the osteogenesis processes [136]. In a clinical study, which involved lithium-treated patients, the mean bone mineral density evaluated in the treated group was significantly higher compared to the non-treated participants [137]. The mechanism behind osteogenesis seems to be associated to the modulation of the Wnt signalling pathway [138,139] as well as the activation of β-catenin signalling, responsible to mediate the proliferation, differentiation and maturation of osteoblasts [138,140], during bone fracture healing process [33].

Biological response to cobalt

Cobalt is a constituent of vitamin B12, which is well known to stimulate the production of red blood cells. Over the recent years, cobalt has been identified as element able to increase the angiogenesis [97]. The mechanism of action has supposed to be related to the hypoxia mimicking capacity through the stabilization of hypoxia inducible factor-1 (HIF-1α) [141,142]. Wu and co-workers [143] demonstrated the efficacy of cobalt-containing mesoporous bioactive glass (MBG) scaffolds to stimulate the hypoxia cascade by activating and stabilizing the hypoxia inducible factor-1 (HIF-1), which is subsequently able to increase the expression of HIF- α target genes, such as VEGF, thus leading to an enhance of vascularization[33,144].

Despite the beneficial effect on biomedical applications, again a high dosage or an uncontrolled release may cause severe detrimental effects, by inducing cell apoptosis, inflammatory response and genotoxic effect [145].

Biological response to magnesium

Over 60% of the magnesium present in the body is accumulated in bone and teeth [146], suggesting the importance of this element in the bone process and thus in the potential therapeutic approaches in orthopaedic clinics. In fact, the depletion of magnesium has been proved to decrease the systemic bone density on rats [147].

On contrary, a Mg-rich diet seems to be beneficial, by efficiently preventing the reduction of bone mineral density (BMD) in patients with osteoporosis [33]. When used with the correct dosage, magnesium is able to up-regulate the pre-osteoblasts viability in mouse, by increasing the stimulation of alkaline phosphate (ALP) activity of osteoblasts as well as the expression of type I collagen (Coll 1) and osteopontin (Opn) [148,149]. For these reasons, several researches focused the attention on biological activities induced by magnesium-doped biomaterial. Interestingly, Suchanek and co-workers [150] demonstrated that a controlled and sustained release of Mg improved the osteoblast attachment and proliferation as well as the ALP production. The osteogenic properties were also improved in *vivo*, observing the inhibition of the osteoclast formation, polarization, and osteoclast bone resorption [151].

Based on these considerations, the importance of Mg dosage is evident and, depending on the selected concentration, a different modulation of osteoblast/osteoclast activity can be evaluated.

Biological response to zinc

Zinc is an essential element present in trace in human body. It is involved in several regulatory actions such as cellular response, oxidative stress, DNA repair, cell apoptosis, and most importantly the regulation of ALP. In fact, ALP is a zinc enzyme, which presents three closely spaced metal ions (two Zn ions and one Mg ion) at the active centre [152]. A zinc deficiency can thus cause the inactivation of ALP activity due to the dissociation of an active centre Zn [153]. In addition, zinc plays a key role in the growing and maintenance of bone. Zinc has proved to stimulate the osteoblastic bone formation and mineralization as well as inhibit osteoclastic bone resorption, resulting an important factor in the osteoporosis [154].

As far as the osteoblastic bone formation is concerned, zinc is involved in the stimulation of the gene expression of several proteins such as Runx2/Cbfa1 (the transcription factor for differentiation into osteoclastic cells), collagen I, ALP and OCN, along with the increasing of the production of growth factors involved in human osteoblast proliferation (IGF-I and TGF-β1) [154]. On contrary, the bone resorption is due to the inhibition of RANKL, the receptor involved in osteoclast differentiation. Several authors investigated the role of the released zinc from Zn-containing bioactive glasses [155,156]. In all cases, the stimulation of osteoblast differentiation, due to an increase of ALP activity have been observed. Yamada *et al.*[157], moreover, demonstrated the inhibition of resorptive activity in mature osteoclasts, induced by ceramics containing 0.6 wt.% of zinc.

In addition, zinc presents a pronounced antibacterial potential [158,159], probably ascribed to oxidative stress induced by both zinc ions and ZnO.

Despite these evidences confirmed the pro-osteogenic properties and antibacterial abilities of zinc, controversial results are reported, due to the discrepancy between the in *vitro* studies and in *vivo* studies.

Biological response to cerium

Cerium is the first element in the lanthanide group, characterized by a similar ionic radius to calcium, but having a higher charge, and thus a high affinity for Ca^{2+} sites on biological species [160–162]. Thanks to the possibility to work in both oxidized (Ce^{4+}) and reduced (Ce^{3+}) forms, cerium can be employed as catalyst, antioxidant-enzyme-like agent (superoxide dismutase mimic, catalase mimic peroxidase-like mimic) and as hydroxyl and nitric oxide radical scavenging agent [163]. In particular, this peculiarity allows the use of cerium as potential therapeutic antioxidant agent [161,163–165] in oxidative stress-related disease and chronic inflammation. As previously reported in fig. 1.11, cerium shows both osteoconductive and antibacterial properties. Morais *et al.* [166] demonstrated the antibacterial properties of cerium-containing glass, evaluating the bacterial adhesion of the material against *S. Aureus*, *S. epidermidis* and *P. Aeruginosa.* Cerium is resulted to decrease the bacterial adhesion of the gram-positive strains but showing no effect against the gram-negative. This behavior could be ascribed to the complex wall of the gram-negative bacteria, composed by peptidoglycan layer and lipidic membrane, resulting less permeable to cerium ions. Moreover, in the same work, cerium ions resulted to increase cell proliferation and an up-regulation on ALP and BMP-2 expression of human osteoblastic-like cell.

The antibacterial potential has been also proved by Lin and co-workers [167], which reported an increasing inhibition zone, by increasing the cerium concentration. The mechanism of action (figure 1.11) which can explain the antibacterial effect of
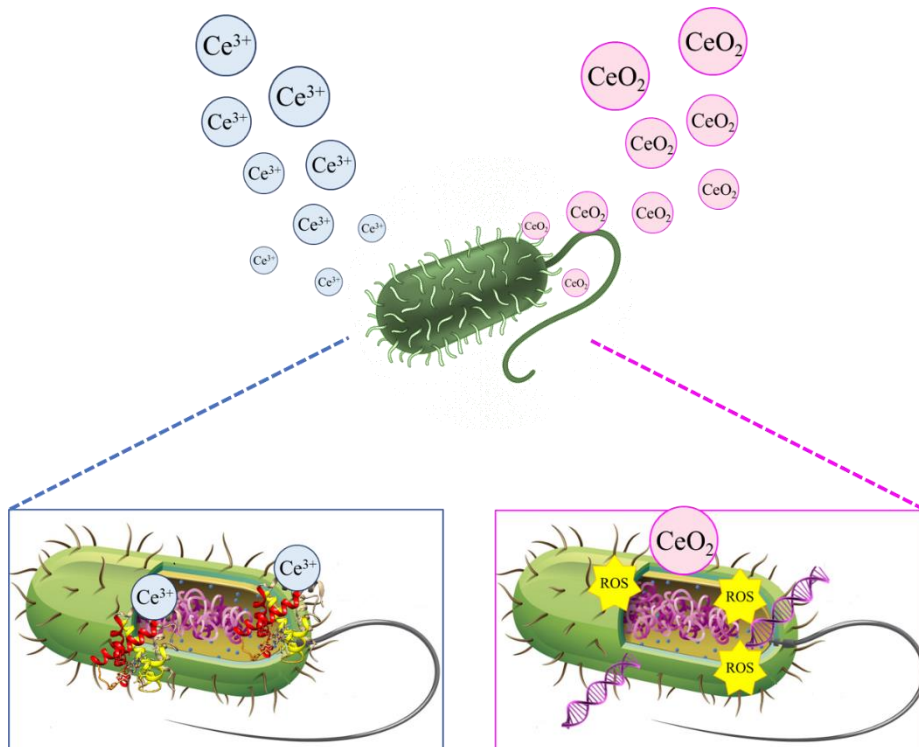
Figure 1.11 Cerium antibacterial mechanism of action.

cerium could be associated to the presence of Ce^{3+} [168–170], able to rapidly bind the protein membrane, decreasing the membrane permeability and causing the bacteria death [171]. Moreover, despite the previously reported antioxidative property of the cerium oxide composites, CeO_2 could also exhibit a pro-oxidative behavior, responsible to the oxidative stress which results toxic for bacterial cells [172].

Hu and co-workers [173] discussed the pro-osteogenic abilities of cerium, showing an increase of the bone marrow stromal cells (BMSCs) migration and differentiation induced by cerium. The mechanism of action seems to be associated to the capability of cerium to stimulate the BMP-2, a well-known protein able to promote osteogenic differentiation. BMP-2 binds the BMPR2, which consequently activate BMPR1, responsible of the regulation of cell differentiation and growth by the phosphorylation and translocation in the nucleus of the protein Smad1/5/8. The activation of the protein Smad1/5/8 induces the up-regulation of the genes related to osteogenic differentiation (Runx2 and SDF-1) [173].

1.5 Drug-loaded Mesoporous bioactive glasses

Over the recent years, the need of effective and safe drug delivery systems continued to increase, in order to develop new therapeutic approaches [174,175]. Specifically, in the field of bone tissue regeneration, the need to develop drug delivery systems is due to several factors, including poor blood circulation and inadequate tissue penetration of bone tissue. Moreover, conventional administration routes, *e.g.,* injection or oral administration, still encountered several drawbacks, presenting low therapeutic tissue levels or, on contrary, serious side effects due to the incapability of the API to reach efficiently and adequately the pathological site [176]. Based on these considerations, the design of a delivery system able to provide local and sustained release over time, and to simultaneously protect the API from degradation, results to be an important challenge in the biomedical industry. Among all the investigated available drug delivery systems, mesoporous bioactive glasses encountered all the above mentioned requirements [177].

The potential of mesoporous silica-based material as controlled delivery system has been identified for the first time by Prof. Maria Vallet-Regì in 2001 [178] who paves the way to a new class of drug delivery biomaterials. In 2006, Xia et.al [179] reported for the first time the drug release properties of well-ordered MBGs and their abilities to increase the delivery of poorly soluble drugs was subsequently investigated [86,180–182]. In fact, the loaded drugs confined into the mesopores do not retain their original crystalline structure but exist in a stabilized amorphous state. Since the amorphous form of a drug has been proved to exhibit higher solubility compared to the crystalline counterpart [183], the confinement into the mesoporous structure could represent a promising strategy to improve the dissolution of several poorly soluble molecules and thus their bioavailability.

To date, the most investigated controlled drug delivery systems are based on biopolymers (*i.e.*, gelatin, chitosan, polycaprolactone) [184–187]. However, most of them cannot be considered suitable for bone repair as filling materials, due to their incapability to chemically bond to living bone. On the contrary, MBGs show a remarkable bioactivity (as discussed in section 1.4) along with several attractive features. In fact, their high exposed surface area and large pore volume allow the loading of drugs and biologically active molecules which can be successively released in a controlled manner, by exploiting the diffusion mechanism (as schematically illustrated in fig. 1.12). The drug loading, dissolution and release kinetics depend on several features, such as high surface area, large pore volume, pore size, and surface functionalisation [175,177].
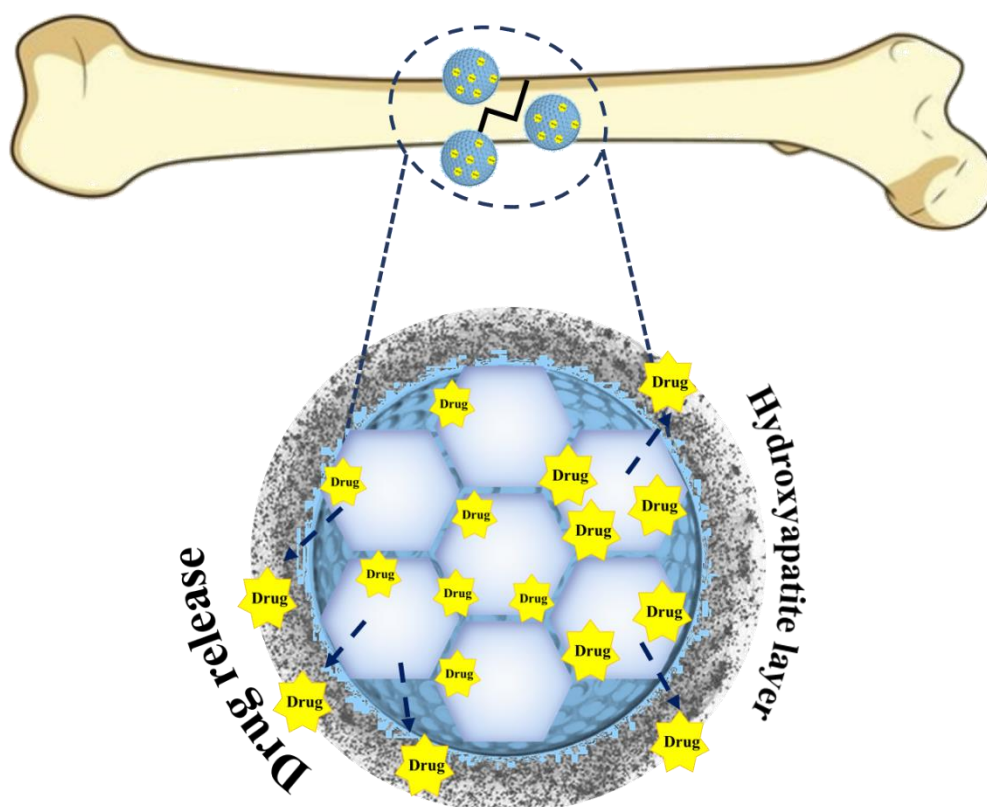
Figure 1.12 Schematically illustration of the use of MBGs as drug delivery system for bone repair.

In addition, MBGs result to be stable upon storage [188] and more resistant to pH, heat, mechanical stress and degradations compared to the most investigated polymer materials used as drug delivery systems [175].
The adsorption of API into the mesoporous structure is expected to be governed by size selectivity, such as the mesopore size and the size of the molecule to be loaded. Depending on the surfactant length employed during the synthesis of MBGs, and thus on the mesopore size, the mesopore is able to host from small molecules to macromolecules such as growth factors and proteins. The size selectivity needs to be taken in account as adsorption parameter. In fact, if the drug to be hosted is smaller compared to the mesopore size, it could be confined in the inner part of the

mesopores. On contrary, if the drug is larger, the adsorption could occur on the external surface of the material, thus influencing the release rate [177]. The relationship between the pore size and the release kinetics has been investigated and discussed by Prof. Vallet-Regì *et al.* [189], loading ibuprofen as model drug into the MCM-41 mesoporous material. As expected, results refer a faster ibuprofen release kinetics for materials with the largest pore diameter.

Along with the mesopore size, also the specific surface area could play a key role in the amount of adsorbed therapeutic agent, as well described in literature by using different drugs. For examples, Balas *et al.* [190] investigated the alendronate loading into two different mesoporous silica materials, MCM-41 an SBA-15, presenting the same mesostructure, but different pore size, 3 and 9 nm respectively, and specific surface area (1157 and 719 m^2 g^{-1} respectively). The calculated maximum amount of incorporated drugs was reported to be 14% w/w and 8% w/w for MCM-41 and SBA-15, respectively, thus confirming the dependence between the drug loading on the surface area. On consequence, the specific surface area also influences the release rate. In fact, the higher the specific surface area, the slower the release due to a greater molecular retention, ascribable to the more extensive area available for the drug-matrix interactions [177,189].

Once the chemical mesoporous matrix and the drug have been selected according to final application, the therapeutic potential and the drug chemical nature, the most suitable drug loading procedure can be selected. Several techniques have been developed over the last years for drug loading into mesoporous materials, mainly categorized as solvent-free and solvent-based methods [191,192] (figure 1.13).

The solvent-free approach is based on a physical mixing of the components, followed by a heating process which allows to melt the drug or by a co-milling between the drug and the material. The solvent-free method offers several advantages, since presents a low environmental impact and allows to avoid the removal of the residual solvent. Despite the green approach, these methods need an optimization on term of loading efficiency and require thermally stable drugs. On contrary, the solvent-based method is simply based on the dissolution of the drugs into a solvent and the resulting solution is then contacted with the mesoporous material. At the end of the process, solvent is removed by evaporation or appropriate drying techniques. The type of solvent, the drug chemical-physical features, the specific surface area, and the pore volume/size of the mesoporous materials are fundamental factors that can influence the overall drug loading process. Compared to solvent-free techniques, the solvent-based approach is proved to exhibit high loading efficiency, but, on the other hands, requires additional steps to remove the solvent prior to the final application [191,192].
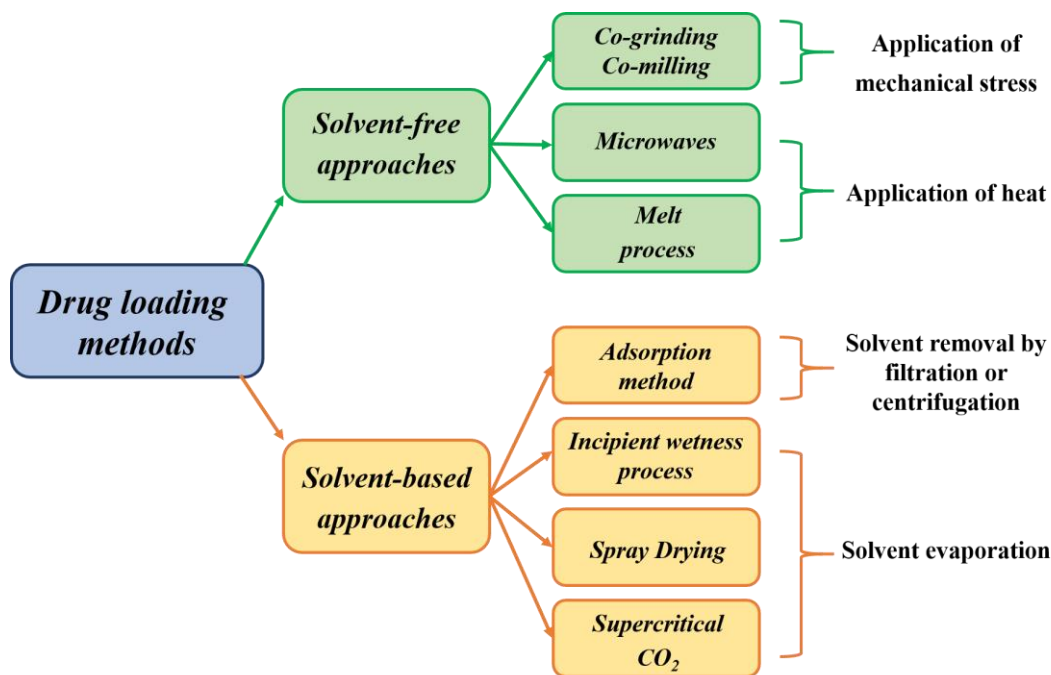
Figure 1.13 Most common procedures for drug loading.

1.5.1 Solvent-free approaches

Melt process

The melt process involves physical mixing of the drug in the crystallin form and the mesoporous material in a predefined ratio, followed by a heating step setting up a temperature above the drug's melting point that allows the amorphization of the drug. The selection of the correct temperature is a crucial aspect in order to avoid the drug degradation [175,193]. After the melting, the drug in its liquid state is then entrapped into the pore by capillary forces.

Mellaerts *et al.*[193] reported the loading of ibuprofen and itraconazole into SBA-15, by exploiting the melt method. The results obtained by the nitrogen adsorption-desorption measurements, as well as DSC analysis revealed that itraconazole was not successfully loaded into the SBA-15 pores but remained located outside on the SBA-15 surface in its crystalline form, underling the failure of liquid itraconazole to diffuse into the material pores. On the contrary, ibuprofen was successfully loaded into the mesopores, presenting an amorphous state and a fast release kinetics. This behaviour could be probably ascribed to the different viscosity of the molten drugs, highlighting the importance of this parameter for assuring the drug penetration into the pores; in fact, the high viscosity of molten itraconazole could hinder the flow of liquid into the pores, thus limiting a homogeneous drug distribution.

An alternative heating source can be represented by microwave irradiations. In a recent work, a novel approach to heat samples with a feedback system has been reported, [194], allowing to control the sample temperature throughout the duration of the experiment. The advantage in this case is the possibility to not exceed a specified temperature, avoiding undesired drug degradation reactions. Waters *et al.*[195] demonstrated the suitability of this procedure, which allowed to load the poor water soluble fenofibrate in the amorphous form in several mesoporous silica samples, resulting in a more sustained release profile compared to the traditional heating methods and physical mixing procedures.

Despite the advantages exhibited by the melt process, as a solvent-free technology, the heating step required to melt the drug results inappropriate for thermolabile drugs.

Co-grinding/Co-milling Method

The co-milling method is an easy and cheap technique that allows to obtain the drug amorphization on a large-scale manufacturing [196].
The process is based on the mixing of the dry crystalline drug and the mesoporous material powder, by controlling the intensity of the milling. The drug amorphization is easily obtained thanks to the formation of hydrogen bonds between the drug functional groups and the silanol-rich surface of the material.
Conventional milling such as ball milling or alternatively cryomilling can be employed under specific controlled conditions. In fact, despite the selected milling, the degree of amorphization and thus, the drug loading efficiency is influenced by several factors, such as mixing time and intensity, pressure, humidity, and surface silanol content. Since higher is the specific surface area, higher is the amorphization degree, this technique resulted particularly useful for mesoporous materials, such as MBGs, characterized by large specific surface area. Despite the clear advantages (no heating or solvent involved), limitations in the up-scaling process and agglomeration of the milled product could be encountered [183].

1.5.2 Solvent-based approaches

Adsorption method

Drug loading into a mesoporous structure can be easily obtained by adsorption from a drug solution by using an appropriate solvent. The mesoporous material is suspended in a volatile solvent solution of drug and after 1-2 hours of stirring, the suspension is filtered or centrifuged in order to remove the solvent and obtain the drug-loaded mesoporous material. The collected wet powder is then dried in an oven to allow the complete solvent evaporation and to get the dried powder. In most cases, a low-yield process is reported, since the adsorption is confined to a monolayer on the surface [175,197]. To increase the amount of drug loaded, a second process can be repeated, after the first evaporation.
Drug loading yield can be conditioned by the interactions involved between drug,

silica and solvent. In fact, too highly polar solvents can race with the drug molecules for surface adsorption sites. A study conducted by Charnay *et al.*[198] reported that polar solvents (*e.g.,* dimethyl sulfoxide (DMSO), dimethylformamide (DMF) and dimethylacetamide (DMA)) allow a low ibuprofen incorporation into MCM-41, compared to the use of nonpolar solvent, such as hexane.

In addition, the concentration of the drug can also influence the adsorption process and needs to be optimized. When the drug concentration is too high, drug molecules are rapidly driven onto the surface and consequently block the mesopores, reducing the diffusion of the drug into the inner pores [199].

Incipient wetness (IW) process

In this process, a concentrated drug solution generally close to the saturation solubility is prepared and then dropped over the material, allowing the penetration into the pores by capillary action. By exploiting the large pore volume of the mesoporous silica material and using a volume of drug solution equal to the pore volume, this technique allows to reach a high degree of drug loading. In a common procedure, small aliquots of concentrated solution of drug are dropped onto mesoporous silica in the form of powder. The impregnated samples are then dried in oven, until the complete solvent evaporation. Repeated impregnations equivalent to the material pore volume are required to fully fill the pores in order to reach high degrees of drug loading [200].

Compared to the adsorption method, the incipient wetness has been proved to enhance the drug loading ability [193,198,201], probably due to the rapid solvent evaporation which characterizes this technique.

In fact, in the incipient wetness process, the drug solution is attracted toward the pores by capillary action and drug molecules are successively driven into the pore by diffusion, during the quick solvent evaporation [200]. On the contrary, in the adsorption, the loading process is slow since the drug molecules need to diffuse from an external solution to the mesoporous silica surface, giving drug molecules time to rearrange and deposit in the mesopores.

As further advantages, the incipient wetness method allows to easily control the amount of the drug loaded into the carrier, making this method particularly suitable for expensive molecules and, in addition, to avoid the time-consuming filtration step required for the adsorption method [200].

Spray Drying Method

The above-mentioned drug loading methods can be considered laboratory procedures suitable for small batch sizes. Since the scale-up for cost-effective commercial production still represents a critical issue, the use of the spray drying process could be useful to address this challenge.

As the adsorption method, the spray drying process starts with a suspension containing both the drug and the material. The difference is the solvent removal step, in fact in this case the solvent is evaporated by atomizing the suspension by spraying nozzle into a drying chamber containing hot air [202]. The permanence of

the drops into the chamber is very short, allowing to minimize the heat process. This technique enables to produce spherical free-flowing particles with high loading yields along with enhanced dissolution properties [203].

The use of spray dryer as potential drug loading method has been explored by Hong and co-workers, who reported that up to 50% (w/w) of fenofibrate can be loaded into the mesoporous silica in amorphous form, compared to the 30% (w/w) reached by using the solvent impregnation [204]. Along with the higher drug loading ability compared to the adsorption, the spray drying can be considered a cost-effective manufacturing industrial technique, with high productivity and capable to produce dried particles in submicron-to-micron range, encountering a wide range of applications (*i.e.,* chemical, pharmaceutical, biotechnology or medical industries) [205].

Supercritical CO$_2$

Among the different described approaches, the use of supercritical fluid (SCF) to load drug into the mesoporous structure offers several advantages thanks to the possibility to exploit the solvent power variation obtained by the manipulation of the fluid pressure and temperature in the supercritical region. The most commonly used fluid is the carbon dioxide (CO_2) thanks to peculiar features: low critical point (7.4 MPa, 31.2 °C), non-flammable, recyclable, eco-friendly and inexpensive. Many API resulted soluble in supercritical CO_2 ($SCCO_2$) [206] and the obtained final drug-loaded material results to be totally solvent-free post fluid evacuation.

By comparing the supercritical fluid process with the solvent adsorption using hexane as solvent, a similar degree of drug loading is obtained, but remarkably reducing the process time [207,208].

Although the advantages in the use of this technology are evident, there are still a limited number of related studies as compared with the other methods. In fact, the yield is still low, since the pressurized gas causes the dispersion of the produced particles all over the chamber.

During this PhD work, the adsorption method and the incipient wetness process have been selected with the final aim to compare the loading efficiency and release properties of mesoporous bioactive glasses loaded with Ibuprofen and N-Acetylcysteine.

1.6 Selected drugs for bone applications: Ibuprofen and N-Acetylcysteine

This section will focus in detail on the Ibuprofen and N-acetylcysteine, the two selected drugs which were investigated during this PhD work, based on the requests of MOZART project.

The first drug loaded into an ordered mesoporous materials dates back to the 2001, when ibuprofen was loaded into a MCM-41 matrix with the idea to develop an implantable delivery system able to locally release the drug in bone tissue, reducing the inflammatory response after the implantation of the device in the bone defect [178].

From that time, several efforts were invested in the design and development of new drug delivery systems based on mesoporous materials, with the aim to encounter different needs:

- Delivery of new therapeutic agents such as unstable or very poorly soluble drugs, proteins or nucleic acids [209], that require new delivery strategies.
- Delivery of new complex drugs that differently would not be possible and to improve the biological responses thanks to the sustained drug release patterns compared to the pulsatile offered by the conventional administration routes [177].
- New therapeutic approaches for pathology requiring local release of the drug or a control of the drug concentration.

In table 1.1, a list of the main drugs employed in drug delivery systems is reported.

Table 1.1 List of the main drugs employed in drug delivery system and related references.

Class of drug	Drug	Reference
Anti-inflammatory	Ibuprofen	[198,210–213]
	Ketoprofen	[214,215]
	Naproxen	[216]
Bisphosphonates	Alendronate	[217–219]
Antibiotics	Levofloxacin	[220,221]
	Vancomycin	[220,222,223]
	Rifampicin	[223]
Antifungal	Itraconazole	[201,224]
	Griseofulvin	[225]
Chemotherapy	Doxorubicin	[226,227]

In this context, during this PhD work, two different drugs were selected and loaded into the MBG pores, Ibuprofen and N-Acetylcysteine. Ibuprofen was employed in combination with Cu-containing MBGs, aiming to design a multifunctional platform with anti-microbic/pro-angiogenic effects associated to the copper and anti-inflammatory potential exerted by ibuprofen to be used *in situ*

both for non-healing wounds and delayed bone healing applications. On the other hands, N-Acetylcysteine was loaded into the Sr-containing MBGs to be used as osteogenesis-enhancing platform, able to deliver into the bony defect both strontium ions and NAC, thus improving bone regeneration and promote bone defect healing.

Ibuprofen (fig. 1.14) is a non-steroidal anti-inflammatory drugs (NSAIDs), commonly used to reduce fever and control pain or inflammation associated with many pathological conditions such as headache, back pain, arthritis, skeletal injuries and chronic skeletal diseases like osteoarthritis. The mechanism of action leads to inhibit the cyclooxygenase (COX) enzymes involved in the arachidonic acid (ArA) pathway, thus reducing prostaglandins production [228]. The ArA pathway and prostaglandins are responsible, respectively, to regulate and induce the inflammation processes [228].
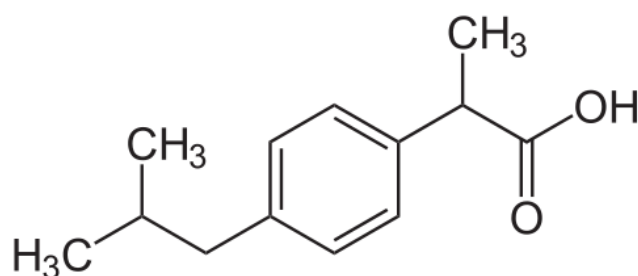
Figure 1.14 Ibuprofen molecule.

In the frame of MOZART project, ibuprofen was suggested in combination with copper to establish a multi-functional platform, which could concurrently target, through a synergistic effect of copper ion and anti-inflammatory ibuprofen, the state of inflammation, poor-vascularization and the persistent infection typical of chronic wounds. In fact, for the wound healing application, all products currently on the market work on a single-modality effect (*i.e.,* target whether an anti-inflammatory effect or anti-bacterial activity or a pro-angiogenic effect), while the synergy between drug (ibuprofen) and antibacterial and pro-angiogenic copper release, could synergistically work together to obtain a multi-modality device. In this scenario, *Prof. Sheila MacNeil (Professor of Tissue Engineering in the Department of Materials Science and Engineering, University of Sheffield, UK)* an academic partner of MOZART project, demonstrated the role of ibuprofen released from a biodegradable fibrous dressing in the reduction of inflammation in wounds and reduction of pain for patients on dressing changes[229,230]. The synthesized drug loaded electrospun fibres showed a rapid release of drug within the first 8 h and then slower release over several days. The ibuprofen released from these scaffolds was proved to significantly reduce the response of fibroblasts to major pro-inflammatory stimulators.

Based on these considerations, the combination of ibuprofen with copper ions could be also considered a promising strategy for bone healing application, with the idea to employ the ibuprofen to contrast the spreading of the inflammatory phase during the first stage of the bone healing process, and copper to simultaneously stimulate the angiogenesis processes, providing a better microenvironment for bone regeneration. In fact, as mentioned in detail in section 1.2, the bone healing process always progresses through an initial pro inflammatory phase that is triggered by the coagulation process after blood vessel disruption caused by the injury. If the inflammation phase in the early stage of the fracture healing process remains unsolved, complications such as a bacterial infection can occur, leading to a tissue damage and healing failure. In this scenario, ibuprofen has been selected to be used as *in situ* anti-inflammatory drug to contrast the uncontrolled progress of the bone healing inflammatory phase. In fact, the ibuprofen incorporation into the MBGs and the subsequent sustained release could guarantee the timely administration of anti-inflammatory drugs at initial stage and for all the duration of the healing process, positively affect the healing.

In addition, due to the injury, the vessels and thus the blood supply are disrupted and anaerobic energy supply advances, resulting in higher lactate levels. Since the vessels are essential to enable supply of the injured and healing tissue but also to allow the removal of unwanted cell products, (*e.g.,* lactate resulting from the anaerobic energy production), the pro-angiogenic potential exerted by the released copper ions results to be essential to support the bone healing process.
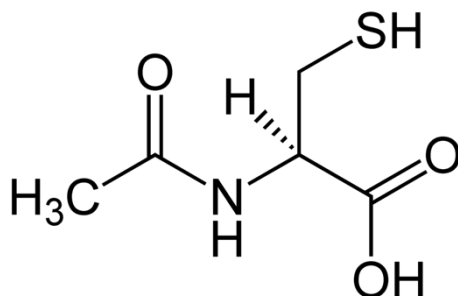
Figure 1.15 N-Acetylcysteine molecule.

N-Acetylcysteine (NAC) is an antioxidant derivative from amino acid cysteine (fig. 1.15). The drug is involved in essential biological functions thanks to the thiol group, which allow the bonding with two other amino acids, glutamine and glycine, forming a powerful antioxidant known as glutathione.

Glutathione plays a pivotal role in the regulation of several cellular activities involved in the immunological system and as an antioxidant, glutathione facilitates the neutralization of free radicals responsible of the cell and tissue damage at the molecular level [231].

The thiol groups present in the molecules allow the internalization of the molecule by means of organic anion transporter and thus to exert the antioxidant capabilities both intra- and extracellularly. In addition, the NAC is proved to activate the

osteoblastic differentiation [232,233]. Yamada *et al.* [232] demonstrated the role of NAC in the increasing of osteoblastic phenotypic expression, ALP activity, and extracellular matrix mineralization on rat osteoblastic culture derived from femur bone marrow. Moreover, an enhancement and an up-regulation expression of bone-related genes (collagen I, osteopontin, osteocalcin, BMP-2) induced by the presence of NAC has been observed.

In the frame of MOZART project, the use of NAC has been proposed by *Charitè – Universitätsmedizin Berlin (Dr. rer. Nat. Katharina Schmidt-Bleek at the Research Group "Bone healing" of the Julius Wolff Institute),* the partners involved in the *in vivo* experiments to confirm the safety and the efficacy of the bone healing device developed within the project.

As a proof of concept*, Charitè* investigated the positive effect of N-Acetylcysteine *in vivo* in a rodent osteotomy model confirming the positive effect of the drug on the bone healing process. A hybrid formulation based on two different concentrations of N-Acetylcysteine loaded into collagen sponge carrier have been applied in the osteotomy gap. Micro-computer tomography images clearly evidenced that the bone healing was enhanced by local application of NAC and that the higher concentration of NAC was more beneficial in supporting the bone regeneration process. The results were further confirmed using histological approaches (Movat Pentachrome staining and van Kossa/ safranin O staining), underlining the pivotal role of higher concentration of N-Acetylcysteine in the promotion of the bone healing. Along with the osteoinductive properties, *Charitè* also demonstrated the NAC pro-angiogenic and anti-inflammatory effect, which optimally support the effect exerted by the strontium ions. In fact, the combination of NAC with strontium ions could be considered a promising strategy to simultaneously promote the osteogenesis processes, stimulate the angiogenesis and contrast the inflammation spreading, resulting in a powerful multifunctional platform able to improve bone regeneration and promote bone defect healing.

1.7 Modification of Mesoporous Bioactive Glass surface

As already mentioned before, the MBGs surface is rich of silanol groups, able to receive organic modification by covalently anchoring organic moieties, by exploiting the alkoxysilane chemistry. The surface functionalization allows to provide an efficient way to overcome some drawbacks that greatly limited MBG practical applications and their clinical translation, among which the lack of target selectivity between healthy and diseased cells and the strong burst release of the loaded drug once in contact with body fluids, due to the weak interactions (van der Waals forces and hydrogen bonds) between the silica surface and the drug. The lack of target selectivity between healthy and diseased cells is usually observed after the drug administration, and is proved to lead to serious side effects, reducing on the other hands the therapeutic efficiency. In this scenario, functionalized MBGs can act as an active drug delivery system by transporting the drugs at the pathological site, using their surface properties in order to target a specific area in the body [234].

As reported in figure 1.16, several ligands can be grafted by using different strategies; usually, after the first step of functionalization by means of the alkoxysilane chemistry, the grafted functional group can react with the ligand exploiting a coupling reaction. Aside from the selected strategies, the ligand has to be grafted in such a way to be easily accessible by the membrane cell [234].

Once grafted on the material surface, the ligand can selectively bind molecules, such as antigens, or receptors overexpressed on the surface or in the nuclei of the diseased target, allowing the MBGs to exert the therapeutic effect directly at the pathological site.
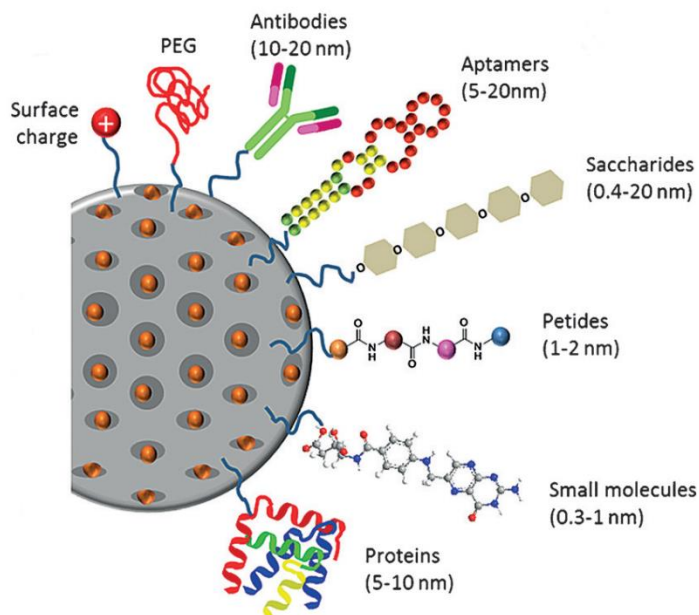
Figure 1.16 Different biomolecules grafted on the material surface for specific targeting.

Moreover, since an ideal drug delivery system should show a zero premature release of the loaded drug prior to reach the target, several approaches based on the alkoxysilane chemistry have been investigated in order to modulate the drug release kinetics. This functionalization process opens the way to a wide range of possibilities to modulate both the drug loading and release by inducing changes in silica surface. Among the different functionalization pathways, two of the easiest and frequently employed are a one-pot synthesis known as co-condensation method and a post-synthesis method, knows also as silylation, schematically illustrated in fig. 1.17 [189].

The co-condensation method is based on the addition of the modifying agent during the material synthesis and the simultaneous condensation of both the corresponding silica and alkoxyorganosilica precursors $(R - O)_3 Si - R$. Moreover, the entire functionalization procedure is carried out in one single step. On the other hands, in the post-synthesis process, the organic modification involves the grafting of organic moieties to the previously synthesized MBGs, performing the process under anhydrous conditions.
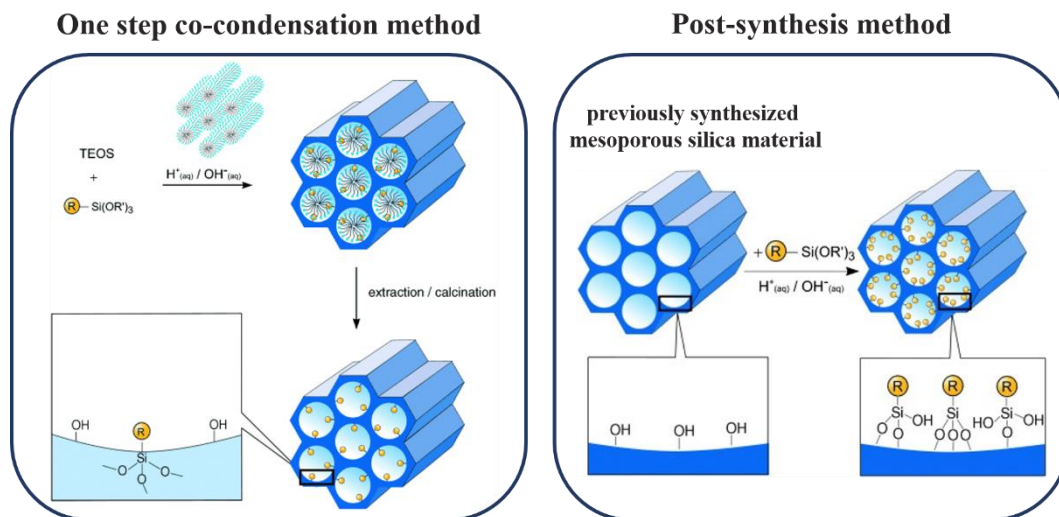
Figure 1.17 Schematic representation of two functionalization processes: the one step co-condensation method and the post-synthesis method.

The grafting is usually carried out by using alkoxyorganosilica $(R - O)_3 Si - R$, or in alternative chlorosilanes $Cl - Si - R_3$ or silazanes $HN (Si - R_3)_3$, able to react and covalently bind the free silanol groups present both on the outer surface and the inner pore surface.

The main difference between the two methods concerns the maximum achievable degree of organic modification. In fact, by following the co-condensation method, the organic groups are bind both to the outer and the inner silica surface. Since increasing the organosilicon precursor in the reaction mixture leads to a decrease in the mesoscopic order [189,235] a maximum degree of functionalization is not expected to exceed 40 mol%, in order to avoid disordering in the mesoporous structure.

On the other hands, the functionalization obtained by using the post-synthesis approach evidences a higher functionalization degree, thanks to the location of the organic functions in the outer surface of the pre-formed mesopore silica surface. However, by using the post-synthesis approach, some disadvantages have been observed, among which the reduction of the textural properties (pore diameter, surface area and pore volume). The functionalization leads to an organic modification of the silica walls, inducing significant modification in the chemical nature of the silica surface, such as the polarity and the drug adsorption capability. On consequence, the functional groups exposed on the functionalized surface are able to chemically interact with the guest drugs, thus increasing the loading ability. Moreover, these chemical modifications can also directly affect the drug release rate due to the increasing of the diffusion resistance [209,234].

During this PhD work, two different surface modification approaches have been evaluated, the Layer by Layer deposition and the *zwitterionization*. The Layer by Layer deposition has been evaluated as suitable non-covalent approach to modulate the release rate of the incorporated ions and drugs, hence

avoiding the burst release that limits the MBG practical applications and clinical translation; on the other hand, *zwitterionization* has been identified as functionalization approach to further enrich the therapeutic potential of the MBGs, imparting anti-adhesive/anti-fouling features.

1.7.1 Layer by Layer deposition (LbL)

As described up to now, most of the currently employed surface modification techniques are based on a covalent binding of therapeutic molecules. Since usually the biomaterials used for hard tissue replacement do not provide any bindings sites for the direct biomolecule grafting, the above mentioned approaches require a first modification step able to create chemical organic moieties essential for the subsequent reaction with the biomolecules [236]. Moreover, since the covalent binding could reduce the activity or denaturate the biomolecule, in the 1997, the layer-by-layer technique (LbL) has been introduced by Decher [237] as alternative
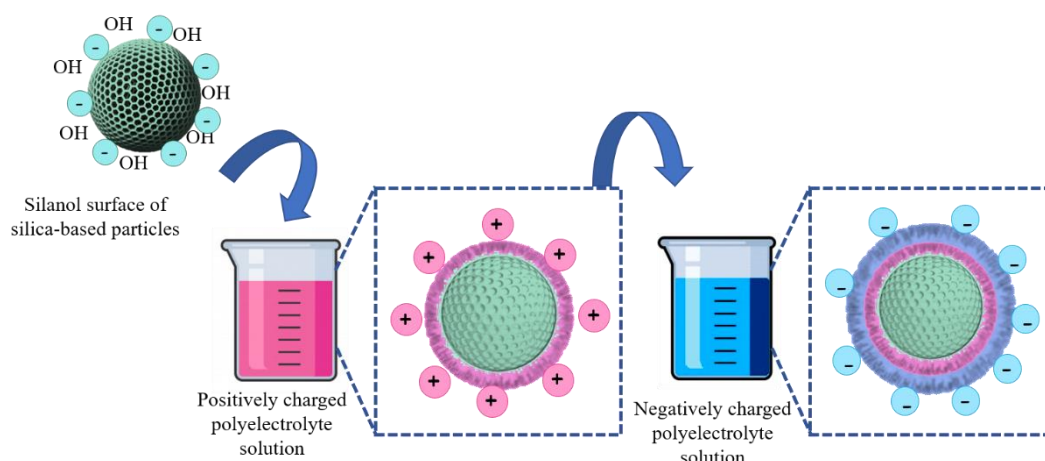
Figure 1.18 Mechanism of LbL deposition which involves the electrostatic interaction between oppositely charged polyelectrolytes alternatively assembled on the outer material surface.

route for the noncovalent engineering of surfaces with the idea to not only directly bind biomolecules on the biomaterial surface, preserving their biological activity, but also as promising approach to modulate the release rate of the entrapped drugs. At neutral pH, the MBG silanol surface results deprotonated and thus negatively charged; by exploiting electrostatic interactions on the outer surface, positively charged moieties can be deposited through noncovalent interactions, creating a multi-layered coating. The LbL deposition is based on this mechanism, involving the electrostatic interactions between oppositely charged polyelectrolytes, which are alternatively assembled on the outer surface [238] (figure 1.18).

Usually, the layer deposition can be repeated several times, leading to the formation of polyelectrolyte multilayers (PEMs), thermally and mechanically stable [236]. By controlling essential parameters, spanning from the polyelectrolyte conformation to environmental conditions, such as the ionic strength, the pH, or the temperature, the obtained PEMs could show peculiar features in terms of layer

organization, thickness, surface charge and wettability [239].

Since PEMs can also be assembled on top of nano and micro particles, the LbL deposition could be considered a promising strategy to design drug delivery systems, in which the therapeutic agent could be both incorporated into the multilayers or, in alternative, replaces selected polyelectrolyte layers. As result, the release can be tailored by the deposited PEMs which act as barrier to control the drug release. In addition, any kind of charged surface can be coated with a remarkable type of molecules, depending on the final application. In fact, almost all the biological macromolecules, such as DNA, growth factors and proteins could present a charge depending on pH value and ionic strength and for this reason can be used as polyelectrolytes with the final aim to create a biomimetic multilayers on biomaterial surfaces [236].

Several examples of LbL applications in the biomedical field can be summarized. Yang *et al.*[240] produced mesoporous silica nanoparticles loaded with antitumor drug and then coated with alginate/chitosan polyelectrolyte multilayers by using the LbL technique. The developed system was able to act as pH-sensitive gatekeepers, enabling the release of drug molecules once in contact with acidic environment. Moreover, cytotoxicity assays demonstrated good biocompatibility and low toxicity compared to the bare samples.

Shi and Caruso [241] investigated the release profiles and rates of pyrene from microcapsules composed of polyelectrolyte multilayers, reporting that the release rate was tailored by modifying the number of polyelectrolyte layers.

Zhou *et al.*[238] employed alginate and chitosan, biodegradable and biocompatible polymers, to coat poly(lactide-co-glycolide) (PLGA) nanoparticles to develop a biocompatible drug delivery system able to impart antifouling properties and in addition to reduce unspecific cell uptake. The authors demonstrated very low interaction with albumin, confirming the antifouling properties, further confirming a decrease in the cellular uptake, compared to the bare samples. Moreover, the subsequent binding of folic acid on the multi-layered coating allowed to achieve selective cell targeting. It is evident that thanks to the possibility to tailor the type of polyelectrolyte or the number of deposited layer, the LbL approach resulted to be suitable to modulate the release rate of the incorporated drugs, to transport the drugs to target a specific area in the body or to modify/improve the biomaterial surface properties.

In this context, during this PhD work, a drug delivery system based on multi-layered copper-containing MBGs has been developed, by following two different routes with the final aim to obtain two different multifunctional platforms showing a sustained release profile of both the ions and drug. In the first strategy the polyelectrolytes chitosan and alginate were selected as natural biodegradable and biocompatible polymers and alternatively deposited by exploiting their opposite positive and negative charges, respectively. Once obtained the desired multi-layered surface in term of layer number, ibuprofen was loaded into the multi-layered MBGs by using the IW technique. In the second approach, the alginate layer

was replaced by the ibuprofen, thus introduced as polyelectrolyte layer, by exploiting the ibuprofen negative charge (COO^-), able to electrostatically interact with the chitosan positive charge. The two obtained systems were then evaluated in term of capability to modulate the release rate of both the incorporated copper ions and ibuprofen and to maintain the typical MBGs bioactivity, essential feature for bone healing application.

1.7.2 *Zwitterionization*

As already mentioned, the LbL strategy could modify the material surface properties, improving the targeting or the biological response.

In the frame of ZODIAC project, advanced biomaterials based on MBGs were designed with the idea to synergistically combine the effects of therapeutic ions with a dual antibacterial potential. In particular, the therapeutic ions will impart a high bioactivity and will exert pro-osteogenesis and pro-angiogenesis effects. The dual antibacterial potential will be obtained through the antiadhesive surface properties capable to repel bacteria and this inhibit their attachment, and the bactericidal effect exerted by the release of antimicrobial agents (ions or/and antibiotics). In fact, the antiadhesive surface can avoid the formation of a protein layer on the material surface once in contact with biological fluids, which is responsible of the reduction of the material performance, due to the inhibition of the effect exerted by the drug/ion release and of the formation of a hydroxyapatite layer [242], essential for the strong bond with living bone tissue and the promotion of osteogenesis. In addition, the attachment of serum proteins plays a key role on the microbial adhesion and bacterial biofilm formation [243,244]. In fact, the initial attachment of individual bacterial cells or small bacterial aggregates has been proved to be usually preceded by the adsorption of biological macromolecules [96,245,246], such as proteins.

Among the several approaches to produce anti-adhesive surfaces, during this PhD work, *zwitterionization* (*e.g* introduction of an equal number of positively and negatively charged moieties that maintains the overall electrical neutrality), has been selected as promising and versatile functionalization method. In fact, specifically for bone tissue regeneration purposes, tailoring the MBG surface by *zwitterionization* could facilitate the development of a biomaterial able to induce the bone bonding, promote osteogenic differentiation and simultaneously avoid bacterial colonization.
A *zwitterionic* surface is characterized by an equal number of both positively and negatively moieties on the material surface, which confer an overall electrical neutrality [247]. The anti-adhesive/non-fouling capability of *zwitterionic* surfaces is due to the formation of a hydration layer around the material surface, able to acts as a physical and energetic barrier, interfering with the protein adhesion, and thus avoiding the bacteria biofilm formation.

The grafting of both positively and negatively charged species onto the biomaterial surfaces consists in the functionalization at atomic level and over the

recent years several *zwitterionization* approaches have been developed to prepare advanced *zwitterionic* biomaterials, as schematically reported in figure 1.19.
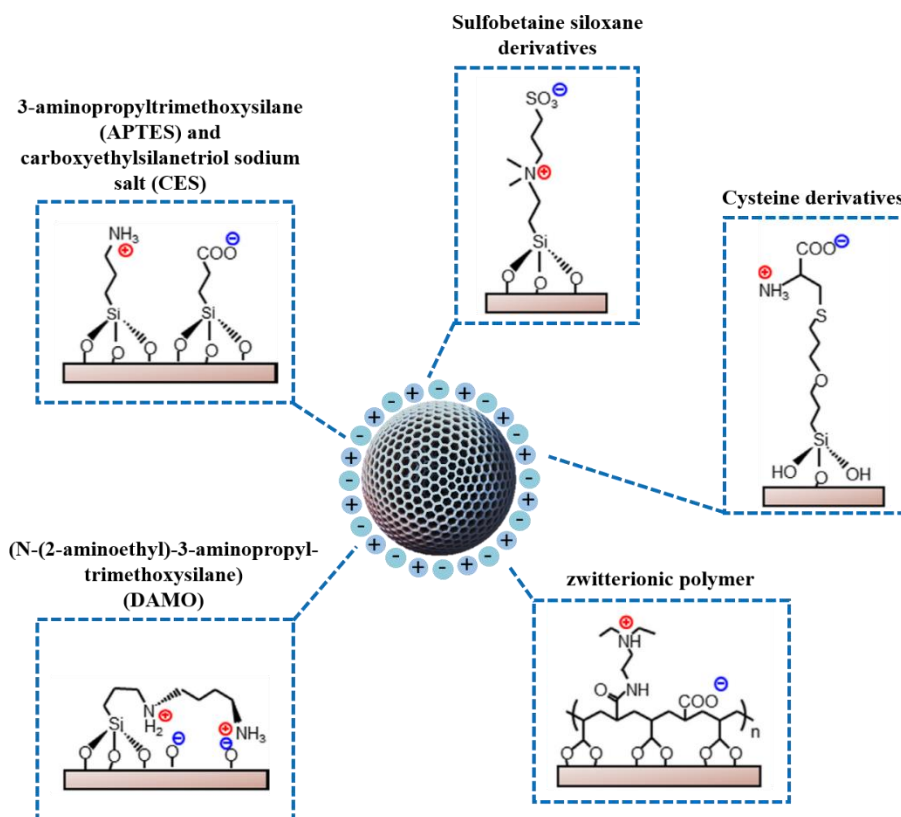
Figure 1.19 Chemical strategies for the zwitterionization of biomaterials.

One of the first described approaches involved the use of *zwitterionic* polymers bearing mixed positively and negatively charged moieties within the same chain, showing an overall charge neutrality. Despite the advantages to graft one single molecule bearing both the negative and the positive charges, the procedure involved several steps with the use of organic solvent and the production of a high number of intermediate products, which make the entire process very complex [247].

As alternative, simpler and "user friendly" methods have been evaluated such as the grafting of low-molecular weight species (amino acids), alkoxysilanes, sulfobetaine derivatives or dopamine, which exhibit *zwitterionic* nature depending on the pH. In addition, in the specific case of grafting nanoparticles, the use of these molecules does not increase the material hydrodynamic size. The use of amino acids involves a two-step procedure. The low cost and widely available amino acid cysteine (Cys) shows both the positive and negative charges on the chain and has been used to provide *zwitterionic* nature to silica nanoparticles by following the approach reported by Rosen *et al.* [248]: the silanol groups of the particles were firstly reacted with an epoxide containing alkoxysilane in an acidic water/ethanol mixture. In a second step, the epoxide surface groups reacted with the free sulfhydryl group of Cys under basic pH conditions, yielding a thioether

linkage.

Schlenoff and co-workers[249] described the grafting to the silica nanoparticle surface of the highly water-soluble sulfobeatine siloxane (SBS). The SBS were synthesized in a separate reaction and then added to the silica nanoparticle suspension. In this work, different amount of material has been employed, in order to evaluate the minimum surface coverage necessary to lend stability on the particles in protein media.

One of the more direct and simple grafting routes consists in the use of two alkoxysilanes bearing functional groups with positive and negative charges, by exploiting the silanes chemistry. As already discussed before, two main strategies can be employed, the co-condensation and the post-synthesis process. The co-condensation approach involves the addition of alkoxysilanes along with the silica precursors during the synthesis step. Colilla and co-workers [250] described for the first time this method, preparing *zwitterionic* mesoporous SBA-15 material containing $-NH_3^+/-COO^-$ *zwitterionic* groups by using two alkoxysilanes, aminopropyltrimethoxysilane (APTES) and carboxyethyl silanetriol sodium salt (CES), bearing the positive and negative charges, respectively. The resulting material has been proved to inhibit unspecific protein adsorption and bacterial adhesion. The post-synthesis approach involved the covalent grafting of suitable alkoxysilanes to the hydroxyl groups of the previous synthesized biomaterial. In the work of Sanchez-Salcedo *et al.* [251] *zwitterionic* nanocrystalline hydroxyapatite (HA) has been produced and the capability to inhibit bacterial adhesion while allowing osteoblast cell colonization has been investigated. Results demonstrated that the developed *zwitterionic* material is able to reduce bacterial adhesion more than 90% compared to bare HA, maintaining a good biocompatibility. One of the main advantages of this methodology is the possibility to tailor the *zwitterionic* properties by adjusting the molar ratio of the two alkoxysilanes.

In this scenario, specifically for this PhD work, strontium-containing MBGs were subjected to a co-grafting reaction by using aminopropyl silanetriol (APST) and carboxyethylsilanetriol (CES), bearing respectively amino and carboxylate groups, with the aim to introduce almost the same amount of $-NH_3^+/-COO^-$ groups on the MBG surface. The resulting multifunctional device could represent a big step towards novel therapies able to target simultaneously all the causes, often mutually interlocked, of the pathologies related to compromised bone healing.

1.8 Hybrid formulations for the design of drug delivery platform

As widely explained in the previous sections, MBGs represent one of the most promising biomaterials to conceive advanced devices for drug delivery in the field of bone tissue repair [90]. However, to date, some drawbacks have greatly limited MBG practical applications and their true clinical translation, among which the strong burst release of incorporated drug once contacted with body fluids, and the difficulties related to their administration at the pathological site (*i.e.,* bone fracture cavity) in the form of powder. Since MBGs alone are not exploitable as long-term drug delivery systems for orthopaedic applications, their combination with polymers able to modulate the release kinetics and/or to act as a vehicle phase to the pathological site would greatly enlarge the clinical potential of these nanocarriers.

Currently, biopolymers (*i.e.,* gelatin, chitosan) are considered one of the most promising polymeric phases for designing drug delivery systems, thanks to their excellent biocompatibility and capacity to retain long-term physical and mechanical properties [255]. However, most of the biopolymers cannot properly support bone tissue reconstruction due to inherent weak osteoconductivity, poor bioactivity, and possible adverse tissue response [179,256].

The combination of MBGs with a polymeric phase to design hybrid functional formulations represents an attractive approach to overcome the issues related to the components alone. In particular, the rheological property of the polymer can facilitate the shaping process to fit the bone defects, while the MBGs are capable of promoting osteogenic property and delivery ability. The design of biomaterials for bone filling and repair is one of the most important targets in orthopaedic surgery. Among the different approaches to reach this target, one the most attractive is to combine in a single device porous architecture, bioactivity and drug delivery capacity, aiming to modulate cellular behaviour, especially when the physiological bone regeneration process is compromised (*e.g.,* osteoporotic, diabetic patients).

To this aim, a promising fabrication strategy relies in the combination of organic and inorganic components, as the organic matrices provide a suitable 3D-architecture, while the inorganic phases can improve the overall system bioactivity, mechanical strength, and also act as drug delivery carriers. Depending on the selected polymer phase, formulations with different therapeutic functions can be designed, spanning from systems intended for drug delivery, in which the polymer has merely the function of vehicle phase, to more advanced systems in which the release properties of MBGs are combined to the biomimicking features typical of biopolymers.

In this context, gelatin, a GRAS material approved by FDA, is a biopolymer widely exploited to this purpose, due to the high biocompatibility and biodegradation, furthermore, compared to collagen, is much less expensive, while preserving several collagen sequences responsible for the cell adhesion. Borrego-

Gonzales S. *et al.* combined the drug delivery properties of MBGs with the ability of gelatin to mimic the nanofibrous bone extracellular matrix [257]. MBGs were loaded with gentamicin sulphate to obtain a system able to guarantee both bioactivity and antibiotic release, in case of bacterial infection. Compared to the Poly(methyl methacrylate (PMMA) commercial product, considered the benchmark standard biomaterial for local antibiotic therapy, the hybrid MBG-Gelatin scaffold (MBG-NfGel) showed increased cargo loading and better release capabilities. The release test performed on the hybrid MBG-NfGel revealed that, after an initial release in the first 72 h, 60% of total loaded gentamicin was retained after 10 days; at variance, the pure gelatin system showed a burst full cargo release in the first 72 hours. The release kinetics of MBG-NfGel in the first 72 h resulted to be appropriate for responding to possible infection just after surgery, while the sustained release over the 10 days would provide the prevention of subsequent infections. The excellent biocompatibility in terms of adhesion and proliferation, associated to the enhanced antibiotic loading capacity and sustained release ability compared to other devices proposed in the literature [257] make this hybrid formulation an excellent candidate to develop multifunctional devices for bone regeneration and therapy.

Nevertheless, in order to avoid the failure of the implantation and achieve a successful bon regeneration process, the prevention of infections and the reduction of an excessive inflammation are two of the main goals to achieve after the placement of bone scaffold. Most of the current drug delivery systems can load a single drug, mainly due to the different drug properties such as solubility and hydrophilicity and usually manifold carriers or solvents are needed for multiple drug release. In response to this challenge, Fu S. *et al.* proposed the idea to fabricate an alginate-scaffold with multi-drugs loading and controllable release behaviours
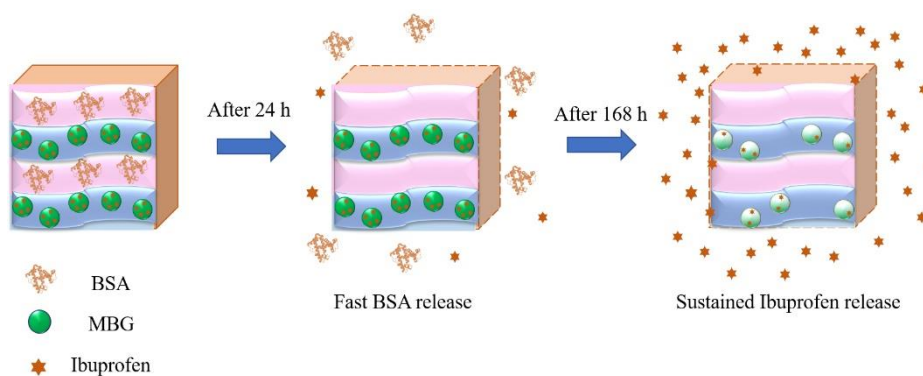
Figure 1.20 Schematic representation of the release mechanisms from a layered 3D printed alginate-scaffold with multi-drugs loading.

[259]. In particular, a structure alternating layer of pure alginate and alginate combined with drug-loaded MBGs was developed using the 3D printing technique, in order to modulate the release kinetics of two molecules chosen as model, ibuprofen and bovine serum albumin (BSA), loaded into MBGs and in the pure alginate layers, respectively. The BSA incorporated in the pure alginate layers is released quickly in the first 24 hours, due to the fast diffusion through the alginate macroporous structure. Conversely, the release of ibuprofen is quick in the first 12

hours, after which a sustained release is maintained up to 168 hours (figure 1.20), thanks to the confinement effect of the mesoporous channels inside the MBG nanocarriers.

The combination of MBG with alginate resulted to be effective to create scaffolds with dual drug loading and specific release properties, potentially suitable for bone regeneration, where different therapeutic effects (anti-infective, anti-inflammatory, pro-angiogenic/osteogenic) require different active agents, release time points and concentrations. Furthermore, the presence of incorporated MBGs increases the cell proliferation and differentiation, due to the release of silicon and calcium ions, upon the progressive dissolution of the inorganic framework.

The design of multifunctional scaffolds for bone therapies has to take into account several factors, including the ability to deliver drug concentrations within the therapeutic windows and to create a biocompatible environment for cell infiltration and proliferation. With this perspective, the hybrid composites based on MBGs and polymers should be designed also with the aim to mimic the composite complex structure of natural bone. With this final objective, Wang D. *et al.* developed a hybrid formulation, which combines silk fibroin with 17β-estradiol (E2) loaded MBGs and aspires to meet all the described requirements [262]. As mentioned in the previous section, silk fibroin is a biodegradable natural polymer, with excellent mechanical properties with low immunogenicity and biomimetic features. E2 can be considered one of the most effective form of natural estrogen, able to inhibit adhesion osteoclasts and induce their apoptosis *in vitro* [263]. Furthermore, in order to obtain a greater and more stable loading, the MBGs have been modified with β- cyclodextrin able to increase the affinity for E2.

Hence, E2 loaded MBGs were mixed with silk fibroin and the resulting hybrid formulation was electrospun to obtain nanofibers combining sustained release properties, osteoconductivity, osteoinductivity and excellent biomineralization capabilities. Release tests showed that the developed system effectively slows down the release kinetics of E2; in fact, after an initial burst release observed in the first 48 h (about 20% of the total E2), the released amount of E2 increases gradually in a sustained manner over time. A total of 42% loaded E2 released from the nanofibers within the first 21 days, associated with the stimulation of osteoblasts and the inhibition of osteoclast activities, proved the great potential of this composite hybrid system for applications in bone tissue repair and regeneration.

A similar strategy to offer scaffolds with bioactivity and drug delivery capacity to regulate cellular behaviours and improve bone regeneration processes was also adopted by El-Fiqi A. *et al.*, who combined DEX loaded MBGs with a matrix of biopolymer fibre composed of gelatin and PCL[264]. In order to increase the amount of drug loading, MBG surface was functionalised by introducing surface protonated amino groups able to interact with the negatively charged DEX molecules and consequently, to improve the loading efficiency. In addition, since the release of ions (*e.g.,* calcium, silicon) is proven to be significantly beneficial in up-regulating several osteogenic genes, their release was evaluated from the

nanocomposite scaffolds up to 4 weeks, evidencing a sustained and long-term release of both ions. Similar behaviour was observed for the DEX release, which shows an initial rapid release within 1 day followed by a sustainable release up to 28 days. The osteogenic differentiation behaviour of cells detected by the alkaline phosphatase (ALP) activity resulted in agreement with the release kinetics of DEX, as the ALP stimulation was maintained stable overtime, evidencing that the stimulating effect of the released DEX was stable on the long-term period. The osteogenic effects of the scaffold were investigated *in vivo*, in order to validate the feasibility of the developed DEX-releasing platform in defective bone tissues. The obtained results demonstrated that 6 weeks after the scaffold implant, the DEX-loaded nanocomposite group showed significantly higher levels of bone volume and bone surface density, detected by using μCT analysis. Furthermore, histological staining revealed a substantial new bone formation, associated to a number of osteoblasts lining the neo-bone tissues with osteocytes embedded within.

Hybrid injectable hydrogels for drug delivery

In the field on tissue regeneration and therapies, injectable hydrogels have been recently proposed as very promising devices, mainly due to their abilities to be applied through minimally invasive surgery and capability, upon gelling, of perfectly filling body defects or cavities. Among the different injectable systems, stimuli-responsive hydrogels, in particular those sensitive to temperature changes, have been proposed as drug delivery for tissue engineering application.

With this perspective, the combination of MBGs with thermosensitive hydrogels, in which an aqueous polymer solution undergoes a sol to gel transition in physiological conditions (37 °C), represents a promising strategy to design non-invasive hybrid devices which can be injected into the clinical site and, after the gelation *in situ*, result in a drug depot system for a sustained and localized release.

In this context, copolymers Pluronic F-127 gained much attention as cell and drug delivery system thanks to the low toxicity, reverse thermal gelation, high drug loading capabilities and ability to gel in physiological conditions at relatively low concentrations [265]. Based on these features, a hybrid injectable platform based on thermosensitive Pluronic F127 carrying doxorubicin-loaded mesoporous silica nanoparticles has been conceived as an anticancer depot system [266], confirming the feasibility of the strategy. However, despite the excellent biocompatibility, Pluronic F127-based hydrogels show an important drawback; in fact, the poor stability in aqueous environment leads to the dissolution of the hydrogels in the first few minutes after injection, limiting their use as a prolonged and sustained release device. In order to overcome this limitation, the Pluronic F127 chain can be extended by exploiting the chemistry of polyurethanes (PURs), which allows to create a versatile and flexible platform for different applications in the regenerative medicine and biomedical fields, in particular as biodegradable scaffolds and delivery systems [267–269]. PUR-based hydrogels are injectable system, able to completely fill the defect cavity and to assume the shape of the defect prior the

complete gelation. In this context, Boffito M. *et al.* [267] reported a procedure to produce a novel amphiphilic PUR based on Poloxamer 407, which, compared to the commercially available PUR Poloxamer 407, exhibits improved gelation ability, mechanical strength and stability.

Due to the ability to solidify at body temperature, the temperature-sensitive cross-linking polymer P-(N-isopropylacrylamide-co-butyl methylacrylate) (PIB) have been considered a promising candidate to develop injectable thermosensitive devices for tissue engineering applications. In order to compensate the lack of osteoconductivity and mechanical properties of the polymer alone, Chen X. *et al.* designed a novel composite scaffold combining PIB nanogels with boron-containing MBGs and investigated the potentiality of the resulting hybrid system for the repair of rat femur defects [270]. The results of the *in vivo* assessment evidenced a superior bone formation due the release of boron ions which significantly enhanced the proliferation and the expression of osteoblasts.

Zhang Q. *et al.*, developed a similar hybrid system, by combining the PIB nanogel with strontium-containing MBGs to create a formulation with increased bone inducing abilities [271]. In addition, by exploiting the water-soluble nature of the nanogel, pre-harvested osteoblasts were added to the PIB in liquid form, to investigate the potential benefit role induced by cell delivery into the bone defect area. PIB nanogel alone showed very low osteogenic ability but the combination with Sr-containing MBGs resulted in a great enhancement of the bone forming ability, in particular due to the release of strontium ions, well known for the ability to inhibit osteoclast function and simultaneously, improve the bone formation, acting both on the repair and maintenance of bone density [95,127,182]. Moreover, the incorporation of osteoblast in the hybrid formulation and the consequent release into the defect area, further accelerated the bone healing process.

To date, a limited number of injectable hybrid systems based on thermo-sensitive hydrogels in combination with MBGs are reported in the literature. These devices could find interesting applications when physiological healing is compromised, through the stimulation of the endogenous molecular signals linked to the regulation of bone remodelling process.

To this purpose, during this PhD work, in order to develop a system with enhanced mechanical properties, osteoconductivity and therapeutic properties, PUR Poloxamer 407 was combined with the above mentioned systems based on strontium-containing MBGs loaded with NAC and copper-containing MBGs loaded with ibuprofen. The resulting hybrid formulations can be exploited as injectable platform for the prolonged and sustained release of therapeutic concentrations of both ions and drugs, due to their recognized and well described therapeutic potential (see section 1.4.1 and 1.5), essential for promoting bone repair in compromised clinical conditions [269].

The high potentiality of the proposed strategy lies in the wide versatility of the proposed formulations. In fact, by tailoring the composition and cargo of MBGs, different ions and bioactive factors can be co-released based on the therapeutic

effects required by the final targeted application. In addition, the use of a custom-made PEU hydrogel as vehicle phase of the MBGs provides the final system with a further degree of freedom. The characteristic LEGO-like chemical structure of PEUs allows a fine tuning of polymer properties by changing their constituting building blocks. This versatility opens the way to the design of stimuli-responsive hydrogels with an enhanced control over payload release and/or hydrogel dissolution/degradation, thus allowing a better tuning of the release properties compared to those observed for MBGs alone.

References

[1]   R. Marsell, T.A. Einhorn, The biology of fracture healing, Injury. 42 (2011) 551–555. doi:10.1016/j.injury.2011.03.031.THE.

[2]   C. Ferguson, E. Alpern, T. Miclau, J.A. Helms, Does adult fracture repair recapitulate embryonic skeletal formation?, Mech. Dev. (1999). doi:10.1016/S0925-4773(99)00142-2.

[3]   R. Dimitriou, E. Tsiridis, P. V. Giannoudis, Current concepts of molecular aspects of bone healing, Injury. 36 (2005) 1392–1404. doi:10.1016/j.injury.2005.07.019.

[4]   K. Schmidt-Bleek, H. Schell, N. Schulz, P. Hoff, C. Perka, F. Buttgereit, H.D. Volk, J. Lienau, G.N. Duda, Inflammatory phase of bone healing initiates the regenerative healing cascade, Cell Tissue Res. 347 (2012) 567–573. doi:10.1007/s00441-011-1205-7.

[5]   N.P. Haas, Callusmodulation Fiktion oder Realität?, Chirurg. 71 (2000) 987–988.

[6]   D. Holmes, Non-union bone fracture: A quicker fix, Nature. 550 (2017) S193. doi:10.1038/550S193a.

[7]   C. Zeckey, The Aseptic Femoral and Tibial Shaft Non-Union in Healthy Patients – An Analysis of the Health-Related Quality of Life and the Socioeconomic Outcome, Open Orthop. J. (2011). doi:10.2174/1874325001105010193.

[8]   K. Schmidt-Bleek, B.J. Kwee, D.J. Mooney, G.N. Duda, Boon and Bane of Inflammation in Bone Tissue Regeneration and Its Link with Angiogenesis, Tissue Eng. - Part B Rev. 21 (2015) 354–364. doi:10.1089/ten.teb.2014.0677.

[9]   P. Kolar, K. Schmidt-Bleek, H. Schell, T. Gaber, D. Toben, G. Schmidmaier, C. Perka, F. Buttgereit, G.N. Duda, The early fracture hematoma and its potential role in fracture healing, Tissue Eng. - Part B Rev. (2010). doi:10.1089/ten.teb.2009.0687.

[10]   L. Claes, S. Recknagel, A. Ignatius, Fracture healing under healthy and inflammatory conditions, Nat. Rev. Rheumatol. 8 (2012) 133–143. doi:10.1038/nrrheum.2012.1.

[11]   L.C. Gerstenfeld, D.M. Cullinane, G.L. Barnes, D.T. Graves, T.A. Einhorn, Fracture healing as a post-natal developmental process: Molecular, spatial, and temporal aspects of its regulation, J. Cell. Biochem. (2003). doi:10.1002/jcb.10435.

[12]   C. Sfeir, L. Ho, B.A. Doll, K. Azari, J.O. Hollinger, Fracture repair, in: Bone Regen. Repair Biol. Clin. Appl., 2005. doi:10.1385/1-59259-863-3:021.

[13]   S.K. Lee, J. Lorenzo, Cytokines regulating osteoclast formation and function, Curr. Opin. Rheumatol. (2006). doi:10.1889/1.2196518.

[14]   T.A. Einhorn, R.J. Majeska, E.B. Rush, P.M. Levine, M.C. Horowitz, The expression of cytokine activity by fracture callus, J. Bone Miner. Res. (1995). doi:10.1002/jbmr.5650100818.

[15]   P.M. Mountziaris, A.G. Mikos, Modulation of the inflammatory response for enhanced bone tissue regeneration, Tissue Eng. - Part B Rev. (2008).

doi:10.1089/ten.teb.2008.0038.

[16]   Z. Xing, C. Lu, D. Hu, T. Miclau, R.S. Marcucio, Rejuvenation of the inflammatory system stimulates fracture repair in aged mice, J. Orthop. Res. (2010). doi:10.1002/jor.21087.

[17]   B. McKibbin, The biology of fracture healing in long bones, J. Bone Jt. Surg. - Ser. B. (1978). doi:10.1302/0301-620x.60b2.350882.

[18]   L.C. Gerstenfeld, Y.M. Alkhiary, E.A. Krall, F.H. Nicholls, S.N. Stapleton, J.L. Fitch, M. Bauer, R. Kayal, D.T. Graves, K.J. Jepsen, T.A. Einhorn, Three-dimensional reconstruction of fracture callus morphogenesis, J. Histochem. Cytochem. (2006). doi:10.1369/jhc.6A6959.2006.

[19]   M. V. Bais, N. Wigner, M. Young, R. Toholka, D.T. Graves, E.F. Morgan, L.C. Gerstenfeld, T.A. Einhorn, BMP2 is essential for post natal osteogenesis but not for recruitment of osteogenic stem cells, Bone. (2009). doi:10.1016/j.bone.2009.04.239.

[20]   A.Y. Ketenjian, C. Arsenis, Morphological and biochemical studies during differentiation and calcification of fracture callus cartilage, CLIN.ORTHOP. (1975). doi:10.1097/00003086-197503000-00031.

[21]   T.A. Einhorn, L.C. Gerstenfeld, Fracture healing: Mechanisms and interventions, Nat. Rev. Rheumatol. 11 (2015) 45–54. doi:10.1038/nrrheum.2014.164.

[22]   C. ANDREW, L. BASSETT, Biophysical Principles Affecting Bone Structure, in: Dev. Growth, 1971. doi:10.1016/b978-0-12-119203-7.50008-8.

[23]   E. Tsiridis, N. Upadhyay, P. Giannoudis, Molecular aspects of fracture healing:Which are the important molecules?, Injury. (2007). doi:10.1016/j.injury.2007.02.006.

[24]   E.Y.S. Chao, N. Inoue, U. Ripamonti, S. Fenwick, Biophysical stimulation of bone fracture repair, regeneration and remodelling, Eur. Cells Mater. (2003). doi:10.22203/eCM.v006a07.

[25]   P. V. Giannoudis, T.A. Einhorn, D. Marsh, Fracture healing: The diamond concept, Int. J. Care Inj. 38S4 (2007) 3–6.

[26]   F. Matassi, F. Nistri, D. Chicon Paez, M. Innocenti, New biomaterials for bone regeneration, Clin. Cases Miner. Bone Metab. 8 (2011) 21–24. doi:10.1007/s00264-012-1525-6.

[27]   C. Gao, S. Peng, P. Feng, C. Shuai, Bone biomaterials and interactions with stem cells, Bone Res. 5 (2017) 1–33. doi:10.1038/boneres.2017.59.

[28]   A.H. Simpson, I.R. Murray, Main differences in osteoporotic fracture models: Which should i use?, Injury. (2016). doi:10.1016/S0020-1383(16)30004-3.

[29]   H. Qu, H. Fu, Z. Han, Y. Sun, Biomaterials for bone tissue engineering scaffolds: A review, RSC Adv. 9 (2019) 26252–26262. doi:10.1039/c9ra05214c.

[30]   K.J.L. Burg, S. Porter, J.F. Kellam, Biomaterial developments for bone tissue engineering, Biomaterials. 21 (2000) 2347–2359. doi:10.1016/S0142-9612(00)00102-2.

[31]   H.J. Haugen, S.P. Lyngstadaas, F. Rossi, G. Perale, Bone grafts: which is the ideal biomaterial?, J. Clin. Periodontol. 46 (2019) 92–102. doi:10.1111/jcpe.13058.

[32]   A.K. Nair, A. Gautieri, S.W. Chang, M.J. Buehler, Molecular mechanics of mineralized collagen fibrils in bone, Nat. Commun. (2013). doi:10.1038/ncomms2720.

[33]   W. Wang, K.W.K. Yeung, Bone grafts and biomaterials substitutes for bone defect repair: A review, Bioact. Mater. 2 (2017) 224–247. doi:10.1016/j.bioactmat.2017.05.007.

[34]   R. Yunus Basha, S.K. Sampath, M. Doble, Design of biocomposite materials for bone tissue regeneration, Mater. Sci. Eng. C. (2015). doi:10.1016/j.msec.2015.07.016.

[35]   T. Goto, K. Sasaki, Effects of trace elements in fish bones on crystal characteristics of hydroxyapatite obtained by calcination, Ceram. Int. (2014). doi:10.1016/j.ceramint.2014.03.067.

[36]   M.A. Hanson, P.D. Gluckman, Early developmental conditioning of later health and disease: physiology or pathophysiology?, Physiol. Rev. (2014). doi:10.1152/physrev.00029.2013.

[37]   R.A. Bhatt, T.D. Rozental, Bone Graft Substitutes, Hand Clin. (2012). doi:10.1016/j.hcl.2012.08.001.

[38]   V.M. Goldberg, S. Akhavan, Biology of bone grafts, in: Bone Regen. Repair Biol. Clin. Appl., 2005. doi:10.1385/1-59259-863-3:057.

[39]   T.T. Roberts, A.J. Rosenbaum, Bone grafts, bone substitutes and orthobiologics the bridge between basic science and clinical advancements in fracture healing, Organogenesis. (2012). doi:10.4161/org.23306.

[40]   T.W. Bauer, G.F. Muschler, Bone graft materials: An overview of the basic science, in: Clin. Orthop. Relat. Res., 2000. doi:10.1097/00003086-200002000-00003.

[41]   S.N. Khan, F.P. Cammisa, H.S. Sandhu, A.D. Diwan, F.P. Girardi, J.M. Lane, The biology of bone grafting., J. Am. Acad. Orthop. Surg. (2005). doi:10.5435/00124635-200501000-00010.

[42]   E. Chiarello, M. Cadossi, G. Tedesco, P. Capra, C. Calamelli, A. Shehu, S. Giannini, Autograft, allograft and bone substitutes in reconstructive orthopedic surgery, in: Aging Clin. Exp. Res., 2013. doi:10.1007/s40520-013-0088-8.

[43]   S. Stevenson, M. Horowitz, The response to bone allografts., J. Bone Jt. Surg. (1992). doi:10.2106/00004623-199274060-00017.

[44]   R. Langer, J.P. Vacanti, Tissue engineering, Science (80-.). (1993). doi:10.1126/science.8493529.

[45]   T. Winkler, F.A. Sass, G.N. Duda, K. Schmidt-Bleek, A review of biomaterials in bone defect healing, remaining shortcomings and future opportunities for bone tissue engineering, Bone Joint Res. 7 (2018) 232–243. doi:10.1302/2046-3758.73.BJR-2017-0270.R1.

[46]   B. Rattier, A. Hoffman, F. Schoen, J. Lemons, Biomaterials Science: An Introduction to Materials in Medicine, J. Clin. Eng. (1997). doi:10.1097/00004669-

199701000-00009.

[47] L.L. Hench, J.R. Jones, Bioactive Glasses: Frontiers and Challenges, Front. Bioeng. Biotechnol. 3 (2015) 1–12. doi:10.3389/fbioe.2015.00194.

[48] L.L. Hench, The story of Bioglass®, J. Mater. Sci. Mater. Med. 17 (2006) 967–978. doi:10.1007/s10856-006-0432-z.

[49] T. Albrektsson, C. Johansson, Osteoinduction, osteoconduction and osseointegration, Eur. Spine J. (2001). doi:10.1007/s005860100282.

[50] E. García-Gareta, M.J. Coathup, G.W. Blunn, Osteoinduction of bone grafting materials for bone repair and regeneration, Bone. (2015). doi:10.1016/j.bone.2015.07.007.

[51] A. Kolk, J. Handschel, W. Drescher, D. Rothamel, F. Kloss, M. Blessmann, M. Heiland, K.D. Wolff, R. Smeets, Current trends and future perspectives of bone substitute materials - From space holders to innovative biomaterials, J. Cranio-Maxillofacial Surg. (2012). doi:10.1016/j.jcms.2012.01.002.

[52] M.J. Webber, E.A. Appel, E.W. Meijer, R. Langer, Supramolecular biomaterials, Nat. Mater. (2015). doi:10.1038/nmat4474.

[53] C. He, X. Jin, P.X. Ma, Calcium phosphate deposition rate, structure and osteoconductivity on electrospun poly(l-lactic acid) matrix using electrodeposition or simulated body fluid incubation, Acta Biomater. (2014). doi:10.1016/j.actbio.2013.08.041.

[54] S. Zwingenberger, C. Nich, R.D. Valladares, Z. Yao, M. Stiehler, S.B. Goodman, Recommendations and considerations for the use of biologics in orthopedic surgery, BioDrugs. (2012). doi:10.2165/11631680-000000000-00000.

[55] N. Eliaz, N. Metoki, Calcium phosphate bioceramics: A review of their history, structure, properties, coating technologies and biomedical applications, Materials (Basel). (2017). doi:10.3390/ma10040334.

[56] Y.K. Pan, C.Z. Chen, D.G. Wang, Z.Q. Lin, Preparation and bioactivity of micro-arc oxidized calcium phosphate coatings, Mater. Chem. Phys. (2013). doi:10.1016/j.matchemphys.2013.06.013.

[57] M. Bohner, Physical and chemical aspects of calcium phosphates used in spinal surgery, Eur. Spine J. (2001). doi:10.1007/s005860100276.

[58] C.G. Finkemeier, Bone-grafting and bone-graft substitutes, J. Bone Jt. Surg. - Ser. A. (2002). doi:10.2106/00004623-200203000-00020.

[59] F. Maehira, I. Miyagi, Y. Eguchi, Effects of calcium sources and soluble silicate on bone metabolism and the related gene expression in mice, Nutrition. (2009). doi:10.1016/j.nut.2008.10.023.

[60] X. Zhou, N. Zhang, S. Mankoci, N. Sahai, Silicates in orthopedics and bone tissue engineering materials, J. Biomed. Mater. Res. - Part A. (2017). doi:10.1002/jbm.a.36061.

[61] E.M. Carlisle, Silicon: A requirement in bone formation independent of vitamin D1, Calcif. Tissue Int. (1981). doi:10.1007/BF02409409.

[62] S. Bose, S. Tarafder, S.S. Banerjee, N.M. Davies, A. Bandyopadhyay, Understanding in vivo response and mechanical property variation in MgO, SrO and SiO2 doped β-TCP, Bone. (2011). doi:10.1016/j.bone.2011.03.685.

[63] C.C. Su, C.T. Kao, C.J. Hung, Y.J. Chen, T.H. Huang, M.Y. Shie, Regulation of physicochemical properties, osteogenesis activity, and fibroblast growth factor-2 release ability of β-tricalcium phosphate for bone cement by calcium silicate, Mater. Sci. Eng. C. (2014). doi:10.1016/j.msec.2014.01.010.

[64] N. Lertcumfu, P. Jaita, S. Manotham, P. Jarupoom, S. Eitssayeam, K. Pengpat, G. Rujijanagul, Properties of calcium phosphates ceramic composites derived from natural materials, Ceram. Int. (2016). doi:10.1016/j.ceramint.2016.03.162.

[65] L.L. Hench, R.J. Splinter, W.C. Allen, T.K. Greenlee, Bonding mechanisms at the interface of ceramic prosthetic materials, J. Biomed. Mater. Res. (1971). doi:10.1002/jbm.820050611.

[66] W. Cao, L.L. Hench, Bioactive materials, Ceram. Int. (1996). doi:10.1016/0272-8842(95)00126-3.

[67] L.L. Hench, N. Roki, M.B. Fenn, Bioactive glasses: Importance of structure and properties in bone regeneration, J. Mol. Struct. 1073 (2014) 24–30. doi:10.1016/j.molstruc.2014.03.066.

[68] M.N. Rahaman, D.E. Day, B. Sonny Bal, Q. Fu, S.B. Jung, L.F. Bonewald, A.P. Tomsia, Bioactive glass in tissue engineering, Acta Biomater. 7 (2011) 2355–2373. doi:10.1016/j.actbio.2011.03.016.

[69] G. Kaur, G. Pickrell, N. Sriranganathan, V. Kumar, D. Homa, Review and the state of the art: Sol–gel and melt quenched bioactive glasses for tissue engineering, J. Biomed. Mater. Res. - Part B Appl. Biomater. 104 (2016) 1248–1275. doi:10.1002/jbm.b.33443.

[70] G. Kaur, O.P. Pandey, K. Singh, D. Homa, B. Scott, G. Pickrell, A review of bioactive glasses: Their structure, properties, fabrication and apatite formation, J. Biomed. Mater. Res. - Part A. 102 (2014) 254–274. doi:10.1002/jbm.a.34690.

[71] X. Zhang, M. Cresswell, Materials for Inorganic Controlled Release Technology, in: Inorg. Control. Release Technol., 2016. doi:10.1016/b978-0-08-099991-3.00001-6.

[72] J. Zarzycki, Past and present of sol-gel science and technology, J. Sol-Gel Sci. Technol. 8 (1997) 17–22. doi:10.1007/BF02436811.

[73] I. Izquierdo-Barba, A.J. Salinas, M. Vallet-Regí, Bioactive glasses: from macro to nano, Int. J. Appl. Glas. Sci. 4 (2013) 149–161. doi:10.1111/ijag.12028.

[74] R. Li, A.E. Clark, L.L. Hench, An investigation of bioactive glass powders by sol-gel processing., J. Appl. Biomater. 2 (1991) 231–239. doi:10.1002/jab.770020403.

[75] M. Erol-Taygun, K. Zheng, A.R. Boccaccini, Nanoscale Bioactive Glasses in Medical Applications, Int. J. Appl. Glas. Sci. 4 (2013) 136–148. doi:10.1111/ijag.12029.

[76] K.D. Lobel, L.L. Hench, In-vitro protein interactions with a bioactive gel-glass, J. Sol-Gel Sci. Technol. (1996). doi:10.1007/BF00401885.

[77] S. Kotani, Y. Fujita, T. Kitsugi, T. Nakamura, T. Yamamuro, C. Ohtsuki, T. Kokubo, Bone bonding mechanism of β-tricalcium phosphate, J. Biomed. Mater. Res. (1991). doi:10.1002/jbm.820251010.

[78] M. Vallet-Regí, Evolution of bioceramics within the field of biomaterials, Comptes Rendus Chim. 13 (2010) 174–185. doi:10.1016/j.crci.2009.03.004.

[79] K.S.W. Sing, Reporting physisorption data for gas/solid systems with special reference to the determination of surface area and porosity (Recommendations 1984), Pure Appl. Chem. 57 (1985) 603–619. doi:10.1351/pac198557040603.

[80] T. Yanagisawa, T. Shimizu, K. Kuroda, C. Kato, The preparation of alkyltrimethylammonium-kanemite complexes and their conversion to microporous materials, Bull. Chem. Soc. Jpn. 63 (1990) 988–992.

[81] C.T. Kresge, M.E. Leonowics, W.J. Roth, J.C. Vartuli, J.S. Beck, Ordered mesoporous molecular sieves synthesized by a liquid-crystal template mechanism, Nature. 359 (1992) 710–712.

[82] I. Izquierdo-Barba, M. Vallet-Regí, Mesoporous bioactive glasses: Relevance of their porous structure compared to that of classical bioglasses, Biomed. Glas. 1 (2015) 140–150. doi:10.1515/bglass-2015-0014.

[83] N.K. Raman, M.T. Anderson, C.J. Brinker, Template-based approaches to the preparation of amorphous, nanoporous silicas, Chem. Mater. 8 (1996) 1682–1701. doi:10.1021/cm960138+.

[84] M. Vallet-Regi, I. Izquierdo-Barba, M. Colilla, Structure and functionalization of mesoporous bioceramics for bone tissue regeneration and local drug delivery, Philos. Trans. R. Soc. A Math. Phys. Eng. Sci. 370 (2012) 1400–1421. doi:10.1098/rsta.2011.0258.

[85] X. Yan, C. Yu, X. Zhou, J. Tang, D. Zhao, Highly ordered mesoporous bioactive glasses with superior in vitro bone-forming bioactivities, Angew. Chemie - Int. Ed. 43 (2004) 5980–5984. doi:10.1002/anie.200460598.

[86] A. López-Noriega, D. Arcos, I. Izquierdo-Barba, Y. Sakamoto, O. Terasaki, M. Vallet-Regí, Ordered mesoporous bioactive glasses for bone tissue regeneration, Chem. Mater. 18 (2006) 3137–3144. doi:10.1021/cm060488o.

[87] C.J. Brinker, Y.F. Lu, A. Sellinger, H.Y. Fan, Evaporation Induced Self-Assembly: Nanostructures Made Easy, Adv. Mater. 11 (1999) 579–585.

[88] J. Zhong, D.C. Greenspan, Processing and properties of sol-gel bioactive glasses, J. Biomed. Mater. Res. (2000). doi:10.1002/1097-4636(2000)53:6<694::AID-JBM12>3.0.CO;2-6.

[89] X.X. Yan, H.X. Deng, X.H. Huang, G.Q. Lu, S.Z. Qiao, D.Y. Zhao, C.Z. Yu, Mesoporous bioactive glasses. I. Synthesis and structural characterization, J. Non. Cryst. Solids. 351 (2005) 3209–3217. doi:10.1016/j.jnoncrysol.2005.08.024.

[90] C. Wu, J. Chang, Mesoporous bioactive glasses: structure characteristics, drug/growth factor delivery and bone regeneration application, Interface Focus. 2 (2012) 292–306. doi:10.1098/rsfs.2011.0121.

[91] D. Arcos, A. López-Noriega, E. Ruiz-Hernández, O. Terasaki, M. Vallet-Regí, Ordered mesoporous microspheres for bone grafting and drug delivery, Chem.

73

Mater. 21 (2009) 1000–1009. doi:10.1021/cm801649z.

[92]   F. Hoffmann, M. Cornelius, J. Morell, M. Fröba, Silica-based mesoporous organic-inorganic hybrid materials, Angew. Chemie - Int. Ed. 45 (2006) 3216–3251. doi:10.1002/anie.200503075.

[93]   S. Kargozar, M. Montazerian, S. Hamzehlou, H.W. Kim, F. Baino, Mesoporous bioactive glasses: Promising platforms for antibacterial strategies, Acta Biomater. (2018) 1–19. doi:10.1016/j.actbio.2018.09.052.

[94]   I. Izquierdo-Barba, D. Arcos, Y. Sakamoto, O. Terasaki, A. López-Noriega, M. Vallet-Regí, High-performance mesoporous bioceramics mimicking bone mineralization, Chem. Mater. 20 (2008) 3191–3198. doi:10.1021/cm800172x.

[95]   S. Fiorilli, G. Molino, C. Pontremoli, G. Iviglia, E. Torre, C. Cassinelli, M. Morra, C. Vitale-Brovarone, The incorporation of strontium to improve bone-regeneration ability of mesoporous bioactive glasses, Materials (Basel). 11 (2018) 678. doi:10.3390/ma11050678.

[96]   C. Pontremoli, I. Izquierdo-barba, G. Montalbano, M. Vallet-regí, C. Vitale-brovarone, S. Fiorilli, Journal of Colloid and Interface Science Strontium-releasing mesoporous bioactive glasses with anti-adhesive zwitterionic surface as advanced biomaterials for bone tissue regeneration, J. Colloid Interface Sci. 563 (2020) 92–103. doi:10.1016/j.jcis.2019.12.047.

[97]   V. Mouriño, J.P. Cattalini, A.R. Boccaccini, Metallic ions as therapeutic agents in tissue engineering scaffolds: an overview of their biological applications and strategies for new developments, J. R. Soc. Interface. 9 (2012) 401–419. doi:10.1098/rsif.2011.0611.

[98]   P. Habibovic, J.E. Barralet, Bioinorganics and biomaterials: Bone repair, Acta Biomater. (2011). doi:10.1016/j.actbio.2011.03.027.

[99]   The dose makes the poison, Nat. Nanotechnol. (2011). doi:10.1038/nnano.2011.87.

[100]   G.F. Hu, Copper stimulates proliferation of human endothelial cells under culture, J. Cell. Biochem. (1998). doi:10.1002/(SICI)1097-4644(19980601)69:3<326::AID-JCB10>3.0.CO;2-A.

[101]   C. Gérard, L.J. Bordeleau, J. Barralet, C.J. Doillon, The stimulation of angiogenesis and collagen deposition by copper, Biomaterials. (2010). doi:10.1016/j.biomaterials.2009.10.009.

[102]   L. Finney, S. Vogt, T. Fukai, D. Glesne, Copper and angiogenesis: Unravelling a relationship key to cancer progression, Clin. Exp. Pharmacol. Physiol. (2009). doi:10.1111/j.1440-1681.2008.04969.x.

[103]   Y. Lin, W. Xiao, B.S. Bal, M.N. Rahaman, Effect of copper-doped silicate 13-93 bioactive glass scaffolds on the response of MC3T3-E1 cells in vitro and on bone regeneration and angiogenesis in rat calvarial defects in vivo, Mater. Sci. Eng. C. 67 (2016) 440–452. doi:10.1016/j.msec.2016.05.073.

[104]   L.B. Romero-sánchez, M. Marí-beffa, P. Carrillo, M. Ángel, A. Díaz-cuenca, Copper-containing mesoporous bioactive glass promotes angiogenesis in an in vivo zebrafish model, Acta Biomater. 68 (2018) 272–285. doi:10.1016/j.actbio.2017.12.032.

[105] M. Dziadek, B. Zagrajczuk, E. Menaszek, K. Dziadek, K. Cholewa-Kowalska, A simple way of modulating in vitro angiogenic response using Cu and Co-doped bioactive glasses, Mater. Lett. 215 (2018) 87–90. doi:10.1016/j.matlet.2017.12.075.

[106] J. Pablo Rodrguez, S. Ros, M. Gonzlez, Modulation of the proliferation and differentiation of human mesenchymal stem cells by copper, J. Cell. Biochem. (2002). doi:10.1002/jcb.10111.

[107] J. Zhang, J. Huang, S. Xu, K. Wang, S. Yu, Effects of Cu2+ and pH on osteoclastic resorption in vitro, Prog. Nat. Sci. (2003). doi:10.1360/03jz9047.

[108] I. Burghardt, F. Lüthen, C. Prinz, B. Kreikemeyer, C. Zietz, H.G. Neumann, J. Rychly, A dual function of copper in designing regenerative implants, Biomaterials. (2015). doi:10.1016/j.biomaterials.2014.12.022.

[109] K.D. Cashman, A. Baker, F. Ginty, A. Flynn, J.J. Strain, M.P. Bonham, J.M. O'Connor, S. Bügel, B. Sandström, No effect of copper supplementation on biochemical markers of bone metabolism in healthy young adult females despite apparently improved copper status, Eur. J. Clin. Nutr. (2001). doi:10.1038/sj.ejcn.1601177.

[110] Y.L. Lai, M. Yamaguchi, Effects of copper on bone component in the femoral tissues of rats: Anabolic effect of zinc is weakened by copper, Biol. Pharm. Bull. (2005). doi:10.1248/bpb.28.2296.

[111] G. Grass, C. Rensing, M. Solioz, Metallic copper as an antimicrobial surface, Appl. Environ. Microbiol. 77 (2011) 1541–1547. doi:10.1128/AEM.02766-10.

[112] S. Bin Zaman, M.A. Hussain, R. Nye, V. Mehta, K.T. Mamun, N. Hossain, A Review on Antibiotic Resistance: Alarm Bells are Ringing, Cureus. (2017). doi:10.7759/cureus.1403.

[113] G. Borkow, Using Copper to Improve the Well-Being of the Skin, Curr. Chem. Biol. (2015). doi:10.2174/2212796809666150227223857.

[114] V.B.P. Sudha, S. Ganesan, G.P. Pazhani, T. Ramamurthy, G.B. Nair, P. Venkatasubramanian, Storing drinking-water in copper pots kills contaminating diarrhoeagenic bacteria, J. Heal. Popul. Nutr. (2012). doi:10.3329/jhpn.v30i1.11271.

[115] S. Mulukutla, R. Kinser, Article Antibacterial Effects of Copper Surfaces, 3 (2020) 1–5.

[116] V.M. Villapún, L.G. Dover, A. Cross, S. González, Antibacterial metallic touch surfaces, Materials (Basel). (2016). doi:10.3390/ma9090736.

[117] G. Grass, C. Rensing, M. Solioz, Metallic copper as an antimicrobial surface, Appl. Environ. Microbiol. (2011). doi:10.1128/AEM.02766-10.

[118] C. Wu, Y. Zhou, M. Xu, P. Han, L. Chen, J. Chang, Y. Xiao, Copper-containing mesoporous bioactive glass scaffolds with multifunctional properties of angiogenesis capacity, osteostimulation and antibacterial activity, Biomaterials. 34 (2013) 422–433. doi:10.1016/j.biomaterials.2012.09.066.

[119] A. Bari, N. Bloise, S. Fiorilli, G. Novajra, M. Vallet-Regí, G. Bruni, A. Torres-Pardo, J.M. González-Calbet, L. Visai, C. Vitale-Brovarone, Copper-containing mesoporous bioactive glass nanoparticles as multifunctional agent for bone

regeneration, Acta Biomater. 55 (2017) 493–504. doi:10.1016/j.actbio.2017.04.012.

[120] X. Wang, F. Cheng, J. Liu, J.H. Smått, D. Gepperth, M. Lastusaari, C. Xu, L. Hupa, Biocomposites of copper-containing mesoporous bioactive glass and nanofibrillated cellulose: Biocompatibility and angiogenic promotion in chronic wound healing application, Acta Biomater. 46 (2016) 286–298. doi:10.1016/j.actbio.2016.09.021.

[121] S.N. Rath, A. Brandl, D. Hiller, A. Hoppe, U. Gbureck, R.E. Horch, A.R. Boccaccini, U. Kneser, Bioactive copper-doped glass scaffolds can stimulate endothelial cells in co-culture in combination with mesenchymal stem cells, PLoS One. (2014). doi:10.1371/journal.pone.0113319.

[122] S.C. Skoryna, METABOLIC ASPECTS OF THE PHARMACOLOGIC USE OF TRACE ELEMENTS IN HUMAN SUBJECTS WITH SPECIFIC REFERENCE TO STABLE STRONTIUM., in: Trace Subst. Environ. Heal. Proc. Univ. Missouri's Annu. Conf., 1984.

[123] J. Coulombe, H. Faure, B. Robin, M. Ruat, In vitro effects of strontium ranelate on the extracellular calcium-sensing receptor, Biochem. Biophys. Res. Commun. (2004). doi:10.1016/j.bbrc.2004.08.209.

[124] S. Peng, X.S. Liu, G. Zhou, Z. Li, K.D.K. Luk, X.E. Guo, W.W. Lu, Osteoprotegerin deficiency attenuates strontium-mediated inhibition of osteoclastogenesis and bone resorption, J. Bone Miner. Res. (2011). doi:10.1002/jbmr.325.

[125] P. Kostenuik, victoria Shalhoub, Osteoprotegerin A Physiological and Pharmacological Inhibitor of Bone Resorption., Curr. Pharm. Des. (2005). doi:10.2174/1381612013397807.

[126] E.M. Brown, Is the calcium receptor a molecular target for the actions of strontium on bone?, Osteoporos. Int. (2003). doi:10.1007/s00198-002-1343-6.

[127] E. Gentleman, Y.C. Fredholm, G. Jell, N. Lotfibakhshaiesh, M.D. O'Donnell, R.G. Hill, M.M. Stevens, The effects of strontium-substituted bioactive glasses on osteoblasts and osteoclasts in vitro, Biomaterials. 31 (2010) 3949–3956. doi:10.1016/j.biomaterials.2010.01.121.

[128] M.J. Bolland, A. Grey, A comparison of adverse event and fracture ef fi cacy data for strontium ranelate in regulatory documents and the publication record, (2014) 1–8. doi:10.1136/bmjopen-2014-005787.

[129] F.H. Nielsen, Is boron nutritionally relevant?, Nutr. Rev. 66 (2008) 183–191. doi:10.1111/j.1753-4887.2008.00023.x.

[130] F.H. Nielsen, The emergence of boron as nutritionally important throughout the life cycle, Nutrition. 16 (2000) 512–514.

[131] C. Wu, R. Miron, A. Sculean, S. Kaskel, T. Doert, R. Schulze, Y. Zhang, Proliferation, differentiation and gene expression of osteoblasts in boron-containing associated with dexamethasone deliver from mesoporous bioactive glass scaffolds, Biomaterials. 32 (2011) 7068–7078. doi:10.1016/j.biomaterials.2011.06.009.

[132] A.A. Gorustovich, J.M.P. López, M.B. Guglielmotti, R.L. Cabrini, Biological

performance of boron-modified bioactive glass particles implanted in rat tibia bone marrow, Biomed. Mater. 1 (2006) 100–105. doi:10.1088/1748-6041/1/3/002.

[133] V. Uskoković, D.P. Uskoković, Nanosized hydroxyapatite and other calcium phosphates: Chemistry of formation and application as drug and gene delivery agents, J. Biomed. Mater. Res. - Part B Appl. Biomater. 96 B (2011) 152–191. doi:10.1002/jbm.b.31746.

[134] P. Balasubramanian, L. Hupa, B. Jokic, R. Detsch, A. Grünewald, A.R. Boccaccini, Angiogenic potential of boron-containing bioactive glasses: in vitro study, J. Mater. Sci. 52 (2017) 8785–8792. doi:10.1007/s10853-016-0563-7.

[135] L.A. Haro Durand, G.E. Vargas, N.M. Romero, R. Vera-Mesones, J.M. Porto-López, A.R. Boccaccini, M.P. Zago, A. Baldi, A. Gorustovich, Angiogenic effects of ionic dissolution products released from a boron-doped 45S5 bioactive glass, J. Mater. Chem. B. 3 (2015) 1142–1148. doi:10.1039/c4tb01840k.

[136] S. Bose, G. Fielding, S. Tarafder, A. Bandyopadhyay, Understanding of dopant-induced osteogenesis and angiogenesis in calcium phosphate ceramics, Trends Biotechnol. (2013). doi:10.1016/j.tibtech.2013.06.005.

[137] A. Zamani, G.R. Omrani, M.M. Nasab, Lithium's effect on bone mineral density, Bone. (2009). doi:10.1016/j.bone.2008.10.001.

[138] C.M. Hedgepeth, L.J. Conrad, J. Zhang, H.C. Huang, V.M.Y. Lee, P.S. Klein, Activation of the Wnt signaling pathway: A molecular mechanism for lithium action, Dev. Biol. 185 (1997) 82–91. doi:10.1006/dbio.1997.8552.

[139] E. Chalecka-Franaszek, D.M. Chuang, Lithium activates the serine/threonine kinase Akt-1 and suppresses glutamate-induced inhibition of Akt-1 activity in neurons, Proc. Natl. Acad. Sci. U. S. A. (1999). doi:10.1073/pnas.96.15.8745.

[140] M. Arioka, F. Takahashi-Yanaga, M. Sasaki, T. Yoshihara, S. Morimoto, M. Hirata, Y. Mori, T. Sasaguri, Acceleration of bone regeneration by local application of lithium: Wnt signal-mediated osteoblastogenesis and Wnt signal-independent suppression of osteoclastogenesis, Biochem. Pharmacol. 90 (2014) 397–405. doi:10.1016/j.bcp.2014.06.011.

[141] W. Fan, R. Crawford, Y. Xiao, Enhancing in vivo vascularized bone formation by cobalt chloride-treated bone marrow stromal cells in a tissue engineered periosteum model, Biomaterials. 31 (2010) 3580–3589. doi:10.1016/j.biomaterials.2010.01.083.

[142] T. Tanaka, I. Kojima, T. Ohse, J.R. Ingelfinger, S. Adler, T. Fujita, M. Nangaku, Cobalt promotes angiogenesis via hypoxia-inducible factor and protects tubulointerstitium in the remnant kidney model, Lab. Investig. 85 (2005) 1292–1307. doi:10.1038/labinvest.3700328.

[143] C. Wu, Y. Zhou, W. Fan, P. Han, J. Chang, J. Yuen, M. Zhang, Y. Xiao, Hypoxia-mimicking mesoporous bioactive glass scaffolds with controllable cobalt ion release for bone tissue engineering, Biomaterials. 33 (2012) 2076–2085. doi:10.1016/j.biomaterials.2011.11.042.

[144] E. Pacary, H. Legros, S. Valable, P. Duchatelle, M. Lecocq, E. Petit, O. Nicole, M. Bernaudin, Synergistic effects of CoCl2 and ROCK inhibition on mesenchymal stem cell differentiation into neuron-like cells, J. Cell Sci. (2006).

doi:10.1242/jcs.03004.

[145] L.O. Simonsen, H. Harbak, P. Bennekou, Cobalt metabolism and toxicology-A brief update, Sci. Total Environ. 432 (2012) 210–215. doi:10.1016/j.scitotenv.2012.06.009.

[146] J. Vormann, Magnesium: Nutrition and metabolism, Mol. Aspects Med. (2003). doi:10.1016/S0098-2997(02)00089-4.

[147] G. Stendig-Lindberg, W. Koeller, A. Bauer, P.M. Rob, Experimentally induced prolonged magnesium deficiency causes osteoporosis in the rat, Eur. J. Intern. Med. (2004). doi:10.1016/j.ejim.2004.01.003.

[148] H.M. Wong, K.W.K. Yeung, K.O. Lam, V. Tam, P.K. Chu, K.D.K. Luk, K.M.C. Cheung, A biodegradable polymer-based coating to control the performance of magnesium alloy orthopaedic implants, Biomaterials. (2010). doi:10.1016/j.biomaterials.2009.11.111.

[149] H.M. Wong, S. Wu, P.K. Chu, S.H. Cheng, K.D.K. Luk, K.M.C. Cheung, K.W.K. Yeung, Low-modulus Mg/PCL hybrid bone substitute for osteoporotic fracture fixation, Biomaterials. (2013). doi:10.1016/j.biomaterials.2013.05.062.

[150] W.L. Suchanek, K. Byrappa, P. Shuk, R.E. Riman, V.F. Janas, K.S. Tenhuisen, Preparation of magnesium-substituted hydroxyapatite powders by the mechanochemical-hydrothermal method, Biomaterials. (2004). doi:10.1016/j.biomaterials.2003.12.008.

[151] E. Landi, G. Logroscino, L. Proietti, A. Tampieri, M. Sandri, S. Sprio, Biomimetic Mg-substituted hydroxyapatite: From synthesis to in vivo behaviour, J. Mater. Sci. Mater. Med. (2008). doi:10.1007/s10856-006-0032-y.

[152] J.E. Coleman, Structure and mechanism of alkaline phosphatase, Annu. Rev. Biophys. Biomol. Struct. (1992). doi:10.1146/annurev.bb.21.060192.002301.

[153] S.L. Hall, H.P. Dimai, J.R. Farley, Effects of zinc on human skeletal alkaline phosphatase activity in vitro, Calcif. Tissue Int. (1999). doi:10.1007/s002239900597.

[154] M. Yamaguchi, Role of nutritional zinc in the prevention of osteoporosis, Mol. Cell. Biochem. 338 (2010) 241–254. doi:10.1007/s11010-009-0358-0.

[155] A. Balamurugan, G. Balossier, S. Kannan, J. Michel, A.H.S. Rebelo, J.M.F. Ferreira, Development and in vitro characterization of sol-gel derived CaO-P2O5-SiO2-ZnO bioglass, Acta Biomater. 3 (2007) 255–262. doi:10.1016/j.actbio.2006.09.005.

[156] A. Oki, B. Parveen, S. Hossain, S. Adeniji, H. Donahue, Preparation and in vitro bioactivity of zinc containing sol-gel-derived bioglass materials, J. Biomed. Mater. Res. - Part A. 69 (2004) 216–221. doi:10.1002/jbm.a.20070.

[157] Y. Yamada, A. Ito, H. Kojima, M. Sakane, S. Miyakawa, T. Uemura, R.Z. LeGeros, Inhibitory effect of Zn2+ in zinc-containing β-tricalcium phosphate on resorbing activity of mature osteoclasts, J. Biomed. Mater. Res. - Part A. (2008). doi:10.1002/jbm.a.31265.

[158] J. Pasquet, Y. Chevalier, J. Pelletier, E. Couval, D. Bouvier, M.A. Bolzinger, The contribution of zinc ions to the antimicrobial activity of zinc oxide, Colloids

Surfaces A Physicochem. Eng. Asp. 457 (2014) 263–274. doi:10.1016/j.colsurfa.2014.05.057.

[159] Y. Xie, Y. He, P.L. Irwin, T. Jin, X. Shi, Antibacterial activity and mechanism of action of zinc oxide nanoparticles against Campylobacter jejuni, Appl. Environ. Microbiol. 77 (2011) 2325–2331. doi:10.1128/AEM.02149-10.

[160] C.A. Barta, K. Sachs-Barrable, J. Jia, K.H. Thompson, K.M. Wasan, C. Orvig, Lanthanide containing compounds for therapeutic care in bone resorption disorders, Dalt. Trans. (2007) 5019–5030. doi:10.1039/b705123a.

[161] K. Wang, R. Li, Y. Cheng, B. Zhu, Lanthanides - The future drugs?, Coord. Chem. Rev. 190–192 (1999) 297–308. doi:10.1016/S0010-8545(99)00072-7.

[162] S.P. Fricker, The therapeutic application of lanthanides, Chem. Soc. Rev. 35 (2006) 524–533. doi:10.1039/b509608c.

[163] C. Xu, X. Qu, Cerium oxide nanoparticle: A remarkably versatile rare earth nanomaterial for biological applications, NPG Asia Mater. 6 (2014) e90. doi:10.1038/am.2013.88.

[164] P. Eriksson, A.A. Tal, A. Skallberg, C. Brommesson, Z. Hu, R.D. Boyd, W. Olovsson, N. Fairley, I.A. Abrikosov, X. Zhang, K. Uvdal, Cerium oxide nanoparticles with antioxidant capabilities and gadolinium integration for MRI contrast enhancement, Sci. Rep. 8 (2018) 1–12. doi:10.1038/s41598-018-25390-z.

[165] S.M. Hirst, A.S. Karakoti, R.D. Tyler, N. Sriranganathan, S. Seal, C.M. Reilly, Anti-inflammatory properties of cerium oxide nanoparticles, Small. 5 (2009) 2848–2856. doi:10.1002/smll.200901048.

[166] D.S. Morais, S. Fernandes, P.S. Gomes, M.H. Fernandes, P. Sampaio, M.P. Ferraz, J.D. Santos, M.A. Lopes, N. Sooraj Hussain, Novel cerium doped glass-reinforced hydroxyapatite with antibacterial and osteoconductive properties for bone tissue regeneration, Biomed. Mater. 10 (2015) 55008. doi:10.1088/1748-6041/10/5/055008.

[167] Y. Lin, Z. Yang, J. Cheng, Preparation, characterization and antibacterial property of cerium substituted hydroxyapatite nanoparticles, J. Rare Earths. 25 (2007) 452–456. doi:10.1016/S1002-0721(07)60455-4.

[168] J.M. Sobek, D.E. Talburt, Effects of the rare earth cerium on Escherichia coli, J. Bacteriol. 95 (1968) 47–51.

[169] Y.F. Goh, A.Z. Alshemary, M. Akram, M.R. Abdul Kadir, R. Hussain, In-vitro characterization of antibacterial bioactive glass containing ceria, Ceram. Int. 40 (2014) 729–737. doi:10.1016/j.ceramint.2013.06.062.

[170] A. Chen, Q. Shi, Y. Ouyang, Y. Chen, Effect of Ce3+on membrane permeability of Escherichia coli cell, J. Rare Earths. 30 (2012) 947–951. doi:10.1016/S1002-0721(12)60159-8.

[171] M. Zhang, C. Zhang, X. Zhai, F. Luo, Y. Du, C. Yan, Antibacterial mechanism and activity of cerium oxide nanoparticles, Sci. China Mater. (2019). doi:10.1007/s40843-019-9471-7.

[172] K. Suresh Babu, M. Anandkumar, T.Y. Tsai, T.H. Kao, B. Stephen Inbaraj, B.H. Chen, Cytotoxicity and antibacterial activity of gold-supported cerium oxide

nanoparticles, Int. J. Nanomedicine. (2014). doi:10.2147/IJN.S70087.

[173] Y. Hu, Y. Du, H. Jiang, G. Jiang, Cerium promotes bone marrow stromal cells migration and osteogenic differentiation via Smad1 / 5 / 8 signaling pathway, Int J Clin Exp Pathol. 7 (2014) 5369–5378.

[174] C.A. Lipinski, Drug-like properties and the causes of poor solubility and poor permeability, J. Pharmacol. Toxicol. Methods. (2000). doi:10.1016/S1056-8719(00)00107-6.

[175] C.A. McCarthy, R.J. Ahern, R. Dontireddy, K.B. Ryan, A.M. Crean, Mesoporous silica formulation strategies for drug dissolution enhancement: a review, Expert Opin. Drug Deliv. 13 (2016) 93–108. doi:10.1517/17425247.2016.1100165.

[176] Y. Li, Y.-Z. Liu, T. Long, X.-B. Yu, T. Tang, K.-R. Dai, B. Tian, Y.-P. Guo, Z.-A. Zhu, Mesoporous bioactive glass as a drug delivery system: fabrication, bactericidal properties and biocompatibility, J. Mater. Sci. Mater. Med. 24 (2013) 1951–1961. doi:10.1007/s10856-013-4960-z.

[177] M. Manzano, M. Vallet-Regí, New developments in ordered mesoporous materials for drug delivery, J. Mater. Chem. 20 (2010) 5593. doi:10.1039/b922651f.

[178] M. Vallet-Regi, A. Rámila, R.P. Del Real, J. Pérez-Pariente, A new property of MCM-41: Drug delivery system, Chem. Mater. 13 (2001) 308–311. doi:10.1021/cm0011559.

[179] W. Xia, J. Chang, Well-ordered mesoporous bioactive glasses (MBG): A promising bioactive drug delivery system, J. Control. Release. 110 (2006) 522–530. doi:10.1016/j.jconrel.2005.11.002.

[180] M. Vallet-Regí, E. Ruiz-Hernández, Bioceramics: From bone regeneration to cancer nanomedicine, Adv. Mater. 23 (2011) 5177–5218. doi:10.1002/adma.201101586.

[181] W. Xia, J. Chang, Preparation, in vitro bioactivity and drug release property of well-ordered mesoporous 58S bioactive glass, J. Non. Cryst. Solids. 354 (2008) 1338–1341. doi:10.1016/j.jnoncrysol.2006.10.084.

[182] C. Wu, J. Chang, Multifunctional mesoporous bioactive glasses for effective delivery of therapeutic ions and drug/growth factors, J. Control. Release. 193 (2014) 282–295. doi:10.1016/j.jconrel.2014.04.026.

[183] P. Kanaujia, P. Poovizhi, W.K. Ng, R.B.H. Tan, Amorphous formulations for dissolution and bioavailability enhancement of poorly soluble APIs, Powder Technol. (2015). doi:10.1016/j.powtec.2015.05.012.

[184] D.G. Wallace, J. Rosenblatt, Collagen gel systems for sustained delivery and tissue engineering, Adv. Drug Deliv. Rev. (2003). doi:10.1016/j.addr.2003.08.004.

[185] M.F. Yagmurlu, F. Korkusuz, I. Gürsel, P. Korkusuz, Ü. Örs, V. Hasirci, Sulbactam-cefoperazone polyhydroxybutyrate-co-hydroxyvalerate (PHBV) local antibiotic delivery system: In vivo effectiveness and biocompatibility in the treatment of implant-related experimental osteomyelitis, J. Biomed. Mater. Res. (1999). doi:10.1002/(SICI)1097-4636(19990915)46:4<494::AID-JBM7>3.0.CO;2-E.

[186] D. Sendil, I. Gürsel, D. L. Wise, V. Hasirci, Antibiotic release from biodegradable

PHBV microparticles, J. Control. Release. (1999). doi:10.1016/S0168-3659(98)00195-3.

[187] X. ZHANG, U.P. WYSS, D. PICHORA, M.F.A. GOOSEN, Biodegradable Controlled Antibiotic Release Devices for Osteomyelitis: Optimization of Release Properties, J. Pharm. Pharmacol. (1994). doi:10.1111/j.2042-7158.1994.tb03890.x.

[188] J. Salonen, A.M. Kaukonen, J. Hirvonen, V.P. Lehto, Mesoporous silicon in drug delivery applications, J. Pharm. Sci. (2008). doi:10.1002/jps.20999.

[189] M. Vallet-Regí, M. Colilla, I. Izquierdo-Barba, Bioactive Mesoporous Silicas as Controlled Delivery Systems: Application in Bone Tissue Regeneration, J. Biomed. Nanotechnol. 4 (2008) 1–15. doi:10.1166/jbn.2008.002.

[190] F. Balas, M. Manzano, P. Horcajada, M. Vallet-Regi, Confinement and controlled release of bisphosphonates on ordered mesoporous silica-based materials, J. Am. Chem. Soc. (2006). doi:10.1021/ja062286z.

[191] Y. Choudhari, H. Hoefer, C. Libanati, F. Monsuur, W. McCarthy, Mesoporous Silica Drug Delivery Systems, in: Amorph. Solid Dispersions Theory Pract., 2014: pp. 665–693. doi:10.1007/978-1-4939-1598-9_23.

[192] T.T. Le, A.K.E. Elyafi, A.R. Mohammed, A. Al-Khattawi, Delivery of poorly soluble drugs via mesoporous silica: Impact of drug overloading on release and thermal profiles, Pharmaceutics. (2019). doi:10.3390/pharmaceutics11060269.

[193] H.C. Randy Mellaerts, Jasper A. G. Jammaer, Michiel Van Speybroeck, and J.A.M. Jan Van Humbeeck, Patrick Augustijns, Guy Van den Mooter, Physical state of poorly water soluble therapeutic\rmolecules loaded into SBA-15 ordered mesoporous silica carriers:\rA case study with itraconazole and ibuprofen., Langmuir. 24 (2008) 8651–8659.

[194] L.J. Waters, S. Bedford, G.M.B. Parkes, Controlled microwave processing applied to the pharmaceutical formulation of ibuprofen, AAPS PharmSciTech. (2011). doi:10.1208/s12249-011-9671-5.

[195] L.J. Waters, T. Hussain, G. Parkes, J.P. Hanrahan, J.M. Tobin, Inclusion of fenofibrate in a series of mesoporous silicas using microwave irradiation, Eur. J. Pharm. Biopharm. (2013). doi:10.1016/j.ejpb.2013.08.002.

[196] J. Stein, T. Fuchs, C. Mattern, Advanced Milling and Containment Technologies for Superfine Active Pharmaceutical Ingredients, Chem. Eng. Technol. (2010). doi:10.1002/ceat.200900590.

[197] K.K. Qian, R.H. Bogner, Application of mesoporous silicon dioxide and silicate in oral amorphous drug delivery systems, J. Pharm. Sci. (2012). doi:10.1002/jps.22779.

[198] C. Charnay, S. Bégu, C. Tourné-Péteilh, L. Nicole, D.A. Lerner, J.M. Devoisselle, Inclusion of ibuprofen in mesoporous templated silica: Drug loading and release property, Eur. J. Pharm. Biopharm. 57 (2004) 533–540. doi:10.1016/j.ejpb.2003.12.007.

[199] A.R. Brás, I.M. Fonseca, M. Dionísio, A. Schönhals, F. Affouard, N.T. Correia, Influence of nanoscale confinement on the molecular mobility of ibuprofen, J. Phys. Chem. C. (2014). doi:10.1021/jp500630m.

[200] V.P. Lehto, J. Riikonen, Drug loading and characterization of porous silicon materials, in: Porous Silicon Biomed. Appl., 2014. doi:10.1533/9780857097156.3.337.

[201] R. Mellaerts, K. Houthoofd, K. Elen, H. Chen, M. Van Speybroeck, J. Van Humbeeck, P. Augustijns, J. Mullens, G. Van den Mooter, J.A. Martens, Aging behavior of pharmaceutical formulations of itraconazole on SBA-15 ordered mesoporous silica carrier material, Microporous Mesoporous Mater. (2010). doi:10.1016/j.micromeso.2009.10.026.

[202] R.S.H. Mansour, P.K. Deb, R.K. Tekade, Role of Amorphous State in Drug Delivery, 2018. doi:10.1016/B978-0-12-814421-3.00004-X.

[203] M. Vogt, K. Kunath, J.B. Dressman, Dissolution enhancement of fenofibrate by micronization, cogrinding and spray-drying: Comparison with commercial preparations, Eur. J. Pharm. Biopharm. (2008). doi:10.1016/j.ejpb.2007.05.010.

[204] S. Hong, S. Shen, D.C.T. Tan, W.K. Ng, X. Liu, L.S.O. Chia, A.W. Irwan, R. Tan, S.A. Nowak, K. Marsh, R. Gokhale, High drug load, stable, manufacturable and bioavailable fenofibrate formulations in mesoporous silica: A comparison of spray drying versus solvent impregnation methods, Drug Deliv. 23 (2016) 316–327. doi:10.3109/10717544.2014.913323.

[205] D. Santos, A.C. Maurício, V. Sencadas, J.D. Santos, M.H. Fernandes, P.S. Gomes, Spray Drying: An Overview, in: Biomater. - Phys. Chem. - New Ed., 2018. doi:10.5772/intechopen.72247.

[206] A. Vetere, A short-cut method to predict the solubilities of solids in supercritical carbon dioxide, Fluid Phase Equilib. (1998). doi:10.1016/S0378-3812(98)00180-0.

[207] R.J. Ahern, A.M. Crean, K.B. Ryan, The influence of supercritical carbon dioxide (SC-CO2) processing conditions on drug loading and physicochemical properties, Int. J. Pharm. (2012). doi:10.1016/j.ijpharm.2012.09.047.

[208] A. Gignone, L. Manna, S. Ronchetti, M. Banchero, B. Onida, Incorporation of clotrimazole in Ordered Mesoporous Silica by supercritical CO_2, Microporous Mesoporous Mater. 200 (2014) 291–296. doi:10.1016/j.micromeso.2014.05.031.

[209] M. Vallet-Regí, Ordered mesoporous materials in the context of drug delivery systems and bone tissue engineering, Chem. - A Eur. J. 12 (2006) 5934–5943. doi:10.1002/chem.200600226.

[210] M. Boffito, C. Pontremoli, S. Fiorilli, R. Laurano, G. Ciardelli, C. Vitale-Brovarone, Injectable Thermosensitive Formulation Based on Polyurethane Hydrogel/Mesoporous Glasses for Sustained Co-Delivery of Functional Ions and Drugs, Pharmaceutics. 11 (2019) 501. doi:10.3390/pharmaceutics11100501.

[211] S.W. Song, K. Hidajat, S. Kawi, Functionalized SBA-15 materials as carriers for controlled drug delivery: Influence of surface properties on matrix-drug interactions, Langmuir. (2005). doi:10.1021/la051167e.

[212] P. Horcajada, A. Rámila, J. Pérez-Pariente, M. Vallet-Regí, Influence of pore size of MCM-41 matrices on drug delivery rate, Microporous Mesoporous Mater. 68 (2004) 105–109. doi:10.1016/j.micromeso.2003.12.012.

[213] R. Mortera, B. Onida, S. Fiorilli, V. Cauda, C.V. Brovarone, F. Baino, E. Vernè, E. Garrone, Synthesis and characterization of MCM-41 spheres inside bioactive glass-ceramic scaffold, Chem. Eng. J. 137 (2008) 54–61. doi:10.1016/j.cej.2007.07.094.

[214] A.A. Abd-Elrahman, M.A. El Nabarawi, D.H. Hassan, A.A. Taha, Ketoprofen mesoporous silica nanoparticles SBA-15 hard gelatin capsules: preparation and in vitro/in vivo characterization, Drug Deliv. (2016). doi:10.1080/10717544.2016.1186251.

[215] A. Abd-Elbary, M.A. El Nabarawi, D.H. Hassen, A.A. Taha, Inclusion and characterization of ketoprofen into different mesoporous silica nanoparticles using three loading methods, Int. J. Pharm. Pharm. Sci. (2014).

[216] Z. Guo, X.M. Liu, L. Ma, J. Li, H. Zhang, Y.P. Gao, Y. Yuan, Effects of particle morphology, pore size and surface coating of mesoporous silica on Naproxen dissolution rate enhancement, Colloids Surfaces B Biointerfaces. (2013). doi:10.1016/j.colsurfb.2012.06.026.

[217] M. Ravanbakhsh, S. Labbaf, F. Karimzadeh, A. Pinna, A.B. Houreh, M.H. Nasr-Esfahani, Mesoporous bioactive glasses for the combined application of osteosarcoma treatment and bone regeneration, Mater. Sci. Eng. C. 104 (2019) 109994. doi:10.1016/j.msec.2019.109994.

[218] A. Nieto, F. Balas, M. Colilla, M. Manzano, M. Vallet-Regí, Functionalization degree of SBA-15 as key factor to modulate sodium alendronate dosage, Microporous Mesoporous Mater. (2008). doi:10.1016/j.micromeso.2008.03.025.

[219] J. Gu, M. Huang, J. Liu, Y. Li, W. Zhao, J. Shi, Calcium doped mesoporous silica nanoparticles as efficient alendronate delivery vehicles, New J. Chem. (2012). doi:10.1039/c2nj40482f.

[220] R. García-Alvarez, I. Izquierdo-Barba, M. Vallet-Regí, 3D scaffold with effective multidrug sequential release against bacteria biofilm, Acta Biomater. 49 (2017) 113–126. doi:10.1016/j.actbio.2016.11.028.

[221] M. Cicuéndez, I. Izquierdo-barba, M. Teresa, M. Vallet-regí, European Journal of Pharmaceutics and Biopharmaceutics Biocompatibility and levofloxacin delivery of mesoporous materials, 84 (2013) 115–124. doi:10.1016/j.ejpb.2012.11.029.

[222] C.Y. Lai, B.G. Trewyn, D.M. Jeftinija, K. Jeftinija, S. Xu, S. Jeftinija, V.S.Y. Lin, A mesoporous silica nanosphere-based carrier system with chemically removable CdS nanoparticle caps for stimuli-responsive controlled release of neurotransmitters and drug molecules, J. Am. Chem. Soc. (2003). doi:10.1021/ja028650l.

[223] D. Molina-Manso, M. Manzano, J.C. Doadrio, G. Del Prado, A. Ortiz-Pérez, M. Vallet-Regí, E. Gómez-Barrena, J. Esteban, Usefulness of SBA-15 mesoporous ceramics as a delivery system for vancomycin, rifampicin and linezolid: A preliminary report, Int. J. Antimicrob. Agents. (2012). doi:10.1016/j.ijantimicag.2012.05.013.

[224] and J.A.M. Randy Mellaerts, Jasper A. G. Jammaer, Michiel Van Speybroeck, Hong Chen, Jan Van Humbeeck, Patrick Augustijns, Guy Van der Mooter, Physical state of poorly water soluble therapeutic\rmolecules loaded into SBA-15 ordered mesoporous silica carriers:\rA case study with itraconazole and ibuprofen., Langmuir. 24 (2008) 8651–8659.

[225] M. Van Speybroeck, V. Barillaro, T. Do Thi, R. Mellaerts, J. Martens, J. Van Humbeeck, J. Vermant, P. Annaert, G. Van Den Mooter, P. Augustijns, Ordered mesoporous silica material SBA-15: A broad-spectrum formulation platform for poorly soluble drugs, J. Pharm. Sci. (2009). doi:10.1002/jps.21638.

[226] J. Zhang, Y. Sun, B. Tian, K. Li, L. Wang, Y. Liang, J. Han, Multifunctional mesoporous silica nanoparticles modified with tumor-shedable hyaluronic acid as carriers for doxorubicin, Colloids Surfaces B Biointerfaces. (2016). doi:10.1016/j.colsurfb.2016.04.015.

[227] H. Meng, M. Liong, T. Xia, Z. Li, Z. Ji, J.I. Zink, A.E. Nel, Engineered design of mesoporous silica nanoparticles to deliver doxorubicin and p-glycoprotein siRNA to overcome drug resistance in a cancer cell line, ACS Nano. (2010). doi:10.1021/nn100690m.

[228] B. Su, J.P. O'Connor, NSAID therapy effects on healing of bone, tendon, and the enthesis, J. Appl. Physiol. (2013). doi:10.1152/japplphysiol.00053.2013.

[229] I. Cantón, R. Mckean, M. Charnley, K.A. Blackwood, C. Fiorica, A.J. Ryan, S. MacNeil, Development of an Ibuprofen-releasing biodegradable PLA/PGA electrospun scaffold for tissue regeneration, Biotechnol. Bioeng. 105 (2010) 396–408. doi:10.1002/bit.22530.

[230] M. Redpath, C.M.G. Marques, C. Dibden, A. Waddon, R. Lalla, S. MacNeil, Ibuprofen and hydrogel-released ibuprofen in the reduction of inflammation-induced migration in melanoma cells, Br. J. Dermatol. 161 (2009) 25–33. doi:10.1111/j.1365-2133.2009.09220.x.

[231] C. Gaucher, A. Boudier, J. Bonetti, I. Clarot, P. Leroy, M. Parent, Glutathione: Antioxidant properties dedicated to nanotechnologies, Antioxidants. (2018). doi:10.3390/antiox7050062.

[232] M. Yamada, N. Tsukimura, T. Ikeda, Y. Sugita, W. Att, N. Kojima, K. Kubo, T. Ueno, K. Sakurai, T. Ogawa, N-acetyl cysteine as an osteogenesis-enhancing molecule for bone regeneration, Biomaterials. (2013). doi:10.1016/j.biomaterials.2013.04.064.

[233] H.J. Ji, S.H. Lee, B.K. Han, H.L. Zang, S.B. Seo, M.W. Kyung, H.M. Ryoo, G.S. Kim, J.H. Baek, N-acetylcysteine stimulates osteoblastic differentiation of mouse calvarial cells, J. Cell. Biochem. (2008). doi:10.1002/jcb.21508.

[234] S. Giret, M. Wong Chi Man, C. Carcel, Mesoporous-Silica-Functionalized Nanoparticles for Drug Delivery, Chem. - A Eur. J. 21 (2015) 13850–13865. doi:10.1002/chem.201500578.

[235] M. Vallet-Regí, I. Izquierdo-Barba, M. Colilla, Structure and functionalization of mesoporous bioceramics for bone tissue regeneration and local drug delivery, Philos. Trans. R. Soc. A Math. Phys. Eng. Sci. 370 (2012) 1400–1421. doi:10.1098/rsta.2011.0258.

[236] K. Kirchhof, K. Hristova, N. Krasteva, G. Altankov, T. Groth, Multilayer coatings on biomaterials for control of MG-63 osteoblast adhesion and growth, J. Mater. Sci. Mater. Med. 20 (2009) 897–907. doi:10.1007/s10856-008-3639-3.

[237] G. Decher, Fuzzy nanoassemblies: Toward layered polymeric multicomposites, Science (80-.). (1997). doi:10.1126/science.277.5330.1232.

[238] J. Zhou, G. Romero, E. Rojas, L. Ma, S. Moya, C. Gao, Layer by layer chitosan/alginate coatings on poly(lactide-co-glycolide) nanoparticles for antifouling protection and Folic acid binding to achieve selective cell targeting, J. Colloid Interface Sci. 345 (2010) 241–247. doi:10.1016/j.jcis.2010.02.004.

[239] J. Schlenoff, G. Decher, Multilayer thin films: sequential assembly of nanocomposite materials, 2003.

[240] H. Yang, Y. Chen, Z. Chen, Y. Geng, X. Xie, X. Shen, T. Li, S. Li, C. Wu, Y. Liu, Chemo-photodynamic combined gene therapy and dual-modal cancer imaging achieved by pH-responsive alginate/chitosan multilayer-modified magnetic mesoporous silica nanocomposites, Biomater. Sci. 5 (2017) 1001–1013. doi:10.1039/c7bm00043j.

[241] X. Shi, F. Caruso, Release behavior of thin-walled microcapsules composed of polyelectrolyte multilayers, Langmuir. (2001). doi:10.1021/la001550d.

[242] S. Lin, J.R. Jones, The effect of serum proteins on apatite growth for 45S5 Bioglass and common sol-gel derived glass in SBF, (2018) 13–20.

[243] C. Blaszykowski, S. Sheikh, M. Thompson, Surface chemistry to minimize fouling from blood-based fluids, Chem. Soc. Rev. 41 (2012) 5599–5612. doi:10.1039/c2cs35170f.

[244] H. Zhang, M. Chiao, Anti-fouling coatings of poly(dimethylsiloxane) devices for biological and biomedical applications, J. Med. Biol. Eng. 35 (2015) 143–155. doi:10.1007/s40846-015-0029-4.

[245] E.P. Magennis, A.L. Hook, M.C. Davies, C. Alexander, P. Williams, M.R. Alexander, Engineering serendipity: High-throughput discovery of materials that resist bacterial attachment, Acta Biomater. 34 (2016) 84–92. doi:10.1016/j.actbio.2015.11.008.

[246] J.W. Costerton, P.S. Stewart, E.P. Greenberg, Bacterial Biofilms : A Common Cause of Persistent Infections, 284 (1999) 1318–1323.

[247] M. Vallet-Regí, M. Colilla, I. Izquierdo-Barba, Drug Delivery and Bone Infection, 1st ed., Elsevier Inc., 2018. doi:10.1016/bs.enz.2018.08.001.

[248] J.E. Rosen, F.X. Gu, Surface functionalization of silica nanoparticles with cysteine: A low-fouling zwitterionic surface, Langmuir. (2011). doi:10.1021/la201940r.

[249] Z.G. Estephan, J.A. Jaber, J.B. Schlenoff, Zwitterion-stabilized silica nanoparticles: Toward nonstick nano, Langmuir. (2010). doi:10.1021/la103095d.

[250] M. Colilla, I. Izquierdo-Barba, S. Sánchez-Salcedo, J.L.G. Fierro, J.L. Hueso, M. Vallet-Regí, Synthesis and characterization of zwitterionic SBA-15 nanostructured materials, Chem. Mater. 22 (2010) 6459–6466. doi:10.1021/cm102827y.

[251] S. Sànchez-Salcedo, M. Colilla, I. Izquierdo-Barba, M. Vallet-Regí, Design and preparation of biocompatible zwitterionic hydroxyapatite, J. Mater. Chem. B. (2013) 1595–1606. doi:10.1039/C3TB00122A.

[252] A. Alenezi, Y. Naito, T. Terukina, W. Prananingrum, Y. Jinno, T. Tagami, T. Ozeki, S. Galli, R. Jimbo, Controlled release of clarithromycin from PLGA microspheres enhances bone regeneration in rabbit calvaria defects, J. Biomed. Mater. Res. Part B Appl. Biomater. 106 (2018) 201–208. doi:10.1002/jbm.b.33844.

[253] J. Wu, G. Miao, Z. Zheng, Z. Li, W. Ren, C. Wu, Y. Li, Z. Huang, L. Yang, L. Guo, 3D printing mesoporous bioactive glass/sodium alginate/gelatin sustained release scaffolds for bone repair, J. Biomater. Appl. 33 (2019) 755–765. doi:10.1177/0885328218810269.

[254] A. Anand, P. Das, S.K. Nandi, B. Kundu, Development of antibiotic loaded mesoporous bioactive glass and its drug release kinetics, Ceram. Int. 46 (2020) 5477–5483. doi:10.1016/j.ceramint.2019.10.264.

[255] T. Cheng, H. Qu, G. Zhang, X. Zhang, Osteogenic and antibacterial properties of vancomycin-laden mesoporous bioglass/PLGA composite scaffolds for bone regeneration in infected bone defects, Artif. Cells, Nanomedicine, Biotechnol. 0 (2017) 1–13. doi:10.1080/21691401.2017.1396997.

[256] X. Li, X. Wang, L. Zhang, H. Chen, J. Shi, MBG/PLGA composite microspheres with prolonged drug release, J. Biomed. Mater. Res. Part B Appl. Biomater. 89B (2009) 148–154. doi:10.1002/jbm.b.31197.

[257] S. Borrego-González, L.B. Romero-Sánchez, J. Blázquez, A. Díaz-Cuenca, Nanostructured hybrid device mimicking bone extracellular matrix as local and sustained antibiotic delivery system, Microporous Mesoporous Mater. 256 (2018) 165–176. doi:10.1016/j.micromeso.2017.08.010.

[258] Y. Xu, Y. Hu, P. Feng, W. Yang, C. Shuai, Drug loading/release and bioactivity research of a mesoporous bioactive glass/polymer scaffold, Ceram. Int. 45 (2019) 18003–18013. doi:10.1016/j.ceramint.2019.06.019.

[259] S. Fu, X. Du, M. Zhu, Z. Tian, D. Wei, Y. Zhu, 3D printing of layered mesoporous bioactive glass/sodium alginate-sodium alginate scaffolds with controllable dual-drug release behaviors, Biomed. Mater. 14 (2019) 065011. doi:10.1088/1748-605X/ab4166.

[260] C. Wu, Y. Zhu, J. Chang, Y. Zhang, Y. Xiao, Bioactive inorganic-materials/alginate composite microspheres with controllable drug-delivery ability, J. Biomed. Mater. Res. Part B Appl. Biomater. 9999B (2010) NA-NA. doi:10.1002/jbm.b.31621.

[261] S. Shiraishi, T. Imai, M. Otagiri, Controlled-release preparation of indomethacin using calcium alginate gel, Biol. Pharm. Bull. 16 (1993) 1164–1168.

[262] D. Wang, S. Chris, W. Zuyong, H.K. Chee, N.L. Poon, S. Zhilong, T. Eng San, W. Wilson, Beta-Cyclodextrin Modified Mesoporous Bioactive Glass Nanoparticles/Silk Fibroin Hybrid Nanofibers as an Implantable Estradiol Delivery System for the Potential Treatment of Osteoporosis, Nanoscale. 10 (2018) 18341–18353. doi:10.1039/C8NR05268A.

[263] D. Saintier, V. Khanine, B. Uzan, H.K. Ea, M.C. de Vernejoul, M.E. Cohen-Solal, Estradiol inhibits adhesion and promotes apoptosis in murine osteoclasts in vitro, J. Steroid Biochem. Mol. Biol. 99 (2006) 165–173. doi:10.1016/j.jsbmb.2006.01.009.

[264] A. El-Fiqi, J.-H. Kim, H. Kim, Osteoinductive Fibrous Scaffolds of Biopolymer/Mesoporous Bioactive Glass Nanocarriers with Excellent Bioactivity and Long-Term Delivery of Osteogenic Drug, ACS Appl. Mater. Interfaces. 7 (2015) 1140–1152. doi:10.1021/am5077759.

[265] E. Gioffredi, M. Boffito, S. Calzone, S.M. Giannitelli, A. Rainer, M. Trombetta, P. Mozetic, V. Chiono, Pluronic F127 Hydrogel Characterization and Biofabrication

in Cellularized Constructs for Tissue Engineering Applications, in: Procedia CIRP, 2016: pp. 125–132. doi:10.1016/j.procir.2015.11.001.

[266] C.P. Silveira, L.M. Apolinário, W.J. Fávaro, A.J. Paula, N. Durán, Doxorubicin-Functionalized Silica Nanoparticles Incorporated into a Thermoreversible Hydrogel and Intraperitoneally Administered Result in High Prostate Antitumor Activity and Reduced Cardiotoxicity of Doxorubicin, ACS Biomater. Sci. Eng. 2 (2016) 1190–1199. doi:10.1021/acsbiomaterials.6b00241.

[267] M. Boffito, E. Gioffredi, V. Chiono, S. Calzone, E. Ranzato, S. Martinotti, G. Ciardelli, Novel polyurethane-based thermosensitive hydrogels as drug release and tissue engineering platforms: design and in vitro characterization, Polym. Int. 65 (2016) 756–769. doi:10.1002/pi.5080.

[268] S. Sartori, V. Chiono, C. Tonda-Turo, C. Mattu, C. Gianluca, Biomimetic polyurethanes in nano and regenerative medicine, J. Mater. Chem. B. 2 (2014) 5128–5144. doi:10.1039/C4TB00525B.

[269] C. Pontremoli, M. Boffito, S. Fiorilli, R. Laurano, A. Torchio, A. Bari, C. Tonda-Turo, G. Ciardelli, C. Vitale-Brovarone, Hybrid injectable platforms for the in situ delivery of therapeutic ions from mesoporous glasses, Chem. Eng. J. 340 (2018) 103–113. doi:10.1016/j.cej.2018.01.073.

[270] X. Chen, Y. Zhao, S. Geng, R. Miron, Q. Zhang, C. Wu, Y. Zhang, In vivo experimental study on bone regeneration in critical bone defects using PIB nanogels/boron-containing mesoporous bioactive glass composite scaffold, Int. J. Nanomedicine. (2015) 839. doi:10.2147/IJN.S69001.

[271] Q. Zhang, X. Chen, S. Geng, L. Wei, R.J. Miron, Y. Zhao, Y. Zhang, Nanogel-based scaffolds fabricated for bone regeneration with mesoporous bioactive glass and strontium: In vitro and in vivo characterization, J. Biomed. Mater. Res. Part A. 105 (2017) 1175–1183. doi:10.1002/jbm.a.35980.

CHAPTER 2

Materials and methods

2.1 Introduction

The general aim of this PhD project was to design multifunctional biomaterials, based on mesoporous bioactive glasses (MBGs), able to exert different therapeutic effects for bone tissue regeneration application and to overcome the drawbacks of the traditional treatments. In this chapter, all the procedures developed to produce MBGs, their functionalization and related hybrid formulations will be reported, as illustrated in the flow chart in figure 2.1.

Firstly, the two synthesis procedures selected to produce the MBGs with a binary composition based on SiO_2 and CaO (ratio 85/15) enriched with different therapeutic ions are described. These two different approaches allowed to produce nano-sized particles with diameter ranging between 100 and 200 nm and pores in the range of 2-4 nm, and micro-sized particles with size in the range of 500 and 5 μm and bigger pores in the range of 8-10 nm. The amount and the type of therapeutic ions added during the synthesis were selected by following the idea to exert peculiar outcomes, in particular copper was added to provide an antibacterial and pro-angiogenic effect, while strontium ions were selected thanks to their well-known pro-osteogenic properties.

In a second step, the therapeutic potential of the MBGs has been enriched by loading ibuprofen and N-acetylcysteine, in order to develop a drug delivery system, able to release the cargo at the pathological site. Two different methods have been investigated, the adsorption and the incipient wetness methods, to identify the most suitable loading procedure in terms of yields and required time.

Furthermore, different surface modification approaches were investigated, with the aim to provide the final device with anti-adhesive properties and to obtain a prolonged and sustained release of the cargo. In details, the *zwitterionization* procedure has been selected to impart anti-adhesive properties to the MBGs, allowing to repel the protein adhesion and thus to prevent the biofilm formation. On the other hands, the Layer by Layer deposition has been chosen as promising strategy to modulate the cargo release rate.

Finally, to make MBGs suitable as long-term therapeutics delivery systems for bone healing, a hybrid formulation based on the conjugation of MBGs with an
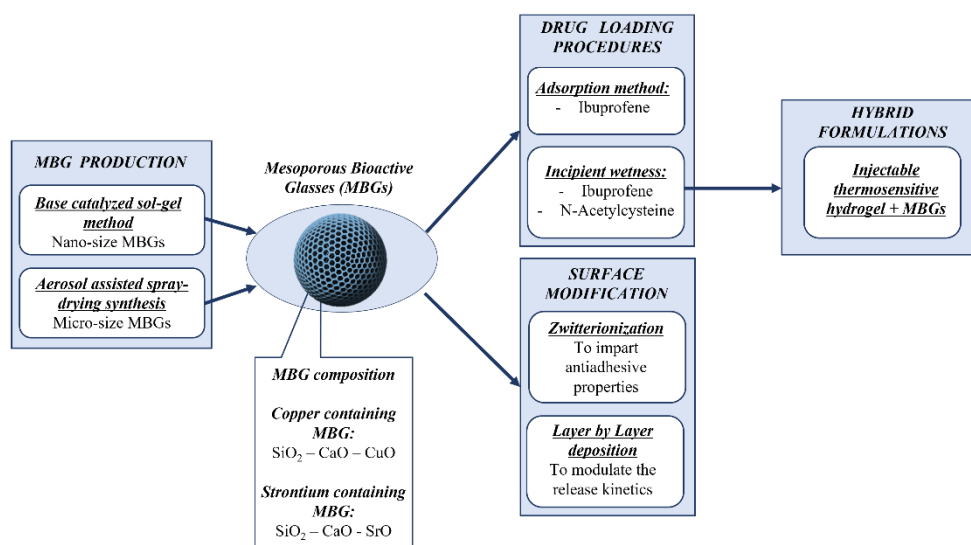
Figure 2.21 Flow chart of the selected procedures to develop multifunctional nanocarriers for the delivery of therapeutic species.

injectable thermosensitive hydrogel, acting as a vehicle phase, has been investigated in order to develop a multifunctional platform to be injected directly in the pathological site for the sustained delivery of therapeutic agent.

2.2 Synthesis of nano-sized MBGs

Part of the work described in this chapter has been already published during the PhD period [1–3].

In order to produce nano-sized particles with a binary composition based on SiO_2 and CaO (ratio 85/15) with mesopores around 4 nm, a base-catalyzed sol-gel method, involving the use of ammonium hydroxide as catalyst, was investigated, by modifying a procedure developed by Wu *et al.* [4]. Copper and strontium containing MBGs were obtained by replacing part of calcium with the selected amount of therapeutic ion. In particular, MBGs with the 2% and 4% molar percentage Sr-containing MBGs (molar ratio Sr/Ca/Si = 2/13/85, named hereafter as MBG_Sr2%_SG and molar ratio Sr/Ca/Si = 4/13/85, named hereafter as MBG_Sr4%_SG) and the 2% molar percentage Cu-containing MBGs (molar ratio Cu/Ca/Si = 2/13/85, named hereafter as MBG_Cu2%_SG) were prepared as follows: 6.6 g of cetyltrimethylammonium bromide (CTAB ≥98%, Sigma Aldrich, Italy) and 12 mL of NH_4OH (Ammonium hydroxide solution, Sigma Aldrich, Italy) were dissolved in 600 mL of double distilled water (ddH_2O). After 30 min of stirring, 30 mL tetraethyl orthosilicate (TEOS, Tetraethyl orthosilicate, reagent grade 98%, Sigma Aldrich, Italy), and, depending on the final particle composition, the proper amount (reported in table 2.1) of calcium nitrate tetrahydrate (Ca(NO_3)$_2$·4H_2O, 99%, Sigma Aldrich, Italy), strontium chloride ($SrCl_2$ 99%, Sigma

Aldrich, Italy) and copper chloride (CuCl$_2$ 99%, Sigma Aldrich, Italy) were added under vigorous stirring for 3 h. The powder was collected by centrifugation (Hermle Labortechnik Z326) at 11,000 rpm for 5 min, washed one time with distilled water and two times with absolute ethanol. The final precipitate was dried at 70 °C for 12 h and calcined at 600 °C in air for 5 h at a heating rate of 1 °C min^{-1} using a FALC FM 8,2, in order to remove CTAB.

All the reagents were purchased from Sigma Aldrich, Italy and used as received.

Table 2.2 Sample composition and reagent amount used in the base-catalyzed sol-gel procedure.

Name	Composition (%mol)	Reagents		
		TEOS (mL)	(Ca (NO$_3$)$_2$·4H$_2$O (g)	Therapeutic ion precursors (g)
MBG_Sr2%_SG	SiO$_2$/CaO/SrO = 85/13/2	30	4.88	SrCl$_2$: 0.85
MBG_Sr4%_SG	SiO$_2$/CaO/SrO = 85/11/4	30	4.13	SrCl$_2$: 1.70
MBG_Cu2%_SG	SiO$_2$/CaO/CuO =85/13/2	30	4.88	CuCl$_2$: 0.43

2.3 Synthesis of micro-sized MBGs

Part of the work described in this chapter has been already published during the PhD period [1–3,5].

The micro-sized MBGs were produced by exploiting a water-based process under mild acidic conditions by using an aerosol assisted spray-drying approach, based on a modification of the procedure reported by Pontiroli *et al.*[6]. This type of technique has been explored for the good repeatability of the process and for the promising scalability to an industrial level. The produced MBGs in form of microspheres with different composition have been summarized in table 2.2. In particular, MBGs the 2% and 4% molar percentage Sr-containing MBGs (molar ratio Sr/Ca/Si = 2/13/85 and molar ratio Sr/Ca/Si = 4/13/85, named hereafter as MBG_Sr2%_SD and MBG_Sr4%_SD, respectively) and the 2% molar percentage Cu-containing MBGs (molar ratio Cu/Ca/Si = 2/13/85, named hereafter as MBG_Cu2%_SD) were prepared as follows: 2.03 g of the non-ionic block copolymer Pluronic P123 (EO$_{20}$PO$_{70}$EO$_{20}$, average Mn ~ 5,800, Sigma Aldrich, Italy) were dissolved in 85 g of ddH$_2$O. In a separate batch, a solution of 10.73 g of TEOS was pre-hydrolysed under acidic conditions using 5 g of an aqueous HCl solution at pH 2 until a transparent solution was obtained. The solution with TEOS

was then added drop by drop into the template solution and kept stirring for 30 min. Then, the proper amount (reported in table 2.2) of ion precursor and calcium nitrate tetrahydrate were added and the final solution was stirred for 15 min and then sprayed (Büchi, Mini Spray-Dryer B-290) using nitrogen as the atomizing gas with the following parameters: inlet temperature 220 °C, N_2 pressure 60 mmHg and feed rate 5 mL/min. The obtained powder was collected and calcined at 600 °C in air for 5 h at a heating rate of 1 °C min^{-1} using a FALC FM 8,2. All the reagents were purchased from Sigma Aldrich, Italy and used as received.

Table 2.3 Sample composition and precursor amount used in the spray-drying procedure.

| Name | Composition (%mol) | Reagents | | |
		TEOS (g)	(Ca $(NO_3)_2 \cdot 4H_2O$ (g)	Therapeutic ion precursors (g)
MBG_Sr2%_SD	$SiO_2/CaO/SrO$ = 85/13/2	10.73	1.86	$SrCl_2$: 0.32
MBG_Sr4%_SD	$SiO_2/CaO/SrO$ = 85/11/4	10.73	1.57	$SrCl_2$: 0.64
MBG_Cu2%_SD	$SiO_2/CaO/CuO$ =85/13/2	10.73	1.86	$CuCl_2$: 0.16

2.4 Drug Loading Procedures

Since one of the final goals of this thesis project is to obtain mesoporous bioactive glasses to be used as a drug delivery system, two different drug loading procedures based on the adsorption method and the incipient wetness impregnation, have been explored in order to identify the best approach in terms of the drug solubility/stability, yield and time.

As reported in the "*state of the art*" chapter (section 1.6), based on the final application of the material, different active pharmaceutical ingredients (APIs) have been tested, the well-known anti-inflammatory ibuprofen as a model drug and the N-Acetylcysteine (NAC), investigated due to the pro-osteogenic effect. The over mentioned loading procedures allow to adjust the final amount of loaded and further released drug, essential aspect for the design of a drug delivery device.

2.4.1 Adsorption method (Ads)

Adsorption of ibuprofen (99.9%, Sigma) has been conducted by modifying a method reported by Mortera *et al.* [7], by contacting the drug ethanol solution (30 mg/mL, 10 mL) with 100 mg of MBGs for 24 h at room temperature under continuous stirring. Particles were collected by filtration (anodisc whatman membrane, pore size 0.02 µm) and dried overnight at +50 °C. The amount of loaded

drug was evaluated through thermogravimetric analysis (TGA). A list of the samples prepared by using the Ads method is reported in table 2.3.

Table 2.4 Samples used for ibuprofen loading by using the adsorption method.

Name	Therapeutic ion	Drugs
MBG_Cu2%_SG + Ibu Ads	Copper	Ibuprofen
MBG_Cu2%_SD + Ibu Ads	Copper	Ibuprofen

2.4.2 Incipient wetness impregnation

Part of the work described in this chapter has been already published during the PhD period[1].

Ibuprofen and NAC were loaded into MBGs through the incipient wetness method (IW) by following a procedure reported by Charnay *et al.*[8]. In brief, 100 mg of MBGs were impregnated several times by dropping consecutive 100 µL aliquots of a drug solution in ethanol (concentration of 30 mg/mL) onto the powders at RT. After each impregnation, ethanol was evaporated at 50 °C for 10 min and the dried powder mixed with a spatula. The impregnation procedure was carried out with four 100 µL aliquots for ibuprofen and with six 100 µL aliquots for NAC. Lastly, the obtained powders were dried at 50 °C overnight. A list of the samples prepared by using the IW method is reported in table 2.4.

Table 2.5 Sample composition and therapeutic species presented in the drug loaded samples prepared by using the Incipient wetness method.

Name	Therapeutic ion	Drugs
MBG_Cu2%_SG + Ibu IW	Copper	Ibuprofen
MBG_Cu2%_SD + Ibu IW	Copper	Ibuprofen
MBG_Sr2%_SG + NAC IW	Strontium	NAC
MBG_Sr2%_SD + NAC IW	Strontium	NAC

2.5 Surface modification: *zwitterionization*

Part of the work described in this chapter has been already published during the PhD period[5].

Thanks to the high number of terminal hydroxyl groups, the MBG surface can be easily functionalized by grafting alkoxysilane moieties with the aim to achieve several targets, such as an improved drug loading ability, the reduction of particle aggregation and nonspecific surface adhesion. In this PhD project, in order to design anti-adhesive/anti-fouling surfaces [9,10], *zwitterionization* has been selected as one of the most promising approach to obtain a material surface with hydrophilic behavior and electrically neutral charges. In fact, *zwitterionic* surfaces are characterized by an equal number of both positive and negative charges which preserve the overall electrical neutrality [11]. The functionalization route based on the post-grafting of aminopropyl silanetriol (APST) (22-25% in water, ALFA Chemistry) and carboxyethylsilanetriol (CES, 25% vol. in water, Carbosynth Limited), bearing respectively amino and carboxylate groups, was optimized based on the different reaction kinetics of the two precursors, both in terms of concentration and addition time, in order to anchor almost the same number of -NH_3^+/-COO^- groups on the surface of the MBGs. Figure 2.2 displays the followed functionalization procedure to obtain the zwitterionic materials.

In particular, 0.5 g of the previous described MBG_Sr2%_SG and MBG_Sr2%_SD were first outgassed overnight in vacuum and then dispersed in 100 mL of absolute ethanol (Ethanol puriss. P.A., absolute = 99.8%, Sigma Aldrich, Italy). The initial amount of APTS and CES to be added to the suspension was calculated referring to the Zhuravlev number [12], which is widely used in the literature for the estimation of the organosilane precursors in post-grafting reactions of mesoporous silicas and MBGs. Indeed, according to the Zhuravlev number, a density 4.9 $SiOH/nm^2$ can be considered, and based on the measured specific surface area of MBGs, the overall number of exposed hydroxyls (acting as anchoring sites for grafting) was estimated and the amount of precursors derived accordingly. The optimization of the overall procedure was not entirely straightforward and required several step-by-step adjustments. To this aim, ζ-potential measurements were conducted as preliminary evaluation of the modification of surface charge imparted by grafting, in order to guide the corrections required to reach the zwitterionic behavior.
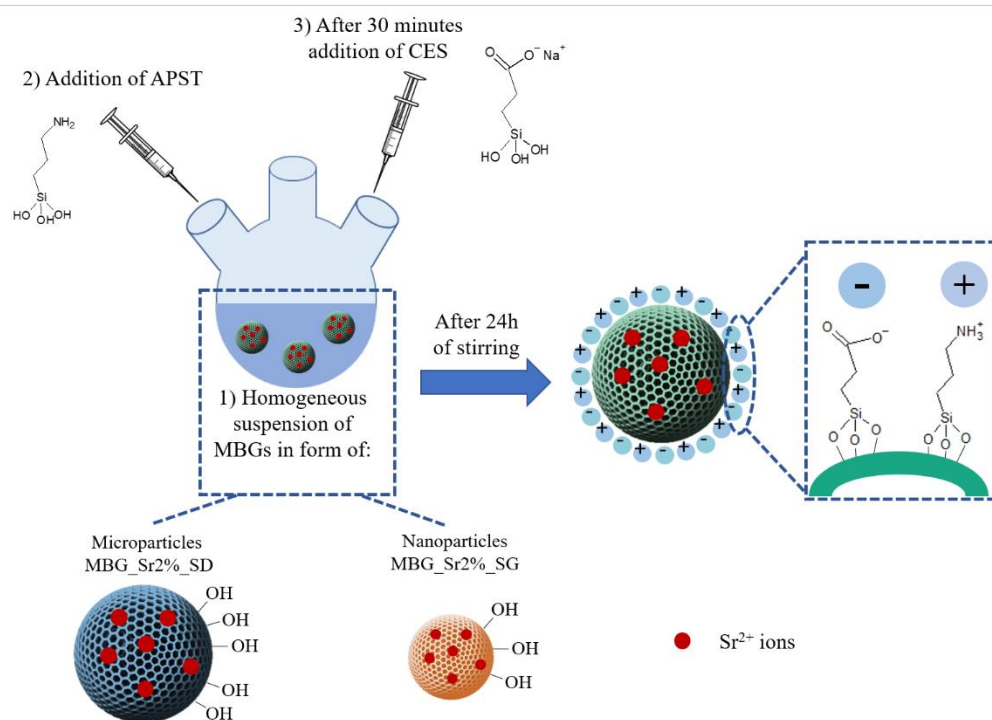
Figure 2.22 Functionalization procedure to obtain zwitterionic Sr-MBGs.

At first, an equimolar concentration of APST and CES (0.3 mmol) was added simultaneously to the ethanol suspension and refluxed 24 h under stirring (200 rpm) at 80 °C under nitrogen atmosphere. The resulting functionalized powders were filtered, washed three times with absolute ethanol and dried overnight at 70°C.

As reported in table 2.5 (first row), ζ-potential measurements at pH 7.4 revealed a negative value (-9 mV), suggesting higher surface reactivity for CES compared to APST. Therefore, to increase the amount of surface positive charges, a double amount of APST (0.6 mmol) was added to the ethanol solution and kept stirring for 30 min prior the addition of CES (0.3 mmol), in order to allow the reaction between MBG surface and APST. Lastly, an amount of APST equal to 0.9 mmol (molar ratio APST:CES 3:1) resulted to be the most appropriate to reach an overall surface charge close to zero, as shown in table 2.5 (third row). The samples reacted with APST:CES 3:1 molar ratio will be referred hereafter as MBG_Sr2%_SG_Z and MBG_Sr2%_SD_Z and were selected for the physic-chemical characterization and for the biological assessment.

Table 2.6 Investigated APST/CES amounts (mmol) and addition time. Zeta potential values measured at pH 7.4 of the resulting functionalized MBG_Sr2%.

mmol APST	mmol CES	Addition time	ζ-potential pH 7.4
0.3	0.3	Simultaneously	-9 mV

| 0.6 | 0.3 | CES added after 30 min | -7 mV |
| 0.9 | 0.3 | CES added after 30 min | -2 mV |

2.6 Surface modification: layer by layer deposition

In order to overcome the drawbacks associated to MBG burst release and produce drug delivery systems able to provide a sustained release of both therapeutic ions (*i.e.,* copper ions) and drug (*i.e.,* ibuprofen), Cu-MBGs were prepared through the above mentioned synthesis approaches and the surface was successively modified by layer-by-layer deposition of oppositely charged polyelectrolytes, which are alternatively assembled on the outer surface.

The multi-layered surface was obtained by following two different routes, which involve the use of different polyelectrolytes as schematically reported in fig. 2.3.
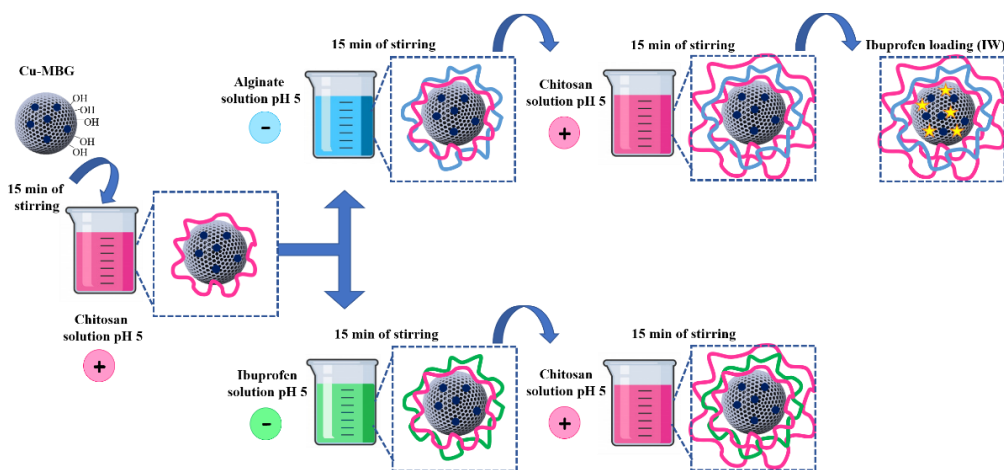
Figure 2.23 Strategies to obtain a multilayered MBG surface.

In the first strategy, chitosan, alginate and chitosan were assembled by forming the multi-layered surface and, successively, ibuprofen was loaded by incipient wetness impregnation, as already reported in section 2.4.2. On contrary, in the second strategy, alginate was replaced by the ibuprofen, by exploiting the ibuprofen negative charge (COO⁻), able to electrostatically interact with the chitosan positive charge.

Layer-by-layer deposition of chitosan and alginate

Chitosan and alginate were assembled from solutions with a concentration of 1 mg/mL in water, by following the procedure reported in the literature by Zhou *et al.* [13]. The pH value of each electrolyte solution was adjusted to 5 by addition of glacial acetic acid or 1 M NaOH. For the assembly of Chi/Alg multilayers on the MBGs surface, 100 mg of Cu-MBGs were incubated with 25 mL of the chitosan

solution under vigorous stirring (300 rpm) for 15 min. After chitosan deposition, particles were centrifuged at 10,000 rpm for 3 minutes and washed 3 times with water. After the last centrifugation, the supernatant was removed, and 25 mL of alginate solution were added to the collected powders and kept stirring for 15 min.

Initially, in the preliminary investigation, up to 10 layers were deposited on the MBG surface. However, based on FE-SEM observations, the samples coated with more than four layers showed the undesired formation of particle agglomerates embedded in a polymer phase. On the contrary, the deposition of three layers were found to be optimal to obtain multilayered coated particles, avoiding the formation of agglomerates and preserving the peculiar features of the MBGs (morphology, size, bioactive behavior).

Based on these considerations, three layers were deposited, a first layer of chitosan, a second of alginate and the last one of chitosan and the related material is referred to Cu2%_SG_CAC and Cu2%_SD_CAC. Ibuprofen was loaded into Cu2%_SG_CAC and Cu2%_SD_CAC through the incipient wetness method, by following the protocol already optimized by the authors [1]. In brief, 100 mg of both multilayered MBGs were impregnated several times by dropping consecutive small aliquots of an ibuprofen solution in ethanol (at the final concentration of 30 mg/mL) onto the powders at RT. After each impregnation, ethanol was evaporated at 50 °C for 10 min and the dried powder mixed with a spatula. In order to completely fill the mesopores with ibuprofen the impregnation procedure was carried out with four 100 µL aliquots. Lastly, the obtained powders were dried at 50 °C overnight and named as follows: Cu2%_SG_CAC_Ibu and Cu2%_SD_CAC_Ibu.

Layer-by-layer deposition of chitosan and ibuprofen

Chitosan and ibuprofen were assembled from solutions (1 mg/mL) of polyelectrolyte and drug in water and ethanol, respectively. The pH value of the chitosan solution was adjusted to 5 by addition 1 M NaOH. For the assembly of the multilayers on the MBGs surface, 100 mg of Cu-MBGs were incubated with 25 mL of the chitosan solution under vigorous stirring (300 rpm) for 15 min. After chitosan deposition, particles were centrifuged at 10,000 rpm for 3 minutes and washed 3 times with water. After the last centrifugation, the supernatant was removed, and 25 mL of ibuprofen solution were added to the collected powders and kept stirring for 15 min. Three layers were deposited, a first layer of chitosan, a second of ibuprofen and the last one of chitosan and the related material is referred to Cu2%_SG_CIC and Cu2%_SD_CIC.

2.7 A hybrid injectable formulation: MBG incorporation into a vehicle phase

Since MBGs alone are not exploitable as long-term drug delivery systems for orthopaedic applications, due to the strong burst release of the therapeutic species (ions/drugs) once in contact with body fluids, and the difficulties related to their administration at the pathological site (*i.e.,* bone fracture cavity) in the form of powder, their combination with polymers able to modulate the release kinetics and/or to act as a vehicle phase to the pathological site has been investigated. In particular, MBGs have been incorporated into an injectable Poly(ether urethane) (PEU) based thermosensitive hydrogel developed by *Professor Ciardelli's group (DIMEAS, Politecnico di Torino, Italy)*. The high versatility of the resulting hybrid formulation can find widespread application in the biomedical field for the localized and sustained co-delivery of therapeutic ions and drugs in the treatment of a variety of pathological conditions of soft (*e.g.*, non-healing wounds) and hard (*e.g.*, delayed bone healing) tissues. In fact, by tailoring the composition and cargo of MBGs, different ions and drugs can be co-released based on the therapeutic effects required by the final targeted application.

During this PhD project, by following MOZART project requirements, different hybrid formulations were developed with the aim to validate *in vivo* an injectable platform for the prolonged and sustained release of therapeutic concentrations ions and drugs. In details, in the first hybrid formulation Cu-containing MBGs loaded with ibuprofen were employed, aiming to design a multifunctional platform with anti-microbic/pro-angiogenic effects associated to the copper release and anti-inflammatory potential exerted by ibuprofen to be used both for non-healing wounds and delayed bone healing applications.
The second hybrid formulation is composed by Sr-containing MBGs loaded with NAC to be used as osteogenesis-enhancing platform, able to deliver into the bony defect both strontium ions and NAC, thus improving bone regeneration and promote bone defect healing.

2.7.1 Injectable thermosensitive hydrogel

Part of the work described in this chapter has been already published during the PhD period [1,2].

Poly(ether urethane) (PEU) based thermosensitive hydrogels were synthesized by Professor Ciardelli's group [14] and used at a final PEU concentration of 15 %w/v, by following a procedure reported by Pontremoli, Boffito *et al.* [2]. MBGs loaded with drugs were encapsulated into the hydrogel with final particle concentration of 20 mg/mL. In detail, hybrid hydrogels were prepared by adding an aliquot of particle suspension in ddH$_2$O (100 mg/mL), previously sonicated for 3 min, to a hydrogel solution previously prepared in physiological saline solution (0.9 % NaCl). The starting concentration of hydrogel solution was determined in order

to reach the desired PEU and particle contents in the final system. Both the hydrogel solubilization and particle addition were carried out at 4 °C to avoid undesired gelation during sample preparation. Sample mixing was conducted using a Vortex mixer for 30s to ensure homogeneous particle dispersion within the sol-gel systems. Particles were added to hydrogel aqueous solutions immediately before use to avoid premature ion/drug release before characterization tests. As control samples, pure hydrogel sol-gel systems and hydrogel loaded with drugs were also prepared. Loading of Ibu into the hydrogel sol-gel systems was carried out by adding the hydrogel aqueous solutions prepared at higher concentration with a predefined volume of an ibuprofen stock solution (at 40 mg/mL in ethanol) to reach an average content equal to the ibuprofen amount incorporated into the MBGs. Based on this calculation, the sol-gel system was loaded with Ibu at a final concentration of 2.5 mg/mL.

Hereafter, the developed sol-gel systems will be referred to with the acronym reported in table 2.6. For all the conducted tests, hydrogels were prepared in Bijou sample containers (inner diameter 17 mm, Carlo Erba Reagents, Italy) at a final volume of 1 mL, to avoid geometry and volume influence on the performed characterizations.

Table 2.7 Sample composition and therapeutic species presented in the hybrid formulation.

Name	Therapeutic ion	Drugs	Incorporation method
PEU_MBG_Cu2%_SG_Ibu	Copper	Ibuprofen	IW
PEU_MBG_Cu2%_SD_Ibu	Copper	Ibuprofen	IW
PEU_MBG_Sr2%_SD_NAC	Strontium	NAC	IW

2.8 Morphological, structural and compositional characterization

The following section will describe the morphological, structural and compositional characterization, performed to investigate the different morphology, particle size, structural features and composition of the produced materials. All the collected data allowed to select the most suitable material to be biologically validated through *in vitro* and *in vivo* tests.

2.8.1 Morphological analysis: Field Emission Scanning Electron Microscopy (FE-SEM) and Transmission Electron Microscopy (TEM)

The Field Emission Scanning Electron Microscopy (FE-SEM). The Field Emission Scanning Electron Microscopy (FE-SEM) is an efficient and non-destructive technique which provides detailed information concerning the morphology, composition and structure of the analysed materials.

The sample surface is scanned with an high energy electron beam generated by an electron gun, which greatly improves spatial resolution and allows to operate at very low potentials (0.02–5 kV). In the case of not electrically conductive samples, a preparation process is required prior to imaging, in order to reduce the surface charging which could hinder the electron path. The conductive layer, usually a very thin (~5-10 nm) conductive heavy metal layer (such as gold, chromium or platinum), deposited on the sample prior to the microscopic process acts as a channel and eliminates the charges created on the sample surface. FE-SEM characterization was carried out on all the above-mentioned samples, in order to assess the particles morphology, size and shape. In addition, FE-SEM observations were conducted on samples after soaking in SBF, in order to investigate the formation of the hydroxyapatite layer (see section 2.10 for more details).

The micro-sized particles produced by using the spray-drying technique was dispersed as dried powder directly onto a conductive carbon tape adhered on a stub and coated with a 7 nm of Cr layer. On contrary, the nano-sized particles produced following the base-catalysed sol-gel method (~10 mg) were dispersed in 10 mL of isopropanol using an ultrasonic bath (Digitec DT 103H, Bandelin) for 5 min in order to obtain a stable suspension. The resulting suspension was dropped on a copper grid (3.05 mm Diam.200 MESH, TAAB), allowed to dry and successively chromium-coated prior to imaging (Cr layer of *ca* 7 nm). All the prepared samples were analysed using a *ZEISS MERLIN* instrument.

Transmission electron microscopy (TEM). TEM exploits energetic electrons to provide morphological, compositional and crystallographic information concerning the materials. The TEM produces a high-resolution, black and white images obtained through the interaction between the source, represented by energetic

electrons, and the prepared sample.

The electron beam emitted from a filament passes through a condenser lens system and an objective lens system and reaches the sample. Since the wavelength of electrons is smaller compared to the wavelength of the light, the optimal resolution obtained by the TEM technique is many orders of magnitude higher compared to those produced by a light microscope. Thus, TEM can reveal the finest details of an internal material structure.

The *zwitterionic* material reported in section 4.4 (MBG_Sr2%_SG_Z and MBG_Sr2%_SD_Z) and the corresponding bare samples were analysed by TEM technique in order to investigate if the mesoporous structure of the samples was affected by the functionalization procedure. The samples in form of dry powder were ultrasonically dispersed in absolute ethanol and placed on copper grid.

TEM images were recorded in a JEOL 3010 electron microscope (JEOL, Japan) operating at 300 keV coefficient of objective lens (Cs) equal to 0.6 mm, resolution 1.7 Å, employing a CCD camera (1024 x 1024 pixels, size 24 x 24 lm; MultiScan model 794, Gatan, UK) under low dose conditions.

TEM analyses were performed at the *Departamento de Química Inorgánica y Bioinorgánica, Universidad Complutense de Madrid, CIBER de Bioingeniería, Biomateriales y Nanomedicina (CIBER-BBN)* during the period that I spent in Madrid thanks to a collaboration with *Prof. Maria Vallet-Regì*.

2.8.2 Structural analyses: Dynamic Light Scattering (DLS), X-Ray Diffraction (XRD) and Differential Scanning Calorimetry (DSC)

Dynamic light scattering (DLS). Dynamic light scattering is a technique which allows to measure the hydrodynamic size of particles, typically in the sub-micron region. The mechanism is based on the light scattering from a laser which passes through colloidal solution and analyzes modulation of the intensity of scattered light as a function of time [15]. Specifically, DLS measures the particle Brownian motion and then, correlates it with particle hydrodynamic diameter. In particular, the bigger the particle, the slower the Brownian motion is. The Brownian motion of particles in suspension causes laser light to be scattered at different intensities. Analysis of these intensity fluctuations yields the velocity of the Brownian motion and hence the particle size by using the Stokes-Einstein:

$$D_r = \frac{k\,T}{6\pi\,\eta\,R_h}$$

Where:

D is diffusion coefficient

k is Boltzmann's constant

T is temperature

η is solvent viscosity

R_h is the rheodynamic radius of particle solution

The DLS technique has been used to confirm the anti-adhesive properties of the zwitterionic samples (see section 4.4), by evaluating the increasing of the hydrodynamic diameter of functionalized MBG_Sr2%_SG and analogue bare sample after incubation with Bovine Serum Albumin solution. In fact, for bare particles, the hydrodynamic diameter is expected to increase due to the formation of a stable adsorbed protein layer on MBG_Sr2%_SG surface. On contrary, the size of the zwitterionic sample is estimated to remain stable due to the imparted anti-adhesive properties.

To assess the effect of MBG *zwitterionization*, the samples before and after functionalization were dispersed into BSA solution (1 mg/mL) in PBS to obtain a final suspension concentration of 1 mg/mL and kept under stirring (300 rpm) for 24 h at 37°C. The suspensions were then centrifuged, the collected powders were washed with ddH$_2$O and re-suspended in PBS for DLS measurement. The mean value of three different experiments was considered as particle hydrodynamic diameter.

ζ- potential is a technique which allows to measure the surface electric potential of a material when in contact with a liquid. When a particle is dispersed in a medium, the functional groups on its surface will react with the surrounding medium, causing a surface charge, which is able to interact with oppositely charged ions. This process leads to a formation of the so called "Stern layer", a charged thin layer made by ions of opposite charge strongly bound to the particle surface. The Stern layer induces the formation of a second diffuse outer layer, the "diffusive ion layer", composed by loosely associated ions. These two layers are collectively called "the electrical double layer"[15]. The ζ- potential is defined as electrostatic potential at the edge of the diffuse layer where it meets the surrounding liquid (slipping plane).

During a ζ- potential measurement, the applied electrical induces the movement of charged particles. The ratio between the particle speed and the external applied field, known as electrophoretic mobility, is then measured and converted to the ζ-potential, by using the Henry equation:

$$\mu_e = \frac{2\,\varepsilon\,z\,f\,(ka)}{3\eta}$$

Where:

ε and η are respectively the dielectric constant and the absolute zero-shear viscosity of the medium

z is the zeta potential

f is the Henry function

α is the radius of the particle

k is known as the Debye parameter, which represents the thickness of the electrical double layer which depends on the ionic strength of the medium and on the temperature of the sample.

ζ- potential measurements were used to assess the modification of MBG surface due to the anchoring of functional groups for *zwitterionization* (see section 4.4) and to evaluate the layer by layer deposition of chitosan/alginate and ibuprofen (see section 3.2.4).

Concerning the *zwitterionic* samples, ζ- potential measurements were conducted in aqueous media at different pH values in order to determine in which pH range the material surface preserves the imparted *zwitterionic* nature, *i.e.,* the isoelectric point, which is closely related to the zero point charge [16]. Each experiment was performed three times for each sample and data are presented as means ± standard deviations.

As far as the samples prepared by the layer by layer deposition (Cu2%_SG_CAC, Cu2%_SD_CAC, Cu2%_SG_CIC and Cu2%_SD_CIC), after each layer deposition, the suspension was centrifuged at 10,000 rpm for 5 minutes, the powder was collected and dried at 70°C overnight. The ζ- potential measurements were conducted by dispersing the dried powder in ddH$_2$O at room temperature. Each experiment was performed three times for each sample and data are presented as means ± standard deviations.

For DLS and ζ- potential measurements, all the prepared samples were analysed by using a *Zetasizer nano ZS90 Malvern Instruments Ltd.*

X-ray diffraction. X-ray diffraction is a non-destructive technique which allows to characterize the crystalline materials, providing qualitative and quantitative information about the structure of the sample. X-ray diffraction measurement is based on the diffraction phenomenon of X-rays by the crystal lattice of the analysed solid. When conditions satisfy Bragg's Law (nλ=2d sin θ), a monochromatic beam of X-rays reaches the sample with λ as wavelength and an angle θ and produces constructive interference (and a diffracted ray).

The Bragg's Law allows to correlate the wavelength of electromagnetic radiation to the diffraction angle and the lattice spacing in a crystalline sample. These diffracted X-rays are then detected, processed and counted. By varying 2θangles, all possible diffraction directions of the lattice should be reached. The resulting diffractogram, obtained by plotting the intensities of the diffracted X-rays as a function of the angular positions, is characteristic of the material. Usually, this is achieved by comparison of d-spacings with standard reference patterns.

Generally, X-ray diffractogram of the sample is recorded on an X-ray

diffractometer operating at known voltages and current using a Cu Kα X-rays (λ = 0.15406 nm) over the 2θ range from 10 to 100 degrees in the steps of 0.01 degree at room temperature in open quartz sample holders. Two different regions can be distinguished:

- the amorphous regions of the samples characterized by a broad peak centred around the θ which shows a sharp peak in the diffractogram of the crystalline material with the same composition.
- the crystalline regions, with the typical sharp peaks resulting from the diffracted beams arising from the different planes. From the intensity of the peak, the quantitative composition can be evaluated; on contrary, the peak shape gives information about the crystal dimension.

All the prepared samples were analysed through XRD in order to obtain different information related to the material structure. The copper containing and strontium containing samples were analysed by XRD to investigate the possible presence of undesired segregated oxidic phases when the therapeutic metallic ions are incorporated into the MBG framework.

The drug loaded samples were analysed in order to assess the amorphous state of incorporated drug. Moreover, the formation of the hydroxyapatite peaks was investigated after the soaking in SBF (see section 2.10), in order to confirm the bioactive behaviour of the materials.

Differential Scanning Calorimetry (DSC). Differential Scanning Calorimetry is a thermal analysis technique which allows to investigate several material properties, such as glass transition temperature, melting, crystallization, purity, oxidation behavior, and thermal stability. In the DCS treatment, the heat flow into or out of a material is measured as a function of temperature or time, highlighting the changes in their physical and chemical properties. The analyzed material and the reference thermocouples are located under the pans in an electrically heated furnace. The sample thermocouple controls the furnace temperature in order to linearly increase the sample temperature. Thus, the difference in temperature between the sample and reference is plotted against sample temperature.

In this PhD project, DSC was used to investigate the amorphous state of the drugs loaded into the MBG pore and to exclude the presence of large crystalline phases. In fact, the physical properties of amorphous materials result different compare to those of the crystalline ones, due to their lower degree of structural order [17]. As widely reported in the literature [18,19], as far as the solubility is concerned, a drug in the amorphous state exhibit higher solubility and dissolution rate compared to crystalline therapeutics, an important parameter which can be exploited pharmaceutically to develop a drug delivery system.

The MBGs loaded with ibuprofen and N-acetylcysteine were weight in an Alumina pan and analyzed with a *DSC 204 F1 Phoenix (Netzsch)* instrument. The samples were heated from 37 °C to 200 °C at a heating rate of 10 °C min^{-1} under N_2 flux.

2.8.3 Textural properties: N2 adsorption-desorption measurements

N$_2$ adsorption-desorption measurements allow to determine the sample specific surface area and pore volume as well as their pore size, pore shape, pore distribution, widely used for determining the textural properties of a variety of different solid materials, such as catalysts, pigments or ceramics/glasses [20]. Physisorption is a general phenomenon which occurs whenever an adsorbable gas (the adsorptive) is put in contact with the solid surface (the adsorbent). The forces involved are intermolecular forces, in particular the van der Waals forces [21]. For most adsorption experiments the temperature at which the measurements are performed is less than the triple point of the gas used but above its freezing point [22]. Once defined the adsorbent (MBG-based samples) and the adsorptive (nitrogen at 77K), an adsorption isotherm is measured. The adsorption isotherm is the measurement of the amount of gas adsorbed as a function of relative pressure (p/p$_0$) at constant temperature and could be summarised in four steps (reported in figure 2.4)[23]:

- Step 1- Isolated sites on the sample surface begin to adsorb gas molecules at low pressure.

- Step 2- As gas pressure increases, coverage of adsorbed molecules increases to form a monolayer.

- Step 3- Further increasing gas pressure will cause the beginning of multi-layer coverage. Smaller pores in the sample will fill fist.

- Step 4- A further increase in the gas pressure will cause complete coverage of the sample and fil all the pores
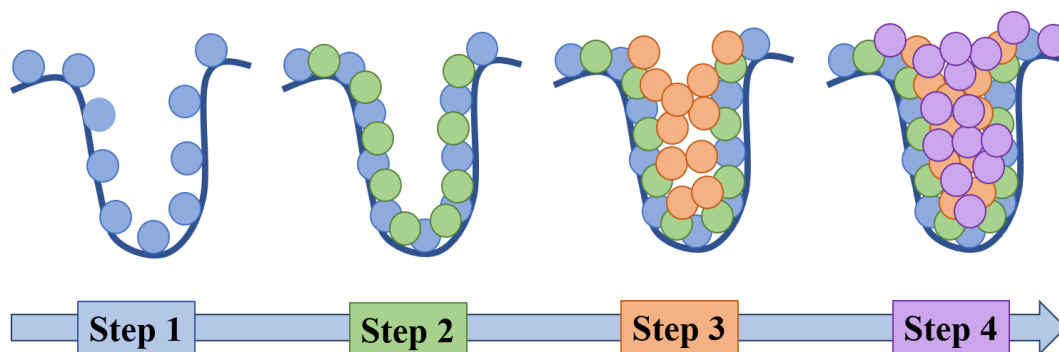
Figure 2.24 Measurement steps of the amount of gas adsorbed as a function of relative pressure (p/p$_0$)

According to IUPAC classification[20,24], six types of isotherms are recognised, as reported in figure 2.5:

- Type I isotherm is typical of microporous (pores < 2 nm) solids with a small external surface. By using nitrogen and argon adsorption at 77 K and 87 K, two different types of isotherms can be obtained: type I(a) isotherms, typical of microporous materials with narrow micropores (of width < ~1 nm) and type I(b) isotherms, given by materials presenting a pore size distribution over a broader range, from micropores to narrow mesopores (< ~2.5 nm).

- Type II isotherm is typical of nonporous or macroporous (pores >50 nm) materials; the shape is due to unrestricted monolayer-multilayer adsorption up to high p/p_0. Point B reported in figure 2.5 is the result of the completion of monolayer coverage.

- Type III isotherms are the result of weak interactions through the adsorbent and the adsorbate, which are typical of nonporous or macroporous materials.

- Type IV isotherms are typical of mesoporous materials, where the adsorption phenomenon depends on the interaction between adsorbent-adsorptive, as well as between the molecules in the condensed state. In this case, the adsorption is due to the adsorbent-adsorptive interactions, but also to the interactions between the molecules in the condensed state. In fact, the initial monolayer-multilayer adsorption phase is followed by the pore condensation. The adsorption at very low p/p_0 corresponds to the monolayer-multilayer adsorption of N_2 on the walls of the mesopores, followed by the condensation of a gas in the pore at a pressure <p_0. As shown in figure 2.5, a typical Type IV isotherm ends with a saturation plateau.

Two different isotherms can be obtained by the mesoporous material, the type IV(a) isotherm, which is typical of materials with pores larger than a critical width (using nitrogen as adsorptive at 77K, it corresponds to 4 nm) and presents a characteristic hysteresis loop in the capillary condensation region; and the type IV(b) isotherm, which is typical of materials with mesopores of smaller width, usually conical and cylindrical mesopores.

- Type V isotherm, very similar to that of Type III, is typical to weak adsorbent–adsorbate interactions, *i.e.*, water adsorption on hydrophobic microporous and mesoporous adsorbents.

• Type VI isotherm is observed when a layer-by-layer adsorption occurs on a highly uniform nonporous surface.
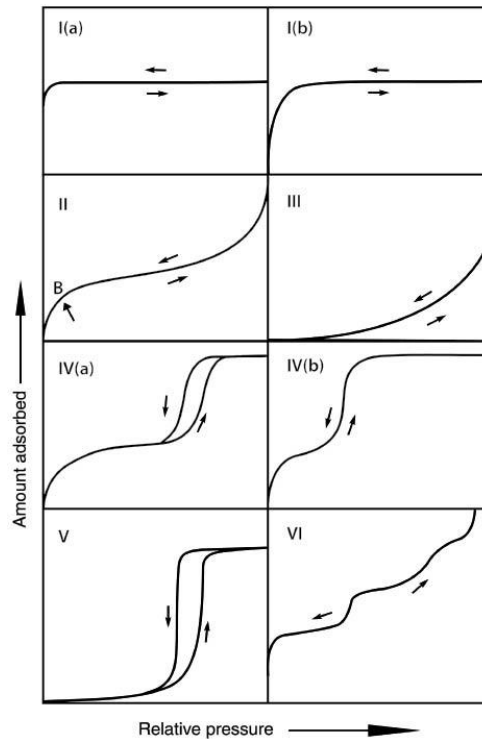
Figure 2.25 The original IUPAC classifications of physisorption isotherms.

A hysteresis loop, located in the multilayer range of physisorption isotherms, can be observed and is typically associated to the capillarity condensation. Usually, five types of hysteresis loops (from H1 to H5) can be generated (figure 2.6), depending on the pore structure and the specific adsorption mechanism. The Type H1 loop is generated by mesoporous material with narrow range of uniform mesopores; the Type H2 is typical of more complex pore features. In particular, type H2(a) could be ascribed to pore-blocking in a narrow range of pore, while type H2(b) loop is associated to pore blocking, in presence of pores with larger neck widths.

Type H3 hysteresis is generated by aggregates of plate-like particles; the H4 is typical of materials with elongated and narrow pore size, while the Type H5 is associated to materials with both open and partially blocked pores [24].
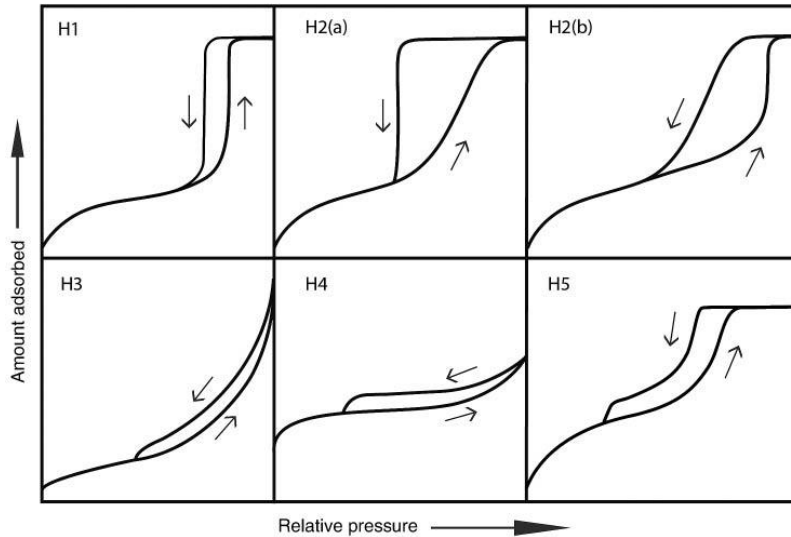
Figure 2.26 Hysteresis loop classification.

Different material features can be obtained through the N_2 adsorption-desorption measurements, in particular the specific surface area (SSA) value, the pore volume and the pore size.

The Brunauer-Emmett-Teller (BET) gas adsorption method is one of the most widely adopted methods to calculate the SSA of porous materials [20,24].

This method is based on the theory that the adsorption enthalpy is constant during the multilayer formation.

The BET equation is reported as follows:

$$\frac{p}{V\,(p_0 - p)} = \frac{1}{V_m C} + \frac{C-1}{V_m C}\frac{p}{p_0}$$

Where

p is the equilibrium pressure (torr)

p_0 is the saturation pressure at 77 K (torr)

V is the adsorbed volume/g of solid

V_m is the monolayer volume of N_2 (mL)

C is the parameter associated to the energy of monolayer adsorption

By plotting $p/(V\,(p_0-p))$ as a function of p/p_0, a linear correlation in a limited range of p/p_0 (0.05 and 0.3) is measured and the values of V_m and C can be

calculated. Finally, the SSA value is determined by using the following equation [14]:

$$SSA = \frac{\sigma \, V_m \, N_a}{v}$$

Where

SSA is the specific surface area (m^2/g)

σ is the molecular cross-sectional area occupied by the adsorbate molecule in the monolayer, which corresponds to 13,5 Å for N_2

N_a is the Avogadro number ($6.02 \cdot 10^{23}$)

v is the molar volume of the adsorbed gas (22,414 mL/mol for N_2)

Along with the SSA, the pore size distribution and the pore volume can be calculated by using the N_2 ads-des method. To this purpose, one of the most applied method is the one of Non-Local-Density Functional Theory (NLDFT), based on the established principles of statistical mechanics. The calculation of the pore size distribution function is obtained by an equation which is able to correlate the isotherm kernel with the experimental isotherm [24].

All the above-mentioned samples were analysed through the N_2 adsorption/desorption measurements in order to evaluate the specific surface area and the mesoporous structure.
Prior to the determination of an adsorption isotherm, the samples were outgassed at 150 °C for 3 h. On contrary, all the drug loaded samples were outgassed at 37 °C for 5 h, in order to avoid the drug degradation. The outgassing procedure allows to remove all of the physiosorbed species from the material surface in order to avoid changes of the surface structure.

The Brunauer-Emmett-Teller (BET) equation was used to calculate the specific surface area (SSA_{BET}) from the adsorption data (relative pressures 0.04–0.2). The pore size distribution was calculated through the DFT method (Density Functional Theory) using the NLDFT kernel of equilibrium isotherms (desorption branch).

The samples were analysed by using an *ASAP2020 (Micromeritics)* instrument, using nitrogen as adsorptive at 77 K.

2.8.4 Compositional analysis: Energy Dispersive Spectroscopy (EDS), Inductively Coupled Plasma Atomic Emission Spectrometry (ICP-AES), Fourier Transform Infrared Spectroscopy (FTIR), Thermogravimetric Analysis (TGA), UV-Vis Spectroscopy and High-Performance Liquid Chromatography (HPLC)

Energy Dispersive Spectroscopy (EDS). The energy dispersive spectroscopy (EDS) technique is mostly used to evaluate the elemental and chemical composition of the analysed materials. The technique is able to detect the x-rays emitted from the sample after the exposure to a high-energy electron beam. In particular, electrons are ejected from the atoms comprising the sample's surface and the resulting electron vacancies are filled by electrons from a higher state. On consequence, an X-ray is emitted to balance the energy difference between the two electrons' states. Since each element has a unique atomic number, a characteristic set of peaks, generated by the electromagnetic emission spectrum of the element, is detected.

The EDS analyses were carried out on all the above-mentioned particles in order to identify the chemical composition and thus, to confirm the proper incorporation of the therapeutic ion in the particle framework.

All the analysed samples were directly dispersed in form of dry powder onto a conductive carbon tape adhered on a stub and, prior the measurement, coated with a 7 nm of Cr layer. An *Aztec EDS* equipment was used for the analysis.

Inductively coupled plasma (ICP). Inductively coupled plasma atomic emission spectroscopy (ICP-AES) is a method of emission spectroscopy that excites atoms and ions with a plasma, causing the emission of electromagnetic radiation at wavelengths characteristic of a particular element. This technique allows to evaluate the amount of a specific chemical element in a water-base medium, also when present in a very low concentration (ppb).

A liquid sample is firstly converted to an aerosol and then atomized by an argon plasma (a neutral conducting gas containing the same amount of cations and electrons) which provides sufficient energy to excite the electrons and promote the electron transfer of atoms into high energy levels. When the electrons decay back to their ground energy state light is emitted. The emitted light at specific wavelengths allows to identify each element. Moreover, the intensity of the light, measured at various wavelengths, is proportional to the concentration of the element in the sample.

The ICP-AES provides the excellent analytical feasibilities such as high sensitivity, good accuracy and precision. In this specific context, it allowed to evaluate the ion concentration released from the MBGs. The ion release test was performed by following the procedure reported in section 2.9 and the collected supernatant solutions were analyzed by ICP. Prior the measurements, the collected

supernatants were diluted in ultrapure water, in order to obtain a suitable concentration detectable by the ICP instrument.

Moreover, to evaluate the effective amount of ion incorporated into MBGs during the synthesis, the powders were dissolved in a mixture of nitric and hydrofluoric acids (0.5 mL of HNO_3 and 2 mL of HF for 10 mg of powder) and the resulting solutions were measured via ICP analysis.

During this PhD work, to conduct the analyses, an *ICP-MS, Thermoscientific, ICAP Q* was used.

Fourier Transform Infrared (FTIR). The Fourier Transform Infrared (FTIR) spectroscopy is a technique which allow to analyze and identify organic, inorganic, and polymeric materials by exploiting infrared light for scanning the samples. A typical FTIR spectrometer includes a source, sample cell, detector, amplifier, A/D convertor, and a computer, as schematically reported in figure 2.7.
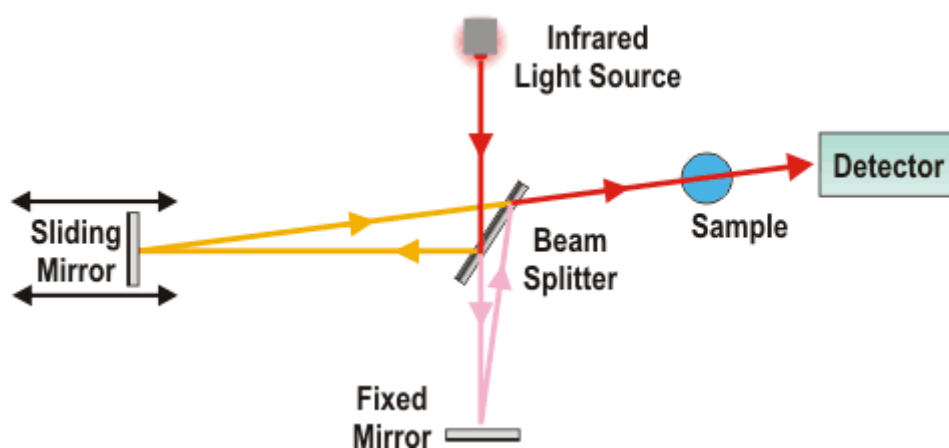
Figure 2.27 Schematic representation of FTIR.

A radiation generated by the sources reaches the detector after the transition through the interferometer. The signal is amplified and converted to a digital signal by the A/D convertor and amplifier and then transferred to the computer, where the Fourier transform is carried out. The sample is passed by an infrared radiation (about 10,000–100 cm^{-1}), part of which is absorbed by the sample and some of it passes through (transmitted). The absorbed radiation is converted by the sample to vibrational or rotational energy. The resultant signal obtained at the detector is a spectrum generally from 4000 to 400 cm^{-1}, which represents the sample's molecular fingerprint. Since every material molecule has a unique fingerprint, with absorption peaks corresponding to the frequencies of vibrations between the bonds of the atoms, FTIR represents an invaluable tool for chemical identification. In this PhD project, FTIR spectroscopy was used to confirm the presence of ibuprofen and NAC in the drug-loaded sample and the successful grafting of NH_3^+ and COO^- groups after *zwitterionization*.

Fourier Transformed Infrared (FT-IR) spectra in transmission mode were collected on a *Bruker Equinox 55 spectrometer* over a range of wavenumbers from 4000 to 400 cm^{-1} (resolution 2 cm^{-1}).

Thermogravimetric analysis (TGA). Thermogravimetric analysis (TGA) in a technique which measures the weight changes in a material as a function of temperature under a controlled atmosphere and allows to identify several features such as a material's thermal stability, filler content in polymers, solvent content, and the percent composition of components in a compound.

The temperature of the sample is gradually increased in a furnace and the weight of the sample is measured on an analytical balance outside of the furnace.

The weight loss is observed if a thermal event involves loss of a volatile component. Finally, the weight of the sample is plotted against temperature.

Thermo-gravimetric analysis was performed on the _zwitterionic_ samples to confirm the presence of NH_3^+ and COO^- groups after _zwitterionization_ and on the drug-loaded sample to evaluate the amount of loaded drug. The drug content was determined from the weight loss between 200 and 600 °C, by applying a correction for the weight loss in the same range of temperature due to the surface silanol condensation as recorded on MBG sample before drug loading.

The analyses were performed by using a _TG 209 F1 Libra instrument from Netzsch_ over a temperature range of 25–600 °C under air flux at a heating rate of 10 °C min^{-1}.

UV-Vis Spectroscopy. UV-Vis Spectroscopy is a quantitative technique used to measure how much light is absorbed by a chemical substance, by measuring the intensity of light that passes through a sample with respect to the intensity of light through a reference sample or blank.

The monochromatic electromagnetic radiations in the ultraviolet (200-350 nm) and visible (350-700 nm) spectral region are absorbed by species composed by specific functional groups, called chromophores.

This absorption in the UV-visible region is due to the excitation of electrons from lower to higher energy levels by using excitation with a specific amount of energy. In the UV-visible spectrometer, the light generated from a source reaches the monochromator which splits the light into its component colours of different wavelengths. Once passed the sample, the light reaches the detector which converts the intensity of the light in an electric signal; after the signal amplification, a diagram reporting the absorbance as a function of the wavelength is obtained. When the light beam passes through the sample, part of the light can be absorbed, and the rest is transmitted through the sample. The ratio between the light which enters the sample and the light that exits the sample at a predefined wavelength is called transmittance. The negative logarithm of transmittance is called absorbance.

By knowing the absorbance, the concentration of a substance can be calculated by using the Lambert-Beer law:

$$A = \varepsilon\, c\, d$$

Where:

ε is the molar extinction, which is peculiar for a substance (mol^{-1} L cm^{-1})

d I the optical path length

c is the concentration of the solution (mol/L)

The UV-Vis spectroscopy was employed to evaluate the release kinetics and the amount of ibuprofen released from the copper-containing MBGs, after the layer by layer deposition.

First, a baseline is recorded by using a blank solution containing the release medium (PBS). Then, the supernatants collected during the release test (see section 2.9) were analysed as such by using a *Thermo Scientific Multiskan GO,* scanning from 200 nm to 500 nm. The absorbance value read at 264 nm were used to quantify the ibuprofen concentration on the base of a predefined calibration curve. On contrary, released ibuprofen carried out on hydrogels incorporating MBG_Cu2%_SG_Ibu, MBG_Cu2%_SD_Ibu (see section 3.2.5) was quantified through a High Performance Liquid Chromatography, by using a *Thermo Scientific, Dionex Ultimate 3000* instrument equipped with a C18 column (5 μm, 120 Å) according to the protocol described by Alsirawan *et al.* [25]. The use of the HPLC equipment to quantify the released ibuprofen from the composite system was selected thanks to the higher sensitivity of the instrument to the low concentration of the drug. In fact, due to the experimental conditions, the amount of released ibuprofen was too low to be detected by the UV-Vis spectrometer.

To this purpose, a mixture of acetonitrile (ACN, CarloErba Reagents, Italy, HPLC grade) and phosphoric acid solution at 0.03 %w/v concentration (pH 2.25) at 60/40 %v/v was used as mobile phase at 1.7 mL/min. Analysis were conducted with an injection volume of 20 μL, at RT and 214 nm for 5 min. In order to prepare the samples, the collected extracts were mixed with ACN at 40/60 volume ratio and filtered through a 0.45 μm syringe filter (Macherey-Nagel, poly(tetrafluoro ethylene) membrane). The ibuprofen concentration was finally quantified with respect to a calibration curve based on ibuprofen standards with concentration ranging between 0 and 1 mg/mL.

HPLC analyses were performed at the *Department of Mechanical and Aerospace Engineering, Politecnico di Torino* by the *Prof. Gianluca Ciardelli*'s research group.

On the other hands, the released NAC carried out on hydrogels incorporating MBG_Sr2%_SG_NAC, MBG_Sr2%_SD_NAC (see section 4.3) was quantified through a High-Performance Liquid Chromatography, by using a HPLC, LC2010 AHT equipped with Diode array SPD-M10AVP, Shimadzu corp., Kyoto, Japan, with a KyaTech C18 HiQSil column.

For the detection of N-acetylcysteine a mixture of Buffer phosphate at pH 4.5 and Methanol (HPLC grade from Sigma Aldrich) at 90/10%v/v was used as mobile phase at 0.8 mL/min. Analysis were conducted with an injection volume of 20 μL,

at RT and 198 nm for 10 min. The NAC concentration was finally quantified with respect to a calibration curve based on NAC standards with concentration ranging between 0 and 1 mg/mL.

HPLC analyses were performed at the *NobilBio Ricerche Srl* by Dr. Marco Morra and Dr. Giorgio Iviglia.

2.9 Ion/drug release test procedures

Part of the work described in this chapter has been already published during the PhD period [2,3,5].

Ion/drug release tests were performed in Tris HCl buffer (Tris(hydroxymethyl)aminomethane (Trizma, Sigma Aldrich) 0.1 M, pH 7.4) at 37°C by modifying the procedure reported by Shi *et al.*[26], adapting the concentration and the time steps, depending on the released species. Each procedure will be described in detail in the following section.

2.9.1 Therapeutic ion release tests

The ability of the copper and strontium-containing MBGs to release the incorporated therapeutic ions was investigated by following the procedure described by Shi *et al.*[26] .

The concentration of the released therapeutic ions was evaluated by soaking the powders in Tris HCl buffer at concentration of 250 μgmL^{-1}. In particular, 5 mg of powder were suspended in 20 mL of buffer up to 14 days at 37°C in an orbital shaker (*Excella E24, Eppendorf*) with an agitation rate of 150 rpm. At predefined time points (3 h, 24 h, 3 days, 7 days and 14 days) the suspension was centrifuged at 10,000 rpm for 5 min by using a *Hermle Labortechnik Z326*, half of the supernatant was collected and replaced by the same volume of fresh buffer solution to keep constant the volume of the release medium. The release experiments were carried out in triplicate. The concentration of the ions was measured by Inductively Coupled Plasma Atomic Emission Spectrometry Technique (ICP-AES), after appropriate dilutions. In order to express the results in terms of released percentage and to evaluate the total amount of ions incorporated into MBGs during the synthesis, the powders were dissolved in a mixture of nitric and hydrofluoric acids (0.5 mL of HNO_3 and 2 mL of HF for 10 mg of powder) and the resulting solutions were measured via ICP analysis. Each experiment was performed three times for each sample and data are presented as means ± standard deviations.

2.9.2 Drug release tests

Part of the work described in this chapter has been already published during the PhD period[1].

The ability of the ibuprofen and NAC loaded MBG samples to release the incorporated drugs was investigated by soaking the particles in Tris-HCl.

More in details, the concentration of drugs released from the ions containing MBGs was evaluated by soaking the powders in Tris HCl buffer (Trizma, Sigma Aldrich) 0.1 M, pH 7.4) at concentration of 20 mg/mL. In particular, 40 mg of powder were suspended in 2 mL of buffer up to 24 hours at 37°C in an orbital shaker (*Excella E24, Eppendorf*) with an agitation rate of 150 rpm. At predefined time points (reported in table 2.7) the suspension was centrifuged at 10,000 rpm for 5 min by using a *Hermle Labortechnik Z326*, the supernatant was collected and replaced by the same volume of fresh buffer solution to keep constant the volume of the release medium. The release experiments were carried out in triplicate. The concentration of the drugs was measured by HPLC, after appropriate dilutions, by following the protocol described in section 2.8.4.

In the following table (table 2.7), the tested samples and the experimental conditions are reported.

Table 2.8 Tested samples and the experimental conditions employed to perform the drug release test.

Samples	Detected drug	Particle concentration	Medium	Time point
MBG_Cu2%_SG + Ibu Ads	Ibuprofen			1h, 3h, 20h, 24h, 48h
MBG_Cu2%_SD + Ibu Ads	Ibuprofen			
MBG_Cu2%_SG + Ibu IW	Ibuprofen	20 mg/mL	Tris HCl buffer 0.1 M, pH 7.4	20 min, 40 min, 1h, 3h, 5h, 8h, 24 h
MBG_Cu2%_SD + Ibu IW	Ibuprofen			
MBG_Sr2%_SG + NAC IW	NAC			
MBG_Sr2%_SD + NAC IW	NAC			

2.9.3 Release test from MBGs after layer by layer deposition

Release studies of both ibuprofen and therapeutic copper ions were performed on Cu2%_SG_CAC_Ibu, Cu2%_SD_CAC_Ibu, Cu2%_SG_CIC and Cu2%_SD_CIC. Tests were conducted at 37 °C up to 14 days and using Trizma® as release medium, by using a particle concentration of 20 mg/mL. In particular, 40 mg of powder were suspended in 2 mL of buffer up to 24 hours at 37°C in an orbital shaker (*Excella E24, Eppendorf*) with an agitation rate of 150 rpm. At predefined time points (1h, 3h, 5h, 8h, 24 h) the suspension was centrifuged at 10,000 rpm for 5 min by using a *Hermle Labortechnik Z326*, the supernatant was collected and replaced by the same volume of fresh buffer solution to keep constant the volume of the release medium. The release experiments were carried out in triplicate. The concentration of the ibuprofen was measured by UV-Vis spectrometer by following the protocol described in section 2.8.4. The collected extracts were also analysed

by ICP to measure the concentration of released therapeutic copper. In order to express the results in terms of released percentage and to evaluate the total amount of ions incorporated into MBGs during the synthesis, the powders were dissolved in a mixture of nitric and hydrofluoric acids (0.5 mL of HNO_3 and 2 mL of HF for 10 mg of powder) and the resulting solutions were measured via ICP analysis. Each experiment was performed three times for each sample and data are presented as means ± standard deviations.

To compare the copper release test with the respective bare samples (MBG_Cu2%_SG and MBG_Cu2%_SD) and confirm the release modulation due to the multilayer deposition, the copper release test was prolonged up to 14 days, by adding further time points (2 d, 3 d, 8 d, 10 d, 14 d).

2.9.4 Ion/drug release test from the hybrid formulation

Part of the work described in this chapter has been already published during the PhD period[1].

Release studies of both drugs and therapeutic ions were carried out on hydrogels incorporating MBG_Cu2%_SG_Ibu, MBG_Cu2%_SD_Ibu and simply dispersed Ibu. Moreover, ion/drug release test was performed on hydrogels incorporating MBG_Sr2%_SD_NAC. Tests were conducted at 37 °C up to 14 days and using Trizma® as release medium. Complete gelation of the samples was ensured through incubation at 37 °C for 15 min; then, 1 mL of release medium was added to each sample and the release test started. Release media were collected and completely refreshed at 1h, 3h, 5h, 1d, 2d, 3d, 4d, 8d, 10d and 14d incubation time. The released of the drugs was quantified by using a HPLC instrument as reported in section 2.8.4. The drug content was finally quantified with respect to a calibration curve based on a standard with concentration ranging between 0 and 1 mg/mL. The collected extracts were also characterized by ICP to measure the concentration of released therapeutic ions.

2.10 Bioactivity test

Part of the work described in this chapter has been already published during the PhD period [2,3,5,27].

Since the bioactivity of the MBGs is considered an essential feature for promoting bone regeneration and thus one of the fundamental properties of the developed materials, bioactivity test was carried out on the previous described MBG samples by following the protocol reported by Maçon *et al.*[28], in which the authors described a unified method to evaluate the apatite-forming ability of the bioactive glasses.

In details, the in *vitro* bioactivity test was performed in, with the aim to evaluate the functionalized Sr-substituted MBGs. To this aim, 30 mg of material were soaked in 30 mL of simulated body fluid (SBF), prepared by using the reagents

reported in table 2.8 and following the protocol described in literature [28] at 37°C up to 14 days in an orbital shaker (*Excella E24, Eppendorf*) with an agitation rate of 150 rpm. At each time point (3 h, 1 day, 3 days, 7 days and 14 days), the suspension was centrifuged at 10,000 rpm for 5 min, the collected powder was washed twice with distilled water and dried in oven at 70°C for 12 h prior FE-SEM and XRD analysis to evaluate the apatite layer formation. Moreover, the pH of each recovered supernatant was measured, to assess if the values are suitable for allowing osteoblasts to maintain their physiological activity[29].

Table 2.9 Reagents used for preparing SBF solution.

Order	Reagent	Amount (g L^{-1})	CAS number
1	NaCl	8.035	7647-14-5
2	NaHCO$_3$	0.355	144-55-8
3	KCl	0.225	7447-40-7
4	K$_2$HPO$_3$ · 3H2O	0.231	16788-57-1
5	MgCl$_2$ · 6H$_2$O	0.311	7791-18-6
6	HCl 1M	38 mL	7647-01-0
7	CaCl$_2$ 2H$_2$O	0.386	10035-04-8
8	Na$_2$SO$_4$	0.072	7757-82-6
9	Tris	6.118	77-86-1

2.11 Biological assessment

Several biological assessments were performed on the developed materials with the aim to explore their biocompatibility and their effect in *vitro* and in *vivo* in view of the potential clinical applications.
In particular, the strontium containing MBGs were tested by *Nobil Bio Ricerche*, in the frame of the MOZART project, in order to evaluate the the biological response of the materials in terms of cytocompatibility and pro-osteogenic effect.

Thanks to a collaboration with *Universidad Complutense de Madrid* in the frame of Zodiac Project, the in *vitro* biocompatibility of the *zwitterionic* materials and their effect on the osteoblastic cell growth and differentiation were evaluated during the period that I spent in Madrid, as well as the anti-adhesive ability imparted by the surface *zwitterionization* (investigated as a reduction in the protein adsorption).

Moreover, the in *vivo* experiments to confirm the safety and the efficacy of the bone healing device developed within the MOZART project were performed at *Charitè – Universitätsmedizin Berlin* during the three months that I spent in Berlin.

2.11.1 *In vitro* biological assessment of Sr-containing MBGs

Part of the work described in this chapter has been already published during the PhD period [3].

The biological response to MBG_Sr2%_SD and MBG_Sr2%_SG and to their ionic release products was assessed by following two different experimental approaches. In particular, through a direct contact method, where cells were seeded directly on the MBG particles, and through a not-contact method, according to which the Sr-MBG suspensions were placed in a Transwell® membrane insert (<3 µm pore, *SARSTEDT AG & Co.*) to allow the passage of the particle dissolution products.

The work was carried out by *Dr. Marco Morra's group* at *Nobil Bio Ricerche Srl,* one of the industrial partners of the MOZART project involved in the biological assessment of the developed materials.

Inflammatory response of Sr-containing MBGs

The inflammatory response test was conducted in direct contact mode, using cells and Sr-MBG particles at concentration of 1 mg/mL. For these tests the murine macrophage cell line J774a.1 (*European Collection of Cell Cultures)* was used. Before the tests, cells were maintained in Dulbecco's modified Eagle's medium (Gibco Invitrogen, Cergy-Pontoise) supplemented with 10% fetal bovine serum, penicillin (100 U mL^{-1}), streptomycin (100 µg mL^{-1}) and 4 mM l-glutamine. Cells were grown in a 100% humidified incubator at 37 °C with 10% CO_2 and passaged 2–3 days before use. Then the J774a.1 cells (2×10^4 mL^{-1}) were seeded onto 24-well tissue culture polystyrene plates (*Falcon™*), containing the Sr-MBG particles. After 4 h, the RNA from J774.a1 cells was isolated by using the *Maxwell® RSC simply RNA Cells Kit (Promega)* and reverse transcribed by the *High-Capacity cDNA Reverse Transcription Kit (Applied Biosystems).* Real-time PCR was performed through the *Applied Biosystems StepOne Plus* instrument with 2.2 Step-one software version. Mouse interleukin-1β (IL-1β), interleukin-6 (IL-6), tumour necrosis factor alpha (TNFα) and Tyrosine 3-Monooxygenase/Tryptophan 5-Monooxygenase Activation Protein Zeta (YWHAZ) were chosen from the collection of the TaqMan Gene Expression Assays as primer sets (*Applied Biosystems Assay's ID: Mm01336189_m1, Mm99999062_m1, Mm00443258_m1, Mm03950126_s1* respectively). Real time PCR was performed in duplicate for all samples in a volume of 20 µL and, after an initial denaturation at 95 °C for 10 min, the PCR amplification was run for 40 cycles at 95 °C for 15 s and at 60 °C for 1 min. The content of cDNA samples was normalized through the comparative threshold cycle (ΔΔCt) method, consisting in the normalization of the number of target gene copies versus the endogenous reference gene YWHAZ.

Biocompatibility test of Sr-containing MBGs

Fibroblast cell line L929 was used to assess the biocompatibility of Sr-MBGs. Experimental cell culture medium (*BIOCHROM KG, Berlin, Germany*) , composed by Minimum Eagle's Medium without L-glutamine, 10 % fetal bovine serum, streptomycin (100 g/L), penicillin (100 U/mL), and 2 mmol/L L-glutamine, was placed in 250 mL plastic culture flask (*Corning TM*). Cells were cultured at 37 °C

in a humidified incubator equilibrated with 5 % CO_2. Cells were harvested prior to confluence by means of a sterile trypsin-EDTA solution (0.5 g/L trypsin, 0.2 g/L EDTA in normal phosphate buffered saline, pH 7.4), re-suspended in the experimental cell culture medium and diluted to 1 x 10^5 cells/mL.

A preliminary qualitative assessment was carried out through optical imaging of the cells in direct contact with Sr-MBGs particles. In parallel, cell viability tests were performed in *Transwell®* permeable inserts. Briefly, fibroblast cells were seeded on polystyrene plate below the *Transwell®* insert containing 1 mg/mL of Sr-MBG suspension, and after 72 h of incubation cell viability was evaluated through MTT assay. This assay allows assessing the possible toxic effect of particle dissolution products on cells, by evaluating the reduction of the mitochondrial succinate dehydrogenase (SDH) enzyme activity, normally involved in the citric acid cycle. For the execution of the MTT test, cells were incubated with a 1 mg/mL solution of soluble tetrazolium salt (3-(4.5-dimethylthiazol – 2yl)-2.5 diphenyl tetrazolium bromide). During the subsequent two hours of incubation at 37°C, the succinate dehydrogenase enzyme causes the transformation of tetrazolium salts into a yellow soluble substance first and then into a blue water-insoluble product, the formazan precipitate. From the quantification of the precipitate product is possible to evaluate the degree of the enzyme activity and, consequently, the number of metabolically active cells. To perform this evaluation, the formazan precipitate was dissolved with dimethylsulphoxide and was spectrophotometrically measured at a wavelength of 570 nm, providing an optical density (OD) value. Cells grown on polystyrene plate were used as negative control, while cells grown with the addition of 20 µL of a solution of 0.08 mg/mL of Sodium nitroprusside (NPS) were used as the positive one.

Osteogenic response to Sr-containing MBGs

Osteoblast-like SAOS-2 cells were cultured at 37 °C in a humidified incubator equilibrated with 5% CO_2. Cell suspension was obtained by adding 2 mL of a sterile 0.5% Trypsin-EDTA solution (*GIBCO by Life Technology, ref 15400-054*) to a 250 mL cell culture flask (*Corning™*), re-suspended in the experimental cell culture medium and diluted to 1.45×10^5 cells/mL.
For these experiments, 5 mL of the cell suspension were seeded onto 24-well tissue culture polystyrene plates (*Falcon™*), provided with the *Transwell®* insert containing 1 mg/mL of Sr-MBG suspension. After 72 h and 7 days of incubation, the expression of GAPDH, COL1a1, RANKL, SPARC, OPG and ALPL genes as cell differentiation markers was assessed using the real time reverse transcription polymerase chain reaction (qRT-PCR) (*Applied Biosystems Assay's ID: Hs00266705_g1, Hs00164004_m1, Hs00234160_m1, Hs00243519_m1, Hs00900358_m1, Hs01029144_m1*, respectively).
The RNA from SAOS-2 cells was isolated by using the *Maxwell® RSC simply RNA Cells Kit (Promega),* by following the manufacturer's instructions. RNA was reverse transcribed by the *High-Capacity cDNA Reverse Transcription Kit* (*Applied*

Biosystems) and RNA quantitation was performed before starting the Rt-PCR using *Quantifluor system kit (Promega)*.

Real-time PCR was performed in the Applied Biosystems StepOne Plus instrument (*Applied Biosystems*). The content of cDNA samples was normalized by making use of the comparative threshold cycle ($\Delta\Delta$Ct) method.

Statistical Analysis

Experimental data are reported as mean ± standard deviation. Statistical differences between groups were analysed using two-way ANOVA using Tukey's post-hoc test and one-way ANOVA using Tukey's pairwise post-hoc test. Statistical significance was represented as * $p < 0.05$, ** $p < 0.01$, *** $p < 0.001$ and **** $p < 0.0001$.

2.11.2   Biological assessment of *zwitterionic* MBGs

The tests described in this section were performed during the period that I spent in Madrid in collaboration with the group led by *Prof. Maria Vallet-Regì*'at *Departamento de Química Inorgánica y Bioinorgánica, Universidad Complutense de Madrid, CIBER de Bioingeniería, Biomateriales y Nanomedicina (CIBER-BBN)*, a partner involved in the Zodiac project. In particular, the in *vitro* biocompatibility assays in the presence of a mouse pre-osteoblastic cell line MC3T3-E1 were performed to evaluate the effect of *zwitterionic* Sr-MBGs on the osteoblastic cell growth and differentiation. Moreover, to assess the anti-adhesive ability imparted by the surface *zwitterionization*, a reduced protein adsorption of serum proteins was evaluated by gel electrophoresis (SDS-PAGE) experiments using bovine serum albumin (BSA) and fibrinogen (Fib), respectively

Part of the work described in this chapter has been already published during the PhD period [5].

In *vitro* biocompatibility tests

Cell culture experiments were performed using the mouse MC3T3-E1 osteoblast cell line, plated at an initial density of 10,000 cells cm^{-2} in a multi-well plates and incubated in 2 mL of Dulbecco's modified Eagle's medium (DMEM) (Sigma Chemical Co.) supplemented with 10% heat-inactivated fetal bovine serum (FBS) (Lonza BioWhittaker), 1 mM L-glutamine (Lonza BioWhittaker), 200 μg mL^{-1} penicillin (Lonza BioWhittaker) and 200 μg mL^{-1} streptomycin (Lonza BioWhittaker) at 37°C in 5% CO$_2$.

Sr-substituted MBGs (before and after functionalisation) were suspended at different concentrations (25, 50 and 75 ug/mL) in completed DMEM, sonicated in order to obtain a stable suspension and placed into each 24-well plates after cell seeding. Wells without MBG particles were used as control.

Three different measurements of two independent experiment were performed in order to determine the statistical analyses.

Mitochondrial activity – MTT

Cell proliferation induced by both unmodified and zwitterionic Sr-substituted MBGs was determined by MTT test. MC3T3-E1 cells were seeded for 24 h as previously described and then incubated at 37 °C in 5% CO_2 with different particle concentrations (25, 50 and 75 ug/mL) for different time periods (1 day, 2 days and 5 days). At each time point, 300 µL of CellTiter 96® AQueous One Solution Reagent (containing 3-(4,5-dimethythizol-2-yl)-5-(3-carboxymethoxyphenyl)-2-(4-sulfophenyl)-2H-tetrazolium salt (MTS) and an electron coupling reagent (phenazine ethosulfate) that combines with MTS to form a stable solution) was added to each well and incubated for 2 h. then, 100 µL of each cell conditioned medium was placed in a 96-well plate and the absorbance at 490 nm was measured in an Opsys MR Reader (*Dynex Technologies*).

Citotoxicity test –Lactate dehydrogenase (LDH) measurement

Biocompatibility and cytotoxic effects of unmodified and zwitterionic Sr-substituted MBGs were tested measuring the amount of released cytosolic lactate dehydrogenase (LDH) enzyme caused by the cellular membrane damage (Spinreact S.A.). The assay is based on the reduction of NAD by LDH. The resulting reduced NAD (NADH) is exploited in the stoichiometric conversion of a tetrazolium dye. The supernatants of particles-cells incubation experiments were collected after 1 day of incubation and mixed with the LDH kit reagents (*SPINREACT®*, imidazole 65 mmol/L, pyruvate 0.6 mmol/L and NADH 0.18 mmol/L). The absorbance of the resulting coloured compound was measured at 340 nm wavelength at 0, 1, 2, and 3 min, calculating the amount of enzyme that transforms 1 mmol of substrate per minute in standard conditions (U/L) as $\Delta A/min \times 4925$ (where ΔA is the average difference per minute and 4925 corresponds to the correction factor for 25–30 °C).

Mineralization assay

Matrix mineralization was measured in MC3T3-E1 cell cultures by alizarin red staining, as described in the protocol reported by Lozano *et al.* [30]. After incubation with the tested materials for 15 days, cells were washed three times with PBS and then fixed with 75% ethanol for 1 h. Cell cultures were stained with 40 mM alizarin red in distilled water (pH 4.2) for 10 min at room temperature. Subsequently, cell monolayers were washed five times with distilled water and the stain was dissolved with 10% cetylpyridinum chloride in 10 mM sodium phosphate, pH 7, measuring absorbance at 620 nm.

Anti-adhesive abilities assessment: serum protein adhesion assay

In *vitro* adhesion of proteins was determined using bovine serum albumin (96% BSA, A2153 Sigma-Aldrich) and fibrinogen (75% Fib, F8630 Sigma-Aldrich). A 50% v/v solution of such proteins (2 mg/mL for BSA and Fib in PBS 1x, respectively) was gently mixed with both unmodified and zwitterionic Sr-MBGs (2 mg/mL in PBS 1x) and kept under orbital agitation (200 rpm) during 24h at 37 ºC. Particle suspensions were then centrifuged (10,000 rpm) and washed with fresh PBS to eliminate free or loosely bound proteins and a one-dimensional sodium dodecyl sulfate-polyacrylamide gel electrophoresis gel (SDS-PAGE) assay was performed. Briefly, the recovered supernatants were mixed with a buffer (Tris 6 mM, SDS 2%, glycerol 10%, 2-β-mercaptoethanol 0.5 M, traces of bromophenol blue, pH = 6.8) and loaded in 10% SDS-PAGE gels. A calibration curve was estimated by loading 0.5, 1.0, 1.5, 2.0 and 2.5 µg/mL protein concentrations. The gels were run with a constant 100 V voltage (45-60 min) and stained in R-250 colloidal Coomassie blue solution for visualization. *Imagen J software* was used in order to determine the amount of adsorbed proteins through calibrated line of the different proteins. Three different measurements of two independent experiment were performed in order to determine the statistical analyses.

The anti-adhesive ability of the bare and zwitterionic Sr-MBGs nanoparticles prepared by SG approach was also evaluated using dynamic light scattering (DLS) method. The size distribution was measured on a *Zetasizer nano ZS90 (Malvern Instruments Ltd.*) before and after powder incubation in the BSA solution for 24 h. In particular, samples at a concentration of 1 mg/mL were soaked in a 1 mg/mL BSA solution in PBS and kept under stirring (300 rpm) for 24h at 37 ºC. The suspensions were then centrifuged, the collected powders were washed with ddH$_2$O and re-suspended in PBS for the measurement. The mean value of three different experiments was used as hydrodynamic diameter (Dh).

2.11.3   Biological assessment of the hybrid formulation

The tests described in this section were carried out during the three months that I spent in Berlin at *Charitè – Universitätsmedizin Berlin* in collaboration with the group of *Dr. rer. Nat. Katharina Schmidt-Bleek* at the *Research Group "Bone healing" of the Julius Wolff Institute,* the MOZART partners involved in the *in vivo* experiments to confirm the safety and the efficacy of the device developed within the MOZART project. In particular, the bone regenerative potential of the hybrid formulation based on strontium-containing MBGs loaded with NAC and incorporated into the thermosensitive hydrogel were investigated *in vivo* in order to assess the safety and efficacy of the bone healing device.

In *vivo* bone healing study: housing conditions, osteotomy surgery and study design

The bone regeneration potential of the different hybrid formulation was studied in a rat osteotomy model of delayed healing [31]. A total of 18 adult female Sprague-Dawley rats (aged >7 months, ≥300 g, Janvier Labs, France), that had three

litters were included in this study. Rats were kept in small gangs under obligatory hygiene standards under non-specific pathogen free (SPF) conditions with controlled temperature set to 20 ± 2 °C, a light/dark period of 12 h and food and water being available ad libitum. All animal experiments were approved by the local animal protection authorities (Landesamt für Gesundheit und Soziales Berlin, Germany: G0258/18) and performed in accordance with the German Animal Welfare Act, the National Institutes of Health Guide for Care and Use of Laboratory Animals and the ARRIVE guidelines.

Before starting the surgery, the rats were anesthetized by inhalation of isofluorane and received a potent analgesic (Bubrenorphine, 0.1 mg/kg), an antibiotic bolus (Clindamycin, 45 mg/kg) and eye ointment. The osteotomy was carried out under deep anesthesia on a heating plate set to 37°C. The operation area of the left femur was clipped and disinfected, the femur was exposed by a longitudinal skin incision and blunt preparation of the muscles. An external fixator (RISytem AG, Switzerland) was mounted on the femur, followed by creation of a 2 mm osteotomy using an oscillating saw and a saw guide. The wound was closed with sutures and the rats were returned to their cages. As post-operative analgesia, Tramadolhydrochloride (Tramal, 0.5-1 mg/mL) was added to the drinking water for three days post-surgery.
At 4 weeks post-surgery, the animals were euthanized under deep anesthesia by intracardiac injection of potassium chloride, and the ostetomized femur was harvested. The bones were fixed in 4% PFA/PBS for 24 h at 4 °C. The bones were again imaged using a higher resolution μCT, and afterwards dehydrated and paraffin-embedded for histological analysis.

Histological analysis

The paraffin-embedded bones were sectioned into five μm-thick sections, de-paraffinized by 2x 10 min of incubation in Xylol and re-hydrated by descending alcohol series and distilled water as the final step before staining, stained for Safranin O and Movat's Pentachrome following the procedure reported in literature [32].

In details, for Safranin O staining, sections were thawed for 1 h at RT and fixed for 10 min in 4% PFA/PBS. Sections were washed twice in PBS/Tween-20 for 5 min. Subsequently, sections were stained with Weigert's iron hematoxylin working solution for 10 min and washed in running tap water for 10 min. After washing, sections were incubated for 5 min in fast green (FCF) solution, fast rinsed with 1% acetic acid solution for no more than 10 –15 sec and successively incubated with 0.1% safranin O solution for 5 min. At the end, tissue slides were dehydrated and cleared with 95% ethyl alcohol, absolute ethyl alcohol, and xylol, using 2 changes each for 2 min each and embedded.

For Movat's Pentachrome staining, sections were incubated for 3 min in 3% acetic acid, for 30 min in 1% Alcian Blue/3% acetic acid and differentiated for 5

min in 3% acetic acid. After washing in ddH$_2$O, sections were incubated for 1 h in ethyl alcohol, washed twice in tap water, shortly in ddH$_2$O and stained in iron hematoxylin (after Weigert) for 10 min. After washing with tap water, sections were incubated for 15 min in brilliant crocein-acid fuchsine. Tissue slides was shortly placed in 0.5% acidic acid, followed by a 20 min incubation in 5% phosphotungstic acid. After 1 min in 0.5% acetic acid, slides were incubated 3x à 5 min in 96% EtOH and stained with Saffron-du-Gatinais for 1 h., they were washed again 3x in 96% EtOH for 2 min each, 2x in Xylol for 10 min each and embedded.

Microscopic images of all slides were taken at 10x magnification under bright field (Axioskop 40, Zeiss, Germany).

References

[1]   M. Boffito, C. Pontremoli, S. Fiorilli, R. Laurano, G. Ciardelli, C. Vitale-Brovarone, Injectable Thermosensitive Formulation Based on Polyurethane Hydrogel/Mesoporous Glasses for Sustained Co-Delivery of Functional Ions and Drugs, Pharmaceutics. 11 (2019) 501. doi:10.3390/pharmaceutics11100501.

[2]   C. Pontremoli, M. Boffito, S. Fiorilli, R. Laurano, A. Torchio, A. Bari, C. Tonda-Turo, G. Ciardelli, C. Vitale-Brovarone, Hybrid injectable platforms for the in situ delivery of therapeutic ions from mesoporous glasses, Chem. Eng. J. 340 (2018) 103–113. doi:10.1016/j.cej.2018.01.073.

[3]   S. Fiorilli, G. Molino, C. Pontremoli, G. Iviglia, E. Torre, C. Cassinelli, M. Morra, C. Vitale-Brovarone, The incorporation of strontium to improve bone-regeneration ability of mesoporous bioactive glasses, Materials (Basel). 11 (2018) 678. doi:10.3390/ma11050678.

[4]   Chengtie Wu, Jiang Chang, Wei Fan, Bioactive mesoporous calcium-silicate nanoparticles with excellent mineralization ability, osteostimulation, drug-delivery and antibacterial properties for filling apex roots of teeth, J. Mater. Chem. 22 (2012) 16801–9. doi:10.1039/c2jm33387b.

[5]   C. Pontremoli, I. Izquierdo-barba, G. Montalbano, M. Vallet-regí, C. Vitale-brovarone, S. Fiorilli, Journal of Colloid and Interface Science Strontium-releasing mesoporous bioactive glasses with anti-adhesive zwitterionic surface as advanced biomaterials for bone tissue regeneration, J. Colloid Interface Sci. 563 (2020) 92–103. doi:10.1016/j.jcis.2019.12.047.

[6]   L. Pontiroli, M. Dadkhah, G. Novajra, I. Tcacencu, S. Fiorilli, C. Vitale-Brovarone, An aerosol-spray-assisted approach to produce mesoporous bioactive glass microspheres under mild acidic aqueous conditions, Mater. Lett. 190 (2017) 111–114. doi:10.1016/j.matlet.2016.12.125.

[7]   R. Mortera, S. Fiorilli, E. Garrone, E. Verné, B. Onida, Pores occlusion in MCM-41 spheres immersed in SBF and the effect on ibuprofen delivery kinetics: A quantitative model, Chem. Eng. J. 156 (2010) 184–192. doi:10.1016/j.cej.2009.10.018.

[8]   C. Charnay, S. Bégu, C. Tourné-Péteilh, L. Nicole, D.A. Lerner, J.M. Devoisselle, Inclusion of ibuprofen in mesoporous templated silica: Drug loading and release property, Eur. J. Pharm. Biopharm. 57 (2004) 533–540. doi:10.1016/j.ejpb.2003.12.007.

[9]   W.H. Kuo, M.J. Wang, H.W. Chien, T.C. Wei, C. Lee, W.B. Tsai, Surface modification with poly(sulfobetaine methacrylate-co-acrylic acid) to reduce fibrinogen adsorption, platelet adhesion, and plasma coagulation, Biomacromolecules. (2011). doi:10.1021/bm2013185.

[10]   A.J. Keefe, N.D. Brault, S. Jiang, Suppressing surface reconstruction of superhydrophobic PDMS using a superhydrophilic zwitterionic polymer, Biomacromolecules. (2012). doi:10.1021/bm300399s.

[11]   S. Chen, L. Li, C. Zhao, J. Zheng, Surface hydration : Principles and applications toward low-fouling / nonfouling biomaterials, Polymer

(Guildf). 51 (2010) 5283–5293. doi:10.1016/j.polymer.2010.08.022.

[12]   L.T. Zhuravlev, Surface characterization of amorphous silica-a review of work from the former USSR, Colloids Surfaces A Physicochem. Eng. Asp. 74 (1993) 71–90. doi:10.1016/0927-7757(93)80399-Y.

[13]   J. Zhou, G. Romero, E. Rojas, L. Ma, S. Moya, C. Gao, Layer by layer chitosan/alginate coatings on poly(lactide-co-glycolide) nanoparticles for antifouling protection and Folic acid binding to achieve selective cell targeting, J. Colloid Interface Sci. 345 (2010) 241–247. doi:10.1016/j.jcis.2010.02.004.

[14]   M. Boffito, E. Gioffredi, V. Chiono, S. Calzone, E. Ranzato, S. Martinotti, G. Ciardelli, Novel polyurethane-based thermosensitive hydrogels as drug release and tissue engineering platforms: design and in vitro characterization, Polym. Int. 65 (2016) 756–769. doi:10.1002/pi.5080.

[15]   N. Raval, R. Maheshwari, D. Kalyane, S.R. Youngren-ortiz, M.B. Chougule, R.K. Tekade, Importance of Physicochemical Characterization of Nanoparticles in Pharmaceutical Product Development, Elsevier Inc., 2019. doi:10.1016/B978-0-12-817909-3.00010-8.

[16]   R.J. HUNTER, Interaction between Colloidal Particles, Zeta Potential Colloid Sci. (1981). doi:10.1016/B978-0-12-361961-7.50017-1.

[17]   R.S.H. Mansour, P.K. Deb, R.K. Tekade, Role of Amorphous State in Drug Delivery, 2018. doi:10.1016/B978-0-12-814421-3.00004-X.

[18]   F. Wang, H. Hui, T.J. Barnes, C. Barnett, C.A. Prestidge, Oxidized mesoporous silicon microparticles for improved oral delivery of poorly soluble drugs., Mol Pharm. 7 (2010) 227.

[19]   S.C. Shen, W.K. Ng, J. Hu, K. Letchmanan, J. Ng, R.B.H. Tan, Solvent-free direct formulation of poorly-soluble drugs to amorphous solid dispersion via melt-absorption, Adv. Powder Technol. 28 (2017) 1316–1324. doi:10.1016/j.apt.2017.02.020.

[20]   K.S.W. Sing, D.H. Everett, R.A.W. Haul, L. Moscou, R.A. Pierotti, J. Rouquerol, T. Siemieniewska, REPORTING PHYSISORPTION DATA FOR GAS/SOLID SYSTEMS with Special Reference to the Determination of Surface Area and Porosity, PURE Appl. Chem. 57 (1985) 603–619.

[21]   K.A. Cychosz, R. Guillet-Nicolas, J. García-Martínez, M. Thommes, Recent advances in the textural characterization of hierarchically structured nanoporous materials, Chem. Soc. Rev. 46 (2017) 389–414. doi:10.1039/c6cs00391e.

[22]   J.B. Condon, An Overview of Physisorption, Surf. Area Porosity Determ. by Physisorption. (2006) 1–27. doi:10.1016/b978-044451964-1/50003-0.

[23]   https://www.micromeritics.com, (n.d.). https://www.micromeritics.com/.

[24]   M. Thommes, K. Kaneko, A. V. Neimark, J.P. Olivier, F. Rodriguez-Reinoso, J. Rouquerol, K.S.W. Sing, Physisorption of gases, with special reference to the evaluation of surface area and pore size distribution (IUPAC Technical Report), Pure Appl. Chem. 87 (2015) 1051–1069. doi:10.1515/pac-2014-1117.

[25]   M.B. Alsirawan, M.A. Mohammad, B. Alkasmi, K. Alhareth, M. El-

Hammadi, Development and validation of a simple HPLC method for the determination of ibuprofen sticking onto punch faces, Int. J. Pharm. Pharm. Sci. 5 (2013) 227–231.

[26] M. Shi, Z. Chen, S. Farnaghi, T. Friis, X. Mao, Y. Xiao, C. Wu, Copper-doped mesoporous silica nanospheres, a promising immunomodulatory agent for inducing osteogenesis, Acta Biomater. 30 (2016) 334–344. doi:10.1016/j.actbio.2015.11.033.

[27] G. Montalbano, G. Borciani, C. Pontremoli, G. Ciapetti, M. Mattioli-belmonte, S. Fiorilli, C. Vitale-brovarone, Development and Biocompatibility of Collagen-Based Composites Enriched with Nanoparticles of Strontium Containing Mesoporous Glass, Materials (Basel). 12 (2019) 1–17.

[28] A.L.B. Maçon, T.B. Kim, E.M. Valliant, K. Goetschius, R.K. Brow, D.E. Day, A. Hoppe, A.R. Boccaccini, I.Y. ong Kim, C. Ohtsuki, T. Kokubo, A. Osaka, M. Vallet-Reg??, D. Arcos, L. Fraile, A.J. Salinas, A. V. Teixeira, Y. Vueva, R.M. Almeida, M. Miola, C. Vitale-Brovarone, E. Vern??, W. H??land, J.R. Jones, A unified in vitro evaluation for apatite-forming ability of bioactive glasses and their variants, J. Mater. Sci. Mater. Med. 26 (2015) 115. doi:10.1007/s10856-015-5403-9.

[29] K.K. Kaysinger, W.K. Ramp, Interaction between Colloidal Particles, in: Zeta Potential Colloid Sci., Elsevier, 1981: pp. 363–369. doi:10.1016/B978-0-12-361961-7.50017-1.

[30] D. Lozano, M. Manzano, J.C. Doadrio, A.J. Salinas, M. Vallet-Regí, E. Gómez-Barrena, P. Esbrit, Osteostatin-loaded bioceramics stimulate osteoblastic growth and differentiation, Acta Biomater. 6 (2010) 797–803. doi:10.1016/j.actbio.2009.08.033.

[31] B. Preininger, H. Gerigk, J. Bruckner, C. Perka, H. Schell, A. Ellinghaus, K. Schmidt-Bleek, G. Duda, An experimental setup to evaluate innovative therapy options for the enhancement of bone healing using BMP as a benchmark - A pilot study, Eur. Cells Mater. (2012). doi:10.22203/eCM.v023a20.

[32] S. Wendler, C. Schlundt, C.H. Bucher, J. Birkigt, C.J. Schipp, H.D. Volk, G.N. Duda, K. Schmidt-Bleek, Immune modulation to enhance bone healing-a new concept to induce bone using prostacyclin to locally modulate immunity, Front. Immunol. (2019). doi:10.3389/fimmu.2019.00713.

CHAPTER 3

Copper-containing MBGs: Results and Discussion

3.1 Introduction

With the final aim to design and develop a multifunctional platform based on Mesoporous Bioactive Glasses (MBGs), to be used as therapeutic delivery system for the treatment of delayed bone healing, several therapeutic ions and drugs were identified and selected to exert a specific therapeutic effect, such as antibacterial, pro-angiogenic, anti-inflammatory or pro-osteogenic. In the present chapter, the related results will be presented and discussed. Specifically, the data provided in this chapter allowed to select the most promising procedures and materials to be further investigated by *in vitro* and *in vivo* experiments, with the final aim to provide evidence for the efficacy and safety of MBG-based carriers in the bone regeneration application.

Two synthesis procedures have been selected to produce the MBGs with a binary composition based on SiO_2 and CaO (ratio 85/15) and successively enriched with different therapeutic ions. The first one is a water-based sol-gel procedure using ammonia as catalyst allowing to produce nano-sized particles with diameter ranging between 100 and 200 nm and pores around 4 nm. The second one consists in an aerosol-assisted spray-drying approach, exploited to produce micro-sized particles with size in the range of 1 and 5 μm and bigger pores in the range of 8-10 nm. The amount and the type of therapeutic ions added during the synthesis were selected to obtain peculiar outcomes in terms of efficacy and biocompatibility. The first ion selected to be incorporated into the MBG framework is copper, since, as mentioned in the section 1.4.1, this element has been widely investigated in the biomedical field, thanks to the well-known antibacterial properties [1,2], along with the capability to stimulate the angiogenic process [3].
The as-synthetized samples were prepared by substituting part of the calcium with the copper (2% mol.) and the related results are described in the sub-chapters 3.2.1 and 3.2.2.

Once characterized the copper-containing MBGs, ibuprofen was loaded into the mesoporous structure by using both the adsorption method and the incipient wetness procedure.

Ibuprofen was selected to be incorporated into the MBGs with the idea to guarantee the timely administration of anti-inflammatory drugs at initial stage and for all the duration of the bone healing process in order to avoid the spreading of the inflammation phase, which could result in delay healing. The combination of the anti-inflammatory effect exerted by ibuprofen with the therapeutic concentration of released copper ions able to simultaneously promote angiogenesis and anti-microbial effect is expected to provide a better microenvironment for bone regeneration. The results related to copper-containing MBGs loaded with ibuprofen will be reported in section 3.2.3. Due to the burst release observed for both the copper and ibuprofen in the first hours after soaking in aqueous medium Tris HCl, the Layer by Layer deposition was investigated as promising strategy to overcome this drawback and modulate the release kinetics of both copper ions and ibuprofen.

As already discussed in chapter 2.6, two different routes were investigated: in the first strategy, chitosan, alginate and chitosan were assembled by forming the multi-layered surface and, successively, ibuprofen was loaded by incipient wetness impregnation. In the second one, alginate was replaced by the ibuprofen, by exploiting the ibuprofen negative charge (COO-), able to electrostatically interact with the chitosan positive charge. The obtained results are discussed in section 3.2.4.

Since MBGs alone are not exploitable as long-term drug delivery systems for orthopaedic applications, due to the strong burst release of the therapeutic species once in contact with body fluids, and the difficulties related to their administration at the pathological site (i.e. bone fracture cavity) in the form of powder, their combination with a hydrogel able to both modulate the release kinetics and to act as a vehicle phase maintaining the carrier in the pathological site has been investigated. In particular, copper-containing MBGs loaded with ibuprofen were incorporated into an injectable Poly(ether urethane) (PEU) based thermosensitive hydrogel developed by *Professor Ciardelli's group (DIMEAS, Politecnico di Torino, Italy)*. Section 3.2.5 reports the results related to the developed hybrid formulation, demonstrating the feasibility to employ this injectable platform for the prolonged and sustained release of therapeutic concentrations of copper and ibuprofen directly in the pathological site.

3.2 Morphological and structural characterization of sol-gel and spray-dryer copper-containing MBGs

3.2.1 Copper-containing MBG-SG: MBG_ Cu2%_SG

Part of the work described in this chapter has been previously published [4,5].

In addition to the antimicrobial effect of copper, previously investigated by our researcher group [6], copper exhibits pro-angiogenic and pro-osteogenic efficiency, which make this ion a promising therapeutic agent for bone regeneration purpose. In this section, the results concerning the characterization of copper-containing nano-sized particles ($85SiO_2/13CaO/2CuO$ %mol, named hereafter MBG_ Cu2%_SG) are presented.

3.2.1a Morphological and structural characterization of MBG_ Cu2%_SG

MBG_SG_Cu2% in form of dried powders were fully characterized in terms of morphology, composition, textural features, Cu^{2+} release and bioactive response properties. FE-SEM images of MBG_Cu2%_SG (Figure 3.1A) showed nanoparticles with a monodispersed spherical shape with size ranging between 150 and 200 nm. EDS mapping analysis revealed the homogeneous distribution of silicon (yellow) and calcium (red) throughout the analysed particles (Fig. 3.1B), at variance the analysis of copper was not reliable due to presence of the element in the sample holder. EDS spectrum of the powder dispersed on carbon tape (Fig. 3.1C) confirmed the incorporation of copper inside the framework, with a Cu/Si molar ratio (as average of three measurements) in fair agreement with the nominal ratio.
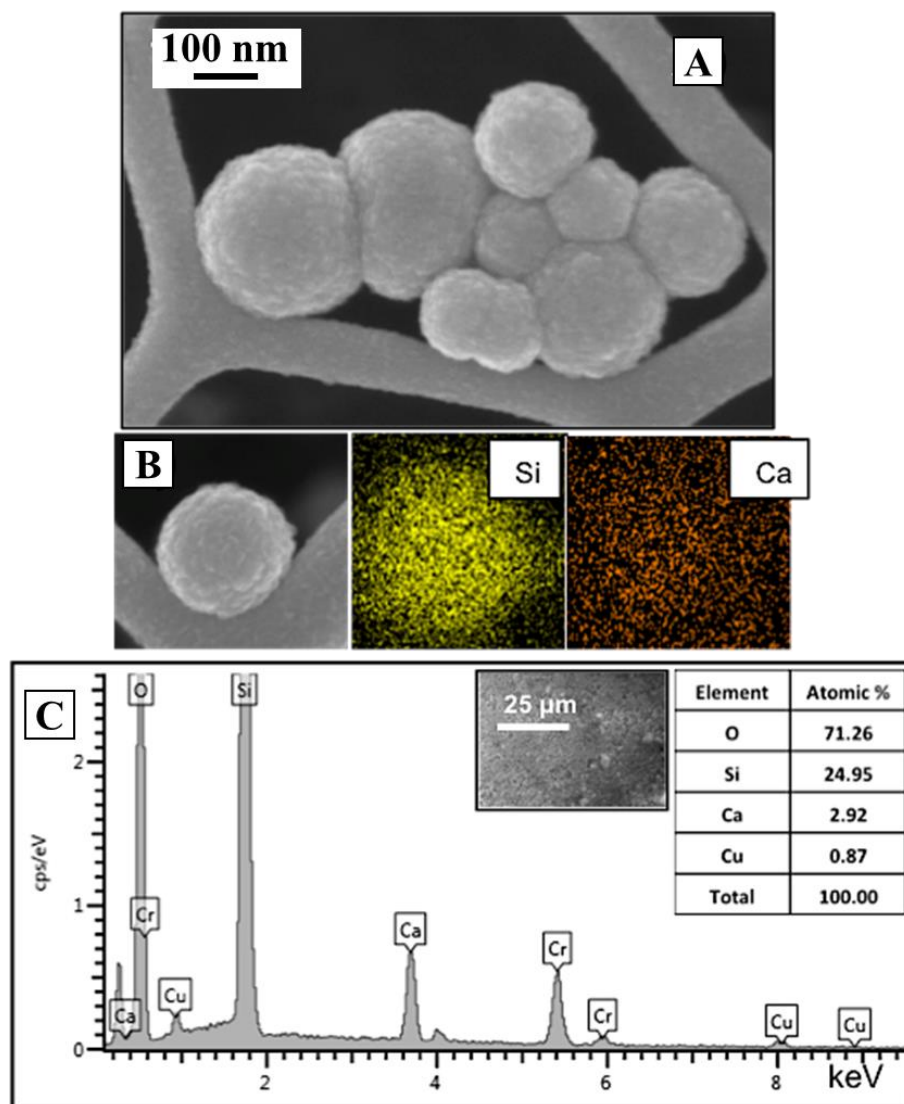
Figure 3.28 FE-SEM image of MBG_Cu2%_SG (A), EDS mapping analysis of MBG_Cu2%_SG single particle (B), EDS spectrum of MBG_Cu2%_SG (C)

Wide-angle XRD (Figure 3.2) confirmed that copper did not form segregated oxide clusters after calcination treatment, as assessed by the absence of crystalline oxide-based phases.
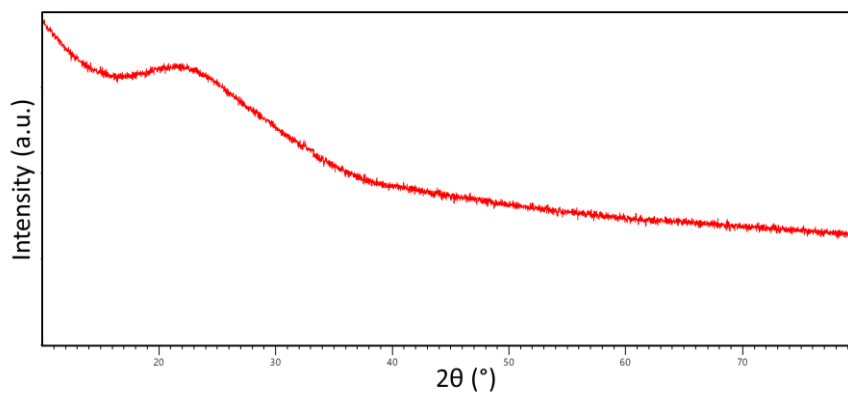
Figure 3.29 Wide-angle XRD spectrum of MBG_Cu2%_SG.

The N$_2$ adsorption-desorption isotherm confirmed the mesoporous structure of copper-containing MBG (Figure 3.3). The type IV isotherm curve of MBG_SG_Cu2% showed a well-defined step around 0.4 (p/p$_0$), indicative of the filling of uniform mesopores. Related DFT pore size distribution (inset in Figure 3.3) confirmed the presence of uniform mesopores with a mean diameter centred at around 4 nm. The BET$_{SSA}$ and pore volume (reported in Table 3.1) resulted remarkably high, slightly lower than those reported for similar systems without copper [7].
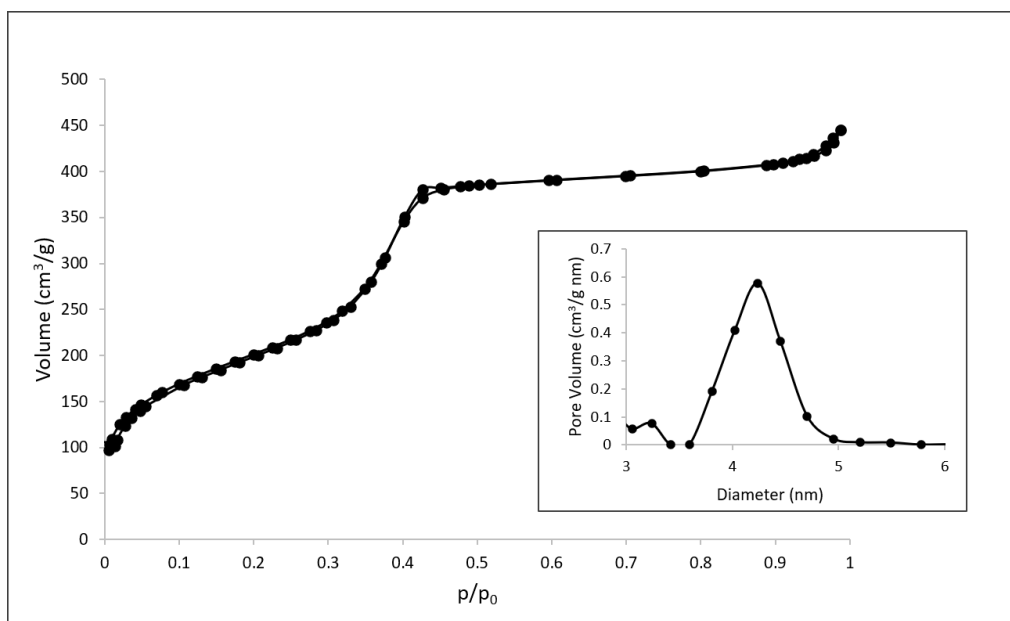
Figure 30.3 N$_2$ adsorption-desorption isotherm of MBG_Cu2%_SG and related DFT pore size distribution (inset).

Table 3.10 Structural features of MBG_Cu2%_SG.

Name	Specific surface area (cm^3/g)	Pore size (nm)	Volume (cm^3/g)
MBG_Cu2%_SG	740	4	0.65

3.2.1b Bioactive behaviour of MBG_Cu2%_SG in SBF

The bioactive response of the MBG_Cu2%_SG was tested by soaking the particles in SBF up to 14 days. After only 1 day of soaking, the particles started to be covered by a rough layer of globe-shaped agglomerate of hydroxyapatite (HA) phase confirming the rapid bioactive response of the sample. After 7 days of soaking (Figure 3.4A), the FE-SEM investigation showed elongated needle-like formation covering the particles, which resembled the HA shape. From EDS investigation (Figure 3.4B), new peak, ascribed to phosphorous, appeared, further

suggesting the deposition of HA. After 14 days, the MBG particles were almost fully covered by a compact layer of needle-like nanocrystals.
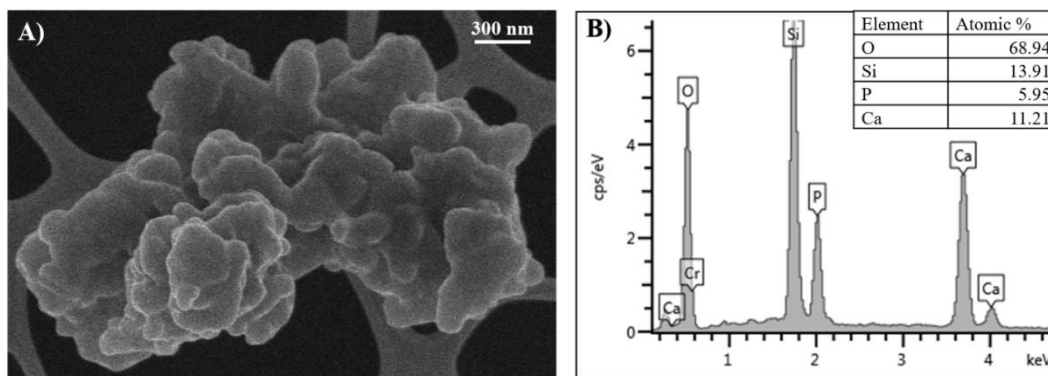
Figure 3.31 FE-SEM image (A) and EDS investigation (B) of MBG_Cu2%_SG after 7 days of soaking in SBF.

The formation of HA cluster was further confirmed by the wide-angle XRD analysis. In fact, XRD spectra of the powder after 7 days of soaking (Figure 3.5) showed the presence of new peaks at 25.84, 29.32 and 32.13 2θ degrees which matched by HA (external reference 01-086-0740).
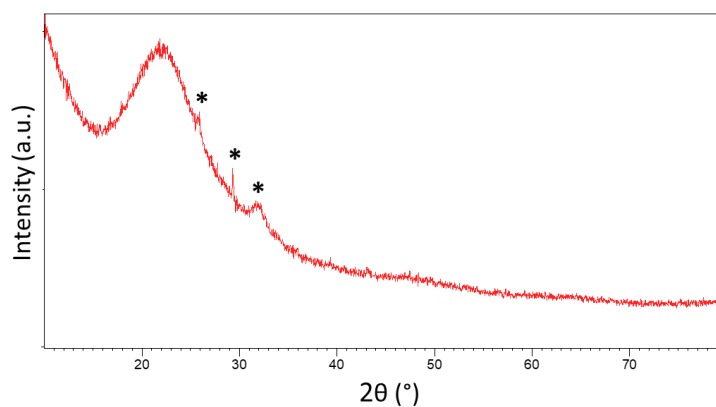
Figure 3.32 Wide-angle XRD of MBG_Cu2%_SG after 7 days of soaking in SBF.

3.2.1c Copper ion release from MBG_Cu2% _SG in Tris HCl

The ionic concentration (ppm) of Cu^{2+} species from MBG_Cu2%_SG powder in Tris HCl medium is reported in figure 3.6: almost the total amount of incorporated copper was released within the first 3 h of incubation with a final released concentration of about 4.7 ppm. After the first hours of soaking, the copper released concentration remained constant till the end of the test (14 days).

132

The fast ion release kinetics observed for the MBG_Cu2%_SG can be associated to the remarkably high surface area and the small particle size (short diffusion paths), which allow fast ion diffusion inside the porous structure.
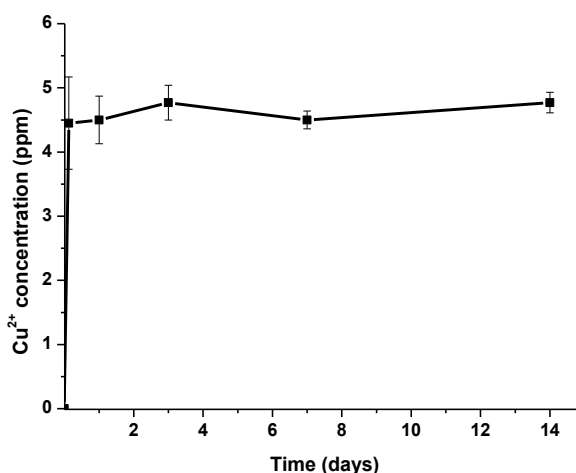
Figure 3.33 Cu^{2+} release profile of MBG_Cu2%_SG in Tris HCl.

3.2.2 Copper-containing MBG-SD: MBG_Cu2%_SD

Part of the work described in this chapter has been previously published in [4,5].

In this section, the results concerning the characterization of copper-containing micro-sized particles (85SiO$_2$/13CaO/2CuO %mol, named hereafter MBG_Cu2%_SD) are reported. The as-synthesized microparticles were produced by modifying the procedure reported by Pontiroli et al. [8].

3.2.2a Morphological and structural characterization of MBG_Cu2%_SD

MBG_Cu2%_SD in form of dried powders were fully characterized in terms of morphology, composition, textural features, Cu^{2+} release and bioactive response properties. The morphology, composition and structural features, as well as the bioactive response and copper release of MBG_Cu2%_SD were investigated. As shown in figure 3.7A, MBG_Cu2%_SD consists of microspheres with size mostly in the range of 1-5 μm, showing silicon (yellow), calcium (green) and copper (light blue) homogeneously distributed into the framework, as revealed by the compositional mapping EDS analysis carried out on a single sphere (Fig. 3.7B). EDS spectrum of the powder supported on the carbon-based tape revealed the incorporation of copper with a molar concentration very close to the nominal ratio (Fig. 3.7C).
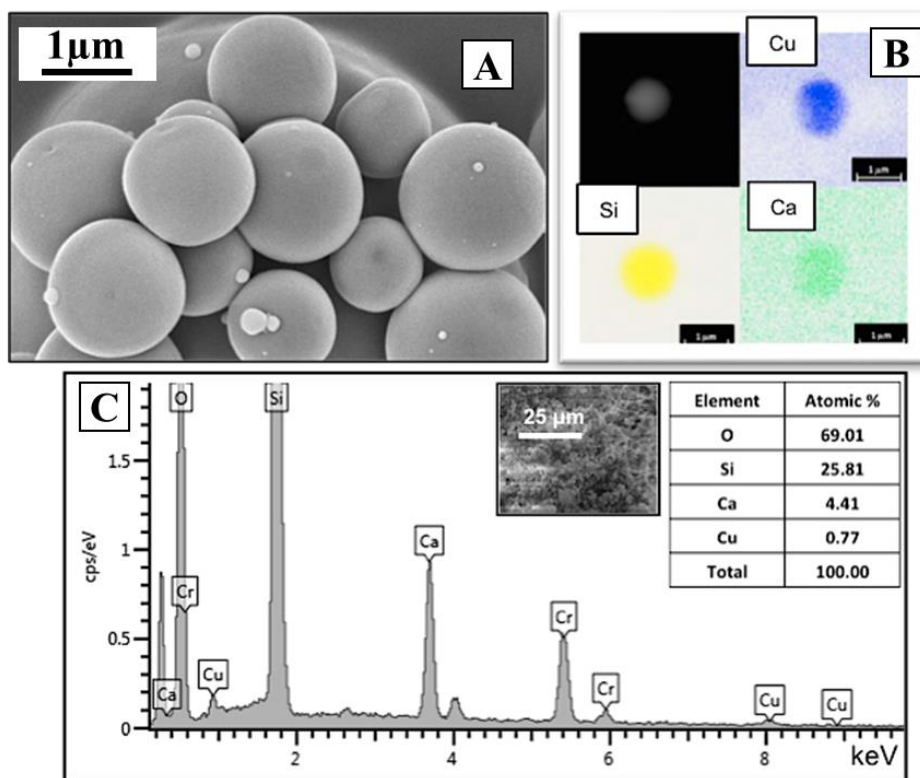
Figure 3.34 FE-SEM image of MBG_Cu2%_SD (A), EDS mapping analysis of MBG_Cu2%_SD single particle (B), EDS spectrum of MBG_Cu2%_SD (C).

Wide-angle XRD spectrum (Figure 3.8) confirmed that copper did not form segregated oxide clusters after calcination treatment, as assessed by the absence of crystalline oxide-based phases.
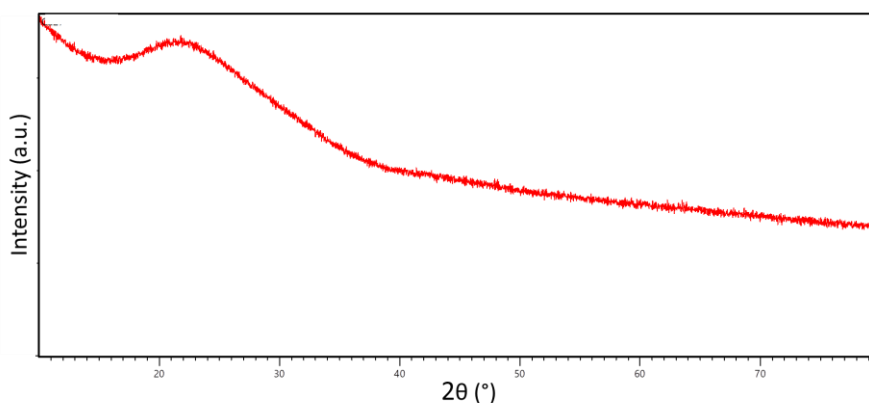

Figure 3.35 Wide-angle XRD analysis of MBG_Cu2%_SD.

N_2 adsorption-desorption measurement performed on the sample obtained by aerosol-assisted procedure also confirmed the mesoporous structure of the sample. The isotherm of the MBG_Cu2%_SD reported in Figure 3.9 is a IV type curve, with H1 hysteresis loop, typical of mesoporous material with pores larger than 4 nm [9]. The pore size distribution showed multi-sized pores with broad distribution, ranging between 8 and 11 nm (inset in Figure 3.9). The BET$_{SSA}$ of MBG_Cu2%_SD of 226 m^2/g, although lower compared to the one shown by MBG_Cu2%_SG (Table 3.2),

is still very higher than the values typical of not-templated sol-gel glasses (few cm^3/g), which confers a high reactivity to MBGs in the biological environment [10].
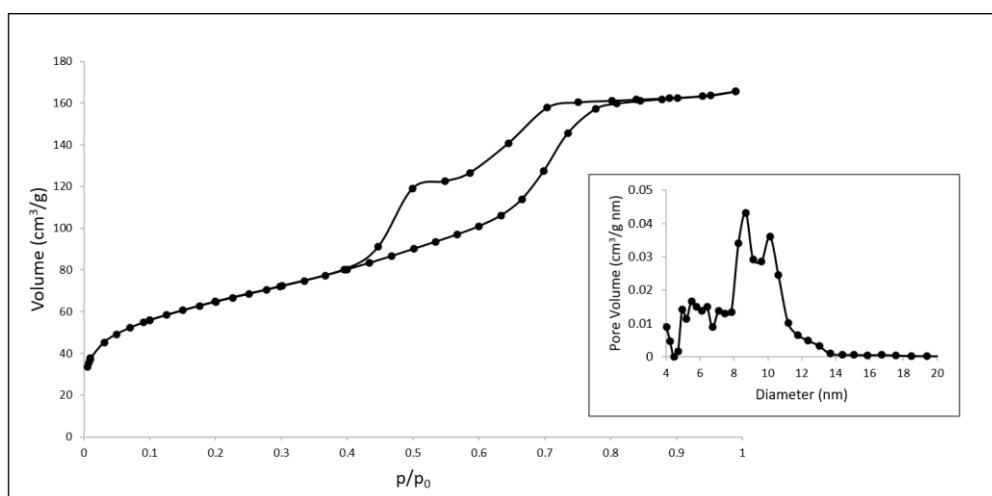
Figure 3.36 N₂ adsorption-desorption isotherm of MBG_Cu2%_SD and related DFT pore size distribution (inset).

Table 3.11 Structural features of MBG_Cu2%_SD.

Name	Specific surface area (cm³/g)	Pore size (nm)	Volume (cm³/g)
MBG_Cu2%_SD	226	8-11	0.24

3.2.2b Bioactive behaviour of MBG_Cu2%_SD in SBF

The remarkable bioactivity of MBG_Cu2%_SD when soaked in SBF was clearly revealed by FE-SEM observations (Figure 3.10A). After only 1 day of soaking, the particles started to be covered by a rough layer of globular agglomerates of Ca-deficient HA phase (Ca/P=1.51), as shown by EDS analysis. After 14 days, MBG particles were almost fully covered by a compact layer of needle-like nanocrystals, composed by calcium and phosphorus. Figure 3.10B

shows MBG_Cu2%_SD after soaking for 14 days. EDS analysis performed on powders evidenced a Ca/P ratio of 1.7, typical of HA [11,12].
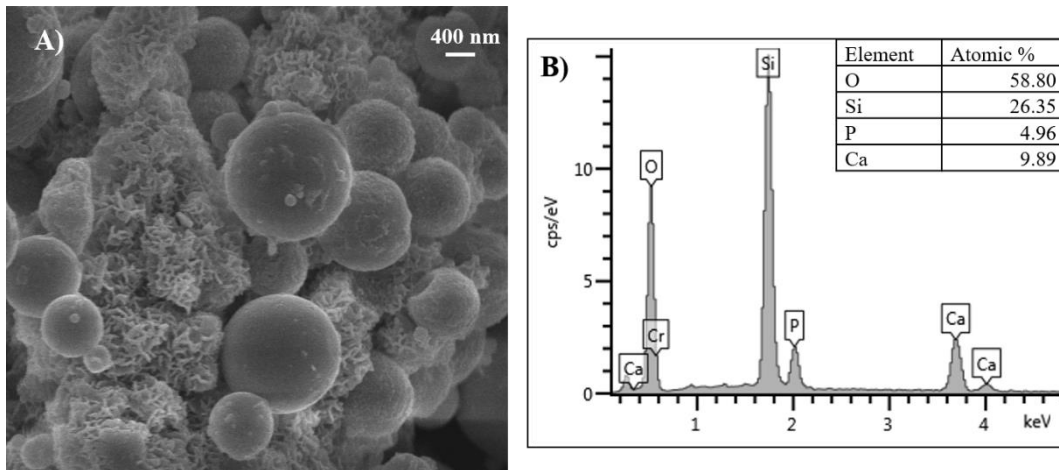
Figure 3.37 FE-SEM image (A) and EDS investigation (B) of MBG_Cu2%_SD after 1 day of soaking in SBF.

The formation of crystalline HA after the bioactivity test has been evaluated also by wide-angle XRD analysis performed on the MBG particles after 7 days of soaking in SBF. As shown in figure 3.11, marked peaks appeared at 25.87° and 31.73° (2θ value) and other less intense reflections are observed at 49.39 ° and 53.17° (2θ value) matched by the hydroxyapatite reference (01-089-6440).
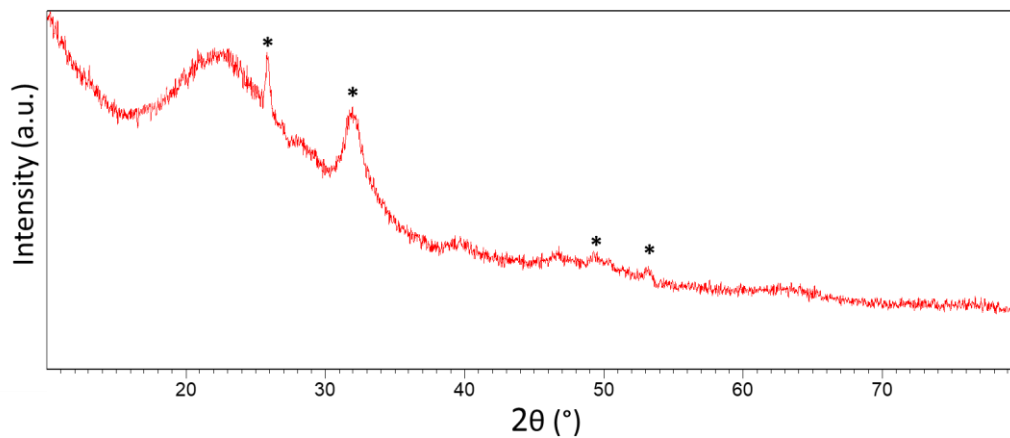
Figure 3.38 Wide-angle XRD of MBG_Cu2%_SD after 7 days of soaking in SB.

3.2.2c Copper ion release from MBG_Cu2%_SD in Tris HCl

The ionic concentration (ppm) of Cu^{2+} species from MBG_Cu2%_SD powder in Tris HCl medium is reported in figure 3.12. The release profile from MBG_Cu2%_SD particles showed a less pronounced burst effect in the first 3 h compared to MBG_Cu2%_SG, followed by a sustained release of copper ions overtime.

The observed release kinetics suggested that the diffusion of Cu^{2+} out of the mesopores is probably hindered or even blocked after the first hours (2–3 h) of incubation. A similar release profile has been already observed for ibuprofen from silica-based mesoporous spheres [13] and was ascribed to the progressive occlusion of mesopores due to the dissolution of the silica framework and its reprecipitation as silica gel at the pore mouth [14,15]. The final concentration of released copper species from MBG_Cu2%_SD was about 2.5 ppm, and corresponding to approximately the 60% of incorporated copper, suggesting the presence of a residual amount of copper into the MBG framework or re-precipitation phenomena.

In addition, since MBG_Cu2%_SD particles are produced by an aerosol-assisted spray-drying process, where a rapid evaporation of the solvent takes place, the resulting powder is expected to show a less condensed framework compared to MBG-SG samples and thus much higher reactivity toward surface dissolution/re-precipitation reactions.
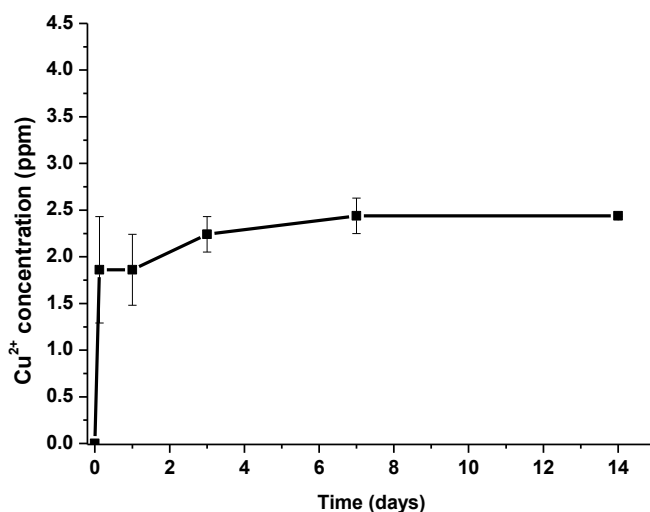
Figure 3.39 Cu^{2+} release profile of MBG_Cu2%_SD in Tris HCl.

3.2.3 Copper-containing MBGs loaded with ibuprofen

Part of the work described in this chapter has been previously published in [16].

One of the final goals of this thesis project is to obtain mesoporous bioactive glasses to be used as a drug delivery system on the pathological site; to this purpose, the therapeutic potential exerted by the copper containing-MBGs has been enriched by loading the ibuprofen. Ibuprofen, as mentioned in the section 1.6, is an anti-inflammatory drug which can be used *in situ* to contrast the uncontrolled progress of the bone healing inflammatory phase. This system was developed with the idea to produce a multifunctional device able to simultaneously release a therapeutic concentration of copper ions to promote angiogenesis and exert an anti-microbial effect [6] and an anti-inflammatory agent to contrast the persistent inflammation. Two different drug loading procedures, the adsorption and the incipient wetness method, have been explored in order to identify the suitable method in terms of the drug solubility/stability, yield and time consuming.

3.2.3.1 Copper-containing MBG-SG loaded with ibuprofen

In this section, the results concerning the characterization of copper-containing MBGs loaded with ibuprofen by using the adsorption method and the incipient wetness method are reported. The adsorption of ibuprofen has been conducted by modifying a method reported by Mortera et al. [13] and named hereafter MBG_Cu2%_SG + Ibu Ads. On the other hands, the loading of Ibuprofen by using the Incipient wetness method has been conducted by exploiting the procedure reported by Charnay et al. [17] and the obtained samples will be hereafter named MBG_Cu2%_SG + Ibu IW.

3.2.3.1a Morphological, structural and chemical characterization of MBG_Cu2%_SG + Ibu Ads and MBG_Cu2%_SG + Ibu IW.

FE-SEM images of MBG_Cu2%_SG + Ibu Ads (Figure 3.13 A1) and MBG_Cu2%_SG + Ibu IW (Figure 3.13 B1) showed nanoparticles with a monodispersed spherical shape with a size ranging between 150-200 nm. EDS spectrum (Figure 3.13 A2 and B2) confirmed the presence of copper inside the framework, with a Cu/Si molar ratio in good agreement with the nominal ratio for both MBGs. FE-SEM observations and EDS analysis evidenced that regardless of the employed loading method, ibuprofen incorporation does not significantly alter the morphological features and the chemical composition of Copper-containing MBGs, which resulted very similar to those reported for not-loaded samples (see figure 3.1). In particular, the amount of copper revealed by EDS before and after the drug loading resulted unaffected, evidencing that the loading procedure did not induce any copper release.

The nitrogen adsorption–desorption isotherms and the pore size distribution of the samples before and after drug loading are reported in Figure 3.14 A (MBG_Cu2%_SG + Ibu Ads) and Figure 3.14 C (MBG_Cu2%_SG + Ibu IW).

As expected, before loading, MBG_Cu2%_SG showed a type IV sorption isotherm, according to the IUPAC classification, with a well-defined step around 0.4 (P/P_0), indicative of uniform mesopores. The specific surface area and pore volume values reported in Table 3.3 are characteristic of mesoporous materials with uniform pores and remarkable value of specific surface area (SSA_{BET})[18].
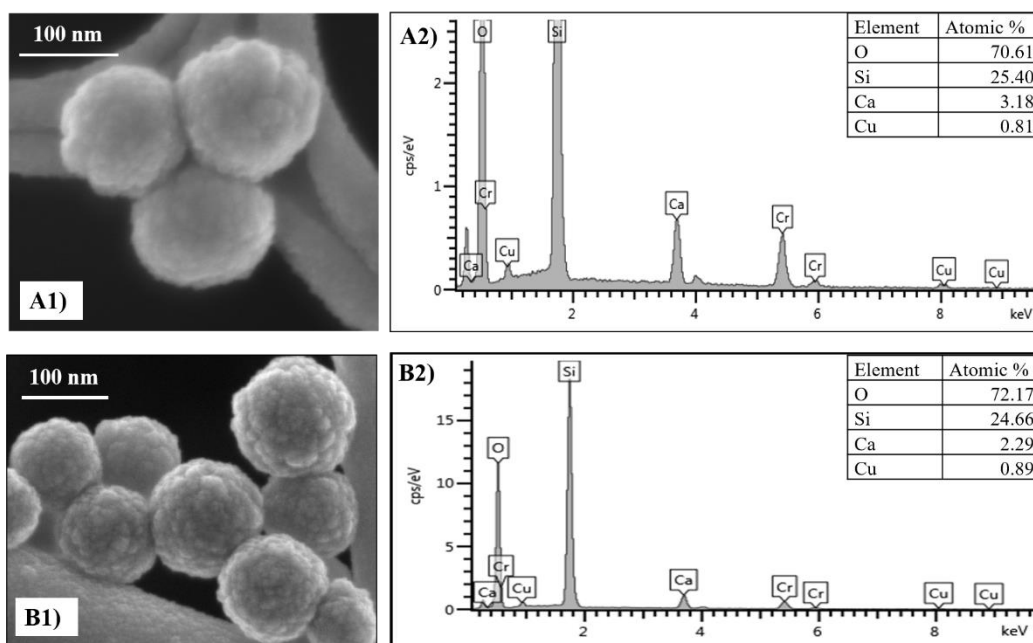
Figure 3.40 FE-SEM image (A1) and EDS spectrum (A2) of MBG_Cu2%_SG + Ibu Ads; FE-SEM image (B1) and EDS spectrum (B2) of MBG_Cu2%_SG + Ibu IW.

The mesopore size distribution was centred at around 4.2 nm, which is sufficiently large to incorporate ibuprofen whose molecular size is about 1 nm [19–21]. For both samples, drug loading induced, as expected, a significant modification of the adsorption-desorption isotherm (reduction of the adsorbed volume and presence of hysteresis loop) and a drastic reduction of the pore volume, as shown in Figure 3.14 B and D. In particular, the modification of the isotherm curve upon drug incorporation suggests that most of the mesopores are completely filled with Ibu and the remaining population experiences size reduction and shape modification from cylinder to ink-bottle pores, in analogy to the results reported by Hong et al. [22] for similar systems. The drastic reduction of pore volume as a consequence of drug incorporation was confirmed by the disappearance of the component centred at 4.2 nm.

Table 3.12 Structural properties of MBG_Cu2%_SG, MBG_Cu2%_SG + Ibu Ads and MBG_Cu2%_SG + Ibu IW.

Acronym	SSA_{BET} (cm^3/g)	Pore volume (cm^3/g)	Pore size (nm)
MBG_Cu2%_SG	740	0.65	4.2
MBG_Cu2%_SG + Ibu Ads	387	0.35	2-8
MBG_Cu2%_SG + Ibu IW	330	0.35	2-6
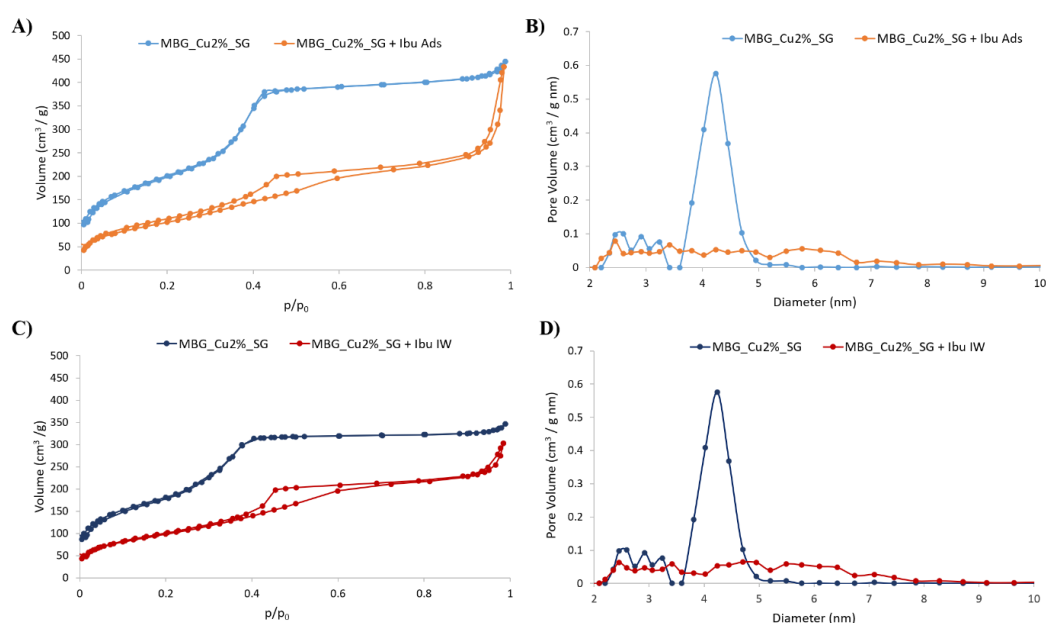
Figure 3.41 N_2 adsorption-desorption isotherm of MBG_Cu2%_SG + Ibu Ads compared to the not-loaded sample (A) and related DFT pore size distribution (B); N_2 adsorption-desorption isotherm of MBG_Cu2%_SG + Ibu IW compared to the not-loaded sample (C) and related DFT pore size distribution (D).

The total amount of loaded drug was quantified by TGA analysis after drug incorporation. As reference, TGA analysis was also conducted on not-loaded MBG samples, proving the complete absence of residual organic species at 600 °C. TGA thermograms of MBG_Cu2%_SG + Ibu Ads (Figure 3.15 A) and MBG_Cu2%_SG + Ibu IW (Figure 3.15 B) exhibited a significant weight decrease between 300 and 400 °C. The latter ascribable to ibuprofen loss [23] is most likely due to the multiple H-bonding interactions between the drug molecules and the large population of hydroxyl groups of the inner MBG surface, suggesting the confinement of ibuprofen molecules, in accordance with the work by Mellaerts and co-workers [20]. The weight percentage of loaded ibuprofen, based on TGA analysis, turned out to be 10% for MBG_Cu2%_SG + Ibu Ads and 12% for MBG_Cu2%_SG + Ibu IW.
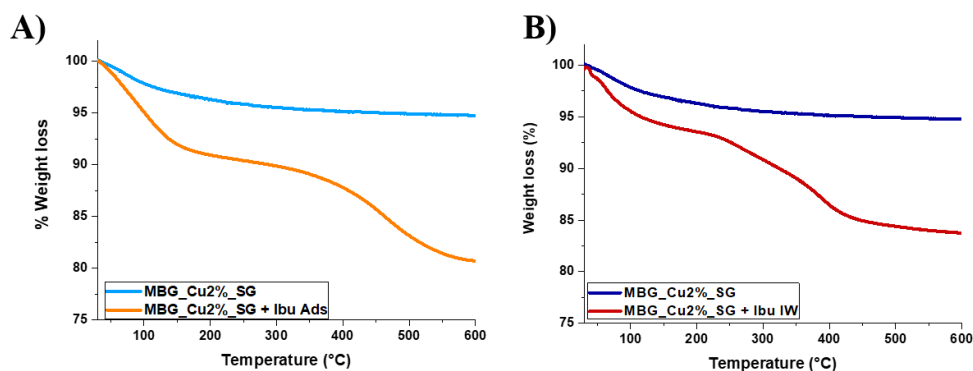
Figure 3.42 TGA thermograms of (A) MBG_Cu2%_SG and MBG_Cu2%_SG + Ibu Ads; (B) MBG_Cu2%_SG and MBG_Cu2%_SG + Ibu IW.

FTIR spectra of both copper-containing MBGs before and after ibuprofen loading are reported in figure 3.16 A and 3.16 B. All samples showed the typical adsorption bands of H-bonded hydroxyls (stretching vibration) in the range of 3750–3000 cm^{-1}. Concerning the drug-loaded samples, FTIR spectrum of both MBG_Cu2%_SG + Ibu Ads and MBG_Cu2%_SG + Ibu IW showed the typical bands of ibuprofen molecule: at 2933 and 2871 cm^{-1} the absorption bands ascribed to C-H stretching modes and at 1550 and 1410 cm^{-1}, due to the asymmetric (v_{as}) and symmetric (v_s) stretching vibration of the carboxylate group COO-, respectively [24]. As far as the MBG_Cu2%_SG + Ibu IW is concerned, the absence of the adsorption band at 1706 cm^{-1}, corresponding to C=O stretching vibration, and the appearance of carboxylate peaks further proved the formation of hydrogen bonds between ibuprofen-COOH and hydroxyl groups at MBG surface [25].
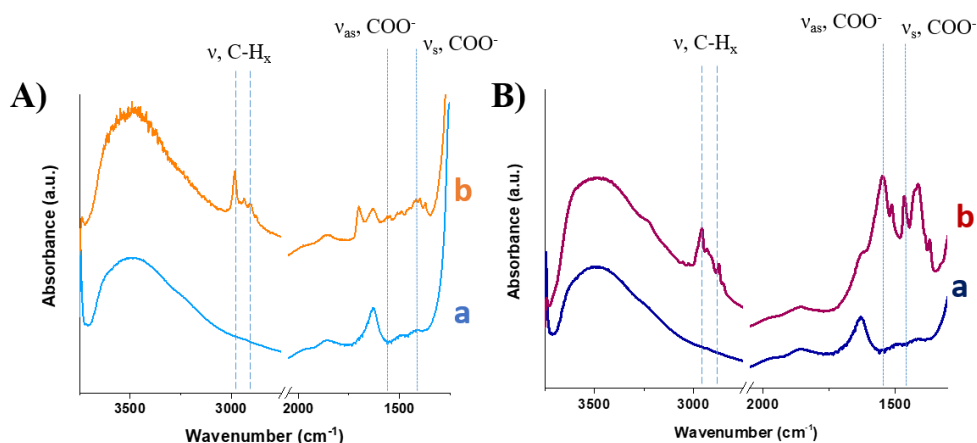
Figure 3.43 FTIR spectra of (A) MBG_Cu2%_SG (a), and MBG_Cu2%_SG + Ibu Ads (b); (B) MBG_Cu2%_SG (a), and MBG_Cu2%_SG + Ibu IW (b).

141

As widely reported in the literature [26,27], drug loading in their amorphous form results in an increased dissolution rates and solubility. Hence, DSC and X-ray powder diffraction (XRD) analysis of ibuprofen-loaded sample were conducted to assess the amorphous state of the drug and exclude the presence of large crystalline aggregates. DSC thermograms of Ibu as such compared to MBG_Cu2%_SG + Ibu Ads and MBG_Cu2%_SG + Ibu IW are reported in Figure 3.17A and figure 3.17B, respectively: a single endothermic melting peak at 76 °C, ascribed to crystal phase melting, was observed only for ibuprofen as such, confirming the non-crystalline state of ibuprofen into the mesopores.
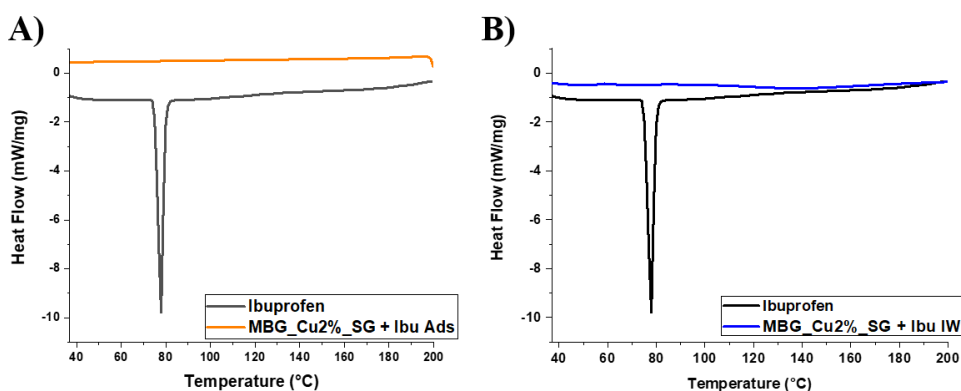
Figure 3.44 DSC thermograms of ibuprofen and MBG_Cu2%_SG + Ibu Ads (A) and ibuprofen and MBG_Cu2%_SG + Ibu IW (B).

The amorphous state of the drug was also confirmed by XRD analysis (Figure 3.18). XRD pattern of ibuprofen powder showed several characteristic X-ray diffraction peaks, which completely disappeared upon drug loading into the pores of copper-containing MBGs, which, in accordance with DSC data, strongly suggested that ri-crystallization did not occur inside the pores upon solvent evaporation during the incorporation process. This behaviour has been previously reported by Bràs et al. [23], who confirmed the amorphous state of ibuprofen confined inside SBA-15 silicas with similar pore size.
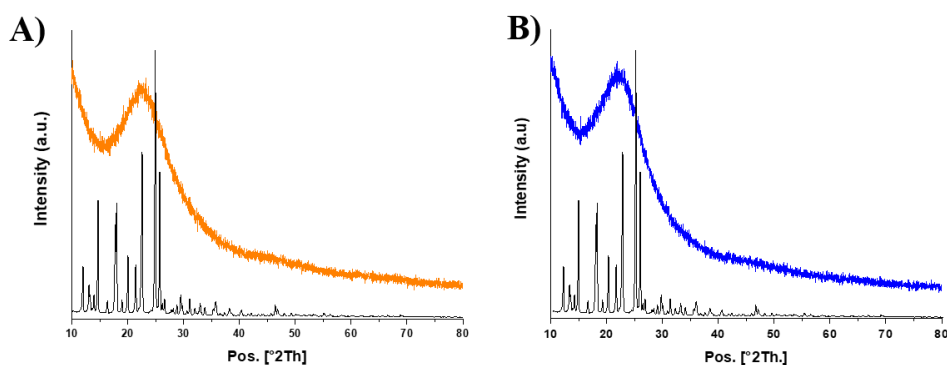
Figure 3.45 XRD patterns of (A) ibuprofen and MBG_Cu2%_SG + Ibu Ads and (B) ibuprofen and MBG_Cu2%_SG + Ibu IW.

The proposed attribution is also supported by several authors [28,29] who reported that re-crystallization of the entrapped drug molecules is suppressed below

a critical pore diameter, showing that crystallization can occur only when pore size is significantly larger (about 20 times) compared to the drug size [28].

3.2.3.1b Bioactive behaviour of MBG_Cu2%_SG + Ibu Ads and MBG_Cu2%_SG + Ibu IW in SBF.

The bioactive behaviour of both MBG_Cu2%_SG + Ibu Ads and MBG_Cu2%_SG + Ibu IW after soaking in SBF was maintained after the ibuprofen loading and is clearly revealed by FE-SEM observations (Figure 3.19). After only 1 day of soaking, the particles started to be covered by a rough layer of globular agglomerates which continued to grow in size over the time. After 7 days, particles were almost fully covered by a compact layer of needle-like nanocrystals, as shown in Figure 3.19 A1 and Figure 3.19 A2 for MBG_Cu2%_SG + Ibu Ads and MBG_Cu2%_SG + Ibu IW, respectively. EDS analysis performed on powders evidenced a Ca/P ratio of 1.7, typical of HA [11,12].

The formation of crystalline HA after the bioactivity test has been evaluated also by wide-angle XRD analysis performed on the MBG particles after 7 days of soaking in SBF. As shown in figure 3.19 B1 and B2, for both samples, marked peaks appeared at 25.87° and 31.73° (2θ value) and other less intense reflections
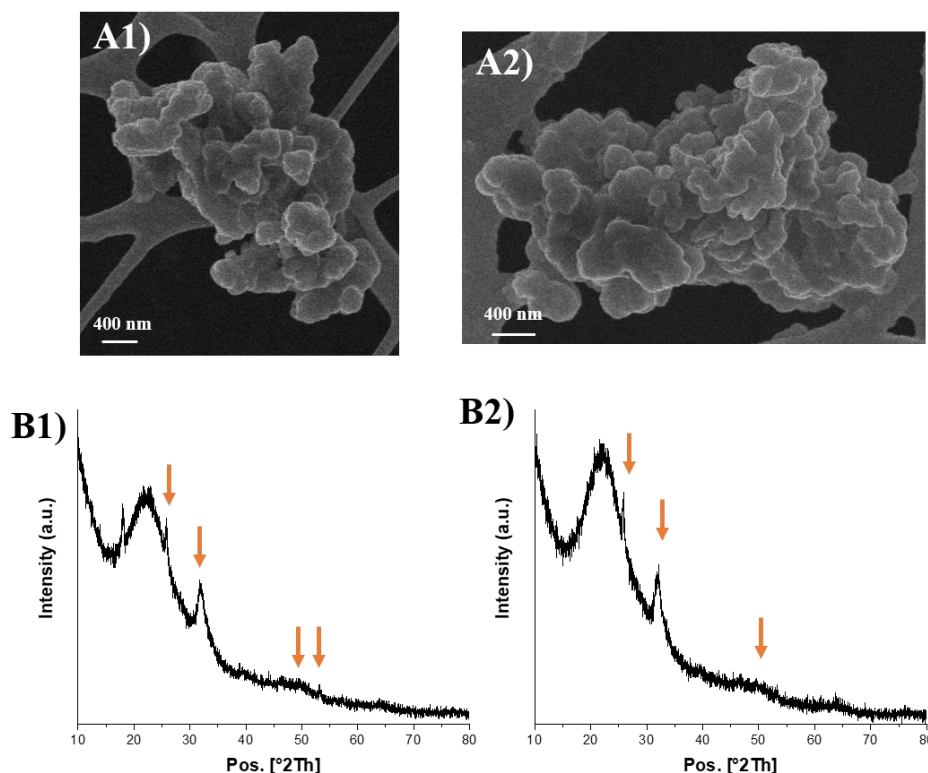
Figure 3.46 FE-SEM observation of (A1) MBG_Cu2%_SG + Ibu Ads and (A2) MBG_Cu2%_SG + Ibu IW; Wide-angle XRD of (B1) MBG_Cu2%_SG + Ibu Ads and (B2) MBG_Cu2%_SG + Ibu IW after 7 days of soaking in SBF.

are observed at 49.39 ° and 53.17° (2θ value) corresponding to the hydroxyapatite reference (01-089-6440).

3.2.3.1c Copper release from MBG_Cu2%_SG + Ibu Ads and MBG_Cu2%_SG + Ibu IW in Tris HCl.

The release profile of copper ions from MBG_Cu2%_SG + Ibu Ads and MBG_Cu2%_SG + Ibu IW powder in Tris HCl medium, following the protocol described in section 2.9.1, is reported in figure 3.20 A and 3.20 B, respectively: for both samples, the total amount of incorporated copper was released within the first 3 h of incubation with a final released concentration of about 3.7 ppm for MBG_ Cu2%_SG + Ibu Ads and 3.85 ppm for MBG_ Cu2%_SG + Ibu IW. As previously observed for the corresponding non-loaded sample (MBG_Cu2%_SG), after the first hours of soaking, the copper released concentration remained constant till the end of the test (14 days).

The fast copper release kinetics observed for both the MBG_Cu2%_SG + Ibu Ads and MBG_Cu2%_SG + Ibu IW is very similar to that observed for the corresponding non-loaded sample, highlighting that drugs loading within the porous structure, irrespective of the conducted loading procedures, did not suppress

A) **B)**
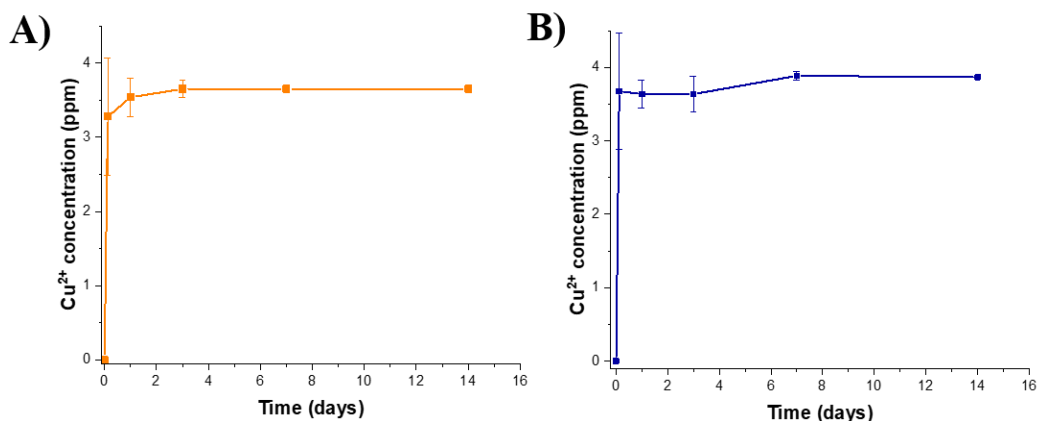
Figure 3.47 Cu^{2+} release profile of (A) MBG_Cu2%_SG + Ibu Ads and (B) MBG_Cu2%_SG + Ibu IW in Tris HCl.

or hinder the capability to release therapeutic ions through ion-exchange reactions.

3.2.3.1d Ibuprofen release from MBG_Cu2%_SG + Ibu Ads and MBG_Cu2%_SG + Ibu IW in Tris HCl.

Ibuprofen release profile has been evaluated in Tris-HCl up to 48 hours. As shown in figure 3.21, a complete release of the drug was observed, with a release of 94±2.0 % for MBG_Cu2%_SG + Ibu Ads and 98±0.8 % for MBG_Cu2%_SG + Ibu IW after 1 hour of soaking in the medium, follows, in both cases, by a plateau till the end of the test (48h). This fast release rate can be associated to the size of MBGs; in fact, a correlation between the drug release rate and the particle size has been proved to influence the release kinetics. As reported in literature, small spherical particles size of around 100-200 nm show the fastest drug release rate [30].
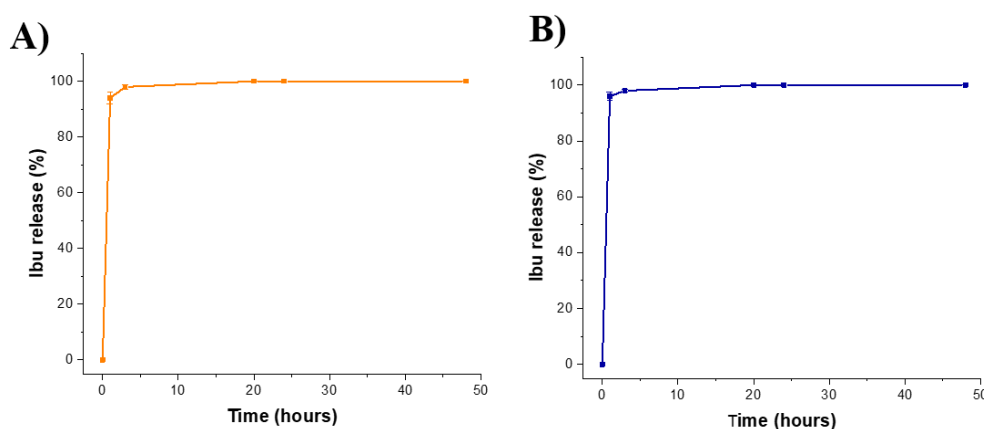
Figure 3.48 Ibuprofen release profile of (A) MBG_ Cu2%_SG + Ibu Ads and (B) MBG_Cu2%_SG + Ibu IW in Tris HCl.

Furthermore, the mesopores result to be accessible to the medium, increasing the drug transport from the pores to the solution, thus allowing the release of the ibuprofen due to unrestricted diffusion pathway through the mesopore network [31]. In addition, the weak interactions between the ibuprofen and the silica surface could further promote the fast diffusion of the drug in the medium [32].

3.2.3.2 Copper-containing MBG-SD loaded with ibuprofen

In this section, the results concerning the characterization of copper-containing MBG-SD loaded with ibuprofen by using the adsorption method and the incipient wetness method are reported. The adsorption of ibuprofen has been conducted by modifying a method reported by Mortera et al. [13] and named hereafter MBG_Cu2%_SD + Ibu Ads.

The loading of Ibuprofen by using the IW method has been conducted by exploiting the procedure reported by Charnay et al. [17] and the as-prepared sample will be hereafter named MBG_Cu2%_SD + Ibu IW.

3.2.3.2a   Morphological,   structural   and   chemical characterization   of   MBG_Cu2%_SD   +   Ibu   Ads   and MBG_Cu2%_SD + Ibu IW.

FE-SEM observations of MBG_Cu2%_SD + Ibu Ads (Figure 3.22 A) and MBG_Cu2%_SD + Ibu IW (Figure 3.22 B1) showed microparticles with a with a size ranging between 1 and 5 μm. The EDS spectra of both samples (Figure 3.22 A2 and B2) revealed the presence of copper inside the framework, with a Cu/Si similar with the nominal ratio. Both FE-SEM images and EDS analysis showed that the both the procedures to load ibuprofen do not significantly interfere with the morphology and the chemical composition of Copper-containing MBG-SD, which resulted very similar to those reported for not-loaded samples (see figure 3.7). In fact, the amount of copper revealed by EDS analysis before and after the drug loading resulted unaffected, further confirming that the adsorption and incipient wetness loading procedure did not induce any copper release.

Element	Atomic %
O	68.09
Si	26.16
Ca	5.12
Cu	0.63

Element	Atomic %
O	68.59
Si	25.56
Ca	5.10
Cu	0.75
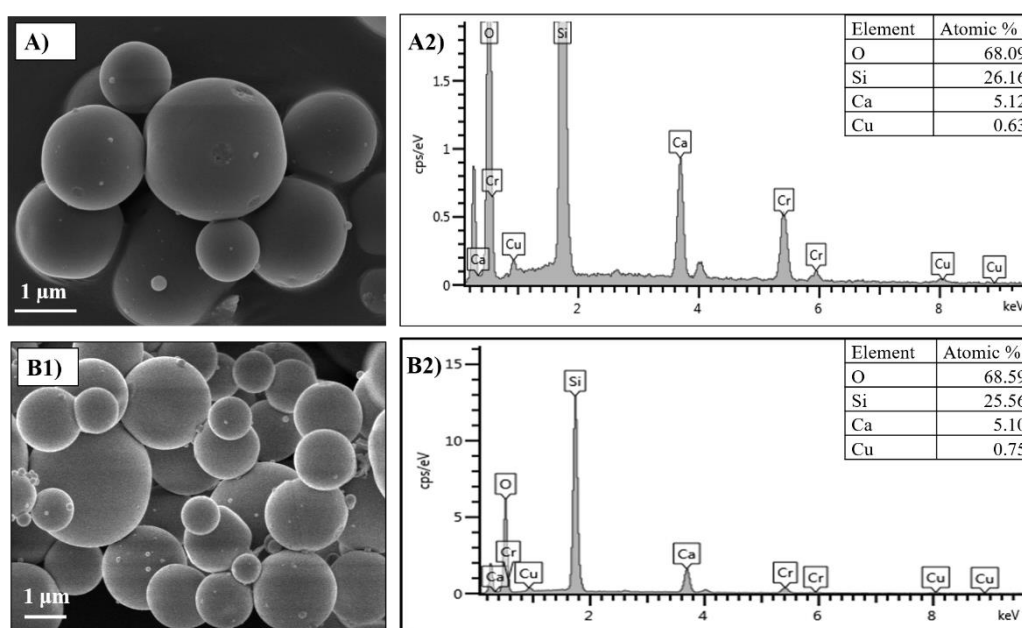
Figure 3.49 FE-SEM image (A1) and EDS spectrum (A2) of MBG_Cu2%_SD + Ibu Ads; FE-SEM image (B1) and EDS spectrum (B2) of MBG_Cu2%_SD + Ibu IW.

The nitrogen adsorption–desorption isotherms and the pore size distribution of the samples before and after drug loading are reported in figure 3.23. The isotherm of MBG_Cu2%_SD was a type IV curve, with H1 hysteresis loop, typical of mesoporous material with pores larger than 4 nm and the pore size distribution showed multisized pores in the range between 8 and 11 nm, which easily allows the diffusion and incorporation of ibuprofen molecules. As far as the MBG_Cu2%_SD + Ibu Ads and MBG_Cu2%_SD + Ibu IW are concerned, a drastic reduction in SSA$_{BET}$ was observed after the loading of ibuprofen, while the pore volume

reduction was lower compared with the MBG-SG sample (Table 3.4). This lower reduction in pore volume could be probably ascribed to the bigger pore size, which allows the incorporation of drug molecules without a full occlusion of the available pore volume.

Table 3.13 Structural properties of MBG_Cu2%_SD, MBG_Cu2%_SD + Ibu Ads and MBG_Cu2%_SD + Ibu.

Acronym	SSA_{BET} (cm³/g)	Pore volume (cm³/g)	Pore size (nm)
MBG_Cu2%_SD	156	0.21	8-10
MBG_Cu2%_SD + Ibu Ads	46	0.064	8-10
MBG_Cu2%_SD + Ibu IW	54	0.081	8-10
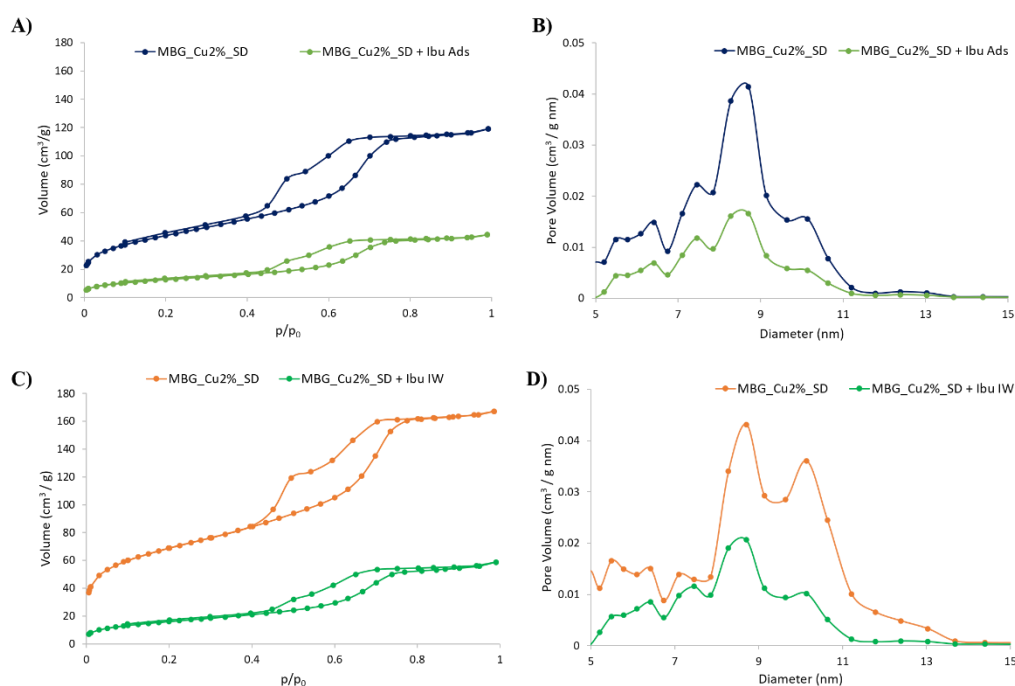
Figure 3.50 N₂ adsorption-desorption isotherm of MBG_Cu2%_SD + Ibu Ads compared to the not-loaded sample (A) and related DFT pore size distribution (B); N₂ adsorption-desorption isotherm of MBG_Cu2%_SD + Ibu IW compared to the not-loaded sample (C) and related DFT pore size distribution (D).

The total amount of loaded drug was quantified by TGA analysis. As reference, TGA analysis was also performed on not-loaded MBG sample, proving the complete absence of residual organic species at 600 °C. TGA thermograms of MBG_Cu2%_SD + Ibu Ads (Figure 3.24 A) and MBG_Cu2%_SD + Ibu IW (Figure 3.24 B) showed a weight decrease between 300 and 500 °C, associated to ibuprofen loss [16], specifically due to the multiple H-bonding interactions between the drug molecules and the large population of hydroxyl groups of the inner MBG surface, suggesting the confinement of ibuprofen molecules, in accordance with the

work by Mellaerts and co-workers [20]. The weight percentage of loaded ibuprofen, based on TGA analysis, resulted to be 6.5% for MBG_Cu2%_SD + Ibu Ads and 10% for MBG_Cu2%_SD + Ibu IW, lower compared to the corresponding MBG-SG samples. The lower amount of incorporated drug could be ascribed to the lower specific surface area and pore volume of the SD samples, compared to the SG samples. These results confirmed that the drug loading capacity increases with the increase of MGB surface area and pore volume, according to data reported in the literature for mesoporous silicas [33].
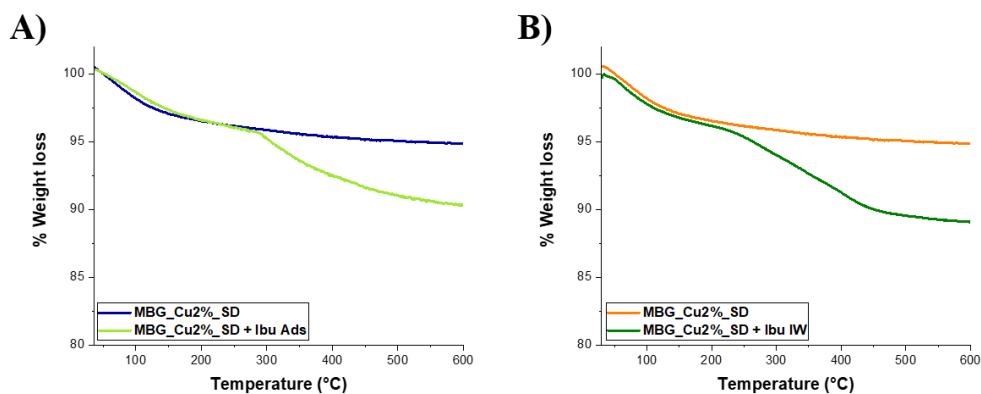
Figure 3.51 TGA thermograms of (A) MBG_Cu2%_SD and MBG_Cu2%_SD + Ibu Ads; (B) MBG_Cu2%_SD and MBG_Cu2%_SD + Ibu IW.

Fig. 3.25 reported the FT-IR spectra of copper containing MBGs before and after ibuprofen loading. For both samples, the typical adsorption bands of H-bonded hydroxyls (stretching vibration) are evident in the range of 3750–3000 cm^{-1}. The spectra of MBG_Cu2%_SD + Ibu Ads and MBG_Cu2%_SD + Ibu IW showed the typical bands of ibuprofen molecule: the absorption bands ascribed to C-H stretching modes at 2933 and 2871 cm^{-1} and the signals due to C-H bending vibrations at 1465 and 1430 cm^{-1}. The two bands appeared at 1556 and 1408 cm^{-1} are ascribed to the asymmetric (ν_{as}) and symmetric (ν_s) stretching vibration of the carboxylate group COO^-, respectively [24]. As widely reported in the literature [26,27], the loading of the drug in the amorphous state could increase the drug dissolution rates and solubility.
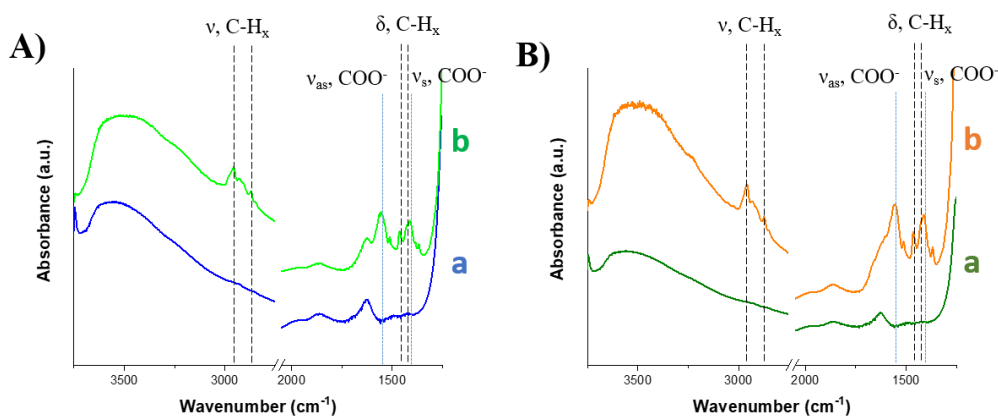
Figure 3.52 FTIR spectra of (A) MBG_Cu2%_SD (a), and MBG_Cu2%_SD + Ibu Ads (b); (B) MBG_Cu2%_SD (a), and MBG_Cu2%_SD + Ibu IW (b).

Hence, DSC and XRD analysis of ibuprofen-loaded samples were conducted to assess the amorphous state of the drug and exclude the presence of large crystalline aggregates. DSC thermograms of Ibu as such and of MBG_Cu2%_SD + Ibu Ads sample and MBG_Cu2%_SD + Ibu IW are reported in Fig. 3.26: the single endothermic melting peak at 76 °C, observed only for ibuprofen as such,
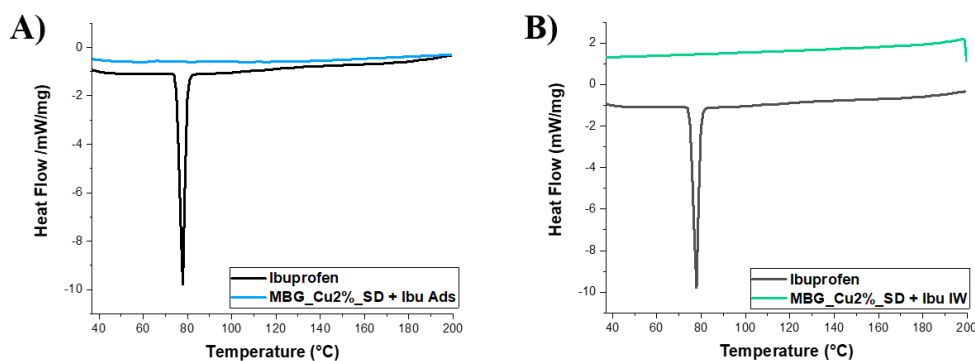
Figure 3.53 DSC thermograms of ibuprofen and MBG_Cu2%_SD + Ibu Ads (A) and ibuprofen and MBG_Cu2%_SD + Ibu IW (B).

corresponds to crystal phase melting. The absence of this peaks in the ibuprofen loaded sample thermograms confirms the non-crystalline state of ibuprofen into the mesopores.

The amorphous state of the drug was further assessed by XRD analysis (Fig. 3.27). XRD pattern of ibuprofen powder showed several characteristic X-ray diffraction peaks, which completely disappeared in the MBG_Cu2%_SD + Ibu Ads and MBG_Cu2%_SD + Ibu IW spectra. In accordance with DSC data, XRD analysis strongly suggested that ri-crystallization of the drug did not occur inside the pores upon solvent evaporation during the incorporation process, as already notified for the corresponding MBG-SG samples.
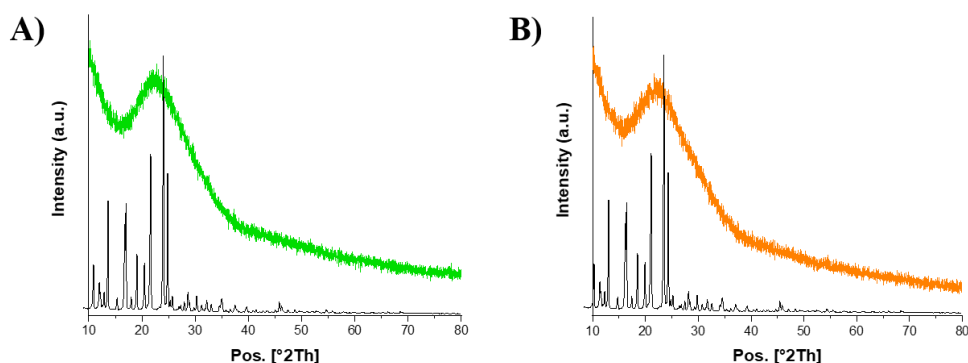
Figure 3.54 XRD patterns of (A) ibuprofen and MBG_Cu2%_SD + Ibu Ads and (B) ibuprofen and MBG_Cu2%_SD + Ibu IW.

3.2.3.2b Bioactive behaviour of MBG_Cu2%_SD + Ibu Ads and MBG_Cu2%_SD + Ibu IW in SBF

FE-SEM observations clearly confirmed that the bioactive behaviour of MBG_Cu2%_SD + Ibu Ads and MBG_Cu2%_SD + Ibu IW was retained when soaking in SBF after the ibuprofen loading, irrespective of the loading procedure. In fact, a rough layer of globular agglomerates on the surface of the particles appeared after just 1 day of soaking. After 7 days, the particles resulted completed covered by a compact layer of needle-like nanocrystals, as shown in Figure 3.28 A1 for MBG_Cu2%_SD + Ibu Ads and in figure 3.28 A2 for MBG_Cu2%_SD + Ibu IW. The presence of HA crystals has been revealed by the EDS analysis performed on powders which evidenced a Ca/P ratio close to 1.7, typical of HA [11,12].

The formation of crystalline HA after the bioactivity test has been evaluated also by wide-angle XRD analysis performed on the MBG particles after 7 days of soaking in SBF. Figure 3.28 B1 and B2 showed marked peaks observed for both MBG_Cu2%_SD + Ibu Ads and MBG_Cu2%_SD + Ibu IW at 25.87° and 31.73° (2θ value) and other less intense reflections at 49.39 ° (2θ value) which matched with the hydroxyapatite reference (01-089-6440). As already notified for the MBG_Cu2%_SG + Ibu Ads and MBG_Cu2%_SG + Ibu IW samples, the ibuprofen loading does not hinder the bioactive behaviour typical of the mesoporous bioactive glasses.
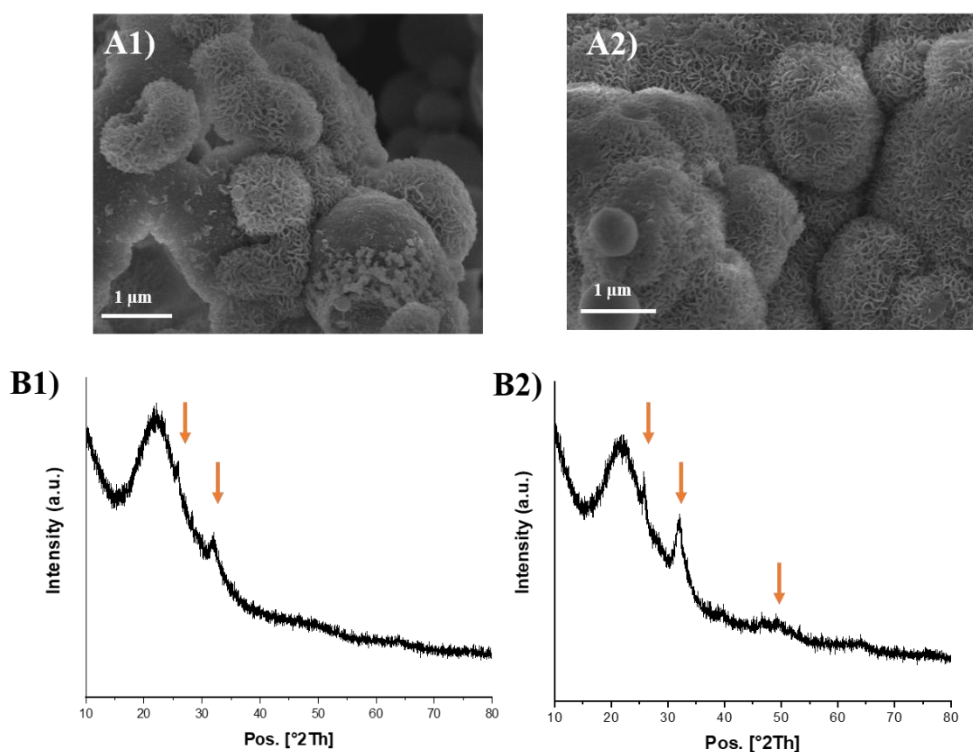
Figure 3.55 FE-SEM observations of (A1) MBG_Cu2%_SD + Ibu Ads and (A2) MBG_Cu2%_SD + Ibu IW; Wide-angle XRD of (B1) MBG_Cu2%_SD + Ibu Ads and (B2) MBG_Cu2%_SD + Ibu IW after 7 days of soaking in SBF.

3.2.3.2c Copper release from MBG_Cu2%_SD + Ibu Ads and MBG_Cu2%_SD + Ibu IW in Tris HCl

The concentration of copper ions released from MBG_Cu2%_SD + Ibu Ads and MBG_Cu2%_SD + Ibu IW powder after soaking in Tris HCl medium, following the protocol described in section 2.9.1, is reported in Figure 3.29 A and B, respectively.

A sustained release profile is observed up to 14 days of incubation with a final released concentration of about 3.8 ppm for MBG_Cu2%_SD + Ibu Ads and 3.9 ppm for MBG_Cu2%_SD + Ibu IW. As previously observed for the corresponding non-loaded sample (MBG_Cu2%_SD), the more sustained release compared to the MBG_Cu2%_SG + Ibu Ads and MBG_Cu2%_SG + Ibu IW samples can be ascribed to the higher reactivity toward surface dissolution/re-precipitation reactions, that causing a slower diffusion of the ions from the particles to the medium. The drug loading within the porous structure seems to not interfere with the capability to release therapeutic ions through ion-exchange reactions.
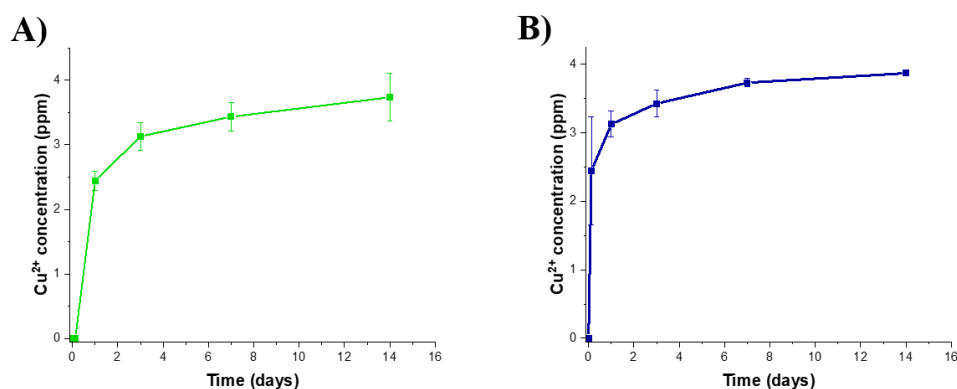
Figure 3.56 Cu²⁺ release profile of (A) MBG_ Cu2%_SD + Ibu Ads and (B) MBG_Cu2%_SD + Ibu IW in Tris HCl.

3.2.3.2d Ibuprofen release from MBG_Cu2%_SD + Ibu Ads and MBG_Cu2%_SD + Ibu IW in Tris HCl

Ibuprofen release test was performed in Tris-HCl up to 48 hours. Figure 3.30 showed the release profile of ibuprofen from MBG_Cu2%_SD + Ibu Ads and MBG_Cu2%_SD + Ibu IW powders, revealing that the total amount of loaded drug was released in the first hour of soaking in the medium. The burst release is then followed by a plateau till the end of the test (48h).

As already reported for the SG samples, the weak interactions between the ibuprofen and the silica surface enhance the fast diffusion of the drug in the medium [32]. Moreover, in addition to the particle size, also the pore diameter can act as drug release modulator. In fact, an increase in pore diameter has been proved to increase the drug release rate. Despite the bigger size of the MBG-SD samples, compared to the corresponding MBG-SG samples, that would assume a slower release kinetics, the bigger pore diameter (8-10 nm, compared to the 4 nm of the SG samples) is responsible of the fast drug release. The mesopores are accessible to the medium, increasing the drug diffusion from the pores to the solution, thus allowing the release of the ibuprofen [31].
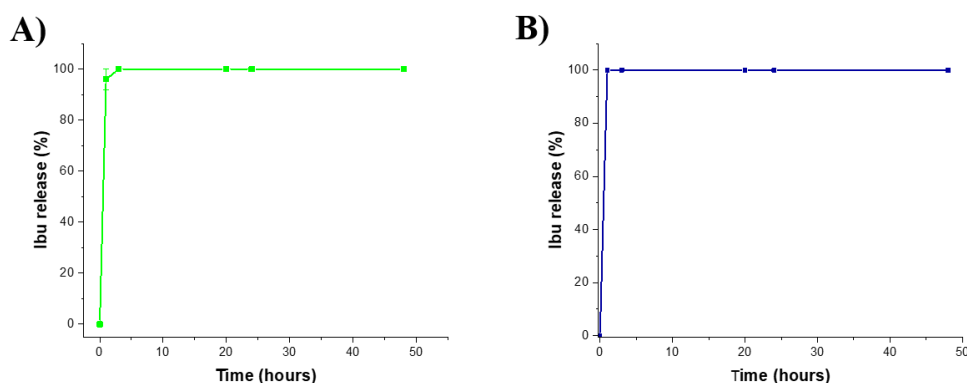
Figure 3.57 Ibuprofen release profile of (A) MBG_Cu2%_SD + Ibu Ads and (B) MBG_Cu2%_SD + Ibu IW in Tris HCl.

3.2.4 Polyelectrolyte layer by layer deposition on Copper-containing MBG

As notified in the previous sections, all the investigated samples show a burst release of both copper and ibuprofen in the first hours of soaking. In order to overcome this MBGs drawbacks and produce drug delivery systems able to differently modulate the release kinetic of both copper ions and ibuprofen, Cu-MBGs were prepared through the above mentioned synthesis approaches and the surface was modified by layer-by-layer deposition of polyelectrolyte molecules, exploiting their opposite charges. The multi-layered surface was obtained by following two different routes, well explained in the section 3.4.1 of the *"materials and methods"* chapter.

In the first strategy involves the assembly of three layers (chitosan, alginate and chitosan) and, successively, ibuprofen was loaded by incipient wetness impregnation, as already reported in section 3.4.1. On contrary, in the second strategy, alginate was replaced by the ibuprofen, by exploiting the ibuprofen negative charge (COO⁻), able to electrostatically interact with the positive charged ammino groups of chitosan.

3.2.4.1 Copper-containing MBG layered with Chitosan, Alginate and Chitosan: Cu2%_SG_CAC_Ibu and Cu2%_SD_CAC_Ibu

In this section, the results concerning the characterization of polyelectrolyte multi-layered copper-containing MBG-SG and MBG-SD obtained through the assembly of three layers (chitosan, alginate and chitosan) and successively loaded with ibuprofen are reported. The polyelectrolyte multi-layered assembly has been conducted by following a method reported by Zhou et al. [13,34] while the

ibuprofen was loaded by using the IW technique. The obtained sample will be hereafter referred as Cu2%_SG_CAC_Ibu and Cu2%_SD_CAC_Ibu.

3.2.4.1a Morphological, structural and chemical characterization of Cu2%_SG_CAC_Ibu and Cu2%_SD_CAC_Ibu

FE-SEM images of Cu2%_SG_CAC_Ibu and Cu2%_SD_CAC_Ibu are reported in Figure 3.31A and 3.31B. Cu2%_SG_CAC_Ibu showed nanoparticles with a size ranging between 100 and 200 nm. Compared to the bare samples, a slight increase in particle size has been observed, justified by the build-up of multi-layers on the particles surface, due to the adsorption of the chitosan and alginate layers.
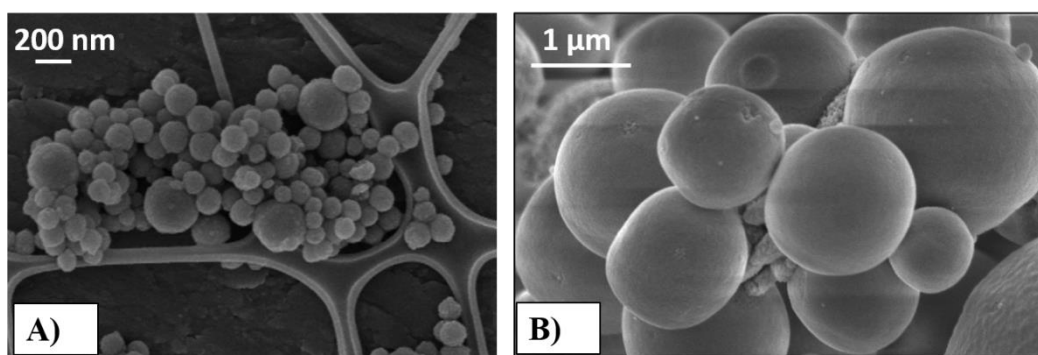
Figure 3.58 FE-SEM image of (A) Cu2%_SG_CAC_Ibu and (B) Cu2%_SD_CAC_Ibu.

As reported in literature, the layer thickness when chitosan and alginate are deposited on a silicon wafer is expected to increase linearly with the number of layers of about 10 nm [35–37] evaluated by ellipsometric measurements. Based on these reference analyses, the growth in size of the CAC system is expected to be around 30 nm but the effective layer thickness cannot be clearly highlighted by the FE-SEM observations due to instrumental limitations. In fact, the thickness of the multilayer system is usually evaluated by ellipsometric measurements or Atomic Force Microscopy (AFM) after the deposition on a flat substrate, which allows to homogeneously cover the material surface [39]. For these reasons, the assessment of the homogeneous coating on the spherical surface of the particles and the coating thickness cannot be clearly evaluated by using FE-SEM images.

FE-SEM images of Cu2%_SD_CAC_Ibu showed microspheres with a size ranging between 1 and 5 μm. As far as the Cu2%_SD_CAC_Ibu is concerned, differently from the Cu2%_SG_CAC_Ibu samples, the increasing in particle size could not be evidenced, due to the bigger size of the SD particles. As mentioned above, since the layer thickness is expected to increase linearly with the number of layer of about 10 nm [35–37], the growth in size due to the build-up of multi-layers on these microsized particles cannot be clearly discerned.
FE-SEM observations confirmed that the LbL procedure and the subsequent

ibuprofen loading do not significantly affect the morphology of both the particles. The chemical composition of copper-containing MBGs, evaluated via ICP analysis after the dissolution of the particles in a mixture of nitric and hydrofluoric acids, resulted very similar to those reported for not-loaded samples.

The stepwise deposition of chitosan, alginate and chitosan layers was monitored by measuring the ζ-potential upon the addition of each polyelectrolyte layer. Along with confirming the presence and coverage of the polymer coating, ζ-potential measurements allow to assess the stability of particle suspensions. In fact, ζ-potential values above +20 mV or around -20mV can be usually considered as indication of stability and enhanced uniformity, ascribed to the strong repulsion forces among particles, allowing to prevent aggregation [40]. As shown in figure 3.32 and reported in table 3.5, for both samples, after the first deposition of chitosan, the surface charge moved from negative values (due to the deprotonation of surface silanols) to positive values, due to the positively charged amine groups of the chitosan. The deposition of the second layer of alginate induces a charge inversion on the surface, due to the negatively charged carboxylate groups of alginate, followed by the last charge inversion after the deposition of the third layer of chitosan.

The last layer of chitosan showed a positive charge, confirming the occurrence
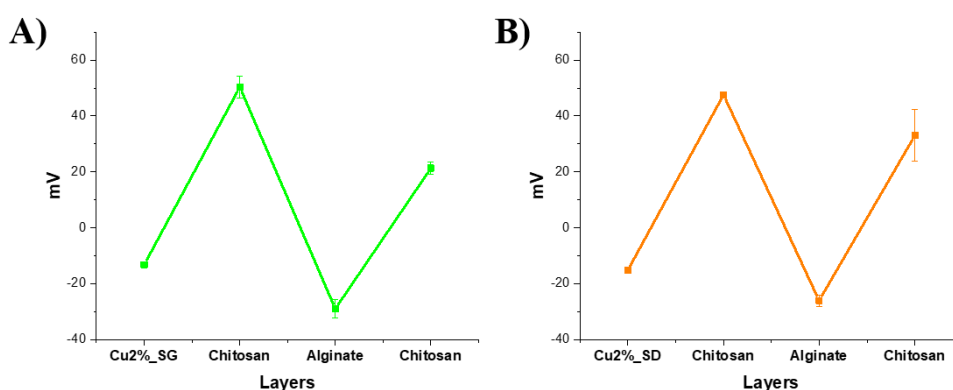
Figure 3.59 ζ-potential measurement of (A) Cu2%_SG_CAC_Ibu and (B) Cu2%_SD_CAC_Ibu after each layer deposition.

of the stepwise deposition driven by the electrostatic interactions. In addition, the high values measured for both the Cu2%_SG_CAC_Ibu and Cu2%_SD_CAC_Ibu samples, indicate the high stability of the particle suspension.

Table 3.14 ζ-potential values of Cu2%_SG_CAC + Ibu and Cu2%_SD_CAC + Ibu after each layer deposition.

	Zeta Potential (mV)
Cu2%_SG	-13 ± 0.6

Chitosan	50 ±3.8
Alginate	-29 ± 3.2
Chitosan	21 ± 2.2
Cu2%_SD	-15 ± 1.2
Chitosan	47 ± 1.2
Alginate	-26 ± 2.1
Chitosan	33 ± 9.3

3.2.4.1b Bioactive behaviour of Cu2%_SG_CAC_Ibu and Cu2%_SD_CAC_Ibu in SBF

FE-SEM images clearly confirmed that the layer by layer deposition and the successive ibuprofen loading do not hinder the bioactive behaviour of Copper-containing MBG samples. Compared to the corresponding bare samples, a slowing delay in the deposition of the hydroxyapatite layer has been observed for both the samples; in fact, a rough layer of globular agglomerates on the surface of the particles appeared after 7 days of soaking (Figure 3.33 A1 and B1), and not after just 1 days, as observed for the corresponding bare samples. As shown in figure 3.33 A2 and B2, the presence of HA crystals has been revealed by the EDS analysis performed on powders which evidenced a Ca/P ratio close to 1.7, typical of HA [11,12].

The slowdown in the HA deposition is ascribed to the presence of the polyelectrolyte multi-layered coating; in fact, the inter-diffusion of the shorter polymer chains of alginate into the longer polymer chains of chitosan, due to the

Element	Atomic %
O	65.90
Si	25.16
P	3.52
Ca	5.42

Element	Atomic %
O	70.63
Si	18.76
P	3.63
Ca	6.99
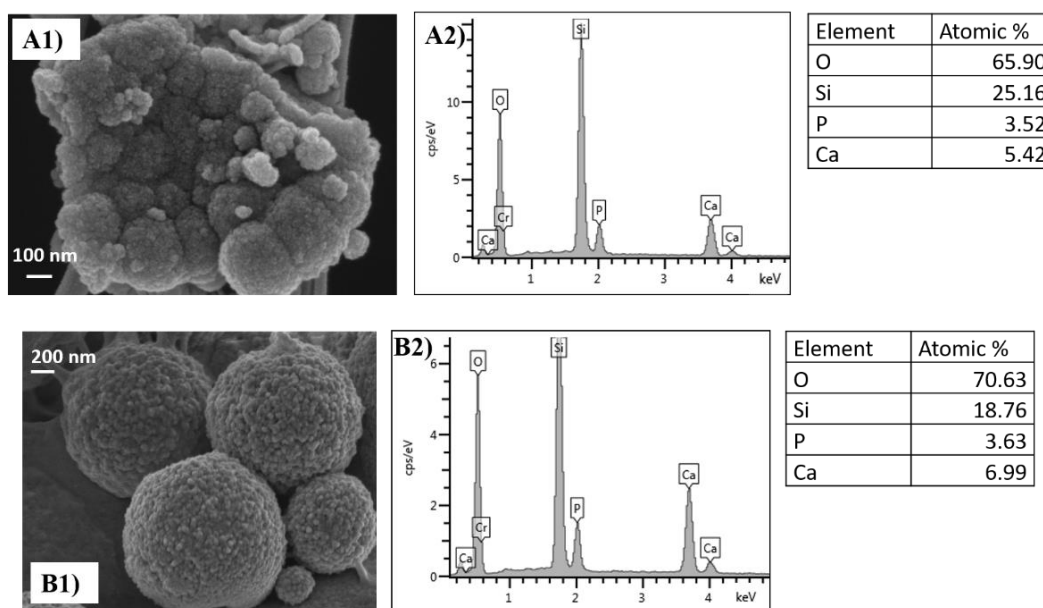
Figure 3.60 FE-SEM observation (A) and EDS spectrum (A1) of Cu2%_SG_CAC_Ibu and FE-SEM observation (B) and EDS spectrum (B1) of Cu2%_SD_CAC_Ibu after 7 days of soaking in SBF.

possibility of molecular rearrangements subsequent to first contact [38], leads to a formation of a denser network [36,38]. This dense polymer network is expected to hinder to some extent the ionic exchange reactions, involved at the interface of the MBGs and the medium and essential to start the HA formation (see section 1.3 in the "*state of the art*" chapter).

Despite this delay, both the Cu2%_SG_CAC_Ibu and Cu2%_SD_CAC_Ibu retained their ability to promote the HA formation, essential feature for promoting bone regeneration.

3.2.4.1c Copper release from Cu2%_SG_CAC_Ibu and Cu2%_SD_CAC_Ibu in Tris HCl

The copper ion release of Cu2%_SG_CAC_Ibu and Cu2%_SD_CAC_Ibu was evaluated in Tris-HCl medium (pH 7.4); samples were incubated at 37°C up to 14 days and, at selected time points (1h, 3h, 5h, 8h, 24 h, 2 d, 3 d, 8 d, 10 d, 14 d) the suspension was centrifuged, and the supernatant withdrawn and analysed by ICP-AES.

As shown in figure 3.34, a significantly prolonged release profile up to 14 days is observed for both the Cu2%_SG_CAC_Ibu and Cu2%_SD_CAC_Ibu samples,
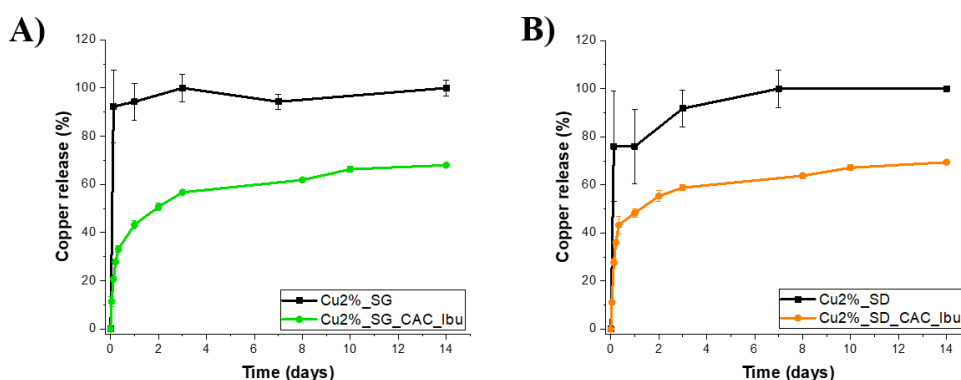
Figure 3.61 Copper release profile of (A) Cu2%_SG_CAC_Ibu in Tris-HCl compared to the bare sample Cu2%_SG and (B) Cu2%_SD_CAC_Ibu in Tris-HCl compared to the bare sample Cu2%_SD.

evidencing that just the 30% of the total amount of copper is released after 1 hour, compared to the 95% and 78% of total amount released by Cu2%_SG and Cu2%_SD, respectively. The slower copper release rate observed for Cu2%_SG_CAC_Ibu and Cu2%_SD_CAC_Ibu could be ascribed to the slowed down diffusion of the medium throughout the polymer layers [41], since the polyelectrolyte multilayer, acting as a barrier, is expected to hinder the contact between the ion and the release medium. The build-up of multi-layers on Cu-containing MBGs successfully decreased the undesirable initial burst release of Cu^{2+} species typically observed for particles as such: in fact, after 1 hour incubation in similar releasing conditions, Cu2%_SG_CAC_Ibu and Cu2%_SD_CAC_Ibu

released an amount of copper ions approximately 80 % and 78 % lower compared to the corresponding bare MBG particles, confirming the ability of the multi-layered coating to limit the typical burst release effect observed for the bare MBG particles. In addition, at the end of the experiment (14 days), Cu2%_SG_CAC_Ibu and Cu2%_SD_CAC_Ibu particles are still present in the medium and, as observed in the figure 3.34, the release kinetics does not reach the plateau. These observations could suggest that the dense polyelectrolyte multilayer effectively acts as a barrier, limiting the contact of the particles surface with the medium, thus slow downing the particles dissolution. For this reason, after 14 days the system is still capable to release copper ions, further confirming that the presence of the multi-layered coating can be exploited to produce multifunctional devices with a sustained release over 14 days.

3.2.4.1d Ibuprofen release from Cu2%_SG_CAC_Ibu and Cu2%_SD_CAC_Ibu in Tris HCl

Ibuprofen release test was performed in Tris-HCl up to 24 hours. Figure 3.35 showed the release profile of ibuprofen from Cu2%_SG_CAC_Ibu and Cu2%_SD_CAC_Ibu powders compared to the corresponding bare samples. An evident sustained release profile of loaded drug up to 1 day of soaking in the release medium is observed, thus confirming the ability of the multi-layered coating to modulate the burst release notified for the bare sample. In fact, compared to the release profile of the corresponding bare samples in which the total amount of loaded ibuprofen was released in the first hour, only the 38% and 25% of the total
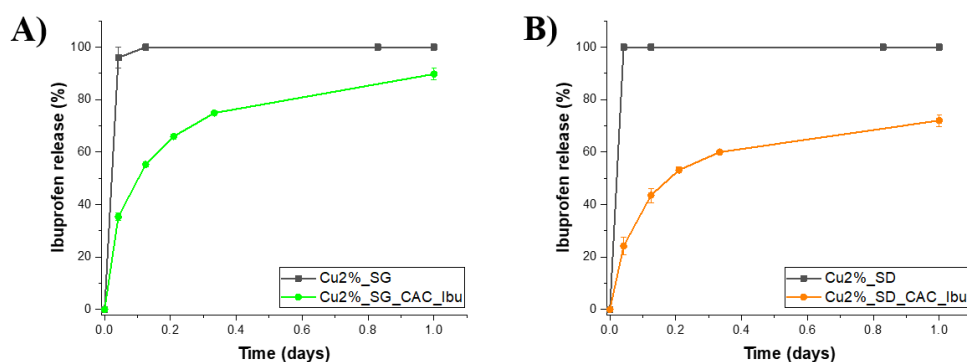
Figure 3.62 Ibuprofen release profile of (A) Cu2%_SG_CAC_Ibu in Tris-HCl compared to the bare sample Cu2%_SG and (B) Cu2%_SD_CAC_Ibu in Tris-HCl compared to the bare sample Cu2%_SD.

amount of loaded drug has been released after one hour of soaking from Cu2%_SG_CAC_Ibu and Cu2%_SD_CAC_Ibu, respectively, suggesting a slowdown in the release rate. The modulation in release rate could be ascribed to the electrostatic interactions between the drug and the polyelectrolyte multilayers; in fact, the strong ionic interactions between the amine groups of the chitosan and the carboxyl groups of the ibuprofen could potentially hinder the diffusion pathways of ibuprofen among the layers, thus delaying the contact between the drug and the release medium, as already notified for the copper release. In addition, the

presence of the polyelectrolyte multilayer increases the diffusional distance, thereby causing the tendency for the delayed release observed for the CAC samples.

Based on these promising results, the Layer by Layer coating could be considered a potential approach to modulate the release of the drug over a longer time scales, depending on the number of deposited layers, preventing the initial burst release from the MBGs.

3.2.4.2 Copper-containing MBGs layered with Chitosan, Ibuprofen and Chitosan: Cu2%_SG_CIC Cu2%_SD_CIC

In this section, the results concerning the characterization of polyelectrolyte multi-layered copper-containing MBG-SG and MBG-SD obtained through the assembly of chitosan, ibuprofen and chitosan are presented. The polyelectrolyte multi-layered assembly has been conducted by modifying the method reported by Zhou et al. [13,34], in which the alginate has been replaced by the ibuprofen, and the obtained sample will be hereafter referred as Cu2%_SG_CIC and Cu2%_SD_CIC.

3.2.4.2a Morphological, structural and chemical characterization of Cu2%_SG_CIC Cu2%_SD_CIC

Figure 3.36 show the FE-SEM observations of Cu2%_SG_CIC (Fig. 3.36 A) and Cu2%_SD_CIC (Fig 3.36 B). Concerning the Cu2%_SG_CIC, as already notified for the Cu2%_SG particle covered with CAC, nanoparticles with a size ranging between 100 and 300 nm were obtained, showing the same morphology of the corresponding bare samples Cu2%_SG. In some isolated cases, the build-up of multi-layers on the particles surface was accompanied by a slight increase in
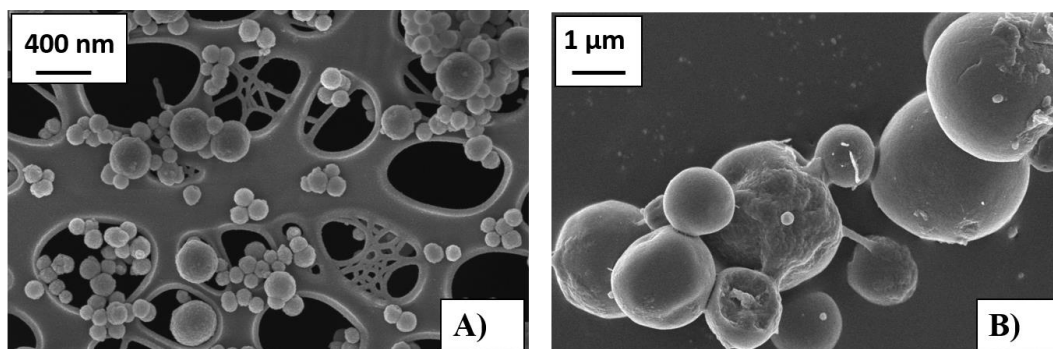
Figure 3.63 FE-SEM images of (A) Cu2%_SG_CIC and (B) Cu2%_SD_CIC.

particle size, due to the adsorption of the polyelectrolyte multilayers, as observed for the Cu2%_SG_CAC_Ibu sample [36]. Since the growth in size of chitosan and ibuprofen layers has never been previously reported in the literature, the layer

thickness of the CIC samples cannot be clearly evaluated by FE-SEM observations. FE-SEM images of Cu2%_SD_CIC showed microspheres with a size ranging between 1 and 5 μm, without any evidence of the increasing in particle size compared to the bare sample. As far as the Cu2%_SD_CIC is concerned, differently from the Cu2%_SG_CIC samples, the increasing in particle size could not be evidenced, due to the bigger size of the SD particles.

Since the morphology of the analysed particles resulted unaffected, as previously observed also for the CAC modified particles, irrespective of the adopted procedures, the LbL deposition do not significantly interfere with the microparticle morphology. In addition, the chemical composition of copper-containing MBGs, evaluated via ICP analysis after the dissolution of the particles in a mixture of nitric and hydrofluoric acids, resulted very similar to those reported for not-loaded samples.

In order to evaluate the correct alternative deposition of chitosan and ibuprofen, the ζ-potential was measured after the addition of each polyelectrolyte layer. Figure 3.37, and the corresponding recorded values reported in table 3.6, confirmed that after the first deposition of chitosan, the surface charge moved from negative values (due to the silanol-rich surface) to positive values, due to the positively charged amine groups of the chitosan. The values become again negative, upon the deposition of the second layer of ibuprofen, due to the negative carboxylate charge, followed by the last charge inversion after the deposition of the third layer of chitosan. The last layer of chitosan showed a positive charge, confirming that the deposition in a stepwise fashion driven by alternating electrostatic interactions.

Along with confirming the presence and coverage of the polymer coating, ζ-
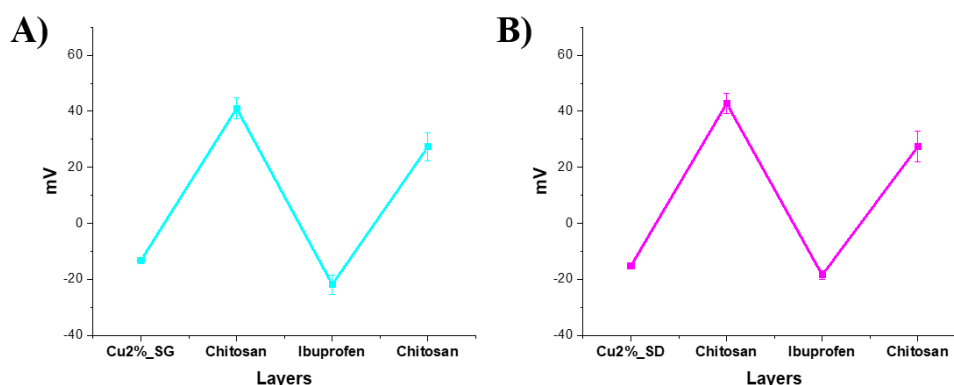
Figure 3.64 ζ-potential measurement of (A) Cu2%_SG_CIC and (B) Cu2%_SD_CIC after each layer deposition.

potential measurements allow to assess the stability of particle suspensions. In fact, ζ-potential values above +20 mV or around -20mV can be usually considered as indication of stability and enhanced uniformity, ascribed to the strong repulsion forces among particles, allowing to prevent aggregation [40].

The high values of ζ-potential obtained for both the Cu2%_SG_CIC and Cu2%_SD_CIC samples, indicates the high stability of the particle suspension, al already notified for the samples coated with the CAC multilayers.

Table 3.15 ζ-potential values of Cu2%_SG_CIC and Cu2%_SD_CIC after each layer deposition.

	Zeta Potential (mV)
Cu2%_SG	-13 ± 0.6
Chitosan	41 ± 3.8
Ibuprofen	-21 ± 3.4
Chitosan	27 ± 5.0
Cu2%_SD	-15 ± 1.2
Chitosan	43 ± 3.5
Ibuprofen	-18 ± 1.5
Chitosan	27 ± 5.4

3.2.4.2b Bioactive behaviour of Cu2%_SG_CIC Cu2%_SD_CIC in SBF

With the aim to investigate the bioactive behaviour of Cu2%_SG_CIC Cu2%_SD_CIC, the particles were soaked in SBF and their ability to induce the formation of a hydroxyapatite layer on their surface was evaluated. FE-SEM images evidenced that hydroxyapatite formation occurred after only 1 day of soaking, resulting in a compact layer of needle-like nanocrystals covering the particle surface. The agglomerates of apatite-like phase increased in size during the test, causing the full embedding of both the particle surface after 7 days of soaking, as highlighted in the figure 3.38 A1 and B1.

EDS analysis, reported in figure 3.38 A2 and B2, further confirms the presence of HA, revealed by the appearance of phosphorous and a Ca/P ratio very close to 1.7, the typical value reported in the literature for hydroxyapatite. Unlike the layer by layer deposition strategy reported previously (Cu2%_SG_CAC_Ibu and Cu2%_SD_CAC_Ibu samples), the polyelectrolyte multi-layered coating based on chitosan, ibuprofen and chitosan seems to not delay the deposition of the hydroxyapatite layer, which results unaffected compared to the corresponding bare samples (see section 3.2.1b and 3.2.2b). This behaviour could be ascribed to the low molecular weight of the ibuprofen, that compared to the steric hindrance of alginate, lead to a formation of a more open network. This behaviour could be

explained from different modes of reaction between ibuprofen/chitosan and alginate/chitosan. In fact, some extents of ibuprofen could stick to chitosan on first contact (diffusion limited mode of interaction) limiting the molecular rearrangement [38], and thus leading to a more open network which allows the faster ion exchanges essential for the HA formation. On contrary, the diffusion of alginate into the longer polymer chains of chitosan allows molecular rearrangements subsequent to first contact, forming a denser network [36], responsible of the delay in the ionic exchange reaction.

Both Cu2%_SG_CIC and Cu2%_SD_CIC retained their ability to induce HA formation, allowing to preserve an essential feature of this material for application in bone regeneration processes.
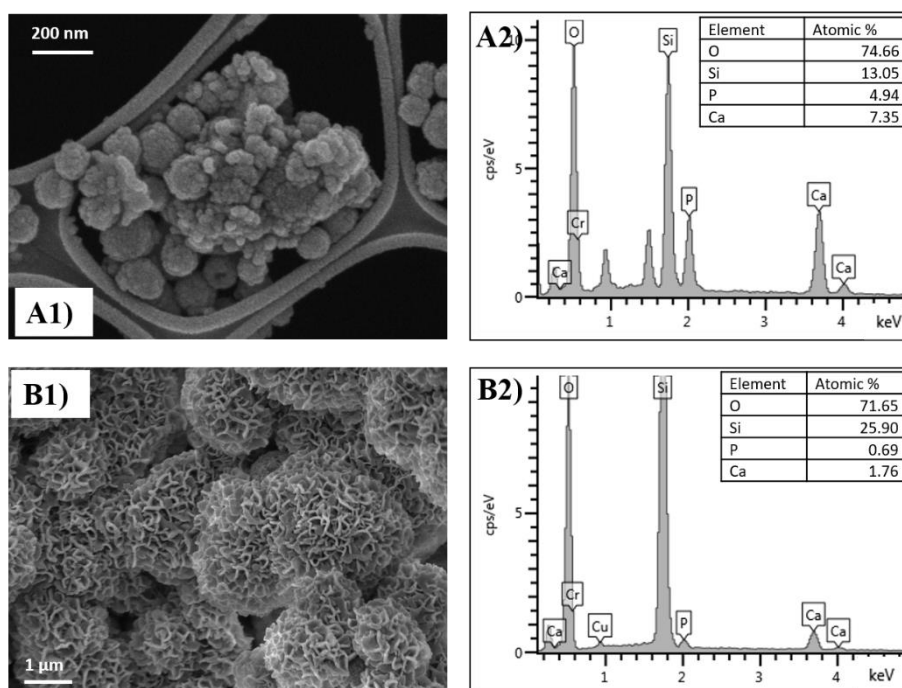
Figure 3.65 FE-SEM observation (A) and EDS spectrum (A1) of Cu2%_SG_CIC and FE-SEM observation (B) and EDS spectrum (B1) of Cu2%_SD_CIC after 7 days of soaking in SBF.

3.2.4.2c Copper release from Cu2%_SG_CIC Cu2%_SD_CIC in Tris HCl

The copper release profile of Cu2%_SG_CIC Cu2%_SD_CIC was evaluated in Tris-HCl medium (pH 7.4) and compared to the copper release profile of the bare samples; samples were incubated at 37°C up to 14 days and, at selected time points (1h, 3h, 5h, 8h, 24 h, 2 d, 3 d, 8 d, 10 d, 14 d) the suspension was centrifuged and the supernatant withdrawn and analysed by ICP-AES.

As shown in figure 3.39, a significantly prolonged release profile up to 14 days is observed for both samples. In particular, Cu2%_SG_CIC (Figure 3.39 A) evidenced a slower release kinetics compared to the bare Cu2%_SG, evidencing that just the 40% of the total amount of copper is released after 3 hours, compared to the burst release observed for the Cu2%_SG sample follows by a sustained release of copper up to 14 days. As far as the Cu2%_SD_CIC sample is concerned (Figure 3.39 B), the effect of the multi-layered coating can be observed in the first hour, showing that the 45% of the total amount of copper is released from Cu2%_SD_CIC compared to the 80% released from the Cu2%_SD. After the first hours, the release kinetics results to be similar to those observed for the bare sample. As already notified for the Cu2%_SG_CAC_Ibu and Cu2%_SD_CAC_Ibu, the slower copper release rate could be associated to the long path length and the amount of time needed for the ions to diffuse into the polyelectrolyte layers, which act as a barrier, thus hindering the contact between the ion and the release medium [41].

It is worth to highlight that the release kinetics observed for the Cu2%_SG_CAC_Ibu and Cu2%_SD_CAC_Ibu results slower compared to the Cu2%_SG_CIC and Cu2%_SD_CIC and this behaviour can be ascribed to the denser polymer network obtained with chitosan/alginate/chitosan deposition, which hinders more extensively the contact between the particles and the medium. On contrary, the more open network of the chitosan/ibuprofen/chitosan coating allows an easier medium diffusion and thus copper release.
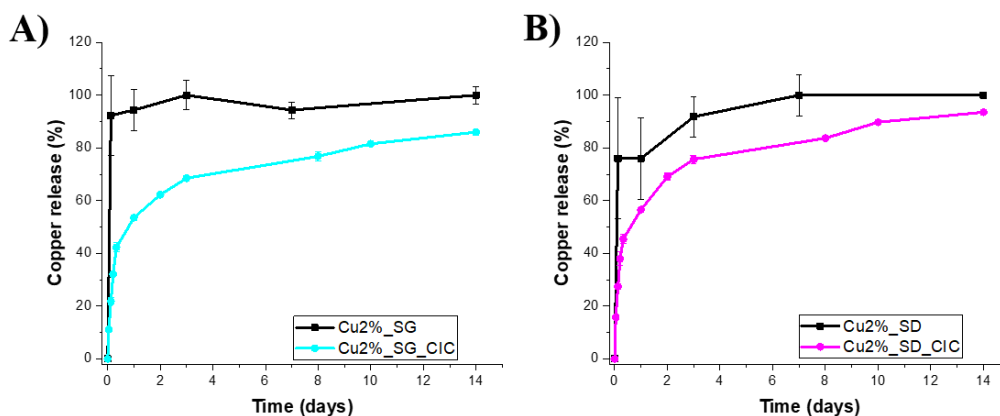
Figure 3.66 Copper release profile of (A) Cu2%_SG_CIC in Tris-HCl compared to the bare sample Cu2%_SG and (B) Cu2%_SD_CIC in Tris-HCl compared to the bare sample Cu2%_SD.

As already observed for the CAC samples, the build-up of multi-layers on Cu-containing MBGs successfully decreased the undesirable initial burst release of Cu^{2+} species typically observed for particles as such: in fact, after 1 hour incubation in similar releasing conditions, Cu2%_SG_CIC and Cu2%_SD_CIC released an

amount of copper ions approximately 80 % and 70 % lower compared to the corresponding bare MBG particles, confirming the ability of the multi-layered coating to limit the typical burst release effect observed for the bare MBG particles. In addition, at the end of the experiment (14 days), as observed in the figure 3.39, the release kinetics does not reach the plateau, suggesting that the system is still capable to release copper ions after 14 days of incubation. This consideration is further confirmed by the presence of the particles in the release medium at the end of the soaking. These observations could suggest that the polyelectrolyte multilayer, acting as a barrier, limited the contact of the particles surface with the medium, thus slow downing the particles dissolution and, as consequence, the copper release.

3.2.4.2d Ibuprofen release from Cu2%_SG_CIC Cu2%_SD_CIC in Tris HCl
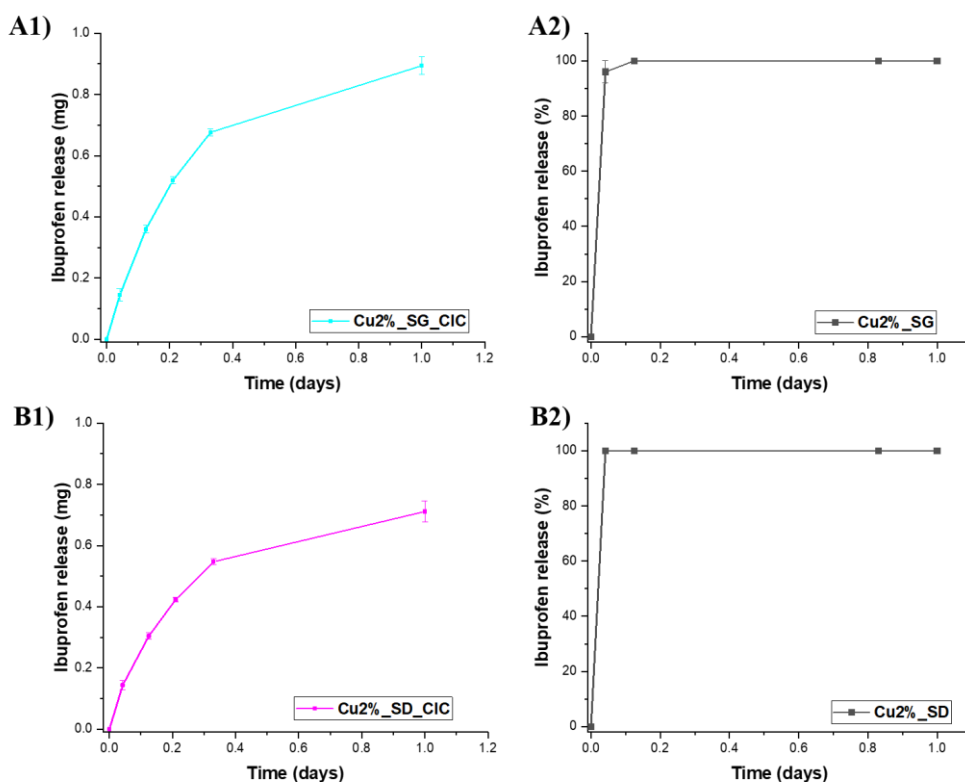
Figure 3.67 Ibuprofen release profile of (A1) Cu2%_SG_CIC in Tris-HCl compared to the bare sample Cu2%_SG (A2) and (B1) Cu2%_SD_CIC in Tris-HCl compared to the bare sample Cu2%_SD (B2).

The release of ibuprofen was evaluated after soaking in Tris-HCl up to 24 hours. Figure 3.40 showed the release profile of ibuprofen from Cu2%_SG_CIC and Cu2%_SD_CIC powders in terms of milligrams of released ibuprofen overtime. In fact, the final amount of ibuprofen effectively incorporated cannot be

evaluated both by the TGA and UV-Vis techniques, due to the presence of chitosan, which hinders the correct quantification of ibuprofen.

An evident sustained release profile of loaded drug up to 1 day of soaking in the release medium is observed, thus confirming the ability of the multi-layered coating to modulate the burst release notified for the bare sample. As supposed for the CAC coated samples, the modulation in release rate could be ascribed to the stronger hydrogen bonding between the amino group of the chitosan and carboxylic acid moiety of ibuprofen.

In addition, since the drug release was a mainly diffusion-controlled process, as confirmed by many previous studies [44–46], the presence of a multi-layered coating can hinder the contact between the drug and the medium, thus delaying the diffusion of the ibuprofen into the release medium. It was worth noticing that the release kinetics of the CIC samples is slower compared to the bare samples (figure 3.40 A2 and B2), demonstrating that the presence of hydrogen bonding between chitosan and ibuprofen and the presence of the multi-layered coating which act as a barrier between the drug and the medium could effectively modulate the ibuprofen release rate. The ability of this multilayer strategy to avoid the burst release notified for the bare samples further confirms the feasibility of the use of the layer by layer deposition as promising technique to design drug delivery system able to modulate the drug release from the MBGs.

3.2.5 Hybrid formulation based on Copper-containing MBGs incorporated into a thermosensitive hydrogel

Part of the work described in this chapter has been previously published in [4,5].

Since MBGs alone are not exploitable as long-term drug delivery systems for orthopaedic applications, due to the strong burst release of the therapeutic species once in contact with body fluids, and the difficulties related to their administration at the pathological site (*i.e.* bone fracture cavity) in the form of powder, their combination with hydrogels able to modulate the release kinetics and/or to act as a vehicle phase to the pathological site has been investigated. In particular, during this PhD work, Copper-containing MBGs loaded with Ibuprofen have been incorporated into an injectable Poly(ether urethane) (PEU) based thermosensitive hydrogel developed by *Professor Ciardelli's group (DIMEAS, Politecnico di Torino, Italy)*.

3.2.5.1 Copper-containing MBGs incorporated into the PEU hydrogel: PEU_MBG_Cu2%_SG_Ibu and PEU_MBG_Cu2%_SD_Ibu

Copper-containing MBGs loaded with Ibuprofen were prepared by following the procedures reported in section 2.4.2 and Ibuprofen was successively loaded by using the incipient wetness method. The so-prepared particles were fully characterized, showing the peculiar features well described in the previous sections. After the characterization, both MBG_Cu2%_SG_Ibu and MBG_Cu2%_SD_Ibu were encapsulated into Poly(ether urethane) (PEU) based thermosensitive hydrogel produced by Prof. Gianluca Ciardelli's group with final particle concentration of 20 mg/mL. Pure PEU sol-gel systems and PEU hydrogels loaded with Ibuprofen were also prepared as control samples. Loading of Ibu in PEU sol-gel systems was carried out by adding PEU aqueous solutions prepared at higher concentration with a predefined volume of an Ibu stock solution (at 40 mg/mL in ethanol) to reach an average content equal to the Ibu amount incorporated into MBG_Cu2%_SG_Ibu and MBG_Cu2%_SD_Ibu, as assessed through TGA analysis. Based on this calculation, PEU sol-gel systems were loaded with Ibu at a final concentration of 2.5 mg/mL. Hereafter, the developed sol-gel systems will be referred to with the acronyms reported in table 3.7.

Table 3.16 Information and acronyms of the designed sol-gel systems.

Acronym	Composition
PEU	PEU at 15% w/v
PEU_Ibu	PEU at 15% w/v + ibuprofen at a concentration equal to the mean drug amount assessed in MBG_Cu2%_SG + Ibu IW and MBG_Cu2%_SD + Ibu IW
PEU_MBG_Cu2%_SG_Ibu	PEU at 15% w/v + MBG_Cu2%_SG + Ibu IW (20 mg/ml MBG concentration and the corresponding amount of ibuprofen)
PEU_MBG_Cu2%_SD_Ibu	PEU at 15% w/v + MBG_Cu2%_SD + Ibu IW (20 mg/ml MBG concentration and the corresponding amount of ibuprofen)

3.2.5.1a Morphological, structural and chemical characterization of PEU_MBG_Cu2%_SG_Ibu and PEU_MBG_Cu2%_SD_Ibu

The morphology and the stability in aqueous environment in the presence of a buffer solution at pH 7.4 at 37 °C of hybrid formulation was characterized through FE-SEM observation (as shows in figure 3.41) before soaking in Tris HCl buffer (time 0) and at different time points (24 h and 7 days). FE-SEM images of both PEU_MBG_Cu2%_SG_Ibu and PEU_MBG_Cu2%_SD_Ibu at time 0 (prior to incubation) revealed a good and homogeneous particle dispersion into the hydrogel network with small aggregates composed by few particles (from 2 to 5 particles).

FE-SEM analysis showed no significant changes in the morphology of the hybrid systems after 24 h and 7 days immersion in Tris HCl solution. Furthermore, the size of MBG particles embedded into the hydrogels was not significantly affected by the immersion into an aqueous medium.

The temperature-dependent sol-to-gel transition of the developed systems was characterized through tube inverting tests carried out in temperature ramp mode to estimate the hydrogel Lower Critical

Gelation Temperature (LCGT) and in isothermal conditions at 37 °C to evaluate the time required for a complete gelation in physiological conditions. Table 3.8 reports LCGT values and gelation time in physiological conditions of pure PEU hydrogel and PEU hybrid hydrogels.

The incorporation of MBG_Cu2%_SG_Ibu and MBG_Cu2%_SD_Ibu or ibuprofen as such was found to slightly influence the transition kinetics of the designed sol-
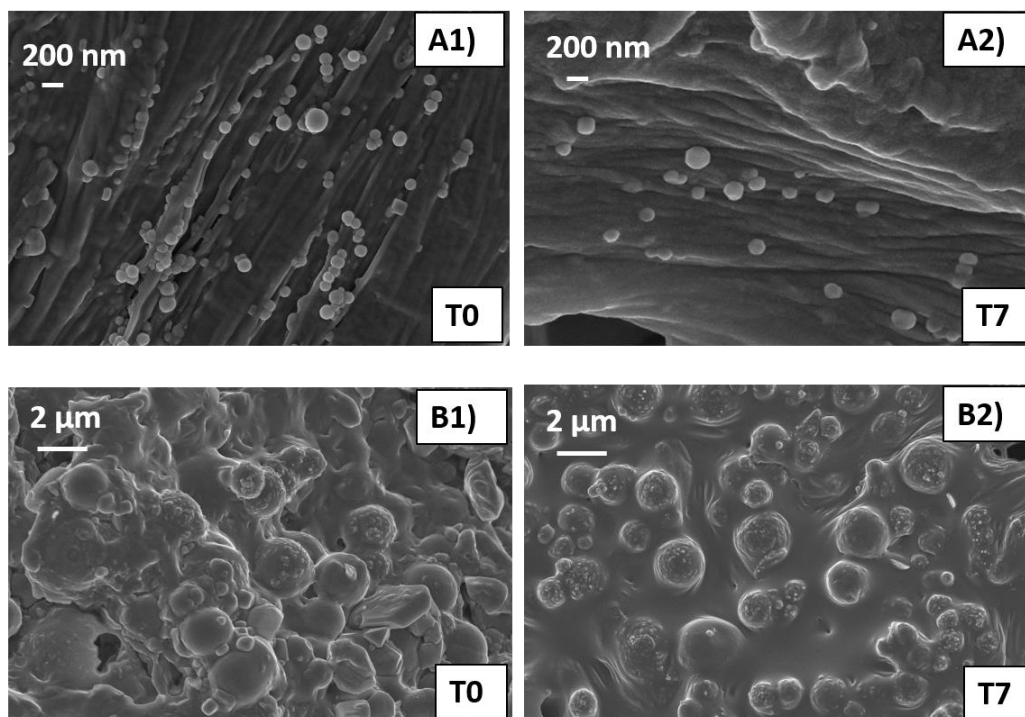
Figure 3.68 FE-SEM images of freeze-dried samples of PEU_MBG_Cu2%_SG_Ibu before soaking in Tris HCl medium (A1), after 7 days (A2) and PEU_MBG_Cu2%_SD_Ibu before soaking in Tris HCl medium (B1), after 7 days (B2).

gel systems, in accordance with results reported in literature [4]. Particle incorporation marginally increased the gelation temperature, a behaviour which suggest that MBG particles act as defects in the gel network, initially hindering and then slowing down the kinetics of the sol-to-gel transition. On the other hand, the slight decrease of gelation time in physiological conditions observed for PEU gels containing MBG_Cu2%_SG_Ibu particles could also result from the criterion adopted to define the "sol" and the "gel" states, i.e., presence or absence of sample flow within 30 s of vial inversion. Indeed, particle addition to the hydrogels induced an increase in viscosity, that, as a consequence, inevitably accounted for the shorter incubation time at 37 °C requested for not observing any flow within the observation time. The slightly lower gelation temperature of PEU_MBG_Cu2%_SG_Ibu compared to PEU_MBG_Cu2%_SD_Ibu could be correlated to their dimensional differences, which result in different hydrogel viscosity. Indeed, at a fixed MBG concentration of 20 mg/mL, the number of MBG_Cu2%_SG_Ibu contained throughout the gel is expected to be higher compared to MBG_Cu2%_SD_Ibu, due to the lower size of SG particles. Regarding the addition of ibuprofen as such, no effects were observed in gelation time in physiological conditions, while LCGT value slightly decreased. This behaviour did not result from the addition of a small volume of EtOH (used to solubilize Ibu) to the sol-gel systems, but rather to the intrinsic nature of the drug. In fact, being hydrophobic, ibuprofen is expected to be partly loaded within the core of the forming PEU micelles, thus inducing an increase of micelle volume, which then achieves the critical value required for the onset of thermal gelation [47] at a

lower temperature. Despite the commented slight changes in LCGT and gelation time at 37 °C, neither the addition of MBG particles of different size nor the incorporation of a hydrophobic drug significantly affected the gelation potential of PEU-based hydrogels upon temperature increase.

Table 3.17 Lower critical gelation temperature (LGCT) and gelation time at 37°C of PEU, PEU_Ibu, PEU_ MBG_Cu2%_SG_Ibu and PEU_ MBG_Cu2%_SD_Ibu

Acronym	LCGT (°C)[1]	Gelation time @ 37 °C (min)[2]
PEU	28	5
PEU _Ibu	27	5
PEU _MBG_Cu2%_SG_Ibu	29	4
PEU_MBG_Cu2%_SD_Ibu	30	6

[1] Error: ± 0.5 °C.

[2] Error: ± 0.5 min.

3.2.5.1b Ibuprofen release from PEU_MBG_Cu2%_SG_Ibu and PEU_MBG_Cu2%_SD_Ibu in Tris HCl

Ibuprofen release profile from PEU-based hydrogels was assessed in
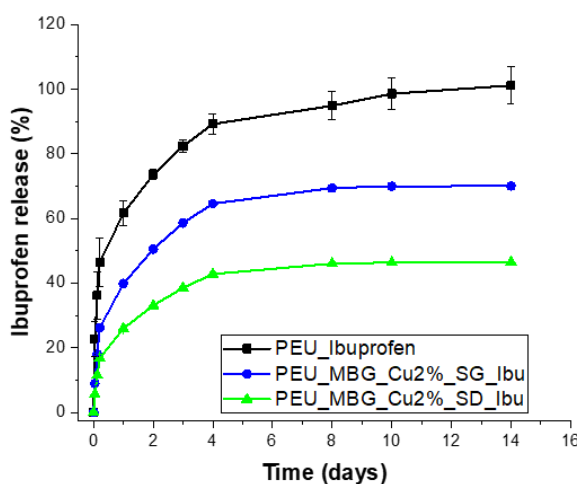
Figure 3.69 (A) Ibuprofen release (%) profile from PEU_Ibu, PEU_MBG_Cu2%_SG_Ibu and PEU_MBG_Cu2%_SD_Ibu hydrogels.

physiological-like conditions, using Tris HCl at 37 °C. Figure 3.42 compares ibuprofen release profiles from PEU_Ibu, PEU_MBG_Cu2%_SG_Ibu and PEU_MBG_Cu2%_SD_Ibu up to 14 days observation time. A complete release of

the drug was observed from the gels loaded with ibuprofen as such, with a release of 98 % at day 10.

On the other hand, MBG-loaded gels showed a sustained release of the drug, reaching a percentage release after 14 days incubation of 70 % and 46 % from PEU_MBG_Cu2%_SG_Ibu and PEU_MBG_Cu2%_SD_Ibu, respectively. The incomplete ibuprofen release observed from particle-loaded gels (starting from day
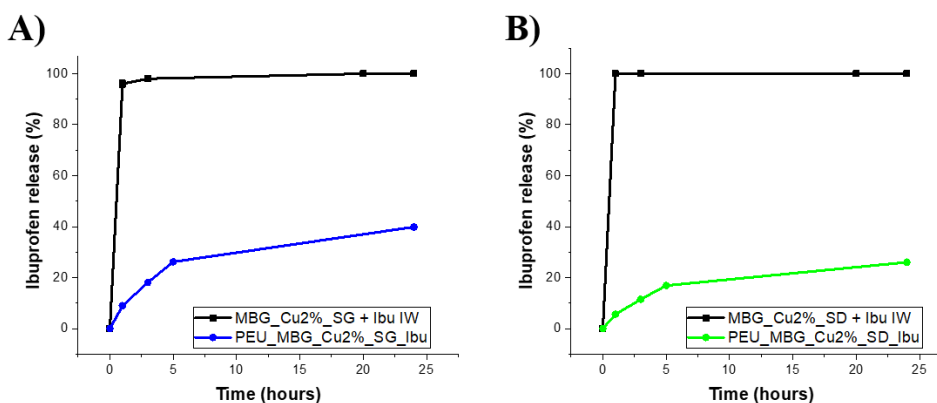
Figure 3.70 Comparison among ibuprofen release profiles assessed from (A) MBG_Cu2%_SG + Ibu IW and PEU_MBG_Cu2%_SG_Ibu and (B) MBG_Cu2%_SD + Ibu IW and PEU_MBG_Cu2%_SD_Ibu.

8 the release profile reached a plateau value for both the particle-loaded gels) could be correlated to the progressive pore occlusion due to the dissolution of silica-based MBG framework and its re-precipitation as silica gel at the pores mouth, in accordance with observations reported by Mortera et al. [13]. In addition, the release profile of ibuprofen from PEU_MBG_Cu2%_SG_Ibu and PEU_MBG_Cu2%_SD_Ibu has been compared with the release kinetics of ibuprofen from the bare samples, MBG_Cu2%_SG_Ibu and MBG_Cu2%_SD_Ibu.

In fact, as reported in section 3.2.3.1d, both MBG_Cu2%_SG_Ibu and MBG_Cu2%_SD_Ibu showed a burst ibuprofen release profile, and the total amount of loaded ibuprofen was released in the first hours of incubation. By the comparison of the kinetics within the first 24 hours of ibuprofen release from free and hydrogel-containing MBG particles, the role exerted by the polymeric matrix in modulating the release profile of ibuprofen was clearly highlighted (Figure 3.43), with a significant reduction ($0.0001 < p < 0.001$) in the initial burst release upon incorporation within PEU gel of about 85% for both kinds of particles investigated.

3.2.5.1c Copper release from PEU_MBG_Cu2%_SG_Ibu and PEU_MBG_Cu2%_SD_Ibu in Tris HCl

The release profile of copper ions from the developed hybrid formulations was investigated, showing a trend similar to that assessed for ibuprofen (Figure 3.44). After 14 days of incubation in aqueous medium, the 66 % and 56 % (corresponding to 291 ppm and 192 ppm, respectively) of the copper initially present in the MBG framework was released from PEU_MBG_Cu2%_SG_Ibu and PEU_MBG_Cu2%_SD_Ibu, respectively. The incorporation of Cu-containing
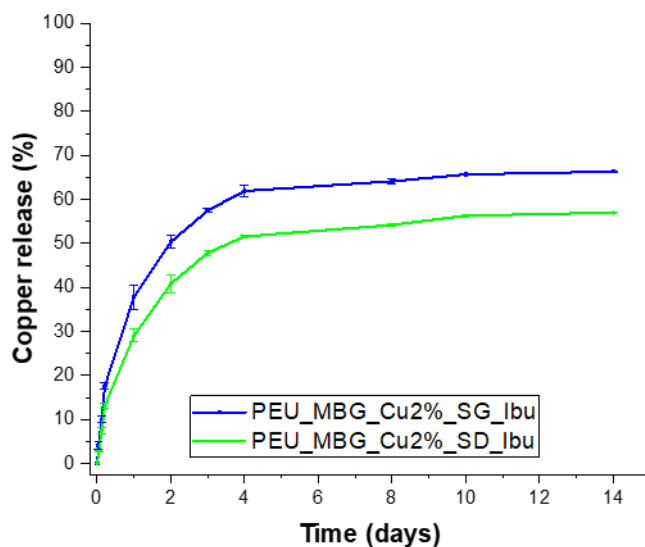
Figure 3.71 Copper ion release (%) profile from PEU_MBG_Cu2%_SG_Ibu and PEU_MBG_Cu2%_SD_Ibu.

MBGs within the polymeric phase successfully decreased the undesirable initial burst release of Cu^{2+} species typically observed for particles as such ($0.0001 < p < 0.001$): after one-hour incubation in similar releasing conditions, PEU_MBG_Cu2%_SG_Ibu and PEU_MBG_Cu2%_SD_Ibu released an amount of copper ions approximately 72 % and 61 % lower compared to the corresponding free MBG particles. Both ibuprofen and copper ions were released faster from PEU_MBG_Cu2%_SG_Ibu compared to PEU_MBG_Cu2%_SD_Ibu, in accordance with the higher surface area of MBG_Cu2%_SG_Ibu compared to MBG_Cu2%_SD_Ibu, which accounts for a fast molecule diffusion, either ions or drugs, through MBG porous network.

References

[1] G. Grass, C. Rensing, M. Solioz, Metallic copper as an antimicrobial surface, Appl. Environ. Microbiol. 77 (2011) 1541–1547. doi:10.1128/AEM.02766-10.

[2] C. Wu, Y. Zhou, M. Xu, P. Han, L. Chen, J. Chang, Y. Xiao, Copper-containing mesoporous bioactive glass scaffolds with multifunctional properties of angiogenesis capacity, osteostimulation and antibacterial activity, Biomaterials. 34 (2013) 422–433. doi:10.1016/j.biomaterials.2012.09.066.

[3] L. Finney, S. Vogt, T. Fukai, D. Glesne, Copper and angiogenesis: Unravelling a relationship key to cancer progression, Clin. Exp. Pharmacol. Physiol. (2009). doi:10.1111/j.1440-1681.2008.04969.x.

[4] C. Pontremoli, M. Boffito, S. Fiorilli, R. Laurano, A. Torchio, A. Bari, C. Tonda-Turo, G. Ciardelli, C. Vitale-Brovarone, Hybrid injectable platforms for the in situ delivery of therapeutic ions from mesoporous glasses, Chem. Eng. J. 340 (2018) 103–113. doi:10.1016/j.cej.2018.01.073.

[5] M. Boffito, C. Pontremoli, S. Fiorilli, R. Laurano, G. Ciardelli, C. Vitale-Brovarone, Injectable Thermosensitive Formulation Based on Polyurethane Hydrogel/Mesoporous Glasses for Sustained Co-Delivery of Functional Ions and Drugs, Pharmaceutics. 11 (2019) 501. doi:10.3390/pharmaceutics11100501.

[6] A. Bari, N. Bloise, S. Fiorilli, G. Novajra, M. Vallet-Regí, G. Bruni, A. Torres-Pardo, J.M. González-Calbet, L. Visai, C. Vitale-Brovarone, Copper-containing mesoporous bioactive glass nanoparticles as multifunctional agent for bone regeneration, Acta Biomater. 55 (2017) 493–504. doi:10.1016/j.actbio.2017.04.012.

[7] A. El-Fiqi, T.H. Kim, M. Kim, M. Eltohamy, J.E. Won, E.J. Lee, H.W. Kim, Capacity of mesoporous bioactive glass nanoparticles to deliver therapeutic molecules, Nanoscale. 4 (2012) 7475. doi:10.1039/c2nr31775c.

[8] L. Pontiroli, M. Dadkhah, G. Novajra, I. Tcacencu, S. Fiorilli, C. Vitale-Brovarone, An aerosol-spray-assisted approach to produce mesoporous bioactive glass microspheres under mild acidic aqueous conditions, Mater. Lett. 190 (2017) 111–114. doi:10.1016/j.matlet.2016.12.125.

[9] K.S.W. Sing, D.H. Everett, R.A.W. Haul, L. Moscou, R.A. Pierotti, J. Rouquelon, T. Siemieniewska, Reporting physisorption data for gas/solid systems with special reference to the determination of surface area and porosity (Recommendations 1984), Pure Appl. Chem. 57 (1985) 603–619. doi:10.1351/pac198557040603.

[10] A. López-Noriega, D. Arcos, I. Izquierdo-Barba, Y. Sakamoto, O. Terasaki, M. Vallet-Regí, Ordered mesoporous bioactive glasses for bone tissue regeneration, Chem. Mater. 18 (2006) 3137–3144. doi:10.1021/cm060488o.

[11] V. Uskoković, D.P. Uskoković, Nanosized hydroxyapatite and other calcium phosphates: Chemistry of formation and application as drug and gene delivery agents, J. Biomed. Mater. Res. - Part B Appl. Biomater. 96 B (2011) 152–191. doi:10.1002/jbm.b.31746.

[12]   K. Lin, C. Wu, J. Chang, Advances in synthesis of calcium phosphate crystals with controlled size and shape, Acta Biomater. 10 (2014) 4071–4102. doi:10.1016/j.actbio.2014.06.017.

[13]   R. Mortera, S. Fiorilli, E. Garrone, E. Verné, B. Onida, Pores occlusion in MCM-41 spheres immersed in SBF and the effect on ibuprofen delivery kinetics: A quantitative model, Chem. Eng. J. 156 (2010) 184–192. doi:10.1016/j.cej.2009.10.018.

[14]   P. Li, I. Kangasniemi, K. de Groot, T. Kokubo, A.U. Yli-Urpo, Apatite crystallization from metastable calcium phosphate solution on sol-gel-prepared silica, J. Non. Cryst. Solids. 168 (1994) 281–286. doi:10.1016/0022-3093(94)90340-9.

[15]   P. Li, K. Nakanishi, T. Kokubo, K. de Groot, Induction and morphology of hydroxyapatite, precipitated from metastable simulated body fluids on sol-gel prepared silica, Biomaterials. 14 (1993) 963–968. doi:10.1016/0142-9612(93)90186-6.

[16]   M. Boffito, A.G. Brancot, O. Lima, S. Bronco, S. Sartori, G. Ciardelli, P. Torino, Injectable thermosensitive gels for the localized and controlled delivery of biomolecules in tissue engineering/regenerative medicine, Biomed. Sci. Eng. 3 (2019) 9–19. doi:10.4081/bse.2019.67.

[17]   C. Charnay, S. Bégu, C. Tourné-Péteilh, L. Nicole, D.A. Lerner, J.M. Devoisselle, Inclusion of ibuprofen in mesoporous templated silica: Drug loading and release property, Eur. J. Pharm. Biopharm. 57 (2004) 533–540. doi:10.1016/j.ejpb.2003.12.007.

[18]   A. El-Fiqi, T.-H. Kim, M. Kim, M. Eltohamy, J.-E. Won, E.-J. Lee, H.-W. Kim, Capacity of mesoporous bioactive glass nanoparticles to deliver therapeutic molecules, Nanoscale. 4 (2012) 7475. doi:10.1039/c2nr31775c.

[19]   M. Vallet-Regí, Ordered mesoporous materials in the context of drug delivery systems and bone tissue engineering, Chem. - A Eur. J. 12 (2006) 5934–5943. doi:10.1002/chem.200600226.

[20]   and J.A.M. Randy Mellaerts, Jasper A. G. Jammaer, Michiel Van Speybroeck, Hong Chen, Jan Van Humbeeck, Patrick Augustijns, Guy Van der Mooter, Physical state of poorly water soluble therapeutic\rmolecules loaded into SBA-15 ordered mesoporous silica carriers:\rA case study with itraconazole and ibuprofen., Langmuir. 24 (2008) 8651–8659.

[21]   G. Gonzalez, A. Sagarzazu, T. Zoltan, Infuence of Microstructure in Drug Release Behavior of Silica Nanocapsules, J. Drug Deliv. 2013 (2013) 1–8. doi:10.1155/2013/803585.

[22]   S. Hong, S. Shen, D.C.T. Tan, W.K. Ng, X. Liu, L.S.O. Chia, A.W. Irwan, R. Tan, S.A. Nowak, K. Marsh, R. Gokhale, High drug load, stable, manufacturable and bioavailable fenofibrate formulations in mesoporous silica: A comparison of spray drying versus solvent impregnation methods, Drug Deliv. 23 (2016) 316–327. doi:10.3109/10717544.2014.913323.

[23]   A.R. Brás, E.G. Merino, P.D. Neves, I.M. Fonseca, M. Dionísio, A. Schönhals, N.T. Correia, Amorphous ibuprofen confined in nanostructured silica materials: A dynamical approach, J. Phys. Chem. C. 115 (2011) 4616–4623.

doi:10.1021/jp107631m.

[24] S. Fiorilli, B. Onida, B. Bonelli, E. Garrone, In situ infrared study of SBA-15 functionalized with carboxylic groups incorporated by a Co-condensation route, J. Phys. Chem. B. 109 (2005) 16725–16729. doi:10.1021/jp045362y.

[25] V. Cauda, S. Fiorilli, B. Onida, E. Vernè, C. Vitale Brovarone, D. Viterbo, G. Croce, M. Milanesio, E. Garrone, SBA-15 ordered mesoporous silica inside a bioactive glass-ceramic scaffold for local drug delivery, J. Mater. Sci. Mater. Med. 19 (2008) 3303–3310. doi:10.1007/s10856-008-3468-4.

[26] F. Wang, H. Hui, T.J. Barnes, C. Barnett, C.A. Prestidge, Oxidized mesoporous silicon microparticles for improved oral delivery of poorly soluble drugs., Mol Pharm. 7 (2010) 227.

[27] S.C. Shen, W.K. Ng, J. Hu, K. Letchmanan, J. Ng, R.B.H. Tan, Solvent-free direct formulation of poorly-soluble drugs to amorphous solid dispersion via melt-absorption, Adv. Powder Technol. 28 (2017) 1316–1324. doi:10.1016/j.apt.2017.02.020.

[28] M. Sliwinska-Bartkowiak, G. Dudziak, R. Gras, R. Sikorski, R. Radhakrishnan, K.E. Gubbins, Freezing behavior in porous glasses and MCM-41, Colloids Surfaces A Physicochem. Eng. Asp. 187–188 (2001) 523–529. doi:10.1016/S0927-7757(01)00637-9.

[29] R. Radhakrishnan, K.E. Gubbins, M. Sliwinska-Bartkowiak, Effect of the fluid-wall interaction on freezing of confined fluids: Toward the development of a global phase diagram, J. Chem. Phys. 112 (2000) 11048–11057. doi:10.1063/1.481745.

[30] F. Qu, G. Zhu, H. Lin, W. Zhang, J. Sun, S. Li, S. Qiu, A controlled release of ibuprofen by systematically tailoring the morphology of mesoporous silica materials, J. Solid State Chem. (2006). doi:10.1016/j.jssc.2006.04.002.

[31] M. Vallet-Regi, A. Rámila, R.P. Del Real, J. Pérez-Pariente, A new property of MCM-41: Drug delivery system, Chem. Mater. 13 (2001) 308–311. doi:10.1021/cm0011559.

[32] S.W. Song, K. Hidajat, S. Kawi, Functionalized SBA-15 materials as carriers for controlled drug delivery: Influence of surface properties on matrix-drug interactions, Langmuir. (2005). doi:10.1021/la051167e.

[33] Y. Zhang, Z. Zhi, T. Jiang, J. Zhang, Z. Wang, S. Wang, Spherical mesoporous silica nanoparticles for loading and release of the poorly water-soluble drug telmisartan, J. Control. Release. 145 (2010) 257–263. doi:10.1016/j.jconrel.2010.04.029.

[34] J. Zhou, G. Romero, E. Rojas, L. Ma, S. Moya, C. Gao, Layer by layer chitosan/alginate coatings on poly(lactide-co-glycolide) nanoparticles for antifouling protection and Folic acid binding to achieve selective cell targeting, J. Colloid Interface Sci. 345 (2010) 241–247. doi:10.1016/j.jcis.2010.02.004.

[35] J. Tian, R. Xu, H. Wang, Y. Guan, Y. Zhang, Precise and tunable time-controlled drug release system using layer-by-layer films as erodible coatings, Mater. Sci. Eng. C. 116 (2020) 111244. doi:10.1016/j.msec.2020.111244.

[36] Z.S. Haidar, R.C. Hamdy, M. Tabrizian, Protein release kinetics for core-shell

hybrid nanoparticles based on the layer-by-layer assembly of alginate and chitosan on liposomes, Biomaterials. 29 (2008) 1207–1215. doi:10.1016/j.biomaterials.2007.11.012.

[37]   Q.L. Li, Y. Sun, Y.L. Sun, J. Wen, Y. Zhou, Q.M. Bing, L.D. Isaacs, Y. Jin, H. Gao, Y.W. Yang, Mesoporous silica nanoparticles coated by layer-by-layer self-assembly using cucurbit[7]uril for in vitro and in vivo anticancer drug release, Chem. Mater. (2014). doi:10.1021/cm503304p.

[38]   G. Maurstad, Y.A. Mørch, A.R. Bausch, B.T. Stokke, Polyelectrolyte layer interpenetration and swelling of alginate-chitosan multilayers studied by dual wavelength reflection interference contrast microscopy, Carbohydr. Polym. (2008). doi:10.1016/j.carbpol.2007.07.019.

[39]   L. Xu, Z. Chu, H. Wang, L. Cai, Z. Tu, H. Liu, C. Zhu, H. Shi, D. Pan, J. Pan, X. Fei, Electrostatically Assembled Multilayered Films of Biopolymer Enhanced Nanocapsules for on-Demand Drug Release, ACS Appl. Bio Mater. 2 (2019) 3429–3438. doi:10.1021/acsabm.9b00381.

[40]   S. Ye, C. Wang, X. Liu, Z. Tong, Multilayer nanocapsules of polysaccharide chitosan and alginate through layer-by-layer assembly directly on PS nanoparticles for release, J. Biomater. Sci. Polym. Ed. (2005). doi:10.1163/1568562054255691.

[41]   J.O. Kim, T. Ramasamy, T.H. Tran, J.Y. Choi, H.J. Cho, J.H. Kim, C.S. Yong, H.G. Choi, Layer-by-layer coated lipid-polymer hybrid nanoparticles designed for use in anticancer drug delivery, Carbohydr. Polym. (2014). doi:10.1016/j.carbpol.2013.11.009.

[42]   C. Picart, J. Mutterer, L. Richert, Y. Luo, G.D. Prestwich, P. Schaaf, J.C. Voegel, P. Lavalle, Molecular basis for the explanation of the exponential growth of polyelectrolyte multilayers, Proc. Natl. Acad. Sci. U. S. A. (2002). doi:10.1073/pnas.202486099.

[43]   P. Lavalle, C. Gergely, F.J.G. Cuisinier, G. Decher, P. Schaaf, J.C. Voegel, C. Picart, Comparison of the structure of polyelectrolyte multilayer films exhibiting a linear and an exponential growth regime: An in situ atomic force microscopy study, Macromolecules. (2002). doi:10.1021/ma0119833.

[44]   Y. Wang, J. Ke, K. Gou, Y. Guo, X. Xu, S. Li, H. Li, Amino functionalized mesoporous silica with twisted rod-like shapes: Synthetic design, in vitro and in vivo evaluation for ibuprofen delivery, Microporous Mesoporous Mater. (2020). doi:10.1016/j.micromeso.2019.109896.

[45]   F. Kesisoglou, S. Panmai, Y. Wu, Nanosizing - Oral formulation development and biopharmaceutical evaluation, Adv. Drug Deliv. Rev. (2007). doi:10.1016/j.addr.2007.05.003.

[46]   B. Muñoz, A. Rámila, J. Pérez-Pariente, I. Díaz, M. Vallet-Regí, MCM-41 organic modification as drug delivery rate regulator, Chem. Mater. 15 (2003) 500–503. doi:10.1021/cm021217q.

[47]   M. Boffito, E. Gioffredi, V. Chiono, S. Calzone, E. Ranzato, S. Martinotti, G. Ciardelli, Novel polyurethane-based thermosensitive hydrogels as drug release and tissue engineering platforms: design and in vitro characterization, Polym. Int. 65 (2016) 756–769. doi:10.1002/pi.5080.

CHAPTER 4

Strontium-containing   MBGs:
Results and Discussion

4.1 Introduction

The second ion selected to be incorporated into the MBG framework is strontium, thanks to the well-known pro-osteogenic and anti-osteoclastogenic properties. In fact, as mentioned in chapter 1.4.1, strontium is able to activate the calcium sensing receptor (CaSR), in both osteoblasts and osteoclasts, causing the promotion of the osteoblast activity and inhibition of the osteoclast activity. The samples were prepared by substituting part of the calcium with the strontium (2% and 4% mol.) and the related results are described in the sub-chapters 4.2.1 and 4.2.2.

Once characterized, the biological response of the strontium ions released from the 2%mol strontium-containing MBGs, was evaluated thanks to a collaboration with *Nobil Bio Ricerche*, in terms of cell viability, inflammatory response and anti-osteoclastogenesis activity, by monitoring the RANKL and OPG pathways, and the obtained results are discussed in section 4.2.3.

Subsequently, with the aim to further improve the osteogenic response of the strontium-containing MBGs, N-acetylcysteine was loaded into the mesoporous structure by following the incipient wetness procedure, which, based on the results obtained with loading of ibuprofen, turned out to be more suitable compared to the adsorption methods, in terms of yields and time-consuming. As previously mentioned in chapter 1.6, thanks to the recently proved osteoinductive properties, as well as the ability to accelerate bone repair by the activation of osteogenic lineages differentiation, NAC has been selected to be used as osteogenesis-enhancing molecule to be delivered into the bony defect in combination with strontium ions, to improve bone regeneration and promote bone defect healing.

In section 4.2.4, the results related to strontium-containing MBGs loaded with NAC are reported.

NAC-loaded Sr-MBGs were then incorporated into the thermosensitive hydrogel, acting as vehicle phase to maintain the nanocarrier at the pathological site; the related results are contained in section 4.3. A preliminary *in vivo* study to

evaluate the efficacy and the safety of the developed bone healing device based on NAC-loaded Sr-MBGs incorporated into the hydrogel was carried out in collaboration with the *Julius Wolff institute, Charitè – Universitätsmedizin Berlin,* during my three months period in Berlin in the group led by Prof. Katharina Schmidt-Bleek (consortium partner in the MOZART project). The *in vivo* response was evaluated in a femoral osteotomy model of compromised healing in female rats. After 4 weeks, the animals have been sacrificed and the bones sectioned and stained with Safranin O and Movat Pentachrome staining, in order to evaluate the bone heling progress, induced by the release of strontium and NAC. The obtained results are described in section 4.3.2.

Finally, in section 4.4, the results concerning the *zwitterionic* samples are reported. *Zwitterionization* has been selected as functionalization approach and employed with the aim to impart anti-adhesive/anti-fouling features, thus enriching the therapeutic potential of the strontium-containing MBGs. The resulting multifunctional device is supposed to target simultaneously all the causes, often mutually interlocked, of the pathologies related to compromised bone tissue healing. In fact, along with the pro-osteogenic effect imparted by the release of strontium ions, the anti-adhesive surface can be exploited to inhibit the protein adhesion and, consequently, avoid the bacteria attachment.

The biological assessment of the *zwitterionic* MBGs were performed in collaboration with the group of *Prof. Maria Vallet-Regì* at *Departamento de Química Inorgánica y Bioinorgánica, Universidad Complutense de Madrid, CIBER de Bioingeniería, Biomateriales y Nanomedicina (CIBER-BBN),* a partner involved in the Zodiac project. In particular, in section 4.4.3, the results related to the in *vitro* biocompatibility assays to evaluate the osteoblastic cell growth and differentiation along with the capability to inhibit protein adhesion are reported.

4.2 Morphological and structural characterization of sol-gel and spray-dryer Strontium-containing MBGs

4.2.1 Strontium-containing MBG-SG: MBG_Sr2%_SG and MBG_Sr4%_SG

Part of the work described in this chapter has been previously published in [1,2].

The ability of strontium to stimulate osteoblastogenesis and inhibit the osteoclastogenesis activity have been widely discussed in the "*state of the art*" chapter and have been extensively investigated in the literature, making this ion a promising therapeutic agent for bone regeneration purpose. In this section, the results concerning the characterization of strontium-containing nano-sized particles with the 2% and 4% molar percentage of strontium (molar ratio Sr/Ca/Si = 2/13/85, named hereafter as MBG_Sr2%_SG and molar ratio Sr/Ca/Si = 4/13/85, named hereafter as MBG_Sr4%_SG) are presented.

4.2.1a Morphological and structural characterization of MBG_Sr2%_SG and MBG_Sr4%_SG

FE-SEM images (figure 4.1) of MBG_Sr2%_SG and MBG_Sr4%_SG revealed particles with uniform spherical morphology and size ranging between 100 and 200 nm. Morphological analysis evidenced that the introduction of higher amount of strontium precursor did not lead to significant morphological variations of the final particles.
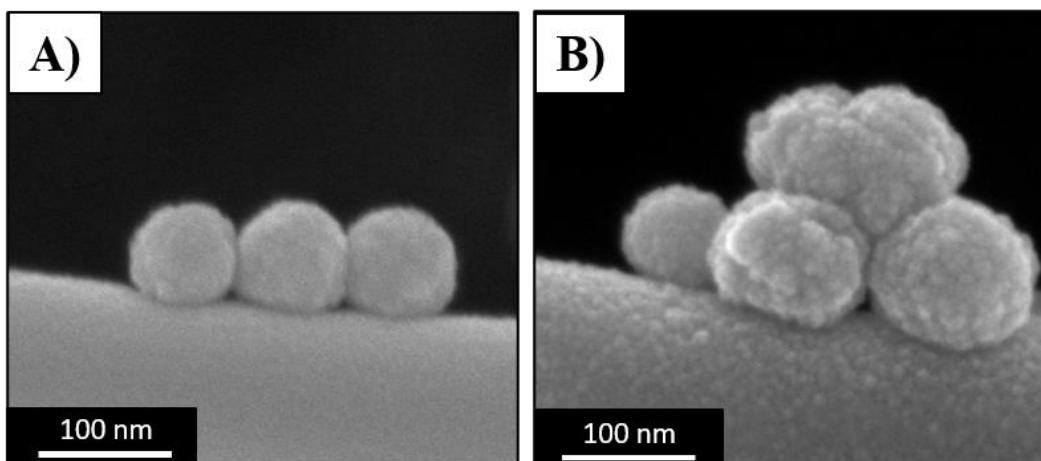
Figure 4.72 FE-SEM images of (A) MBG_Sr2%_SG and (B) MBG_Sr4%_SG.

Nitrogen adsorption-desorption isotherms (figure 4.2a) of MBG_Sr2%_SG and MBG_Sr4%_SG samples are both classified as type IV isotherms, conventionally associated with mesoporous materials, with H2 hysteresis loop. Pore size distributions of both samples showed uniform mesopores with a mean diameter of about 4 nm (figure 4.2b).
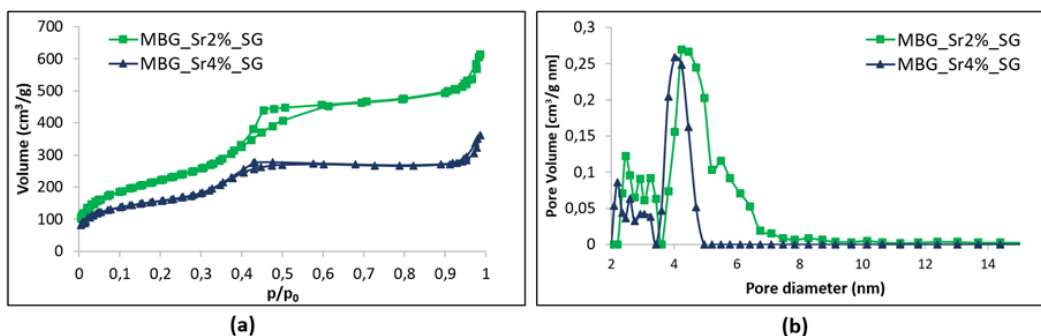
Figure 4.73 N₂ adsorption-desorption curves of MBG_Sr2%_SG and MBG_Sr4%_SG: (a) isotherms; (b) DFT pore size distributions

The increase of Sr molar concentration from 2 to 4 mol % led to a decrease in the specific surface area (SSA) from 803 to 551 cm^3 g^{-1} and of the pore volume from 0.82 to 0.45 cm^3 g^{-1} (table 4.1)[3]. In the literature, other works have shown that the incorporation of increasing amount of strontium, or trivalent element as Ce, into the framework of MBGs, affected their structural features [3–5], leading to a reduction of specific surface area and pore volume, associated to the appearance of disorganized non-porous domains [5]. In addition, the higher incorporation of Sr^{2+} may interfere during the self-assembly interactions between SiO_4^{4-} species and the cationic heads of the template, which can cause structural defects in the polymerized framework and the consequent alteration of the final mesopore structure [3].

Table 4.18 Structural features of MBG_Sr2%_SG and MBG_Sr4%_SG.

Name	Specific surface area (cm^3/g)	Pore size (nm)	Volume (cm^3/g)
MBG_Sr2%_SG	803	4.8	0.82
MBG_Sr4%_SG	551	4.1	0.45

4.2.1b Bioactive behaviour of MBG_Sr2%_SG and MBG_Sr4%_SG in SBF

The very high SSA and the mesoporous texture of MBGs enhance their bioactivity, namely the ability to induce the formation of a HA layer on their surface through a series of ionic exchanges with physiologic fluids [6]. In fact, while melt-derived and non-porous sol-gel glasses exhibit bioactivity after several days of soaking in SBF, MBGs are able to induce the deposition of the HA layer in shorter time [7]. This behavior was also notified for Sr-containing samples produced during this PhD work. In particular, MBG_Sr2%_SG and MBG_Sr4%_SG showed the formation of nanometric crystals of HA after 3 days of soaking in SBF that grew in size during
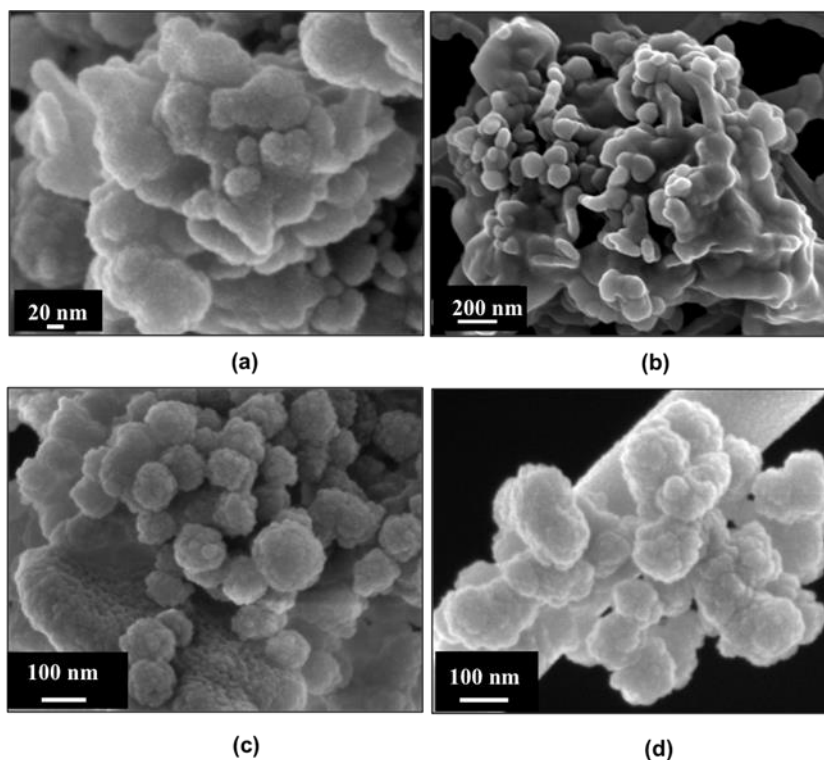
Figure 4.74 FE-SEM images of powders after soaking in SBF: (a) MBG_Sr2%_SG after 3 days; (b) MBG_Sr2%_SG after 7 days; (c) MBG_Sr4%_SG after 3 days; (d) MBG_Sr4%_SG after 7 days.

the test, causing the embedding of MBG particles after 7 days (figure 4.3).

The precipitation of a HA layer on the Sr-containing samples and its crystalline nature was confirmed by XRD analysis: new peaks appeared at 25.8 and 32.0 2θ degrees in both the MBG_Sr2%_SG and MBG_Sr4%_SG samples matching the HA reference (00-001-1008) as can be observed in figure 4.4.

Furthermore, during the *in vitro* bioactivity test the pH of the SBF solution remained below 7.8 which is considered the threshold value for allowing osteoblasts to maintain their physiological activity [8], making these systems appropriate for bone regenerative applications.
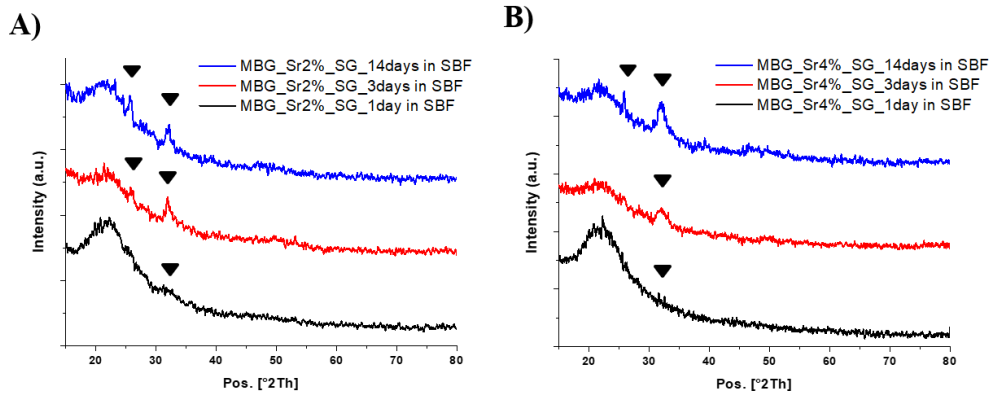
Figure 4.75 XRD spectra after different time of soaking in SBF of: (A) MBG_Sr2%_SG and (B) MBG_Sr4%_SG.

4.2.1c Strontium ion release from MBG_Sr2%_SG and MBG_Sr4%_SG in Tris HCl

Release tests carried out in Tris HCl medium evidenced, as expected, that the released ionic concentration (ppm) of Sr^{2+} ions is dependent on MBG composition, as higher Sr substitution resulted in higher released amount (figure 4.5). Analogous behavior was reported for similar systems, such as Sr-containing bioactive glass nanoparticles or Sr-substituted MBG scaffolds, which showed a release capacity well-correlated to the Sr^{2+} incorporated amounts [9–12].
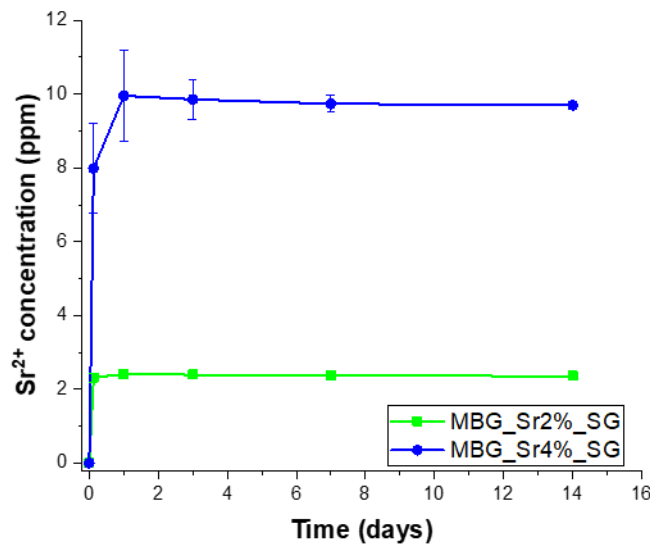
Figure 4.76 Sr^{2+} release profile of MBG_Sr2%_SG and MBG_Sr4%_SG in Tris HCl.

The release profile of Sr^{2+} from MBG_Sr2%_SG and MBG_Sr4%_SG showed a burst effect in the first 3 h for both samples followed by a plateau (as reported in table 4.2). The fast ion release kinetics is attributed to the remarkably high surface

area and to the particle size (short diffusion paths), which allow fast ion diffusion inside the porous structure [13]. The chemical composition of MBG_Sr2%_SG and MBG_Sr4%_SG, determined by ICP-AES, revealed a reduced incorporation of strontium compared to the nominal values. A similar behavior was reported for Sr-substituted glasses, prepared by sol-gel method, which revealed incorporated amounts lower than the nominal ones [14]. This difference can be tentatively ascribed to the larger ionic radius of strontium (1.16 Å) compared to calcium (0.94 Å) [15], which can limit its incorporation into the framework during silica polymerization. Moreover, a lower charge density (charge/ionic radius) can account for weaker charge interactions between Sr^{2+} ions and the silicate framework and can contribute to the observed lower Sr^{2+} incorporation rate.

However, as far as MBG_Sr4%_SG sample is concerned, the total amount of incorporated strontium was released with a final concentration of about 9.7 ppm. Similarly, the final released concentration of Sr^{2+} from MBG_Sr2%_SG results slightly lower compared to that expected based on the incorporated amount (about 95%), with a final concentration of about 2.4 ppm (table 4.2).

Table 4.19 Sr^{2+} amount incorporated expressed in mol % and ppm, Sr^{2+} released quantity in ppm after 3 h and 72 h of soaking in Tris HCl.

Sample	Sr^{2+} Incorporated mol %	Sr^{2+} Incorporated ppm	Sr^{2+} Released at 3 h (ppm)	Sr^{2+} Released at 72 h (ppm)
MBG_Sr2%_SG	1.0%	2.40	2.19	2.36
MBG_Sr4%_SG	2.0%	7.60	6.68	7.60

4.2.2 Strontium-containing MBG-SD: MBG_ Sr2%_SD and MBG_ Sr4%_SD

Part of the work described in this chapter has been previously published in [1,2].

In this section, the results concerning the characterization of strontium-containing micro-sized particles with the 2% and 4% molar percentage of strontium (molar ratio Sr/Ca/Si = 2/13/85, named hereafter as MBG_Sr2%_SD and molar ratio Sr/Ca/Si = 4/13/85, named hereafter as MBG_Sr4%_SD) are presented.

4.2.2a Morphological and structural characterization of MBG_ Sr2%_SD and MBG_ Sr4%_SD

FE-SEM images (figure 4.6) of MBG_Sr2%_SD and MBG_Sr4%_SD revealed spherical particles with micrometric size between 1 and 5 µm, in analogy with those obtained in copper containing MBGs. Morphological analysis evidenced that for both methods the introduction of higher amount of strontium precursor did not lead to significant morphological variations of the final particles.
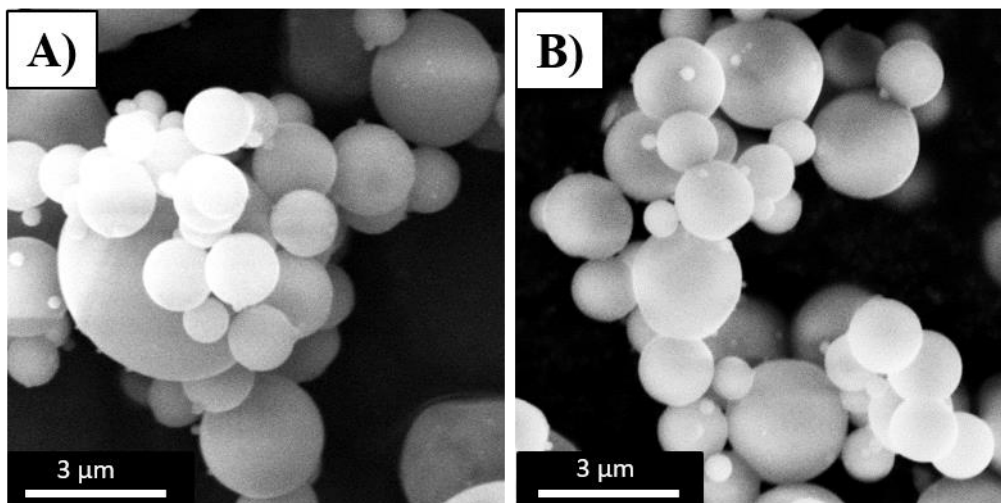
Figure 4.77 FE-SEM images of (A) MBG_Sr2%_SD and (B) MBG_Sr4%_SD.

N_2 adsorption-desorption measurement performed on the sample obtained by aerosol-assisted procedure also confirmed the mesoporous structure of the sample, showing type IV isotherms, with a pronounced H2 hysteresis (figures 4.7a).
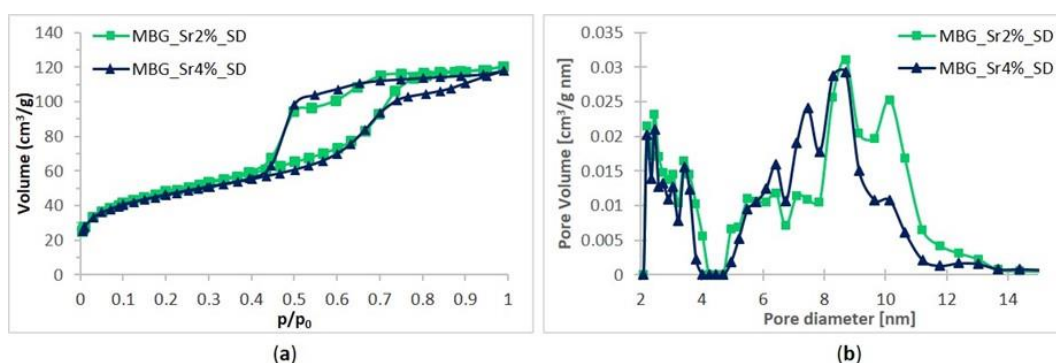
Figure 4.78 N_2 adsorption-desorption curves of MBG_Sr2%_SD and MBG_Sr4%_SD: (a) isotherms; (b) DFT pore size distributions.

According to the literature, this could be associated to the presence of a complex pore network undergoing the pore-blocking phenomenon, due to the presence of

mesopores connected to the external surface through narrow necks that caused the emptying of pores at lower vapor pressures [16,17]. This less organized porous structure could result from the fast kinetics of the spray-drying process, which reduce the time available for the mesophase organization and the degree of silica framework condensation. The values of specific surface area, pore volume and average pore size are reported in table 4.3. The obtained spray-dried MBGs showed SSA values comparable to those obtained for the copper containing samples produced through analogous synthesis, evidencing the reliability and versatility of this preparation method.

A slight decrease of SSA values, from 167 cm^3 g^{-1} of MBG_Sr2%_SD to 154 cm^3 g^{-1} of MBG_Sr4%_SD, was observed for increasing amount of substituting element, as already reported for Sr-containing glasses [15]. Nevertheless, the obtained SSA values are remarkably higher than those of conventional sol-gel glasses, allowing an improved reactivity in physiologic environment [7]. As expected, based on the features of the used templating agent (Pluronic P123), spray-dried samples showed an average pore size of about 8 nm [18], irrespective of the amount of strontium in the synthesis solution.

Table 4.20 Structural features of MBG_Sr2%_SD and MBG_Sr4%_SD.

Name	Specific surface area (cm^3/g)	Pore size (nm)	Volume (cm^3/g)
MBG_Sr2%_SD	167	8.3	0.18
MBG_Sr4%_SD	154	7.8	0.17

4.2.2b Bioactive behaviour of MBG_ Sr2%_SD and MBG_ Sr4%_SD in SBF

The remarkable bioactivity of MBG_Sr2%_SD and MBG_Sr4%_SD when soaked in SBF was clearly revealed by FE-SEM observations (figure 4.8). In fact, irrespective of the strontium content, both MBG_Sr2%_SD and MBG_Sr4%_SD exhibited a faster bioactive behavior inducing the deposition of numerous HA crystals on their surface after only 3 days of soaking in SBF (figure 4.8 (a) and 4.8
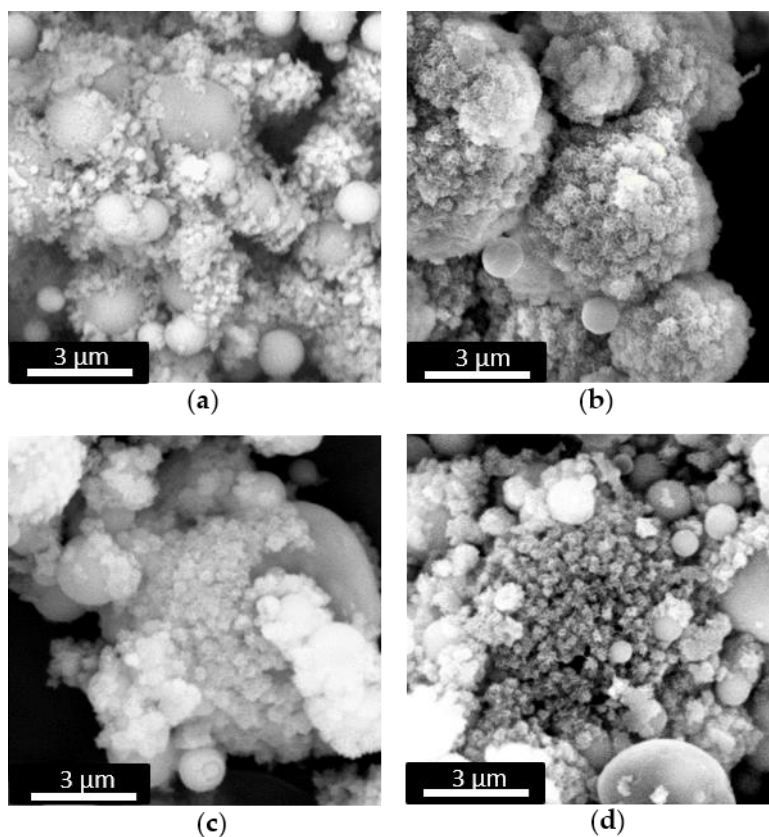
Figure 4.79 FE-SEM images of powders after soaking in SBF: (a) MBG_Sr2%_SD after 3 days; (b) MBG_Sr2%_SD after 7 days; (c) MBG_Sr4%_SD after 3 days; (d) MBG_Sr4%_SD after 7 days.

(c)). After 7 days of soaking, the particles appeared completely covered by a compact layer of HA having the typical cauliflower morphology.

The precipitation of a HA layer on the Sr-containing samples and its crystalline nature was confirmed by XRD analysis: new peaks appeared at 25.8 and 32.0 2θ degrees in all MBG samples matching the HA reference (00-001-1008) as can be observed in figure 4.9.
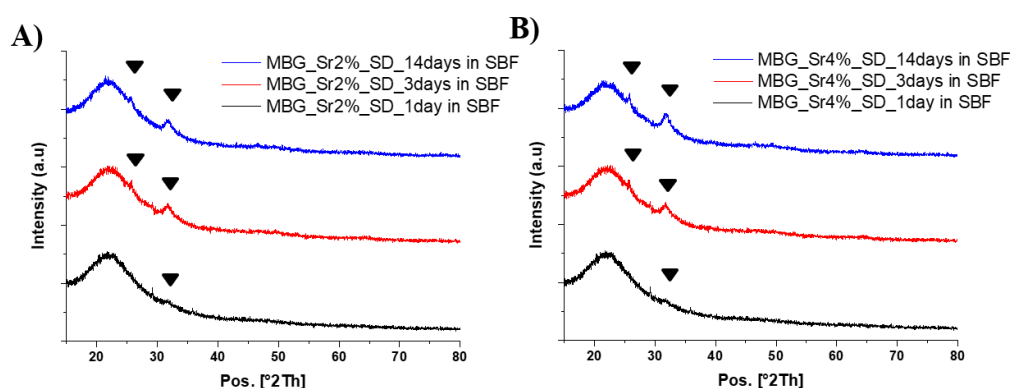
Figure 4.80 XRD spectra after different time of soaking in SBF of: (A) MBG_Sr2%_SD and (B) MBG_Sr4%_SD.

The effect of strontium content in bioactive glasses on HA formation remains an open issue in the literature. Arepalli *et al.* [19] and Taherkhani *et al.* [20] reported that the introduction of relatively high amount of strontium increased the HA formation both for melt-derived and sol-gel bioactive glasses, due to the decrease of the silica network connectivity. On the contrary, Moghanian *et al.* [12] and Hu *et al.* [21] found that the partial molar substitution of Ca^{2+} with Sr^{2+} induced a decreased release of calcium ions from the glass into the SBF, causing consequently the reduction of its apatite-forming ability. In this PhD work, based on morphological and structural analysis irrespective of the synthesis procedure, the kinetics of HA formation of Sr-containing MBGs appeared not significantly influenced by the amount of incorporated strontium.

In addition, as already notified for the SG samples, during the *in vitro* bioactivity test the pH of the SBF solution remained below 7.8 which is considered the threshold value for allowing osteoblasts to maintain their physiological activity [8], making these systems appropriate for bone regenerative applications.

The overall characterization demonstrated the versatility and the reliability of the two employed preparation methods to produce Sr-containing MBGs with tailored morphology (particle size), structural features (surface area, pore size), incorporated amount of bivalent ions and release properties, without affecting the excellent bioactive behavior typical of MBGs.

4.2.2c Strontium ion release from MBG_ Sr2%_SD and MBG_ Sr4%_SD in Tris HCl

As previous reported for the strontium-containing SG samples, both MBG_Sr2%_SD and MBG_Sr4%_SD showed also a burst release of Sr^{2+} in the first 3 h of soaking in Tris-HCl, followed by a stationary trend (figure 4.10).
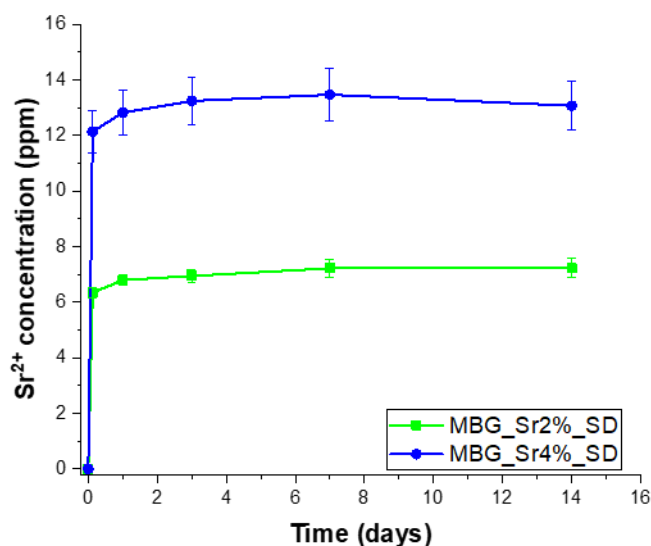
Figure 4.81 Sr^{2+} release profile of MBG_Sr2%_SD and MBG_Sr4%_SD in Tris HCl.

Similarly, the fast ion release could be attributed to the high accessibility of medium into the porous structure and the fast ionic exchange reactions occurring at the surface. The final strontium concentration after 72 h of soaking was 7.2 ppm for MBG_Sr2%_SD and 13.2 ppm for MBG_Sr4%_SD, which represented respectively the 94% and the 100% of the amount initially incorporated into the two samples, which resulted very similar to the theoretical value (see table 4.4).

Table 4.21 Sr^{2+} amount incorporated expressed in mol % and ppm, Sr^{2+} released quantity in ppm after 3 h and 72 h of soaking in Tris HCl.

Sample	Sr^{2+} Incorporated mol %	Sr^{2+} Incorporated ppm	Sr^{2+} Released at 3 h (ppm)	Sr^{2+} Released at 72 h (ppm)
MBG_Sr2%_SD	2.0%	7.20	6.30	6.90
MBG_Sr4%_SD	3.7%	13.20	12.1	13.2

4.2.3 *In vitro* Biological Assessment of Sr-containing MBGs

Part of the work described in this chapter has been previously published in [2].

The following *in vitro* biological assessment was performed in collaboration with *Nobil Bio Ricerche*, in the frame of the MOZART project and aimed to evaluate if the developed Sr-containing samples and their released products allow cell survival and can exhibit a therapeutic effect by stimulating pre-osteoblastic cells. In order to study this aspect and the role of both the particles size and the structural features on the induced biological response, the experiments described in "*materials and methods*" chapter, were carried out on MBG_Sr2%_SD and MBG_Sr2%_SG. This section reported the obtained results related to the biocompatibility, the inflammatory response and the pro-osteogenic response of both MBG_Sr2%_SG and MBG_Sr2%_SD.

4.2.3a Biocompatibility of Sr-containing MBGs

Fibroblast cells were selected as a model cell line to explore the biocompatibility of MBG_Sr2%_SG and MBG_Sr2%_SD samples, by using a polystyrene plate as negative control and a polystyrene plate added with 0.08 mg/mL of Sodium
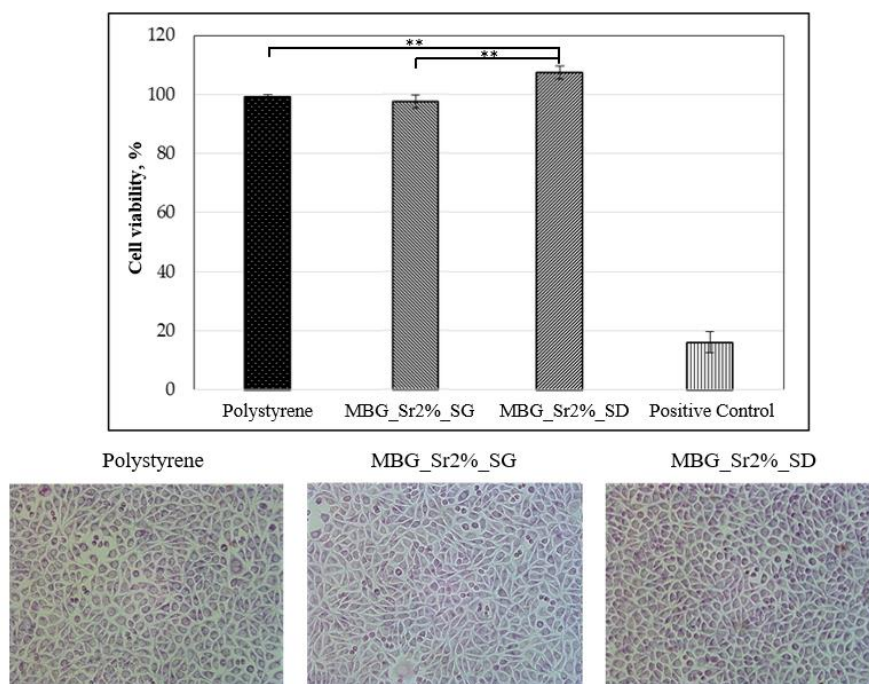
Figure 4.82 Section above: quantification of cell viability through MTT assay for MBG_Sr2%_ SG and MBG_ Sr2%_SD compared with polystyrene (negative control) and positive control (polystyrene with 0.08 μg/mL of NPS). (* p ≤ 0.05, ** p ≤ 0.01, ***p ≤ 0.001 and **** p ≤ 0.0001.). Section below: optical images of cells after 72 h of incubation with MBG_Sr2%_ SG and MBG_ Sr2%_SD at concentration of 1 mg/1 mL, compared to cells seeded on polystyrene plate.

Nitroprusside to induce cell death as positive control. The results of cell viability tests and the optical images of cell morphology are reported in figure 4.11 and

confirmed that the presence of Sr-containing MBG particles did not significantly alter the cell morphology, which appeared comparable to that shown by the cells grown on polystyrene plate (negative control). MTT assay evidenced that both MBG_Sr2%_SG and MBG_Sr2% SD showed excellent biocompatibility, with a cell viability percentage higher than 70%, which according to the international standard ISO 10993-5: 2009-Biological Evaluation of Medical Devices Tests for *In vitro* cytotoxicity -, is the minimum value required for considering biocompatible the tested material.

4.2.3b Inflammatory Response of Sr-containing MBGs

Usually, one of the major issues associated to nano- and micro-sized material is the induction of the inflammatory response, which could be even more severe if associated to particle dissolution products. In order to investigate the effect of both material size and ion release from the particles in inducing pro-inflammatory reactions, murine macrophage cell line were seeded in the presence of MBG_Sr2%_SG and MBG_Sr2%_SD and the expression of three pro-inflammatory genes was evaluated: interleukin 1β (IL1β), an important mediator of the inflammatory response and involved in a variety of cellular activities, including cell proliferation, differentiation and apoptosis; interleukin 6 (IL6), an important mediator of fever and of the acute phase response and, finally, tumor necrosis factor-α (TNF-α), involved in the systemic inflammation response and in the make-up of the acute phase reaction. figure 4.12 shows the fold expression of the listed genes obtained for MBG_Sr2%_SD and MBG_Sr2%_SG compared with the polystyrene plate control. The results showed that there was no increase in the inflammatory response due to the presence of both Sr-containing MBGs. In particular, a significant reduction of IL6 and of IL1β expression was detected for MBG_Sr2%_SD compared with polystyrene and MBG_Sr2%_SG. At variance, a slightly increase of cytokines expression was identified for the MBG_Sr2%_SG. The reason could be associated to the smaller size of the latter compared to the micro-size of MBG_Sr2%_SD. Several studies have shown that nanoparticles and sub-micro particles are more pro-inflammatory compared to their microparticle counterparts [22–24] although the question is still controversial as conflicting results have been obtained in other studies [25,26]. In particular, Kusaka *et al.* reported a study on the effect of amorphous silica particle size on macrophages inflammatory response, where they showed an increase in the expression of IL1β and consequently of TNFα for particles with a size between 30 nm–1000 nm due to a lysosomal damage caused by their internalization by macrophages [23].
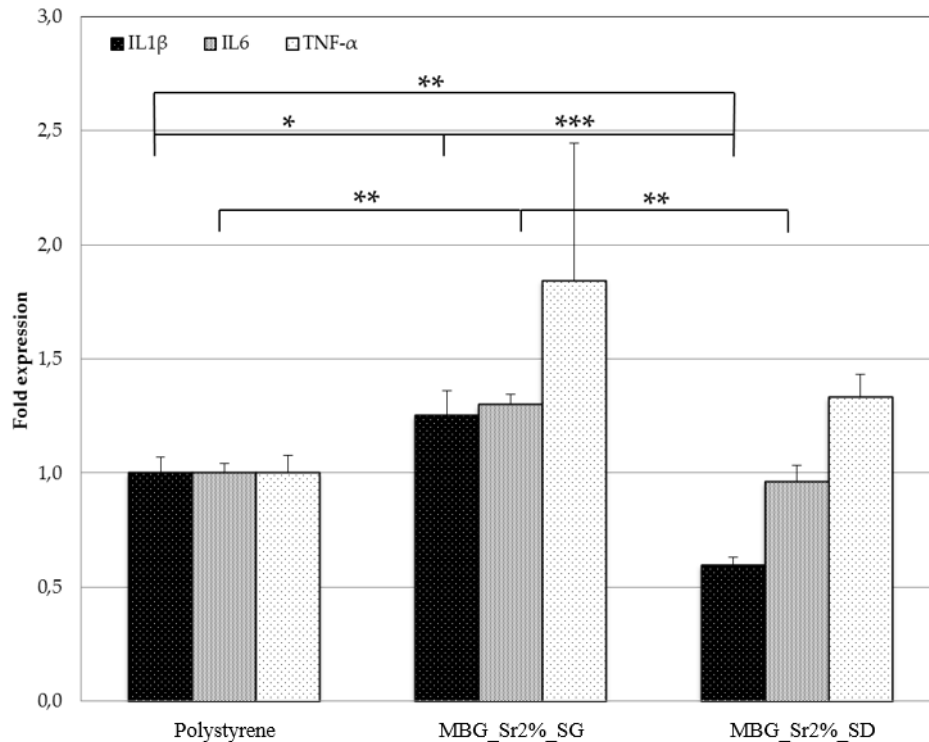
Figure 4.83 Gene expression of macrophages after 4 h of cell culture in direct contact with MBG_Sr2%_SD and MBG_Sr2%_SG. Fold expression of cytokines IL1β, IL 6 and TNFα. (* p < 0.05, ** p < 0.01, *** p < 0.001 and **** p < 0.0001.).

On the other hand, the reduction of IL1β, IL6 and TNFα expression observed for the MBG_Sr2%_SD, could be also ascribed to the release of strontium ions. In the literature, the release of Sr^{2+} is reported to produce a positive effect on cytokines production, decreasing the inflammatory reaction. Renaudin *et al.* demonstrated that monocyte cells, stimulated with lipopolysaccharide (LPS) to induce an inflammatory reaction, produced a significantly lower amount of TNFα when incubated with particles able to release strontium ions [27]. Since MBG_Sr2%_SD was able to release three times the amount of Sr^{2+} compared to MBG_Sr2%_SG (see section 3.1.2), a correlation between the amount of released Sr^{2+} and the reduction of pro-inflammatory cytokines could be postulated.

4.2.3c Pro-osteogenesis of Sr-containing MBGs

Pro-osteogenic response of Sr-containing MBGs, was evaluated by performing the experiments with Transwell® permeable insert, which by hindering to a large extent the direct contact between the particles and the cells, allowed to elucidate the role of the released ions. The effect on the expression of pro-osteogenic genes due to the ionic extracts of MBG_Sr2%_SG and MBG_Sr2%_SD was evaluated by Rt-PCR analysis and the related results are shown in figure 4.13.
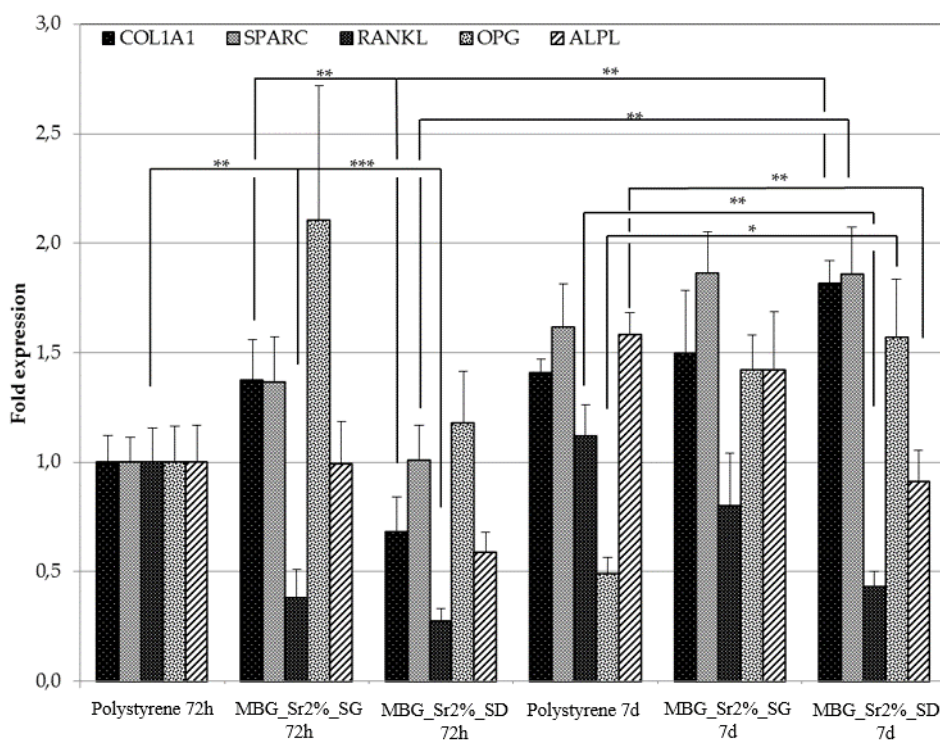
Figure 4.84 The expression level of the COL1A1, SPARC, RANKL, OPG and ALPL genes of osteoblast-like cells (SAOS2) analyzed by qRT-PCR at 72 h and at 7 days (* p ≤ 0.05, ** p ≤ 0.01, *** p ≤ 0.001 and **** p ≤ 0.0001).

The pro-osteogenic effect was evaluated by considering the expression of different type of genes involved in the process of bone regeneration. In particular, RANKL and OPG genes are fundamental markers for the assessment of the osteogenic potential. In fact, OPG can reduce the production of osteoclasts and consequently the excessive bone resorption, by inhibiting the differentiation of osteoclast precursors. When OPG binds to RANKL on osteoblasts, it blocks the RANKL-RANK interaction between osteoblasts and osteoclast precursors, then inhibiting their differentiation into mature osteoclasts [28,29]. Therefore, the RANKL/OPG ratio is widely considered an important indication of bone mass and skeletal integrity [30,31].

At 72 h and 7 days, gene expression analysis showed a decreased expression of RANKL for both types of Sr-containing MBGs, with a RANKL/OPG ratio in favour of OPG expression being ≤1, as reported in table 4.5. Interestingly, at 7 days this ratio switched in favour of RANKL in the polystyrene cultured cells, while remained almost unchanged in presence of both Sr-containing MBGs. In particular, this ratio was 2.291 for cells grown on polystyrene plates, and 0.563 and 0.275 in the presence of MBG_Sr2%_SG and MBG_Sr2%_SD, respectively. The increase of the OPG expression of cells cultured in the presence of ionic extracts from Sr-containing MBGs suggests the inhibition of osteoclastogenesis, confirming the osteogenic activity induced by released Sr^{2+} ions in amount suitable to exert *in vitro* a therapeutic effect.

Table 4.22 RANKL/OPG ratio at 72 h and 7 days, for MBG_Sr2%_SG, MBG_Sr2%_SD and polystyrene. A significant down regulation of RANKL and an overexpression of OPG, results in a RANKL/OPG ratio in favour of bone remodelling at both time points.

Sample	RANKL/OPG
Polystyrene 72 h	1.000
MBG_Sr2%_SG 72 h	0.181
MBG_Sr2%_SD 72 h	0.230
Polystyrene 7 d	2.291
MBG_Sr2%_SG 7 d	0.563
MBG_Sr2%_SD 7 d	0.275

A non-negligible increase of the RANKL/OPG ratio was observed for MBG_Sr2%_SG at 7 days. The increased expression of RANKL gene of osteoblast cells is consistent with the results of pro-inflammatory response experiment, in which MBG_Sr2%_SG showed an increased expression of TNFα gene. Indeed, in inflammatory bone diseases, the systemic increase of TNF stimulates the generation of osteoclast precursors (OCPs) in the bone marrow and enhances their transfer into the bloodstream. These OCPs differentiate into osteoclasts and sustain their production in response to TNF and RANKL, by significantly affecting the final bone volume and turnover [32]. However, the RANKL increase of cells cultured with MBG_Sr2%_SG was not enough substantial to overturn the ratio. An over-expression of COLL1A1 gene (an early precursor of mineralization) was detected for MBG_Sr2%_SG at 72 h, without further increase at 7 days. Conversely, an initial down regulation was detected for MBG_Sr2%_SD, which at variance showed a significant over expression at 7 days.

In addition, an earlier and late expression of osteonectin in presence of both MBG_Sr2%_SG and MBG_Sr2%_SD particles has been observed. Osteonectin, known as SPARC, is a glycoprotein expressed in bone during the remodelling process. The over- expression of SPARC at 72 h and in particular after 7 days, may suggest that strontium ions could have an active role during bone regeneration. Osteonectin is synthesized by osteoblast cells and plays a role in binding bone minerals (HA) and type I collagen [33,34] and, in addition, is proved to inhibit mineralization *in vitro* [35,36]. This last property finds partial confirmation in the downregulation of ALPL, which is an early and late mineralization gene.

The overall data suggest that both MBG_Sr2%_SG and MBG_Sr2%_SD are able to promote bone formation, stimulating the expression of COLL1A1, SPARC and OPG and a down regulation of RANKL.

This preliminary in *vitro* biological assessment evidenced the biocompatibility of the produced Sr-containing MBGs and confirmed the anti-inflammatory and pro-osteogenic effect of Sr^{2+} ions [27,35,37–39] released by MBGs nano and microparticles.

4.2.4 Strontium-containing MBGs loaded with N-Acetylcysteine by IW method

Since the release of strontium has been proved to induce bone formation, in order to further boost the therapeutic potential of the produced multifunctional device, N-Acetylcysteine (NAC) has been selected and loaded into the strontium-containing MBG mesopores as osteogenesis-enhancing molecule to be delivered into the bony defect where might improve bone regeneration and promote bone defect healing. In addition, based on the results obtained with the ibuprofen loading, the incipient wetness method has been selected as loading procedure against the adsorption method, since allows to avoid the time-consuming filtration step and to control the amount of drug loaded into the carrier. In addition, the IW method has been proved to be the most suitable compared to the adsorption, in term of yield and time-consuming. In this section, the results concerning the characterization of strontium-containing MBGs loaded with N-Acetylcysteine (NAC) by using the incipient wetness method are reported.

The loading of NAC by using the IW method has been conducted by exploiting the procedure reported by Charnay *et al.* [40] and the produced samples will be hereafter named MBG_Sr2%_SG + NAC IW and MBG_Sr2%_SD + NAC IW.

4.2.4a Morphological, structural and chemical characterization of MBG_Sr2%_SG + NAC IW and MBG_Sr2%_SD + NAC IW.

FE-SEM images of MBG_Sr2%_SG + NAC IW (figure 4.14A) showed nanoparticles with a monodispersed spherical shape with a size ranging between 150-200 nm. Since the particles size results very similar to those reported for not-loaded MBG_Sr2%_SG samples (see figure 4.1A), it is possible to assume that NAC incorporation does not significantly alter the morphological features and the chemical composition of strontium-containing MBGs.

Figure 4.14B showed the FE-SEM images of MBG_Sr2%_SD + NAC IW, revealing microparticles with a with a size ranging between 1 and 5 μm. Also in this case, FE-SEM observation showed that the incorporation of NAC by IW method does not significantly interfere with the morphology and the chemical composition of strontium-containing MBGs; in fact, the particle size resulted very close to those reported for not-loaded samples (see figure 4.6A).
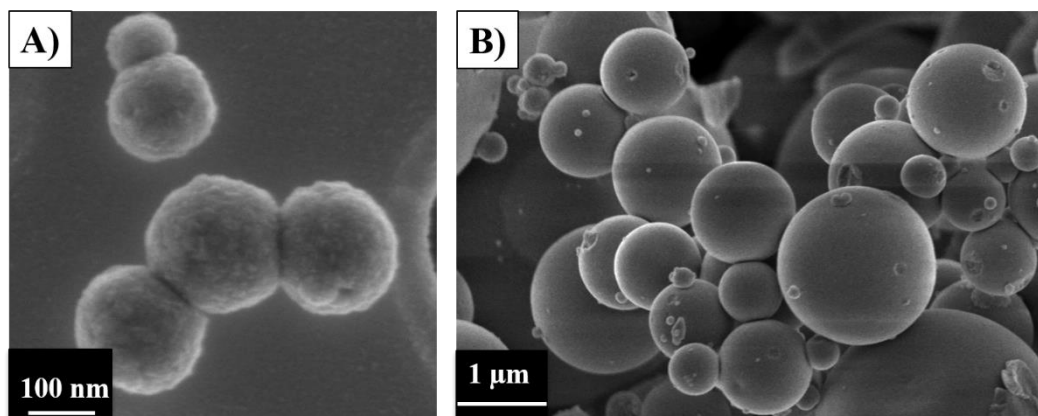
Figure 4.85 FE-SEM images of (A) MBG_Sr2%_SG + NAC IW and (B) MBG_Sr2%_SD + NAC IW.

The nitrogen adsorption–desorption isotherms and the pore size distribution of MBG_Sr2%_SG before and after drug loading are reported in figure 4.15 A and B respectively.

As expected, before loading, MBG_Sr2%_SG showed a type IV sorption isotherm, according to the IUPAC classification, with a well-defined step around 0.4 (P/P_0), indicative of uniform mesopores. The specific surface area and pore volume values reported in table 4.6 are characteristic of mesoporous materials with uniform pores and remarkable value of specific surface area (SSA_{BET})[41]. The mesopore size distribution showed two different peaks around 5 and 6 nm, which is sufficiently large to incorporate NAC. The isotherm of MBG_Sr2%_SD was a type IV curve (fig. 4.15C), with H1 hysteresis loop, typical of mesoporous material with pores larger than 4 nm and the pore size distribution showed multisided pores in the range between 8 and 11 nm, with a high population centred around 9 nm (fig. 4.15D), which easily allows the diffusion and incorporation of NAC molecules.
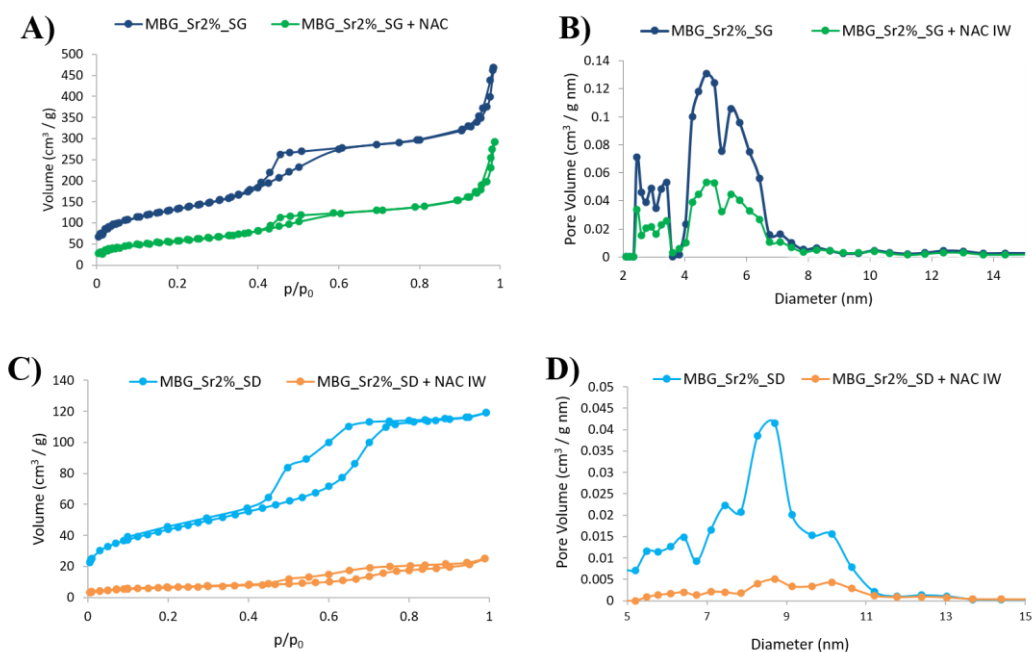
Figure 4.86 N₂ adsorption-desorption isotherm of MBG_Sr2%_SG + NAC IW compared to the not-loaded sample (A) and related DFT pore size distribution (B); N₂ adsorption-desorption isotherm of MBG_Sr2%_SD + NAC IW compared to the not-loaded sample (C) and related DFT pore size distribution (D).

For both samples, drug loading induced, as expected, a significant modification of the adsorption-desorption isotherm (reduction of the adsorbed volume and presence of hysteresis loop) and a drastic reduction of the pore volume, as shown in figure 4.15 and reported in table 4.6. In details, MBG_Sr2%_SG + NAC IW showed a reduction in both SSA and pore volume, lower compared to the market reduction observed for MBG_Cu2%_SG + Ibu IW samples, discussed in the previous section. On contrary, as far as the MBG_Sr2%_SD + NAC IW is concerned, the modification of the isotherm curve upon drug incorporation suggests that most of the mesopores are completely filled with NAC and the remaining population experiences size reduction and shape modification from cylinder to ink-bottle pores, in analogy to the results reported by Hong *et al.* [42] for similar systems. The drastic reduction of pore volume as a consequence of drug incorporation was confirmed by the disappearance of the multisized pore distribution and the component centred around 9 nm (Figure 4.15D).

The lower reduction in pore volume evidenced to the MBG_Sr2%_SG + NAC IW samples could be probably ascribed to the bigger pore volume, which allows the incorporation of drug molecules without a full occlusion of the available pore volume.

Acronym	SSA_{BET} (cm^3/g)	Pore volume (cm^3/g)	Pore size (nm)
MBG_Sr2%_SG	477	0.58	8-10
MBG_Sr2%_SG + NAC IW	211	0.32	8-10
MBG_Sr2%_SD	156	0.18	8-10
MBG_Sr2%_SD + NAC IW	22	0.035	8-10

The total amount of loaded NAC was quantified by TGA analysis. As reference, TGA analysis was also performed on not-loaded MBG sample, proving the complete absence of residual organic species at 600 °C. TGA thermograms of MBG_Sr2%_SG + NAC IW (figure 4.16A) exhibited a significant weight decrease between 200 and 400 °C. The latter ascribable to NAC loss [43] is most likely due to the multiple H-bonding interactions between the drug molecules and the large population of hydroxyl groups of the inner MBG surface, suggesting the confinement of NAC molecules, as already notified in literature for different drugs
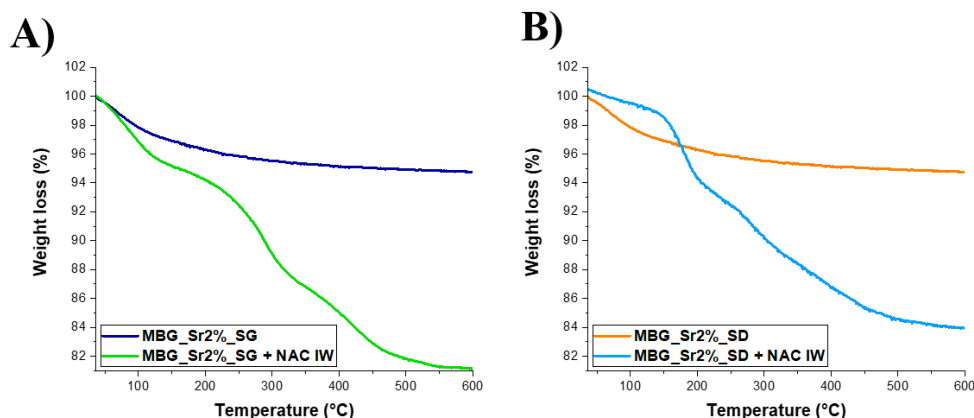
Figure 4.87 TGA thermograms of (A) MBG_Sr2%_SG and MBG_Sr2%_SG + NAC IW and (B) MBG_Sr2%_SD and MBG_Sr2%_SD + NAC IW.

[44]. The weight percentage of loaded NAC, based on TGA analysis, turned out to be 15% for MBG_Sr2%_SG + NAC IW.

As far as the MBG_Sr2%_SD + NAC IW (figure 4.16B) is concerned, a weight loss between 200 and 400 °C, is observed, also in this case associated to NAC loss [16] The weight percentage of loaded NAC, based on TGA analysis, resulted to be 12%, lower compared to the corresponding MBG-SG samples. The lower amount of incorporated drug could be ascribed to the lower specific surface area and pore volume of the SD samples, compared to the SG samples. These results confirmed

that the drug loading capacity increases with the increase of MGB surface area and pore volume, according to data reported in the literature for mesoporous silicas [45].

FTIR spectra of both strontium-containing MBGs before and after NAC loading are reported in figure 4.17A and 4.17B. All samples showed the typical adsorption bands of H-bonded hydroxyls (stretching vibration) in the range of 3750–3000 cm^{-1}. Concerning the drug-loaded samples, FTIR spectrum of both MBG_Sr2%_SG + NAC IW and MBG_Sr2%_SD + NAC IW showed the typical bands which could be associated to the NAC: at 2935 the absorption bands ascribed to C-H stretching modes and at 1535 and 1430 cm^{-1}, due to the asymmetric (v_{as}) and symmetric (v_s) stretching vibration of the carboxylate group COO$^-$, respectively [46]. In addition, for both samples, the typical peak associated to the S-H stretching of the thiol groups appeared at 2565 cm^{-1}, further proving the successfully incorporation of NAC into the MBG pores.
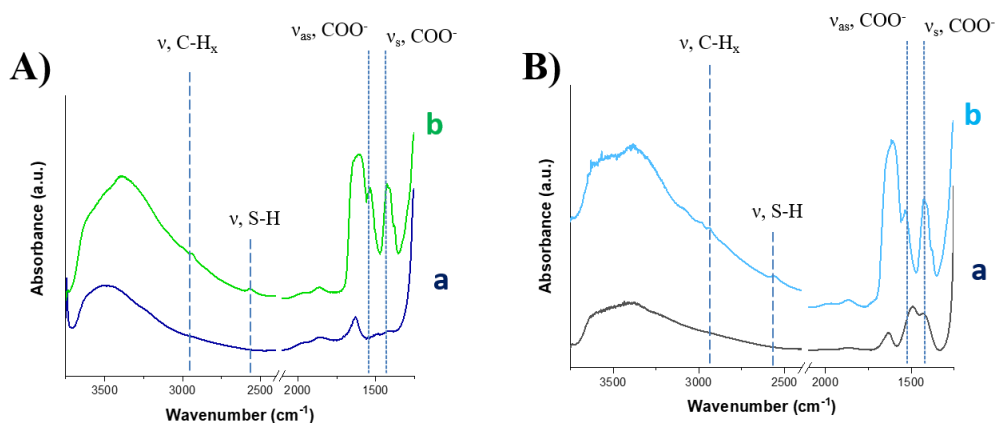
Figure 4.88 FTIR spectra of (A) MBG_Sr2%_SG and MBG_Sr2%_SG + NAC IW and (B) MBG_Sr2%_SD and MBG_Sr2%_SD + NAC IW.

As widely reported in the literature[47,48], the loading of the drug in the amorphous state could increase the drug dissolution rates and solubility.

Hence, DSC and XRD analysis of NAC-loaded samples were conducted to assess the amorphous state of the drug and exclude the presence of large crystalline aggregates. Both the DSC thermograms of NAC as such and of MBG_Sr2%_SG + NAC IW and MBG_Sr2%_SD + NAC IW are reported in fig. 4.18B and 4.18A, respectively: the single endothermic melting peak at 120 °C, observed only for NAC as such, corresponds to crystal phase melting. The absence of this peaks in

both the NAC loaded sample thermograms confirms the non-crystalline state of the drug into the mesopores.
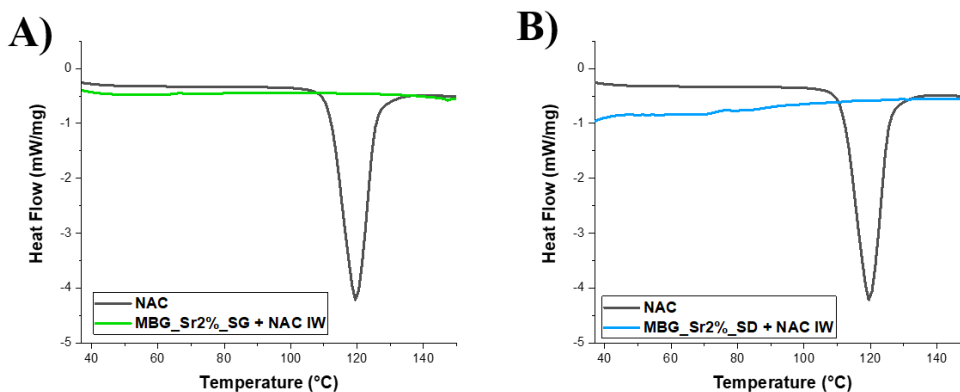
Figure 4.89 DSC thermograms of (A) NAC and MBG_Sr2%_SG + NAC IW and (B) NAC and MBG_Sr2%_SD + NAC IW.

The amorphous state of the drug was further assessed by XRD analysis (fig. 4.19). XRD pattern of both MBG_Sr2%_SG + NAC IW and MBG_Sr2%_SD + NAC IW powder showed a broad peak typical of amorphous materials, confirming the absence of crystalline oxide-based phases.

In accordance with DSC data, XRD analysis strongly suggested that ri-crystallization of the drug did not occur inside the pores upon solvent evaporation during the incorporation process, as already previously notified for the corresponding copper-containing MBGs loaded with ibuprofen.
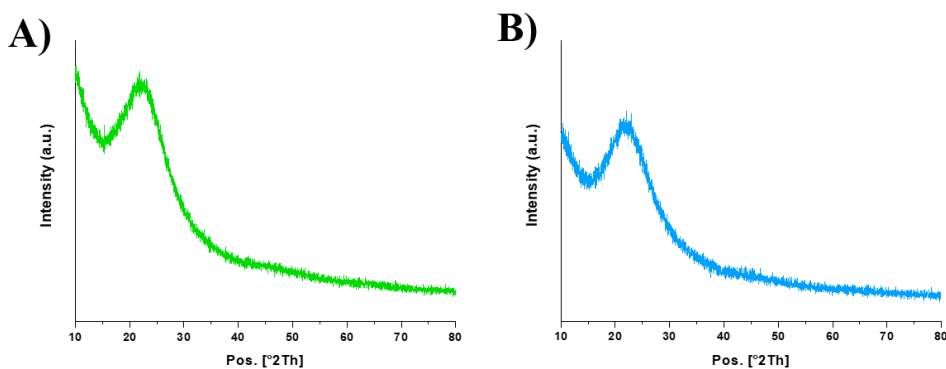
Figure 4.90 XRD patterns of (A) MBG_Sr2%_SG + NAC IW and (B) MBG_Sr2%_SD + NAC IW.

4.2.4b Bioactive behaviour of MBG_Sr2%_SG + NAC IW and MBG_Sr2%_SD + NAC IW in SBF

FE-SEM observations clearly confirmed that the bioactive behaviour of both MBG_Sr2%_SG + NAC IW and MBG_Sr2%_SD + NAC IW was retained after soaking in SBF after the NAC loading. In fact, a rough layer of globular agglomerates on the surface of the particles appeared after just 1 day of soaking as shown in figure 4.20A1 for MBG_Sr2%_SG + NAC IW and in figure 4.20B1 for MBG_Sr2%_SD + NAC IW. After 7 days, the particles were fully covered by a
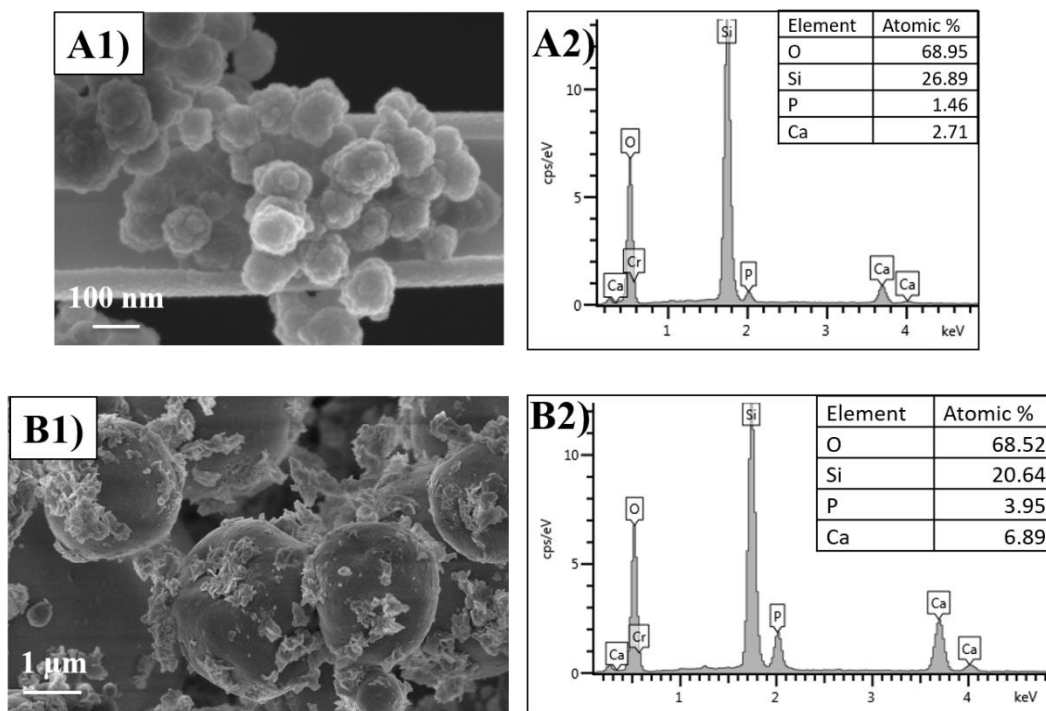
Figure 4.91 (A1) FE-SEM observation of MBG_Sr2%_SG + NAC IW; (A2) EDS spectrum of MBG_Sr2%_SG + NAC IW; (B1) FE-SEM observation of MBG_Sr2%_SD + NAC IW; (B2) EDS spectrum of MBG_Sr2%_SD + NAC IW after 1 days of soaking in SBF.

compact layer of needle-like nanocrystals. As shown in figure 4.20A2 and B2, the presence of HA crystals has been revealed by the EDS analysis performed on powders which evidenced a Ca/P ratio close to 1.7, typical of HA [49,50].

The formation of crystalline HA after the bioactivity test has been evaluated also by wide-angle XRD analysis performed on both the MBG_Sr2%_SG + NAC IW and MBG_Sr2%_SD + NAC IW particles after 1 days of soaking in SBF. Figure 4.21 showed marked peaks observed for both the samples at 25.87° and 31.73° (2θ value) which matched with the hydroxyapatite reference (01-089-6440). As already notified for the Copper-containing MBGs loaded with ibuprofen, the drug loading does not hinder the bioactive behaviour typical of the mesoporous bioactive glasses.
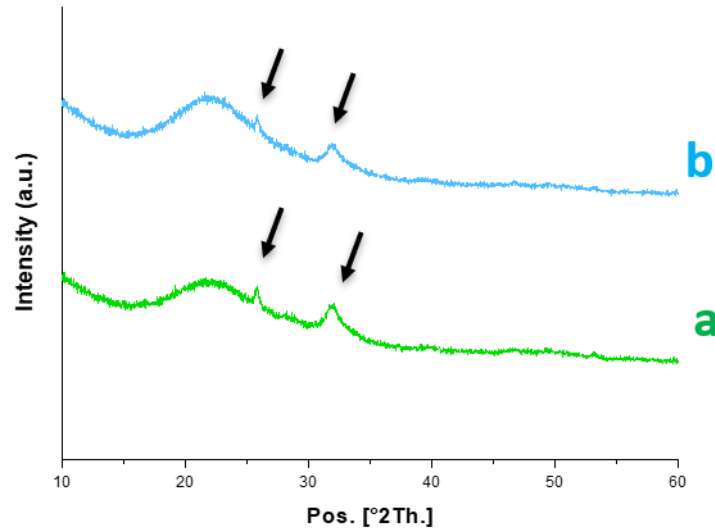
Figure 4.92 XRD spectra of (a) MBG_Sr2%_SG + NAC IW and (b) MBG_Sr2%_SD + NAC IW after 1 day of soaking in SBF.

4.2.4c Strontium release from MBG_Sr2%_SG + NAC IW and MBG_Sr2%_SD + NAC IW in Tris HCl

The concentration of strontium ions released from MBG_Sr2%_SG + NAC IW and MBG_Sr2%_SD + NAC IW powder after soaking in Tris HCl medium is reported in figure 4.22A and B, respectively.

A burst release of Sr^{2+} in the first 3 h of soaking in Tris-HCl, followed by a stationary trend up to 14 days of incubation is observed for both samples, as already notified for the non-loaded strontium containing MBGs. In fact, similarly, the fast ion release could be attributed to the high accessibility of medium into the porous
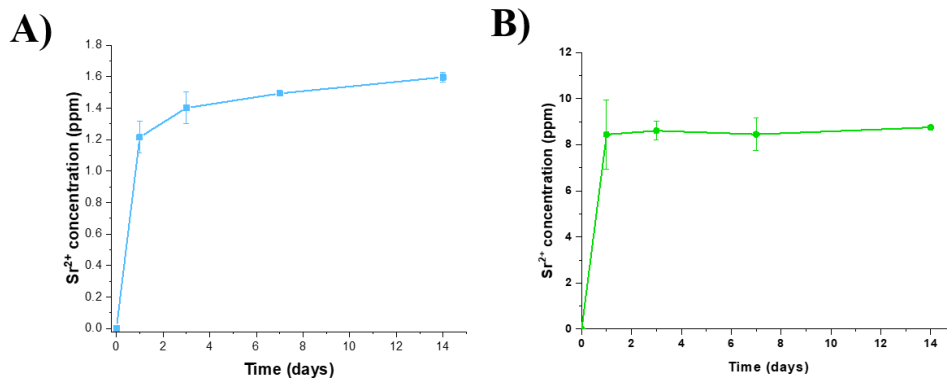
Figure 4.93 Sr^{2+} release profile of (A) MBG_Sr2%_SG + NAC IW and (B) MBG_Sr2%_SD + NAC IW in Tris HCl.

200

structure and the fast ionic exchange reactions occurring at the surface. The final strontium concentration after 3 h of soaking was 1.4 ppm for MBG_Sr2%_SG + NAC IW and 8.1 ppm for MBG_Sr2%_SD + NAC IW, which represented respectively the 90% and the 100% of the amount initially incorporated into the two samples.

As already observed for the Copper-containing MBGs loaded with ibuprofen, the NAC loading within the porous structure seems to not interfere with the capability to release therapeutic ions through ion-exchange reactions.

4.2.4d NAC release from MBG_Sr2%_SG + NAC IW and MBG_Sr2%_SD + NAC IW in Tris HCl

N-Acetylcysteine release test was performed in Tris-HCl up to 24 hours. Figure 4.23 showed the release profile of NAC from MBG_Sr2%_SG + NAC IW and MBG_Sr2%_SD + NAC IW powders respectively, revealing that the total amount of loaded drug was released in the first hour of soaking in the medium. The burst release is then followed by a plateau till the end of the test (24h). As already reported for the copper-containing MBGs samples loaded with ibuprofen, the weak interactions between the NAC and the silica surface enhance the fast diffusion of the drug in the medium [51].
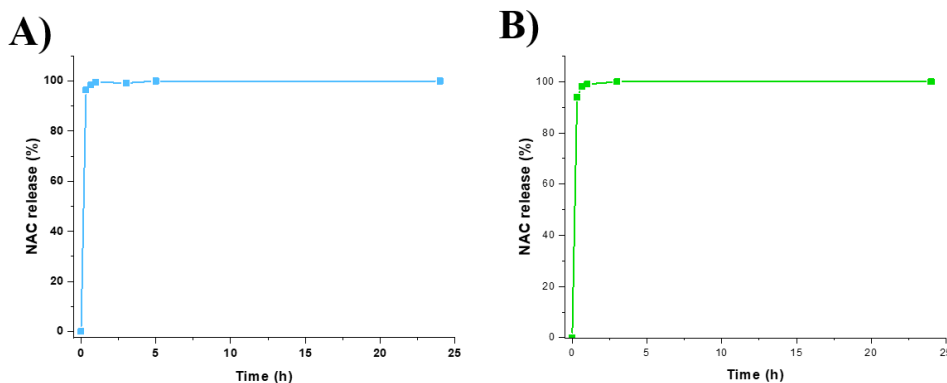
Figure 4.94 NAC release profile of (A) MBG_Sr2%_SG + NAC IW and (B) MBG_Sr2%_SD + NAC IW in Tris HCl.

Concerning the MBG_Sr2%_SG + NAC IW sample, the fast release kinetics can be ascribed to the size of MBGs; in fact, a correlation between the drug release rate and the particle size has been proved to influence the release kinetics. As reported in the literature, small spherical particles size of around 100-200 nm show the fastest drug release rate [52].
The burst release rate of MBG_Sr2%_SD + NAC IW sample, on the contrary, can be associated to the pore diameter. In fact, as widely discussed in the literature, an increase in pore diameter has been proved to increase the drug release rate. Despite the bigger size of the MBG-SD samples, compared to the corresponding MBG-SG

samples, that would assume a slower release kinetics, the bigger pore diameter (8-10 nm, compared to the 6 nm of the SG samples) is responsible for the fast drug release. Furthermore, the mesopores result to be accessible to the medium, increasing the drug transport from the pores to the solution, thus allowing the release of the NAC due to unrestricted diffusion pathway through the mesopore network [53].

4.3 Hybrid formulation based on strontium-containing MBGs incorporated into a thermosensitive hydrogel

Since MBGs alone are not exploitable as long-term drug delivery systems for orthopaedic applications, due to the strong burst release of the therapeutic species once in contact with body fluids, and the difficulties related to their administration at the pathological site (*i.e.,* bone fracture cavity) in the form of powder, their combination with polymers able to modulate the release kinetics and/or to act as a vehicle phase to the pathological site has been investigated. In particular, during this PhD work, MBGs have been incorporated into an injectable Poly(ether urethane) (PEU) based thermosensitive hydrogel developed by *Professor Ciardelli's group (DIMEAS, Politecnico di Torino, Italy)*. A preliminary *in vivo* study to evaluate the efficacy and the safety of the developed bone healing device based on MBG_Sr2%_SD + NAC IW incorporated into the hydrogel was carried out in collaboration with the *Julius Wolff institute, Charitè – Universitätsmedizin Berlin,* during my three months period in Berlin in the group of Prof. Katharina Schmidt-Bleek (consortium partner in the MOZART project).

4.3.1 Strontium-containing MBGs incorporated into the PEU hydrogel: PEU_MBG_Sr2%_SD_NAC

Strontium-containing MBG-SD loaded with NAC were prepared by following the procedures reported in section 2.4.2. N-acetylcysteine was successively loaded by using the incipient wetness method. The so-prepared particles were fully characterized, showing the peculiar features well described in the previous sections. After the characterization, MBG_Sr2%_SD + NAC IW was encapsulated into the PEU-based hydrogels produced by Prof. Gianluca Ciardelli's group with final particle concentration of 20 mg/mL. Hereafter, the developed sol-gel systems will be referred as PEU_MBG_Sr2%_SD_NAC.

The morphology and the stability in aqueous environment in the presence of a buffer solution at pH 7.4 at 37 °C of hybrid formulation, as well as the temperature-dependent sol-to-gel transition of the developed systems was characterized by Prof. Gianluca Ciardelli's group (data not reported). Once assessed that the size of MBG particles embedded into the hydrogels was not significantly affected by the immersion into an aqueous medium and that the incorporation of the particles into the hydrogel does not affected the gelation potential of PEU-based hydrogels upon temperature increase, both the strontium ion and NAC release tests were performed.

In this section, the results concerning the release kinetics of both strontium and NAC from the hybrid formulations PEU_MBG_Sr2%_SD_NAC are presented.

4.3.1a NAC release from PEU_MBG_Sr2%_SD_NAC in Tris HCl

NAC release profile from PEU_MBG_Sr2%_SD_NAC was assessed in physiological-like conditions, using Tris HCl at 37 °C (figure 4.24), showing a sustained release of the drug, reaching a percentage release after 7 days incubation of 90 %. In addition, the release profile of NAC from PEU_MBG_Sr2%_SD_NAC has been compared with the release kinetics of NAC from the bare samples, MBG_Sr2%_SD + NAC IW.
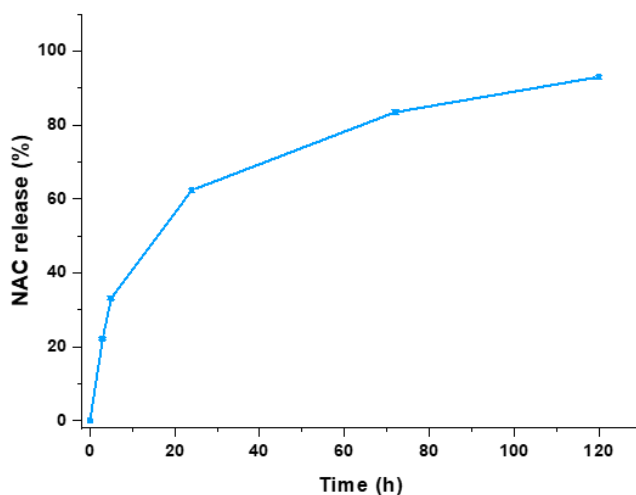
Figure 4.95 NAC release (%) profile from PEU_MBG_Sr2%_SD_NAC hydrogel.

Figure 4.25 shows the NAC release profiles from MBG_Sr2%_SD + NAC IW and PEU_MBG_Sr2%_SD_NAC up to 24 hours observation time.
As previous reported in section 4.2.4, MBG_Sr2%_SD + NAC IW showed a burst NAC release profile, and the total amount of loaded NAC was released in the first hours of incubation. By the comparison of the kinetics within the first 24 hours of NAC release from free and hydrogel-containing MBG particles, the role exerted by the polymeric matrix in modulating the release profile of drug was clearly highlighted, with a significant reduction in the initial burst release upon incorporation within PEU hydrogel of about 40%.
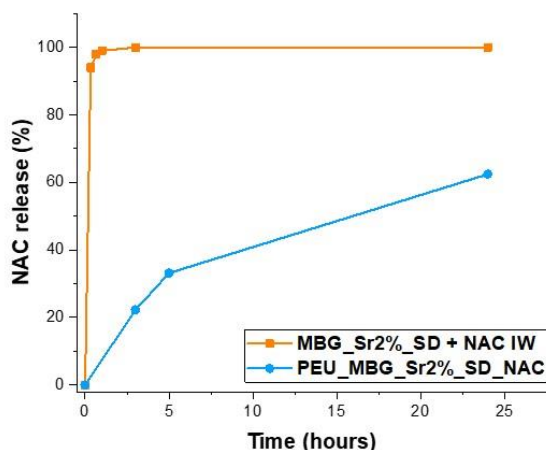
Figure 4.96 Comparison among NAC release profiles assessed from MBG_Sr2%_SD + NAC IW and PEU_MBG_Sr2%_SD_NAC up to 24 h observation time.

4.3.1c Strontium release from PEU_MBG_Sr2%_SD_NAC in Tris HCl

The release profile of strontium ions from the developed hybrid formulation was investigated, showing a trend similar to that assessed for the N-Acetylcysteine (figure 4.26). After 7 days of incubation in aqueous medium, the 56% of the strontium initially present in the MBG framework was released from PEU_MBG_Sr2%_SD_NAC. The incorporation of strontium-containing MBGs within the polymeric phase successfully decreased the undesirable initial burst release of Sr^{2+} species typically observed for particles as such. In fact, after 1 hour of incubation in similar releasing conditions, PEU_MBG_Sr2%_SD_NAC released an amount of strontium ions approximately 80 % lower compared to the corresponding free MBG particles, further confirming the role exerted by the

hydrogel in modulating the release rate of strontium, as already observed for the NAC release.
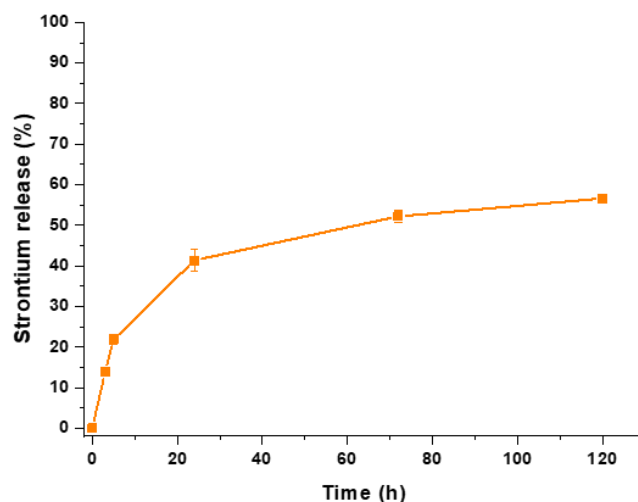
Figure 4.97 Strontium release (%) profile from PEU_MBG_Sr2%_SD_NAC hydrogel.

4.3.2 *In vivo* Biological Assessment of PEU_MBG_Sr2%_SD_NAC

Once assessed the biocompatibility of the MBG_Sr2%_SD samples and the ability of strontium to induce a pro-osteogenic effect on osteoblast-like cells (SAOS2) (see section 4.2.3), the MBG microspheres were firstly loaded with N-Acetylcysteine to further boost the therapeutic potential of the produced multifunctional device and successively incorporated into the thermosensitive hydrogel, acting as a modulator of the ion/drug release rate, but also to be used as a place-keeper for the MBG microspheres. Based on the promising results in the ion/drug release modulation described in the previous section, the ability of PEU_MBG_Sr2%_SD_NAC to exert a therapeutic effect *in vivo*, (without delaying the progression of bone healing) has been investigated. The *in vivo* biological assessment was performed at the *Julius Wolff institute, Charitè – Universitätsmedizin Berlin,* during my three months period in Berlin thanks to the collaboration with the research group led by Prof. Katharina Schmidt-Bleek, one of the academic partners involved in the MOZART project.

The *in vivo* response induced by PEU_MBG_Sr2%_SD_NAC was evaluated in a femoral osteotomy model of compromised healing in female rats [54]. After creating a 2 mm defect in the femoral shaft, one group of animals received the hybrid formulation comprised of PEU_MBG_Sr2%_SD_NAC, one group of animals did not receive any material (empty) and a third one received the hydrogel as such, serving as a control group, in order to evaluate the effective efficacy of the multifunctional device; in addition, a hybrid formulation comprised of PEU_MBG_SD_BMP-2 has been injected and refers as positive control and gold

standard. The bone morphogenetic protein 2 (BMP-2), belonging to the TGF-β superfamily, is a molecule well known for the substantial potential to enable and accelerate bone regeneration and thus was selected as gold standard and reference to be compared with the bone regeneration capability of the developed PEU_MBG_Sr2%_SD_NAC.

The healing progress was monitored radiologically by *in vivo* μCT analysis at two and four weeks (data not reported), showing an increase in both, bone volume (BV) and tissue volume (TV) for all groups, with the PEU_MBG_ SD_BMP-2 group exhibiting the highest values, as expected. After finalization at four weeks, the osteotomized bones were prepared for analysis by *ex vivo* μCT and histology. The reconstructed μCT images were used to study the bridging stage of the fracture gap (data not presented). After the decalcification and dehydration processes, bones were embedded in paraffin and finally, cut in 5 mm sections. The histological sections were then stained with Safranin O staining, to detect the new cartilage development and MOVAT's pentachrome staining in order to evaluate the relative amount of mineralized bone, cartilage, connective tissue and bone marrow.

Safranin O is commonly used as histological stain capable of staining nuclei black, cytoplasm a grayish green, collagen green and cartilage a reddish orange color. This first staining allows to highlight and quantified the formation and the amount of cartilage in and around the osteotomy gap four weeks after injury as a good measure to evaluate the healing status. As shown in figure 4.27, the empty and the hydrogel groups reveal no or low formation of cartilage, on contrary, the PEU_MBG_Sr2%_SD_NAC group showed a great amount of cartilage (the red zone), evidencing the more advanced healing status compared to the empty and hydrogel groups.
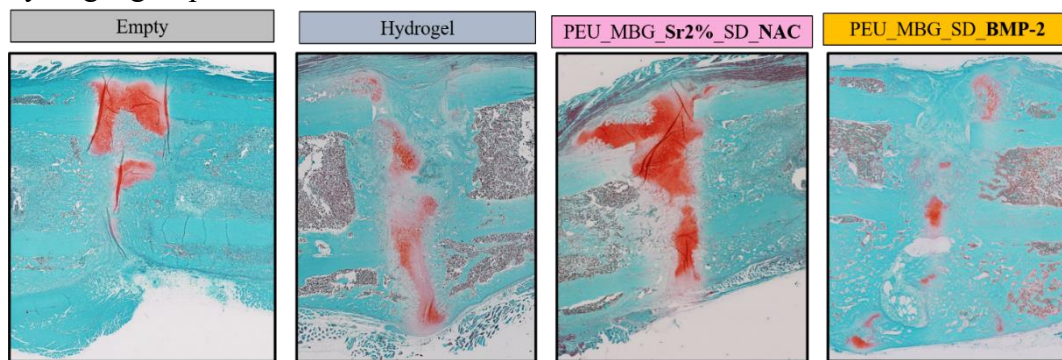
Figure 4.98 Histological analysis of rat femora at 4 weeks post osteotomy of the osteotomy gap area, reporting the representative images (10X magnification) of the gap area for all groups stained with Safranin O.

As expected, the PEU_MBG_ SD_BMP-2 group did not show any red staining, due to the presence of mineralized-cartilage or even woven bone, a clear evidence of the advanced progression of the healing process. To confirm these considerations, and to better distinguish between the non-mineralized and mineralized cartilage, bones were evaluated by Movat's pentachrome staining.

This procedure allows to consistently obtain good results, with an excellent and colorful contrast between mineralized and unmineralized compartments of both cartilage and bone. In addition, this staining is especially useful for the study of bone growth and bone repair, in fact, after the staining procedure, different tissues or components can be distinguished, as reported in table 4.7.

Table 4.24 Different tissue/components and the relative colour obtained after Movat Pentachrome staining.

Component	Colour
Nuclei	Black to blu-grey
Cartilage	Light green
Calcified cartilage	Sea green
Mineralized bone	Yellow
Muscles	Orange/red
Bone marrow	Dark red
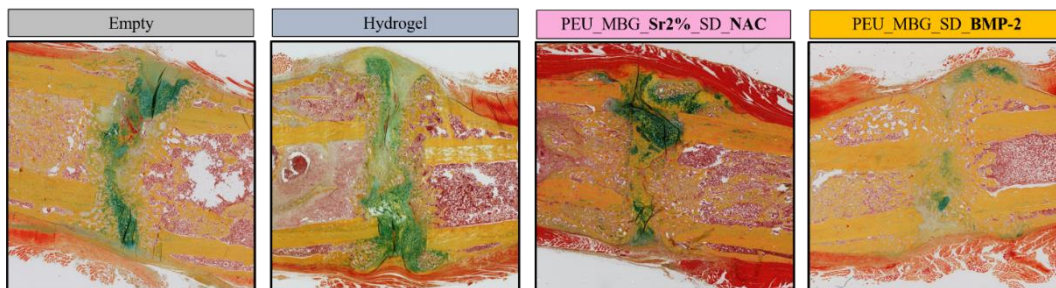
Figure 4.99 Histological analysis of rat femora at 4 weeks post osteotomy of the osteotomy gap area, reporting the representative images (10X magnification) of the gap area for all groups stained with MOVAT's pentachrome.

The histological sections of the harvested bones based on the MOVAT's pentachrome staining are reported in figure 4.28, to illustrate the tissue formation in and around the osteotomy gap four weeks after injury.

No residual of hybrid formulation or hydrogel as such was detected anymore in or around the osteotomy area. A highest non-mineralized cartilage (light green area) amounts could be observed for the empty and hydrogel groups. On contrary, the PEU_MBG_Sr2%_Sr_NAC group revealed a significantly higher amount of cartilage tissue and mineralized bone (sea green area with yellow spots, respectively), confirming the more advance progression in healing process, compared to the empty and hydrogel group, as observed with the Safranin O staining.

As expected, the PEU_MBG_SD_BMP-2 group results to be already in later stages of healing, showing woven bone formation (in yellow), a clear evidence of the

remodeling phase.

Furthermore, no significant differences could be determined between groups in terms of overall callus area, albeit a larger callus could be observed for the hydrogel, PEU_MBG_Sr2%_Sr_NAC and PEU_MBG_ SD_BMP-2 groups.

Based on these considerations, the beneficial effects on the bone healing outcome exerted by the multifunctional device allowed to validate the strontium-containing MBGs loaded with NAC as a suitable carrier to be used for bone regeneration purposes for the delivery of therapeutic agent in the pathological site.

4.4 Morphological and structural characterization of sol-gel and spray-dryer *Zwitterionic* Strontium-containing MBGs

4.4.1 *Zwitterionic* Strontium-containing MBG-SG: MBG_Sr2%_SG_Z

Part of the work described in this chapter has been previously published in [1,2].

In order to develop a multifunctional biomedical device, able to synergistically combine the release of therapeutic ion/drug with anti-fouling/antibacterial properties, during this PhD work, strontium containing MBGs have been produced and successively subjected to a co-grafting reaction to introduce almost the same amount of $-NH_3^+/-COO^-$ surface groups, which are expected to impart effective anti-adhesive properties.

MBG_Sr2%_SG was prepared through the base-catalysed sol-gel method by following the procedures reported in chapter "*materials and methods*", section 2.2 and results related to the complete characterization are reported in the previous section (see section 4.2.1). MBG_Sr2%_SG was post-functionalized by co-grafting aminopropyl silanetriol (APST) and carboxyethylsilanetriol (CES) as organosilane agents, whose relative amount and reaction time were properly adjusted to reach an almost neutral overall surface charge. In this section, the results concerning the characterization of *zwitterionic* strontium-containing MBG-SG, referred hereafter as MBG_Sr2%_SG_Z, are reported.

4.4.1a Morphological and structural characterization of MBG_Sr2%_SG_Z

The mesostructure of MBG_Sr2%_SG_Z and the corresponding bare sample has been evaluated by TEM and low-angle XRD. Figure 4.29 showed the TEM images of both samples, evidencing a worm-like mesoporosity throughout the bare nanoparticles (figure 4.29A) also clearly discernible after the functionalization (figure 4.29B).

Low-angle XRD patterns, reported in figure 4.29C, further confirm the worm-like porous structure[55–57], in fact both MBG_Sr2%_SG and MBG_Sr2%_SG_Z showed a single peak at around 1.24°, corresponding to the (100) reflection. The decrease of the reflection intensity revealed upon silane co-grafting can be ascribed to a limited and confined collapse of the mesoporous structure.
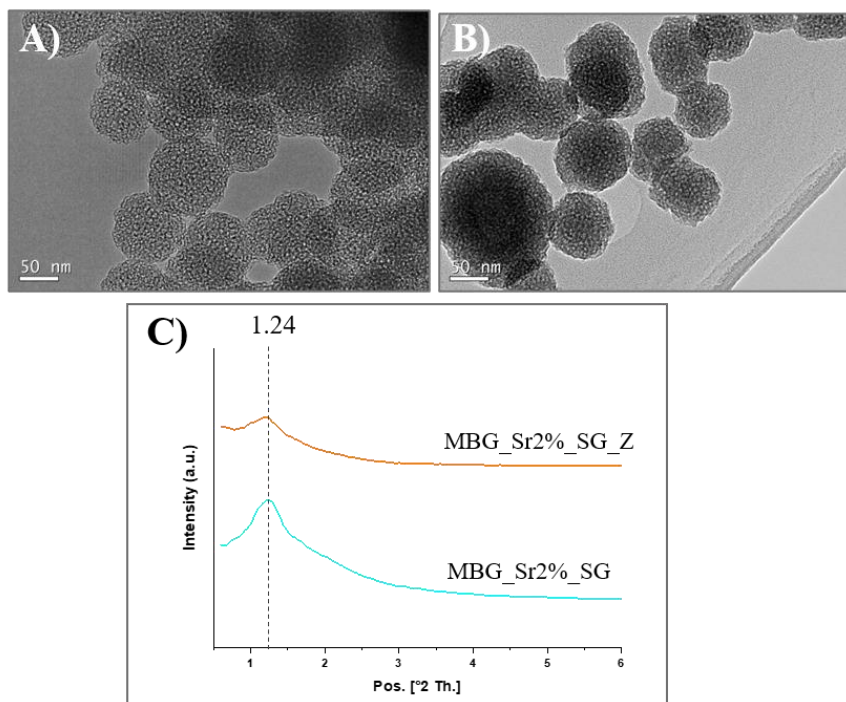
Figure 4.100 TEM images of (A) MBG_Sr2%_SG and (B) MBG_Sr2%_SG_Z; (C) Low-angle XRD of MBG_Sr2%_SG and MBG_Sr2%_SG_Z.

Morphological analysis of MBG_Sr2%_SG_Z showed particles with uniform spherical shape and size ranging between 100 and 200 nm, as shown in figure 4.30. The observed morphology resulted in good agreement with morphology, size and shape revealed by the observation of unmodified analogues materials (see section 4.2.1), evidencing that the post-synthesis modification did not significantly alter the morphological features of MBG_Sr2%_SG sample.
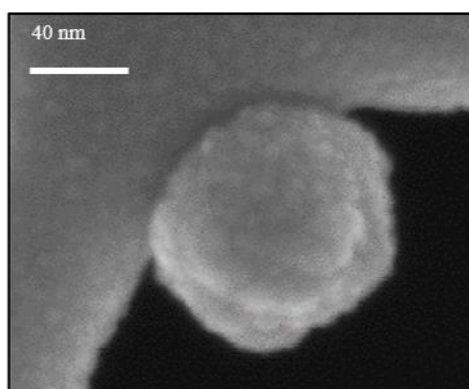
Figure 4.101 FE-SEM image of MBG_Sr2%_SG_Z.

In order to evaluate the total amount of incorporated strontium, ICP-AES analysis were conducted on acid-digested powder, revealing that only 30% of strontium precursor was effectively incorporated for MBG_Sr2%_SG. ICP analysis on samples after the post-synthesis reaction evidenced that incorporated strontium amount resulted unaffected, demonstrating that the functionalization reaction did not induce any loss of incorporated strontium amount.

The textural features of the samples before and after functionalization were investigated by N$_2$ adsorption/desorption measurements. As reported in figure 4.31A, MBG_Sr2%_SG showed a type IV isotherm, characteristic of mesoporous materials and a pore size distribution centred at around 4.2 nm (figure 4.31B).
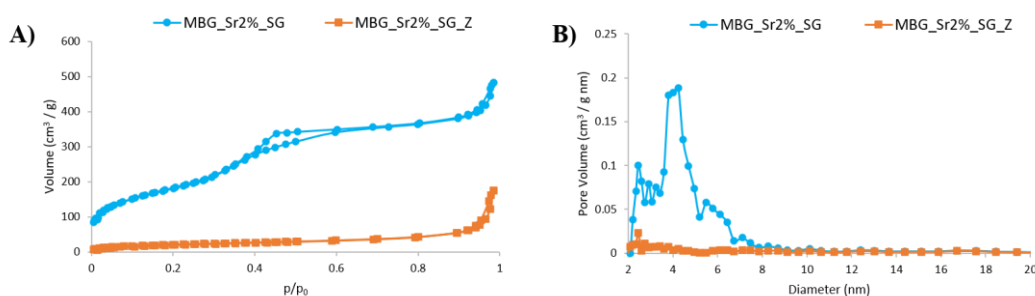
Figure 4.102 N$_2$ adsorption-desorption isotherm of MBG_Sr2%_SG_Z compared to the bare sample MBG_Sr2%_SG (A) and related DFT pore size distribution (B).

The material exhibits excellent textural properties, in terms of very high surface area (670 cm³ g^{-1}) and pore volume (0.63 cm³ g^{-1}), as reported in table 4.8. After the functionalization, a modification of the isotherm and a drastic decrease in SSA and pore volume is observed, suggesting that mesopore entrances are partially or even fully blocked by the organosilane grafting [57,58], as already notified after the drug loading in the previous section. In fact, the surface area decreases from 670 cm³ g^{-1} to 76 cm³ g^{-1} while the pore volume from 0.63 cm³ g^{-1} to 0.16 cm³ g^{-1}. In this context, if the organosilanes react at the pore entrances during the initial phases of reaction, the diffusion of precursors within the mesopore can be compromised, leading to an uneven distribution and, in some cases, to the almost closure of the pores [58].

Table 4.25 Textural parameters of MBG_Sr2%_SG and MBG_Sr2%_SG_Z.

	MBG_Sr2%_SG	**MBG_Sr2%_SG_Z**
BET surface area	670 m² g^{-1}	76 m² g^{-1}
Average Pore size	4.2 nm	-
Pore volume	0.63 cm³ g^{-1}	0.16 cm³ g^{-1}

FT-IR spectroscopy allowed to assess the successful anchoring of functional groups. In figure 4.32, the FT-IR spectra of both bare and *zwitterionic* samples are

reported. All spectra display in the range of 3750–3000 cm^{-1} the typical absorption bands, corresponding to the stretching vibrational frequencies of the H-bonded hydroxyls. The spectrum of functionalized sample MBG_Sr2%_SG_Z shows significant changes compared to the bare analogues, in particular, two bands at 1550 and 1407 cm^{-1}, ascribed respectively to the asymmetric (v_{as}) and symmetric (v_s) stretching vibration of the carboxylate group COO$^-$ [46], and two shoulders at around 1650 cm^{-1} and 1520 cm^{-1} corresponding to the bending mode of protonated amine group NH$_3^+$ [59]. On contrary, the C=O adsorption band of protonated COOH group, displayed at 1706 cm^{-1}, and the band at 1595 cm^{-1}, ascribable to the bending mode of neutral -NH$_2$ do not appear in the FT-IR spectrum of *zwitterionic* sample. Taken together these FT-IR observations reveal that MBG_Sr2%_SG_Z exhibits, as required for a *zwitterionic* material, a mixed charged surface, due to the co-presence of NH$_3^+$ and COO$^-$ groups, respectively.
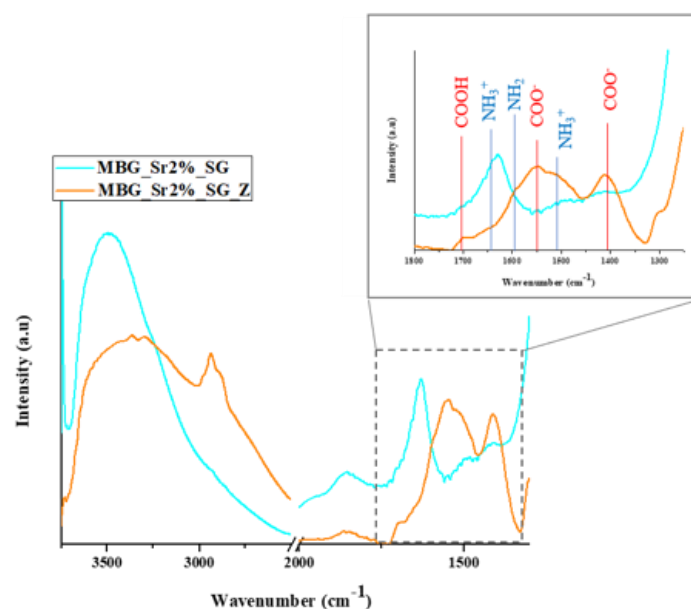
Figure 4.103 FTIR spectra of MBG_Sr2%_SG_Z compared to MBG_Sr2%_SG.

212

Thermogravimetric analysis has been used to estimate the anchored organic components based on the weight loss. As reported in figure 4.33, TG profiles of bare MBG_Sr2%_SG show solely a weight loss in the range 30-180 °C, related to the elimination of the adsorbed water, revealing the absence of additional surface moieties, as already notified in section 4.2.4. At variance, *zwitterionic* MBG_Sr2%_SG_Z sample, two clear weight loss components were observed: the first below 200 °C due to the release of the adsorbed water, and a more significant step between 300 and 600 °C, ascribable to the decomposition of anchored amino and carboxylate organic moieties, thus confirming the grafting of organic components.

Since these materials are intended for biomedical applications where the surface charge plays an essential role, their behaviour in aqueous media at different pH was investigated by ζ-potential measurements, in order to determine the pH values at which the *zwitterionic* nature is preserved. As can be observed from the ζ-potential *vs.* pH plots reported in figure 4.34, bare MBG_Sr2%_SG exhibited negative ζ-potential values within the whole pH range, due to the presence of deprotonated silanols (-Si $-O^-$). These data are in good agreement with those reported in the literature, where the isoelectric point at around pH = 2 is reported for similar silica-based systems [60,61].
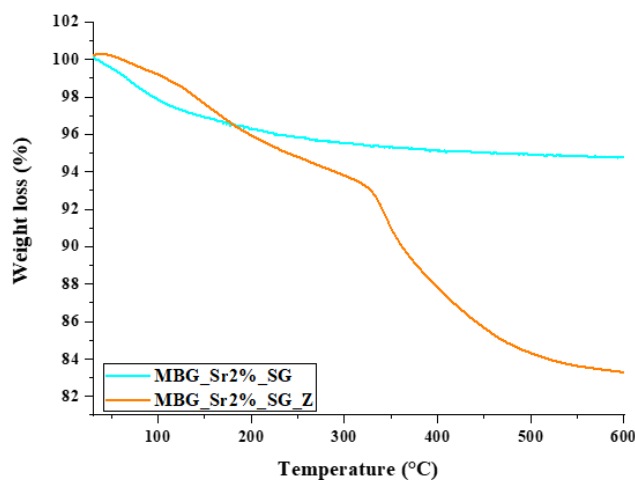
Figure 4.104 TGA profiles of MBG_Sr2%_SG_Z compared to the bare MBG_Sr2%_SG.

ζ-potential analysis supported the optimisation of the functionalization protocol in term of organosilane initial ratio and reaction times. The first attempt conducted with an equimolar concentration of APST and CES, added simultaneously (ratio 1:1) led to the ζ-potential value at pH 7.4 around -9 mV. This negative value can be ascribed both to a preferential grafting of CES with respect to APST or the presence of residual unreacted deprotonated silanols groups, leading to a larger population of negative charged (COO^- and SiO^-), compared to protonated amino groups ($-NH_3^+$). A double concentration of APTS, followed by CES addition after 30 minutes of reaction (ratio 1:2), allowed to obtain lees negative ζ-potential value at pH 7.4 (-6 mV), thanks to a larger amount of amino groups grafted on the particle surface.

Finally, a further increase of APTS concentration on equal addition time of CES led to a closer value of ζ-potential to a global zero charge, given by the balance of positive and negative charges.

ζ-potential measurements of MBG_Sr2%_SG_Z with a ratio 1:3, reveals positive values in the pH range 3-7, due to the protonation of amino groups ($NH_2 >$ NH_3^+), which reach a value close to zero (2.2 ± 0.9 mV) at pH 7.4, which indicates
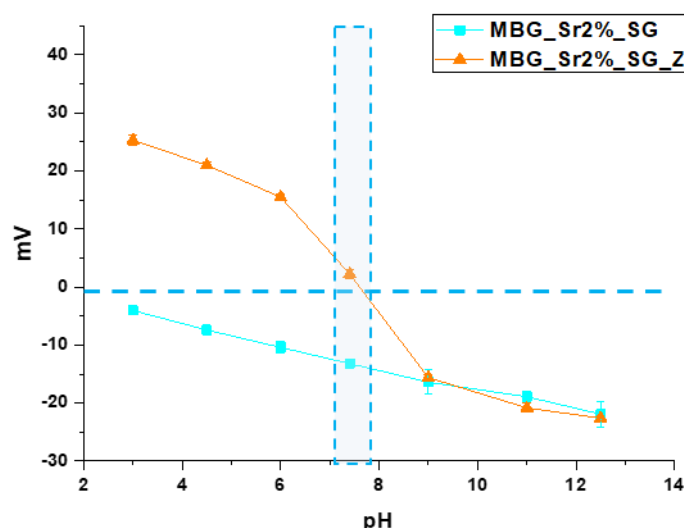
Figure 4.105 ζ-potential measurements of MBG_Sr2%_SG and MBG_Sr2%_SG_Z recorded at different pH.

the *zwitterionic* behaviour of MBG_Sr2%_SG_Z sample in physiological conditions.

Since MBG_Sr2%_SG_Z and MBG_Sr2%_SD_Z samples exhibited the required NH_3^+/-COO^- *zwitterionic* pairs and net surface charges close to zero at the physiological pH of 7.4, the biocompatibility and the capability to inhibit protein adhesion of these two functionalized samples have been tested and compared to the bare analogues.

4.4.1b Bioactive behaviour of MBG_Sr2%_SG_Z in SBF

After the grafting of APST and CES, MBG_Sr2%_SG_Z shows a remarkable bioactive behaviour, retaining the ability to induce the deposition of the HA layer with fast kinetics [7]. In fact, after only 1 day of soaking, the *zwitterionic* material appeared covered by a rough layer of globular agglomerates of apatite-like phase, that grew in size during the test, causing the final embedding of MBG particles overtime. Figure 4.35A reported the FE-SEM images of MBG_Sr2%_SG_Z samples after 7 days of soaking and the particles resulted fully covered by a compact layer of needle-like nanocrystals. EDS analysis performed on dried powders evidenced a Ca/P ratio of 1.7, typical value reported in the literature for carbonated

hydroxyapatite [49,50]. Furthermore, XRD patterns reported in figure 4.35B confirmed the formation of apatite-like layer with nanocrystalline nature, as revealed by peaks at 25.8 and 32.0 2θ, matching the HA reference (00-001-1008).

Finally, at each time point, the pH of the SBF solution was measured, resulting along the overall duration below 7.8, which allows osteoblasts to maintain their physiological activity[62].
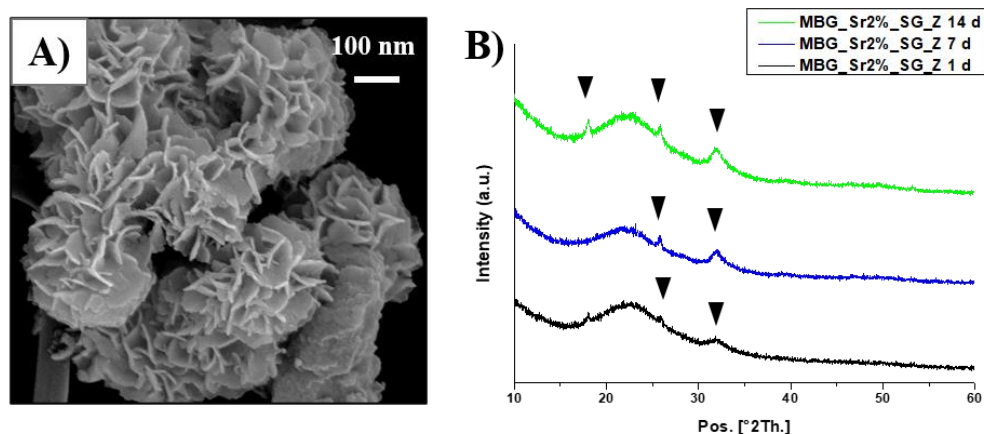
Figure 4.106 FE-SEM image (A) and XRD patterns (B) of MBG_Sr2%_SG_Z after 1d, 7d and 14d of soaking in SBF (the most representative diffraction peaks of apatite phase are highlighted). The FE-SEM image are related to the surface after 7 days of incubation.

The preservation of the bioactive behaviour after *zwitterionization* was not fully predictable as the ion-exchange reactions which promote HA deposition could have been hampered or even fully blocked by the presence of the silane moieties. The assessment of this aspect was one the major goal of the investigation as it represents an essential feature for promoting bone regeneration.

4.4.1c Strontium ion release from MBG_Sr2%_SG_Z in Tris HCl

The ion release of bare and functionalized samples was evaluated in Tris-HCl medium (pH 7.4); samples were incubated at 37 °C up to 14 days and, at selected time points (3 h, 1 day, 3 days, 7 days and 14 days), were centrifuged, aliquots were withdrawn and analysed by ICP-AES. As expected, the release properties of MBG_Sr2%_SG before functionalization resulted fully in agreement with those already reported in the previous section (see section 4.2.1), confirming the fast ion diffusion inside the porous structure [2,13].

Figure 4.36 shows the strontium release from MBG_Sr2%_SG_Z, evaluated in the same experimental conditions, revealing that sample after functionalization was able to release the total amount of incorporated Sr^{2+} ions with kinetics to those shown by the corresponding bare samples [2].

215
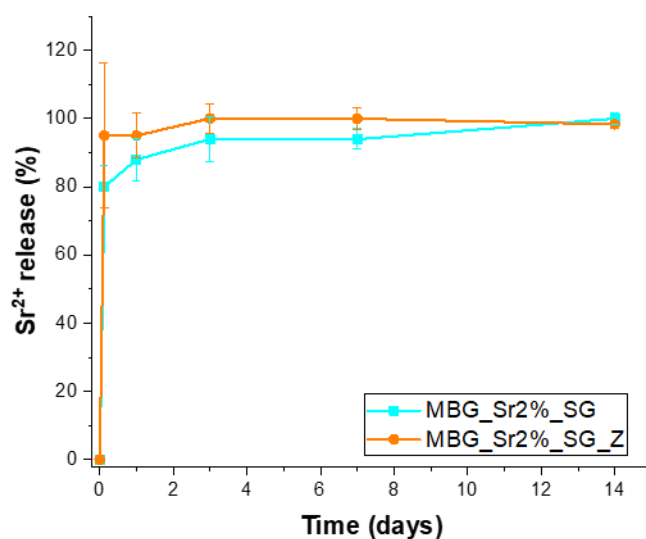
Figure 4.107 Strontium release profile of MBG_Sr2%_SG_Z in Tris HCl compared to the bare sample MBG_Sr2%_SG.

The final release Sr^{2+}concentration (1.6 ppm for MBG_Sr2%_SG_Z) has the potential to stimulated osteogenic response as shown in several work, without inducing any cytotoxic effect [63]. In fact, as reported in section 4.2.3, the same concentration of Sr^{2+} was able to stimulate the expression of pro-osteogenic genes (COLL1A1, SPARC and OPG) of osteoblast-like cells cultured in the presence of only the dissolved ions released from strontium-containing MBG particles, confirming the key role exerted by strontium in stimulating osteoblast cell activity. Newly, the dissolution products released by Sr-containing bioactive glass nanoparticle were successfully proved to induce the stimulation of osteogenic response in hMSCs with the expression of genes associated to early-, mid- and late-osteogenic marker in the absence of osteogenic supplements [63].

4.4.2 *Zwitterionic* strontium-containing MBG-SD: MBG_Sr2%_SD_Z

Part of the work described in this chapter has been previously published in [1,2].

In order to develop a multifunctional biomedical device with different textural features in term of exposed specific surface area, pore size and pore volume compared to the MBG_Sr2%_SG_Z sample, MBG_Sr2%_SD was produced and successively functionalised through a co-grafting reaction to introduce almost the same amount of $-NH_3^+/-COO^-$ surface groups, which are expected to impart effective anti-adhesive properties.

MBG_Sr2%_SD was prepared through the spray-dryer-assisted approach by following the procedures reported in chapter "*materials and methods*", section 2.3 and results related to the complete characterization are reported in the previous section (see section 4.2.2). MBG_Sr2%_SD was post-functionalized by co-grafting aminopropyl silanetriol (APST) and carboxyethylsilanetriol (CES) as organosilane agents, whose relative amount and reaction time were properly adjusted to reach an almost neutral overall surface charge. In this section, the results concerning the characterization of *zwitterionic* strontium-containing MBG-SD, referred hereafter as MBG_Sr2%_SD_Z, are reported.

4.4.2a Morphological and structural characterization of MBG_Sr2%_SD_Z

TEM and low-angle XRD were employed to investigate the mesostructure of the bare MBG_Sr2%_SD and *zwitterionic* MBG_Sr2%_SD_Z. As shown in figure 4.37A and B, TEM images revealed a worm-like mesoporosity for both the bare and functionalized samples respectively, similar to the structure observed for the MBG-SG particles, clearly discernible also after the functionalization. In addition, the low-angle XRD patterns reported in fig. 4.37C further confirm the worm-like porous structure: in fact, MBG_Sr2%_SD, before and after functionalization, showed a single peak at around 0.92°, matching with the (100) reflection.
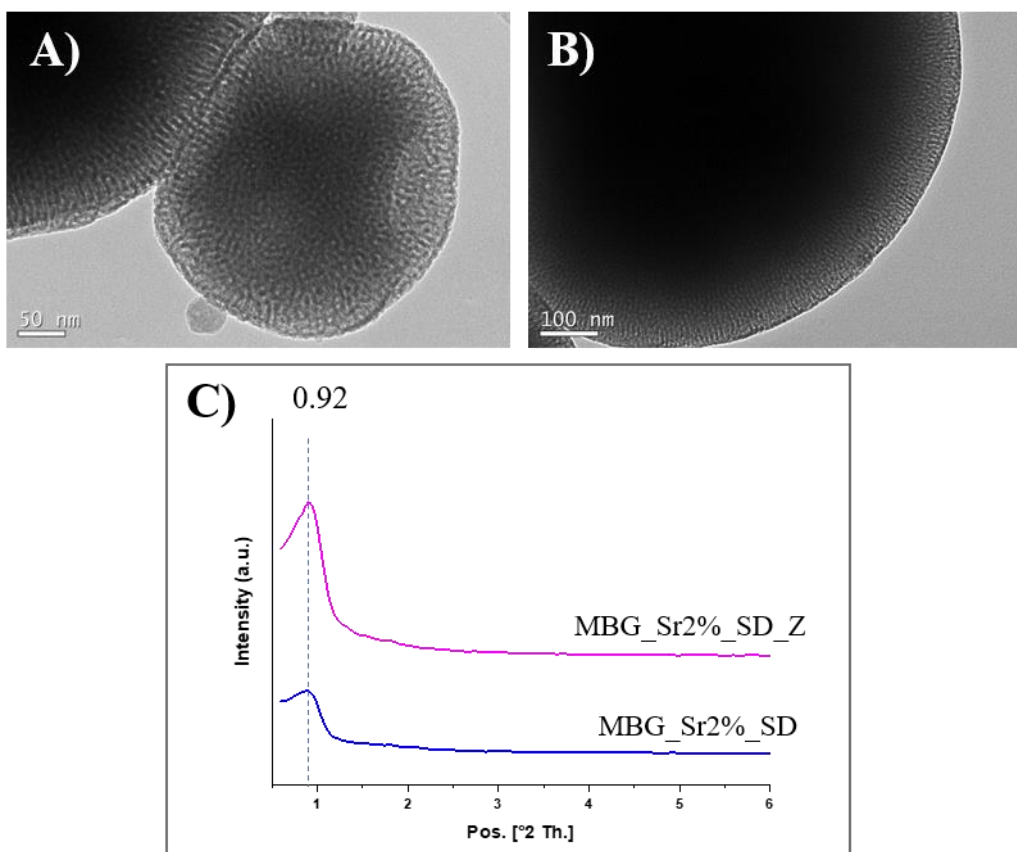
Figure 4.108 TEM images of (A) MBG_Sr2%_SD and (B) MBG_Sr2%_SD_Z; (C) Low-angle XRD of MBG_Sr2%_SD and MBG_Sr2%_SD_Z.

Morphological analysis of MBG_Sr2%_SD_Z reported in figure 4.38, revealed spherical particles with micrometric size between 0.5 and 5 µm, in accordance with morphology, size and shape revealed by the observation of unmodified analogues material MBG_Sr2%_SD, previously reported in section 4.2.2, evidencing that the post-synthesis modification did not induce any significant alterations in the morphological features of MBG_Sr2%_SD samples.
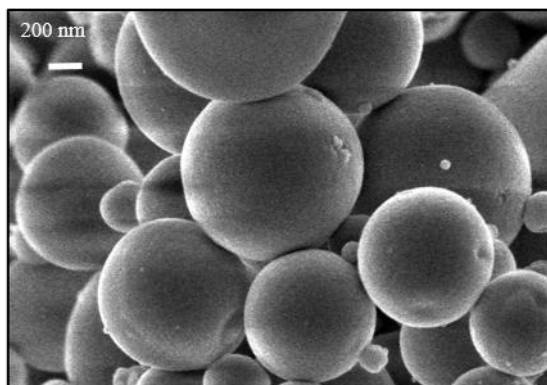
Figure 4.109 FE-SEM image of MBG_Sr2%_SD_Z.

Since the amount of strontium cannot be detected by EDS analysis, due to the overlapping with the silicon signal, ICP-AES analysis was conducted on acid-digested powder to assess the amount of incorporated strontium. Results revealed that the incorporated strontium amount resulted very similar to the theoretical value, unlike the MBG_Sr2%_SG sample, in which only 30% of strontium precursor was effectively incorporated.

As already evidenced for the SG samples, ICP analysis on MBG_Sr2%_SD after the post-synthesis reaction evidenced that incorporated strontium amount resulted unaffected, demonstrating that the functionalization reaction did not induce any loss of incorporated strontium amount.

The textural features of the samples before and after functionalization were investigated by N_2 adsorption/desorption measurements. Figure 4.39 shows the N_2 adsorption-desorption isotherm of MBG_Sr2%_SD, a IV type isotherm with a pronounced hysteresis loop.
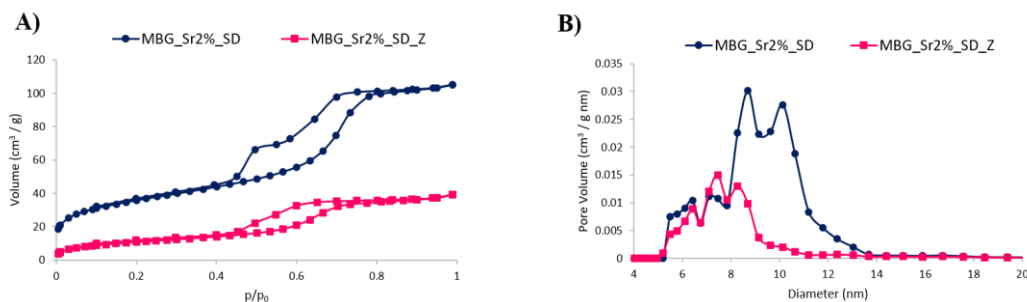
Figure 4.110 N_2 adsorption-desorption isotherm of MBG_Sr2%_SD_Z compared to the bare sample MBG_Sr2%_SD (A) and related DFT pore size distribution (B).

The related values of specific surface area SSA, pore volume and pore size are reported in table 4.9 and result comparable to those previously obtained for MBG_Sr2%_SD investigated in section 4.2.2. As expected after grafting, MBG_Sr2%_SD_Z exhibits lower specific surface area and pore volume and size compared with unmodified sample, but at variance with MBG_Sr2%_SG_Z, a noticeable residual surface area and pore volume is retained after silane anchoring, evidencing that pores do not undergo complete occlusion but experienced a size reduction (from 8-11 nm to 6-9 nm).

Table 4.26 Textural parameters of MBG_Sr2%_SD and MBG_Sr2%_SD_Z.

	MBG_Sr2%_SD	**MBG_Sr2%_SD_Z**
BET surface area	126 m^2 g^{-1}	40 m^2 g^{-1}
Average Pore size	8-11 nm	6-9 nm
Pore volume	0.16 cm^3 g^{-1}	0.06 cm^3 g^{-1}

FT-IR spectra of both the bare and functionalized samples, recorded to assess the successful anchoring of functional groups, are shown in figure 4.40.

As already reported for the SG samples, both the spectra of MBG_Sr2%_SD and MBG_Sr2%_SD_Z display in the range of 3750–3000 cm^{-1} the typical absorption bands, corresponding to the stretching vibrational frequencies of the H-bonded hydroxyls. Compared to the bare spectrum, the MBG_Sr2%_SD_Z spectrum reveals two bands at 1550 and 1407 cm^{-1}, ascribed respectively to the asymmetric (ν_{as}) and symmetric (ν_s) stretching vibration of the carboxylate group COO$^-$ [46], and two shoulders at around 1650 cm^{-1} and 1520 cm^{-1} corresponding to the bending mode of protonated amine group NH$_3^+$ [59]. On contrary, the C=O adsorption band of protonated COOH group, displayed at 1706 cm^{-1}, and the band at 1595 cm^{-1}, ascribable to the bending mode of neutral -NH$_2$ do not appear in the FT-IR spectrum of *zwitterionic* samples.

Results obtained by FTIR evaluation confirmed the presence of a mixed charged surface, due to the co-presence of NH_3^+ and COO^- groups, respectively.
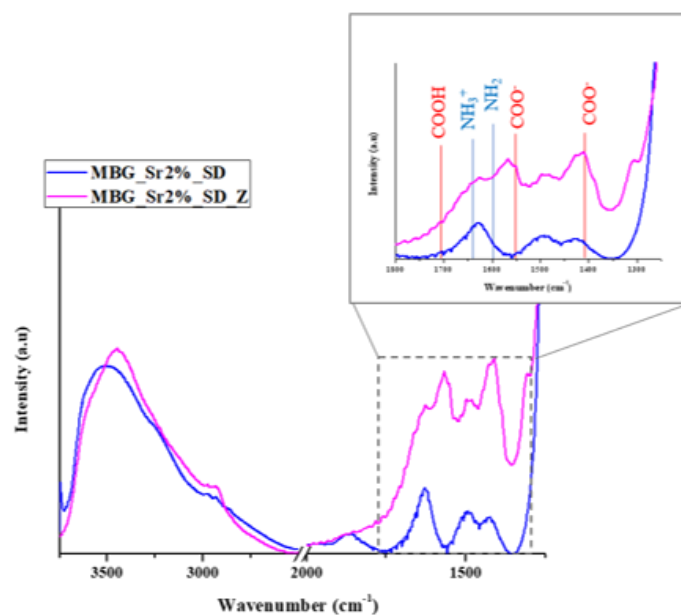
Figure 4.111 FTIR spectra of MBG_Sr2%_SD_Z compared to MBG_Sr2%_SD.

TGA measurements were performed to evaluate the weight loss, useful to estimate the anchored organic components. Figure 4.41 reports the TG profiles of bare MBG_Sr2%_SD sample, compared to MBG_Sr2%_SD_Z. The weight loss in the range 30-180 °C observed for the bare sample is ascribed to the elimination of the adsorbed water, revealing the absence of additional surface moieties. On contrary two discernible weight loss components were observed in the TG profile
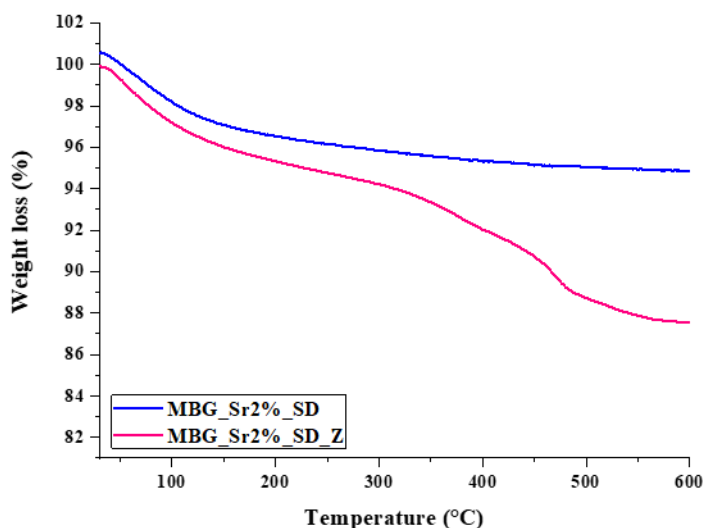
Figure 4.112 TGA profiles of MBG_Sr2%_SD_Z compared to the bare MBG_Sr2%_SD.

of MBG_Sr2%_SD_Z: the first below 200 °C due to the release of the adsorbed

water, and a more significant step between 300 and 600 °C, ascribable to the decomposition of anchored amino and carboxylate organic moieties.

In order to obtain a material with a surface charge close to zero at physiological conditions, essential to induce anti-fouling/antibacterial properties, the behaviour in aqueous media at different pH was investigated by ζ-potential measurements, in order to determine the pH values at which the *zwitterionic* nature is preserved. Figure 4.42 shows the ζ -potential *vs.* pH plots of both the bare and functionalised samples.
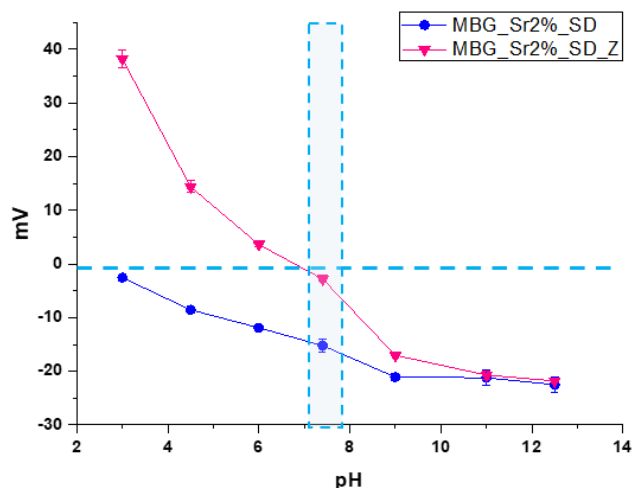
Figure 4.113 ζ-potential measurements of MBG_Sr2%_SD and MBG_Sr2%_SD_Z recorded at different pH.

As expected, MBG_Sr2%_SD exhibited negative ζ-potential values within the whole pH range, due to the presence of deprotonated silanols (-Si –O⁻), in good agreement with those reported in section 4.4.1 for the SG samples and the literature, where the isoelectric point at around pH = 2 is reported for similar silica-based systems [60,61].

After the same optimisation of the functionalization protocol in term of organosilane initial ratio and reaction times reported for the SG samples, the ratio APST:CES most appropriate to obtain closer value of ζ-potential to a global zero charge, given by the balance of positive and negative charges, resulted to be the 1:3.

ζ-potential measurements of MBG_Sr2%_SD_Z reveals positive values in the pH range 3-7, due to the protonation of amino groups ($NH_2 > NH_3^+$), which reach a value close to zero (-2.8 ± 1.2 mV) at pH 7.4, which indicates the *zwitterionic* behaviour of both systems in physiological conditions.

4.4.2b Bioactive behaviour of MBG_Sr2%_SD_Z in SBF

After the grafting of APST and CES, MBG_Sr2%_SD_Z demonstrated to retain the ability to induce the deposition of the HA layer with fast kinetics, showing noteworthy bioactive behaviour. In fact, after only 1 day of soaking, a rough layer of globular agglomerates of apatite-like phase appeared on the MBG surface, growing in size during the test, causing the final embedding of MBG particles
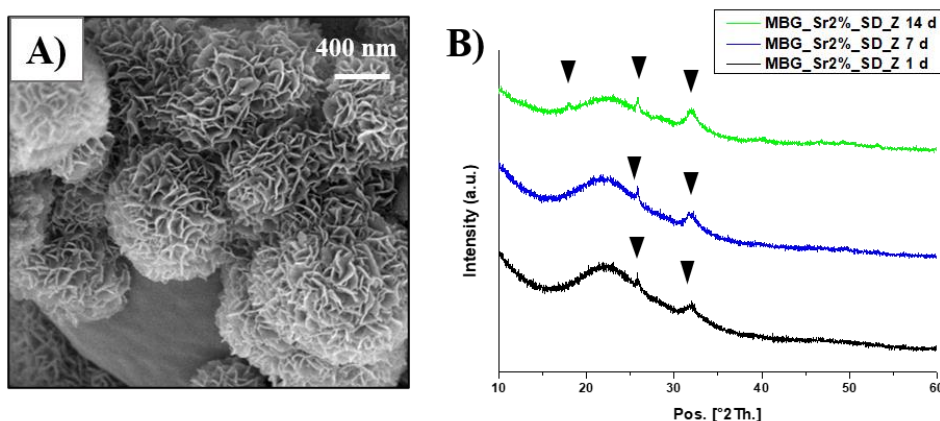
Figure 4.114 FE-SEM image (A) and XRD patterns (B) of MBG_Sr2%_SD_Z after 1d, 7d and 14d of soaking in SBF (the most representative diffraction peaks of apatite phase are highlighted). The FE-SEM image are related to the surface after 7 days of incubation.

overtime. Figure 4.43A showed the FE-SEM images of MBG_Sr2%_SD_Z 7 days on soaking, in which a compact layer of needle-like nanocrystals with the characteristic cauliflower morphology fully covered the particle surface. XRD patterns reported in figure 4.43B further confirmed the formation of apatite-like layer with nanocrystalline nature, as revealed by peaks at 25.8 and 32.0 2θ, matching the HA reference (00-001-1008). Also for the MBG_Sr2%_SD_Z particles, the preservation of bioactivity has been notified, confirming that the *zwitterionization* did not hamper the ion-exchange reactions essential to induce HA deposition and thus to promote bone regeneration.

4.4.2c Strontium ion release from MBG_Sr2%_SD_Z in Tris HCl

The ion release profiles of MBG_Sr2%_SD and MBG_Sr2%_SD_Z was evaluated in Tris-HCl medium (pH 7.4); samples were incubated at 37 °C up to 14 days and, at selected time points (3 h, 1 day, 3 days, 7 days and 14 days), were centrifuged, aliquots were withdrawn and analysed by ICP-AES. As expected, the same behaviour previously notified for the SG samples is observed for the release properties of SD samples before functionalization; in fact, the release profile of MBG_Sr2%_SD resulted fully comparable with those already reported in section 4.2.2, confirming the fast ion diffusion inside the porous structure.

The release profile of MBG_Sr2%_SD_Z samples was evaluated in the same experimental conditions. Figure 4.44 shows both the release profiles of bare and functionalised samples in comparison, highlighting that samples after

functionalization were able to release the total amount of incorporated Sr^{2+} ions with the same release kinetics observed for the corresponding bare samples. The final release Sr^{2+}concentration of 4.4 ppm for MBG_Sr2%_SD_Z, has been already proved to stimulate osteogenic response without inducing any cytotoxic effect.

In fact, as evaluated in section 4.2.3, similar concentrations of Sr^{2+} is able to stimulate the expression of pro-osteogenic genes (COLL1A1, SPARC and OPG) of osteoblast-like cells cultured in the presence of only the dissolved ions released from Strontium-containing MBG particles, confirming the key role exerted by strontium in stimulating osteoblast cell activity.
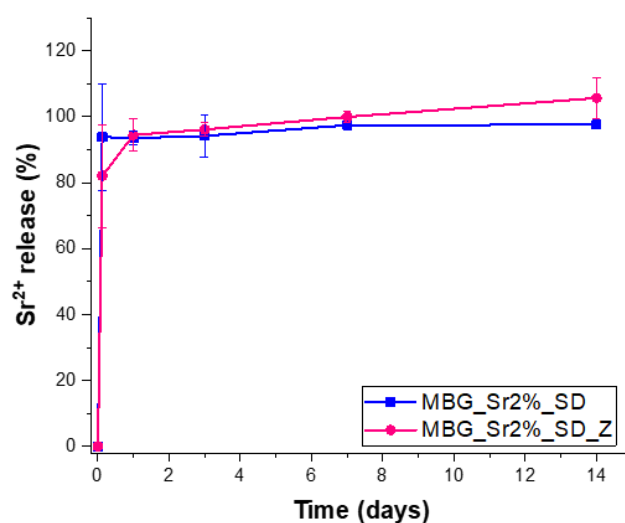
Figure 4.115 Strontium release profile of MBG_Sr2%_SD_Z in Tris HCl compared to the bare sample MBG_Sr2%_SD.

4.4.3 *In vitro* Biological Assessment of *zwitterionic* Sr-containing MBGs

Since both the MBG_Sr2%_SG_Z and MBG_Sr2%_SD_Z samples exhibited the required NH_3^+/-COO^- zwitterionic pairs and net surface charges close to zero at the physiological pH of 7.4, the biocompatibility and the capability to inhibit protein adhesion of these two functionalized samples have been tested and compared to the bare analogues. In this section, the results concerning the biological assessment of both the *zwitterionic* strontium containing MBGs (MBG_Sr2%_SG_Z and MBG_Sr2%_SD_Z) are reported.

In vitro biocompatibility assays in the presence of a mouse pre-osteoblastic cell line MC3T3-E1 were performed to study the effect of both the post-grafted Sr-MBGs on the osteoblastic cell growth and differentiation. In addition, to assess the anti-adhesive ability imparted by the surface *zwitterionization*, a reduced protein adsorption of serum proteins was evaluated by gel electrophoresis (SDS-PAGE) experiments using bovine serum albumin (BSA) and fibrinogen (Fib).

4.4.3a Biocompatibility of zwitterionic Sr-containing MBGs

The use of MBG nanocarriers for clinical applications requires excellent biocompatibility and absence of any cytotoxicity. In the literature, silica-based bioactive glass particles were widely proved to be biocompatible materials that exhibits low toxicity and lack of immunogenicity, degrading into nontoxic compounds (mainly silicic acid) in relatively short time periods [2,10,64,65].

Despite this lack of toxicity, the surface modification could provoke the appearance of toxicity due to several consequent aspects, among the other an enhanced uptake within the cells or the release of functional groups degradation products. To evaluate cytotoxicity, MC3T3-E1 preosteoblast cells were incubated with different amount of both the MBG-SD and MBG-SG particles before and after *zwitterionization* in cell culture medium. At determined incubation times (1, 2 and 5 days), cell viability was evaluated via the standard cell viability test by MTS reduction. The results showed that all the tested particles, irrespective of their size and surface features, did not exhibit any cytotoxicity in preosteoblastic MC3T3-E1 (Fig. 4.45) [66].
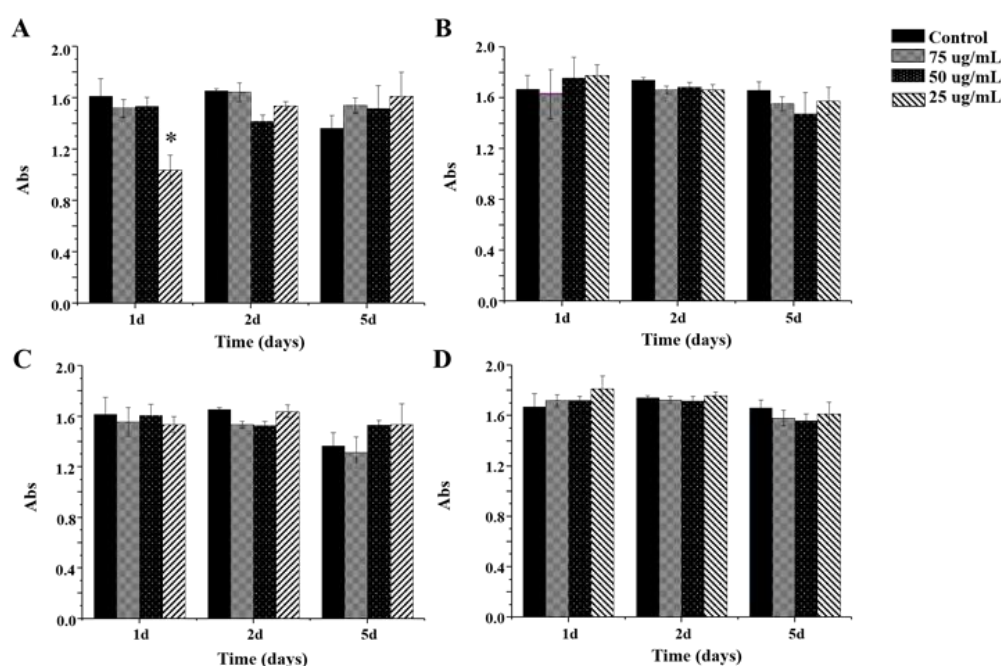
*Figure 4.116 Cell viability studies of the samples MBG_Sr2%_SG (A), MBG_Sr2%_SG_Z (B), MBG_Sr2%_SD (C) and MBG_Sr2%_SD_Z (D) at different concentration for MC3T3-E1 cell line and 1 d, 2 d and 5 d of exposure time. *p <0.05 vs corresponding control without particles (ANOVA).*

In order to further confirm these results, lactate dehydrogenase (LDH) production was evaluated after 1 day of cell incubation with the different Strontium-containing MBG particles (before and after *zwitterionization*) at different concentrations. LDH is an enzyme released by cells in case of cell membrane rupture, thus indicating a cytotoxic effect. Interestingly, the results of LDH tests

related to MBG_Sr2%_SG and MBG_Sr2%_SD and the *zwitterionic* analogues and reported in figure 4.46A evidenced no cytotoxic effect up to the concentration of 75 µg/mL and no significant differences were registered in comparison with the control test. These results were also confirmed by the optical microscopy, as shown in figure 4.46B, where the cells adhered to the surface of the well appeared well spread without any apparent cell damage.

4.4.3b Mineralization assay

Differentiation is a process which induces unspecialized cells, pre-osteoblasts, to become specialized cells with the function to restore the bone. During this PhD work, a preliminary experiment has been carried out to monitor the mineralization
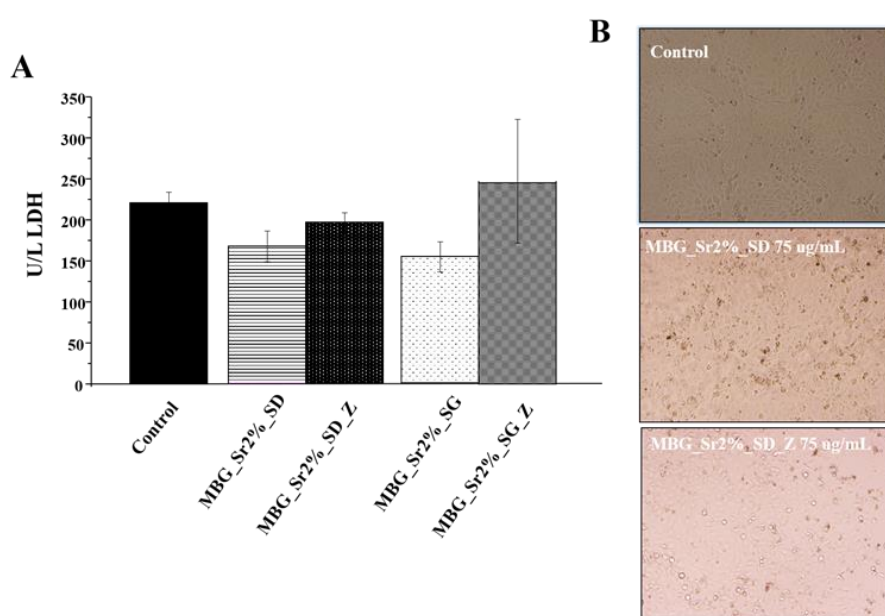
Figure 4.117 LDH studies of Sr-MBGs (SD and SG) before and after zwitterionization at 75 µg/mL concentration for MC3T3-E1 cell line and after 1 day of exposure time (A) and optical microscopy images corresponding to the wall-plate of the preosteoblast MC3T3E-1 after incubation with Sr-MBG_SD particles before and after functionalization (B)

process in term of alizarin assay and to verify if the *zwitterionization* process affect or not to the differentiation. Related results, reported in fig. 4.47 evidenced an increase of matrix mineralization for all strontium-containing MBGs materials with respect to control, which could be ascribed to the osteogenic capability of released Sr^{2+} ions as already reported in the previous section and in the literature [2,9,63]. After functionalization, no significant differences with respect to both bare samples were observed, confirming that the *zwitterionization* process does not affect the alizarin production. These findings could be explained since the functionalized samples exhibit similar strontium release compared to the bare samples, and consequently, also the associated osteogenic capability (in this case the mineralization).
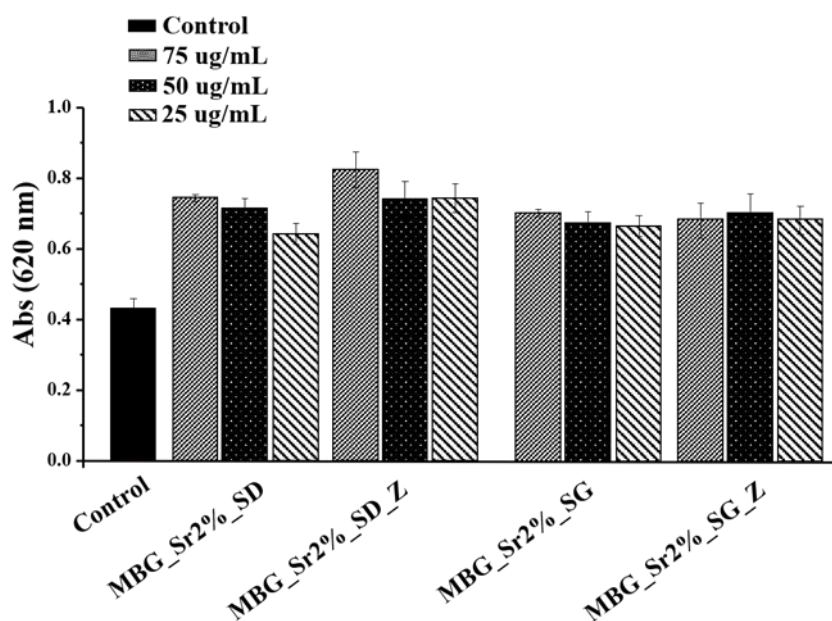
Figure 4.118 Mineralization process in terms of alizarin assays of Strontium-containing MBGs before and after zwitterionization at different concentration (25, 50 and 75 µg/mL).

4.4.3c In vitro non-specific protein adhesion

Once demonstrated the *zwitterionic* nature and the biocompatibility of both the MBG_Sr2%_SG_Z and MBG_Sr2%_SD_Z particles, their tendency to undergo nonspecific protein adsorption when soaked in biological fluids was evaluated by *in vitro* adsorption assays with two serum proteins, BSA and fibrinogen, respectively. Related results, reported in table 4.10, show a remarkable decrease of protein adsorption for both proteins after *zwitterionization* process with a reduction of *c.a.* 85% and 86% of BSA and 70% and 54% of Fib for the MBG_Sr2%_SG_Z and MBG_Sr2%_SD_Z, respectively.

Table 4.27 Amount of BSA and fibrinogen adsorbed on the surfaces of Sr-MBGs before and after zwitterionization determined by SDS-PAGE technique.

Sample	BSA (mg/g)	Fibrinogen (mg/g)
MBG_Sr2%_SG	348 ± 75	463 ± 79
MBG_Sr2%_SG_Z	51 ± 18	134± 58
MBG_Sr2%_SD	170± 50	243± 58

226

MBG_Sr2%_SD_Z	24± 13	133± 57

This significant reduction is ascribed to the presence of *zwitterionic* pairs, which are known to act as a barrier to non-specific protein adsorption [67,68] via a strongly adsorbed layer of water molecules solvating the charged terminal COO^-/NH_3^+ groups via multiples hydrogen bounds.

In addition, after protein non-specific adsorption occurs, the hydrodynamic diameter (Dh) of the bare samples is expecting to increase, while the *zwitterionic* particle size will remain stable [68]. In fact, the hydrodynamic diameter of MBG_Sr2%_SG increased from 142 nm to 475 nm (fig. 4.48), confirming the protein adsorption on the particle surface, due to an electrostatic interaction
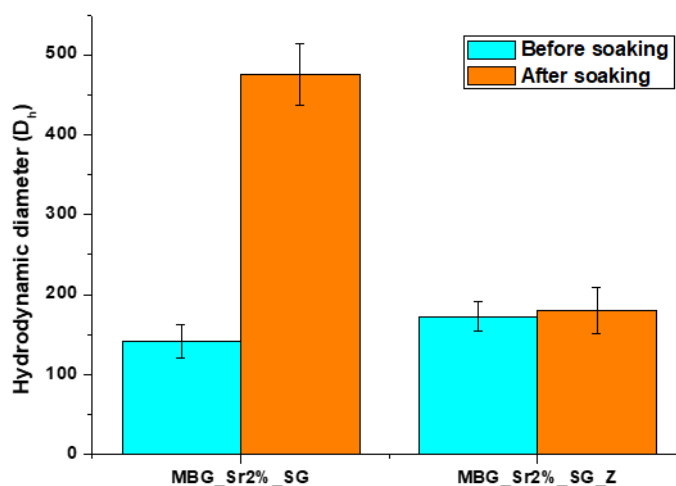
Figure 4.119 Evolution of the hydrodinamic diameter of MBG_Sr2%_SG and MBG_Sr2%_SG_Z after 24h of incubation in the BSA solution. The experiment was performed three times for each sample and data are presented as means ± standard deviations.

between the protein positive charges and the particle negative ones. On the other hands, the Dh of the MBG_Sr2%_SG_Z remained stable after the incubation in the BSA solution, as shown in figure 4.48, confirming the anti-adhesive properties of the *zwitterionic* MBG_Sr2%_SG_Z particles. This behaviour can be associated to the strong surface hydration layer formed by the neutral *zwitterionic* structure [68].

The obtained data reveal a significant larger reduction in protein adhesion for MBG_Sr2%_SG_Z compared MBG_Sr2%_SD_Z, when both compared to their corresponding bare samples, that can be attributed to the drastic decrease of surface area upon functionalization evidenced by nitrogen adsorption-desorption analysis (table 4.10) for Strontium containing MBG prepared by the base catalysed sol gel procedure.

References

[1] C. Pontremoli, I. Izquierdo-barba, G. Montalbano, M. Vallet-regí, C. Vitale-brovarone, S. Fiorilli, Journal of Colloid and Interface Science Strontium-releasing mesoporous bioactive glasses with anti-adhesive zwitterionic surface as advanced biomaterials for bone tissue regeneration, J. Colloid Interface Sci. 563 (2020) 92–103. doi:10.1016/j.jcis.2019.12.047.

[2] S. Fiorilli, G. Molino, C. Pontremoli, G. Iviglia, E. Torre, C. Cassinelli, M. Morra, C. Vitale-Brovarone, The incorporation of strontium to improve bone-regeneration ability of mesoporous bioactive glasses, Materials (Basel). 11 (2018) 678. doi:10.3390/ma11050678.

[3] C. Wu, Y. Zhou, C. Lin, J. Chang, Y. Xiao, Strontium-containing mesoporous bioactive glass scaffolds with improved osteogenic/cementogenic differentiation of periodontal ligament cells for periodontal tissue engineering, Acta Biomater. 8 (2012) 3805–3815. doi:10.1016/j.actbio.2012.06.023.

[4] C. Wu, J. Chang, Multifunctional mesoporous bioactive glasses for effective delivery of therapeutic ions and drug/growth factors, J. Control. Release. 193 (2014) 282–295. doi:10.1016/j.jconrel.2014.04.026.

[5] A.J. Salinas, S. Shruti, G. Malavasi, L. Menabue, M. Vallet-Regí, Substitutions of cerium, gallium and zinc in ordered mesoporous bioactive glasses, Acta Biomater. 7 (2011) 3452–3458. doi:10.1016/j.actbio.2011.05.033.

[6] J.R. Jones, L.L. Hench, Materials perspective - Biomedical materials for new millennium: perspective on the future, Mater. Sci. Technol. 17 (2001) 891–900. doi:10.1179/026708301101510762.

[7] I. Izquierdo-Barba, M. Vallet-Regí, Mesoporous bioactive glasses: Relevance of their porous structure compared to that of classical bioglasses, Biomed. Glas. 1 (2015) 140–150. doi:10.1515/bglass-2015-0014.

[8] K.K. Kaysinger, W.K. Ramp, Interaction between Colloidal Particles, in: Zeta Potential Colloid Sci., Elsevier, 1981: pp. 363–369. doi:10.1016/B978-0-12-361961-7.50017-1.

[9] J. Zhang, S. Zhao, Y. Zhu, Y. Huang, M. Zhu, C. Tao, C. Zhang, Three-dimensional printing of strontium-containing mesoporous bioactive glass scaffolds for bone regeneration, Acta Biomater. 10 (2014) 2269–2281. doi:10.1016/j.actbio.2014.01.001.

[10] P. Naruphontjirakul, A.E. Porter, J.R. Jones, In vitro osteogenesis by intracellular uptake of strontium containing bioactive glass nanoparticles, Acta Biomater. 66 (2018) 67–80. doi:10.1016/j.actbio.2017.11.008.

[11] E. Gentleman, Y.C. Fredholm, G. Jell, N. Lotfibakhshaiesh, M.D. O'Donnell, R.G. Hill, M.M. Stevens, The effects of strontium-substituted bioactive glasses on osteoblasts and osteoclasts in vitro, Biomaterials. 31 (2010) 3949–3956.

doi:10.1016/j.biomaterials.2010.01.121.

[12] A. Moghanian, S. Firoozi, M. Tahriri, Characterization, in vitro bioactivity and biological studies of sol-gel synthesized SrO substituted 58S bioactive glass, Ceram. Int. 43 (2017) 14880–14890. doi:10.1016/j.ceramint.2017.08.004.

[13] C. Pontremoli, M. Boffito, S. Fiorilli, R. Laurano, A. Torchio, A. Bari, C. Tonda-Turo, G. Ciardelli, C. Vitale-Brovarone, Hybrid injectable platforms for the in situ delivery of therapeutic ions from mesoporous glasses, Chem. Eng. J. 340 (2018) 103–113. doi:10.1016/j.cej.2018.01.073.

[14] J. Lao, E. Jallot, J.M. Nedelec, Strontium-delivering glasses with enhanced bioactivity: A new biomaterial for antiosteoporotic applications?, Chem. Mater. 20 (2008) 4969–4973. doi:10.1021/cm800993s.

[15] Y.C. Fredholm, N. Karpukhina, R. V. Law, R.G. Hill, Strontium containing bioactive glasses: Glass structure and physical properties, J. Non. Cryst. Solids. 356 (2010) 2546–2551. doi:10.1016/j.jnoncrysol.2010.06.078.

[16] J.C. Groen, L.A.A. Peffer, J. Pérez-Ramírez, Pore size determination in modified micro- and mesoporous materials. Pitfalls and limitations in gas adsorption data analysis, Microporous Mesoporous Mater. 60 (2003) 1–17. doi:10.1016/S1387-1811(03)00339-1.

[17] M. Thommes, K. Kaneko, A. V. Neimark, J.P. Olivier, F. Rodriguez-Reinoso, J. Rouquerol, K.S.W. Sing, Physisorption of gases, with special reference to the evaluation of surface area and pore size distribution (IUPAC Technical Report), Pure Appl. Chem. 87 (2015) 1051–1069. doi:10.1515/pac-2014-1117.

[18] D. Arcos, A. López-Noriega, E. Ruiz-Hernández, O. Terasaki, M. Vallet-Regí, Ordered mesoporous microspheres for bone grafting and drug delivery, Chem. Mater. 21 (2009) 1000–1009. doi:10.1021/cm801649z.

[19] S.K. Arepalli, H. Tripathi, S.K. Hira, P.P. Manna, R. Pyare, S.P.Singh, Enhanced bioactivity, biocompatibility and mechanical behavior of strontium substituted bioactive glasses, Mater. Sci. Eng. C. 69 (2016) 108–116. doi:10.1016/j.msec.2016.06.070.

[20] S. Taherkhani, F. Moztarzadeh, Influence of strontium on the structure and biological properties of sol–gel-derived mesoporous bioactive glass (MBG) powder, J. Sol-Gel Sci. Technol. 78 (2016) 539–549. doi:10.1007/s10971-016-3995-2.

[21] Q. Hu, W. Jiang, X. Chen, Y. Li, Q. Liang, The effects of Sr concentration on physicochemical properties, bioactivity and biocompatibility of sub-micron bioactive glasses spheres, Adv. Powder Technol. 28 (2017) 2713–2722. doi:10.1016/j.apt.2017.07.024.

[22] T. Kaewamatawong, N. Kawamura, M. Okajima, M. Sawada, T. Morita, A. Shimada, Acute pulmonary toxicity caused by exposure to colloidal silica: particle size dependent pathological changes in mice, Toxicol Pathol. 33 (2005) 743–749.

doi:10.1080/01926230500416302.

[23] T. Kusaka, M. Nakayama, K. Nakamura, M. Ishimiya, E. Furusawa, K. Ogasawara, Effect of silica particle size on macrophage inflammatory responses, PLoS One. 9 (2014) 1–9. doi:10.1371/journal.pone.0092634.

[24] L.M. Costantini, R.M. Gilberti, D.A. Knecht, The phagocytosis and toxicity of amorphous silica, PLoS One. 6 (2011). doi:10.1371/journal.pone.0014647.

[25] T. Morishige, Y. Yoshioka, H. Inakura, A. Tanabe, S. Narimatsu, X. Yao, Y. Monobe, T. Imazawa, S.I. Tsunoda, Y. Tsutsumi, Y. Mukai, N. Okada, S. Nakagawa, Suppression of nanosilica particle-induced inflammation by surface modification of the particles, Arch. Toxicol. 86 (2012) 1297–1307. doi:10.1007/s00204-012-0823-5.

[26] K.M. Waters, L.M. Masiello, R.C. Zangar, B.J. Tarasevich, N.J. Karin, R.D. Quesenberry, S. Bandyopadhyay, J.G. Teeguarden, J.G. Pounds, B.D. Thrall, Macrophage responses to silica nanoparticles are highly conserved across particle sizes., Toxicol. Sci. 107 (2009) 553–69. doi:10.1093/toxsci/kfn250.

[27] G. Renaudin, P. Laquerrière, Y. Filinchuk, E. Jallot, J.M. Nedelec, Structural characterization of sol–gel derived Sr-substituted calcium phosphates with anti-osteoporotic and anti-inflammatory properties, J. Mater. Chem. 18 (2008) 3593. doi:10.1039/b804140g.

[28] U.H. Lerner, Inflammation-induced bone remodeling in periodontal disease and the influence of post-menopausal osteoporosis, J. Dent. Res. 85 (2006) 596–607. doi:10.1177/154405910608500704.

[29] William J. Boyle, W. Scott Simonet, David L. Lacey, Osteoclast differentiation and activation, Nature. 423 (2003) 337–342. doi:10.1038/nature01658.

[30] D.L. Cochran, Inflammation and Bone Loss in Periodontal Disease, J. Periodontol. 79 (2008) 1569–1576. doi:10.1902/jop.2008.080233.

[31] T. Wada, T. Nakashima, N. Hiroshi, J.M. Penninger, RANKL-RANK signaling in osteoclastogenesis and bone disease, Trends Mol. Med. 12 (2006) 17–25. doi:10.1016/j.molmed.2005.11.007.

[32] J.H. Kim, K. Kim, H.M. Jin, I. Song, B.U. Youn, J. Lee, N. Kim, Silibinin inhibits osteoclast differentiation mediated by TNF family members, Mol. Cells. 28 (2009) 201–207. doi:10.1007/s10059-009-0123-y.

[33] H. Sage, R.B. Vernon, S.E. Funk, E.A. Everitt, J. Angello, SPARC, a secreted protein associated with cellular proliferation, inhibits cell spreading in vitro and exhibits Ca+2-dependent binding to the extracellular matrix, J. Cell Biol. 109 (1989) 341–356. doi:10.1083/jcb.109.1.341.

[34] R.J. Keim, N.A. Swords, T. Orfeo, K.G. Mann, Osteonectin in matrix remodeling: A plasminogen-osteonectin-collagen complex, J. Biol. Chem. 269 (1994) 30147–30153.

[35] M. Sila-Asna, A. Bunyaratvej, S. Maeda, H. Kitaguchi, N. Bunyaratavej, Kobe University Repository : Kernel Osteoblast Differentiation and Bone Formation Gene Expression in Strontium-inducing Bone Marrow, Kobe J. Med. Sci. 53 (2007) 25–35.

[36] Y. Doi, R. Okuda, Y. Takezawa, S. Shibata, Y. Moriwaki, N. Wakamatsu, N. Shimizu, K. Moriyama, H. Shimokawa, Osteonectin inhibiting de novo formation of apatite in the presence of collagen, Calcif. Tissue Int. 44 (1989) 200–208. doi:10.1007/BF02556565.

[37] D. Cheng, Q. Liang, Y. Li, J. Fan, G. Wang, H. Pan, C. Ruan, Strontium incorporation improves the bone-forming ability of scaffolds derived from porcine bone, Colloids Surfaces B Biointerfaces. 162 (2018) 279–287. doi:10.1016/j.colsurfb.2017.11.070.

[38] A. Oryan, M. Baghaban Eslaminejad, A. Kamali, S. Hosseini, F.A. Sayahpour, H. Baharvand, Synergistic effect of strontium, bioactive glass and nano-hydroxyapatite promotes bone regeneration of critical-sized radial bone defects, J. Biomed. Mater. Res. Part B Appl. Biomater. (2018) 1–15. doi:10.1002/jbm.b.34094.

[39] W. Querido, A.L. Rossi, M. Farina, The effects of strontium on bone mineral: A review on current knowledge and microanalytical approaches, Micron. 80 (2016) 122–134. doi:10.1016/j.micron.2015.10.006.

[40] C. Charnay, S. Bégu, C. Tourné-Péteilh, L. Nicole, D.A. Lerner, J.M. Devoisselle, Inclusion of ibuprofen in mesoporous templated silica: Drug loading and release property, Eur. J. Pharm. Biopharm. 57 (2004) 533–540. doi:10.1016/j.ejpb.2003.12.007.

[41] A. El-Fiqi, T.-H. Kim, M. Kim, M. Eltohamy, J.-E. Won, E.-J. Lee, H.-W. Kim, Capacity of mesoporous bioactive glass nanoparticles to deliver therapeutic molecules, Nanoscale. 4 (2012) 7475. doi:10.1039/c2nr31775c.

[42] S. Hong, S. Shen, D.C.T. Tan, W.K. Ng, X. Liu, L.S.O. Chia, A.W. Irwan, R. Tan, S.A. Nowak, K. Marsh, R. Gokhale, High drug load, stable, manufacturable and bioavailable fenofibrate formulations in mesoporous silica: A comparison of spray drying versus solvent impregnation methods, Drug Deliv. 23 (2016) 316–327. doi:10.3109/10717544.2014.913323.

[43] A.R. Brás, E.G. Merino, P.D. Neves, I.M. Fonseca, M. Dionísio, A. Schönhals, N.T. Correia, Amorphous ibuprofen confined in nanostructured silica materials: A dynamical approach, J. Phys. Chem. C. 115 (2011) 4616–4623. doi:10.1021/jp107631m.

[44] and J.A.M. Randy Mellaerts, Jasper A. G. Jammaer, Michiel Van Speybroeck, Hong Chen, Jan Van Humbeeck, Patrick Augustijns, Guy Van der Mooter, Physical state of poorly water soluble therapeutic\rmolecules loaded into SBA-15 ordered mesoporous silica carriers:\rA case study with itraconazole and ibuprofen., Langmuir. 24 (2008) 8651–8659.

[45] Y. Zhang, Z. Zhi, T. Jiang, J. Zhang, Z. Wang, S. Wang, Spherical mesoporous silica nanoparticles for loading and release of the poorly water-soluble drug telmisartan, J. Control. Release. 145 (2010) 257–263. doi:10.1016/j.jconrel.2010.04.029.

[46] S. Fiorilli, B. Onida, B. Bonelli, E. Garrone, In situ infrared study of SBA-15 functionalized with carboxylic groups incorporated by a Co-condensation route, J. Phys. Chem. B. 109 (2005) 16725–16729. doi:10.1021/jp045362y.

[47] F. Wang, H. Hui, T.J. Barnes, C. Barnett, C.A. Prestidge, Oxidized mesoporous silicon microparticles for improved oral delivery of poorly soluble drugs., Mol Pharm. 7 (2010) 227.

[48] S.C. Shen, W.K. Ng, J. Hu, K. Letchmanan, J. Ng, R.B.H. Tan, Solvent-free direct formulation of poorly-soluble drugs to amorphous solid dispersion via melt-absorption, Adv. Powder Technol. 28 (2017) 1316–1324. doi:10.1016/j.apt.2017.02.020.

[49] V. Uskoković, D.P. Uskoković, Nanosized hydroxyapatite and other calcium phosphates: Chemistry of formation and application as drug and gene delivery agents, J. Biomed. Mater. Res. - Part B Appl. Biomater. 96 B (2011) 152–191. doi:10.1002/jbm.b.31746.

[50] K. Lin, C. Wu, J. Chang, Advances in synthesis of calcium phosphate crystals with controlled size and shape, Acta Biomater. 10 (2014) 4071–4102. doi:10.1016/j.actbio.2014.06.017.

[51] S.W. Song, K. Hidajat, S. Kawi, Functionalized SBA-15 materials as carriers for controlled drug delivery: Influence of surface properties on matrix-drug interactions, Langmuir. (2005). doi:10.1021/la051167e.

[52] F. Qu, G. Zhu, H. Lin, W. Zhang, J. Sun, S. Li, S. Qiu, A controlled release of ibuprofen by systematically tailoring the morphology of mesoporous silica materials, J. Solid State Chem. (2006). doi:10.1016/j.jssc.2006.04.002.

[53] M. Vallet-Regi, A. Rámila, R.P. Del Real, J. Pérez-Pariente, A new property of MCM-41: Drug delivery system, Chem. Mater. 13 (2001) 308–311. doi:10.1021/cm0011559.

[54] B. Preininger, H. Gerigk, J. Bruckner, C. Perka, H. Schell, A. Ellinghaus, K. Schmidt-Bleek, G. Duda, An experimental setup to evaluate innovative therapy options for the enhancement of bone healing using BMP as a benchmark - A pilot study, Eur. Cells Mater. (2012). doi:10.22203/eCM.v023a20.

[55] N. Gomez-Cerezo, ab D.A. and M.V.-R. I. Izquierdo-Barba, Tailoring the biological response of mesoporous bioactive materials, (2015) 3810–3819. doi:10.1039/C5TB00268K.

[56] M. Guembe, I. Izquierdo-Barba, B. González, M. Vallet-Regí, J. Díez, M. Colilla, D. Pedraza, Mesoporous silica nanoparticles decorated with polycationic dendrimers for infection treatment, Acta Biomater. 68 (2018) 261–271.

doi:10.1016/j.actbio.2017.12.041.

[57] N. Encinas, M. Angulo, C. Astorga, I. Izquierdo-barba, M. Vallet-regí, Acta Biomaterialia Mixed-charge pseudo- zwitterionic mesoporous silica nanoparticles with low-fouling and reduced cell uptake properties, 84 (2019) 317–327. doi:10.1016/j.actbio.2018.12.012.

[58] F. Hoffmann, M. Cornelius, J. Morell, M. Fröba, Silica-based mesoporous organic-inorganic hybrid materials, Angew. Chemie - Int. Ed. 45 (2006) 3216–3251. doi:10.1002/anie.200503075.

[59] S. Fiorilli, L. Rivoira, G. Calì, M. Appendini, M.C. Bruzzoniti, M. Coïsson, B. Onida, Iron oxide inside SBA-15 modified with amino groups as reusable adsorbent for highly efficient removal of glyphosate from water, Appl. Surf. Sci. (2017). doi:10.1016/j.apsusc.2017.03.206.

[60] L. Dalstein, E. Potapova, E. Tyrode, The elusive silica/water interface: Isolated silanols under water as revealed by vibrational sum frequency spectroscopy, Phys. Chem. Chem. Phys. 19 (2017) 10343–10349. doi:10.1039/c7cp01507k.

[61] R.K. Iler, I.R. K, The Chemistry of Silica: Solubility, Polymerization, Colloid and Surface Properties and Biochemistry of Silica, 1979. doi:10.1016/0160-9327(80)90074-5.

[62] K.K. Kaysinger, W.K. Ramp, Extracellular pH modulates the activity of cultured human osteoblasts, J. Cell. Biochem. (1998). doi:10.1002/(SICI)1097-4644(19980101)68:1<83::AID-JCB8>3.0.CO;2-S.

[63] P. Naruphontjirakul, O. Tsigkou, S. Li, A.E. Porter, J.R. Jones, Human mesenchymal stem cells differentiate into an osteogenic lineage in presence of strontium containing bioactive glass nanoparticles, Acta Biomater. 90 (2019) 373–392. doi:10.1016/j.actbio.2019.03.038.

[64] J. Lu, M. Liong, Z. Li, J.I. Zink, F. Tamanoi, Biocompatibility, biodistribution, and drug-delivery efficiency of mesoporous silica nanoparticles for cancer therapy in animals, Small. 6 (2010) 1794–1805. doi:10.1002/smll.201000538.

[65] T.H. Qazi, S. Hafeez, J. Schmidt, G.N. Duda, A.R. Boccaccini, E. Lippens, Comparison of the effects of 45S5 and 1393 bioactive glass microparticles on hMSC behavior, (2017) 2772–2782. doi:10.1002/jbm.a.36131.

[66] I. Izquierdo-Barba, S. Sánchez-Salcedo, M. Colilla, M.J. Feito, C. Ramírez-Santillán, M.T. Portolés, M. Vallet-Regí, Inhibition of bacterial adhesion on biocompatible zwitterionic SBA-15 mesoporous materials, Acta Biomater. 7 (2011) 2977–2985. doi:10.1016/j.actbio.2011.03.005.

[67] R. Jin, Z. Liu, Y. Bai, Y. Zhou, X. Chen, Multiple-Responsive Mesoporous Silica Nanoparticles for Highly Accurate Drugs Delivery to Tumor Cells, (2018). doi:10.1021/acsomega.8b00427.

[68] S. Sanchez-salcedo, M. Vallet-regí, S. Allaf, C.A. Glackin, I. Zink, Mesoporous

core-shell silica nanoparticles with anti-fouling properties for ovarian cancer therapy, 340 (2018) 114–124. doi:10.1016/j.cej.2017.12.116.

CHAPTER 5

Conclusions and perspectives

The activities conducted during the present PhD work were mainly aimed to design and develop multifunctional devices based on Mesoporous Bioactive Glasses to be used as platform for the delivery of therapeutic agents (ions/drug/growth factors) for bone tissue regeneration.

The first aim of this PhD thesis was to produce mesoporous bioactive glass (MBG) particles with a binary composition based on SiO_2 and CaO enriched with two different therapeutic ions, copper and strontium, and loaded with two selected drugs, ibuprofen and N-Acetylcysteine. The second aim was to investigate different surface modification approaches able to impart to MBGs further peculiar features, in particular the Layer by Layer deposition and the *zwitterionization*. The third aim was to identify a strategy to overcome the drawbacks which limits the MBG practical applications and clinical translation. In fact, the developed MBGs are not exploitable alone as long-term therapeutics delivery systems for bone healing. Thus, the conjugation with a thermosensitive polymer able to both modulate the release kinetics and act as a vehicle phase to deliver the therapeutic agent directly at the pathological site were investigated. Finally, the last objective was to evaluate the therapeutic potential of the different developed systems through different *in vitro* and *in vivo* biological assessments.

Nano and micro-sized particles containing copper (2% mol) and strontium (2% mol and 4% mol) in their framework were successfully produced by a base-

catalysed sol-gel route and aerosol-assisted spray-drying method, respectively. These two approaches allowed to produce particles with different morphology, size, structural features and ion release kinetics in order to obtain different drug delivery systems for bone tissue applications.

Concerning the morphology, the base-catalysed sol-gel route allowed to obtain particles with quite uniform size ranging between 100 and 200 nm, with a spheroidal shape. On the other hands, the spray-drying route leads to a production of spherical, well dispersed particles with size mostly ranging between 1 and 5 μm. Both types of synthesis procedures enabled the formation of mesoporous structure with pores of about 4 nm for the base-catalysed sol-gel route (MBG-SG samples) and around 8-10 nm for aerosol-assisted spray-drying (MBG-SD samples).
The related specific surface area and pore volume, especially for MBG-SG samples, were higher compared to the not-templated conventional sol-gel glasses and in line with similar ion-containing MBG particles.
Concerning the release kinetics, the release profile of Cu^{2+} and Sr^{2+} species were evaluated in Tris HCl medium showing a burst release in the first 3 h for both the copper and strontium, followed by a plateau. As far as the bioactive behaviour is concerned, irrespective of the synthesis procedure and the incorporated ion, both MBG-SG and MBG-SD samples showed a fast reactivity after soaking in SBF. In fact, they started to be covered after only one day of soaking by a rough layer of hydroxyapatite. The bioactivity test confirmed that the incorporation of copper and strontium did not hamper the ion exchange with the SBF which led to the deposition of the hydroxyapatite. On the basis of the obtained results, it can be affirmed that the substitution of small amount (2% or 4% mol) of CaO with specific ion precursors (i.e. copper and strontium) did not significantly affect the MBG morphology and the textural properties. Moreover, the inclusion of different metallic ions did not hamper the deposition of HA layer, essential feature for promoting bone regeneration.

The copper-containing MBGs were subsequently loaded with ibuprofen, by following two different procedures, the adsorption and the incipient wetness method. Along with the angiogenesis and anti-microbial effect promoted by copper ions, the introduction of ibuprofen allowed to simultaneously act also against persistent inflammation.
Based on the obtained results, irrespective of the adopted loading procedure, the particle morphology, size, structural features and copper release kinetics did not result affected by the ibuprofen loading.
In fact, FESEM observations and EDS analysis evidenced that ibuprofen loading does not significantly alter the morphological features and the chemical composition of Cu-containing MBGs, which resulted very similar to those reported for not-loaded samples. A drastic reduction of the specific surface area, pore size and pore volume has been notified for all the evaluated ibuprofen-loaded samples, as a consequence of drug incorporation.
DSC and X-ray powder diffraction (XRD) analyses were performed to assess the

amorphous state of the drug and exclude the presence of large crystalline aggregates. Irrespective of the loading procedure, both the DSC thermograms and XRD analysis revealed the amorphous state of ibuprofen into the mesopores, thus confirming that ri-crystallization did not occur inside the pores upon solvent evaporation during the incorporation process.

The release profile of both copper and ibuprofen was evaluated in aqueous medium. No changes were notified for the copper release, confirming that the ibuprofen loading did not suppress or hinder the capability to release therapeutic ions through ion-exchange reactions. Concerning the ibuprofen release, the total amount of loaded drug was released in the first hour of soaking in the medium. The burst release is then followed by a plateau till the end of the test.

No relevant differences in the loading procedures have been identified, except for the amount of loaded ibuprofen in relation to the initial employed amount. In fact, the incipient wetness method allows to use a lower amount of initial ibuprofen compared to the adsorption method, however resulting in a higher loading amount (10% with the adsorption against 12% with the IW for the MBG-SG; 6.5% with the adsorption against 10% with the IW for the MBG-SD). Based on these considerations, compared to the adsorption method, the incipient wetness process has been selected as the most suitable loading procedure in terms of yield and required time and thus employed in the subsequent experiments.

As mentioned before, a burst release of both copper and ibuprofen in the first hours of soaking was observed. In order to overcome these drawbacks and produce drug delivery systems able to provide sustained release of both copper ions and ibuprofen, Cu-containing MBG surface was modified by layer-by-layer deposition of the polyelectrolyte multilayers, exploiting the opposite charges of alginate and chitosan. The multi-layered surface was obtained by following two different routes, well explained in the section 2.6 of the *"materials and methods"* chapter.

In the first strategy the polyelectrolytes chitosan and alginate were selected as natural biodegradable and biocompatible polymers and alternatively deposited by exploiting their opposite positive and negative charges, respectively. Once obtained the desired multi-layered surface in term of layer number, ibuprofen was loaded into the multi-layered MBGs by using the IW technique. In the second approach, the alginate layer was replaced by the ibuprofen, thus introduced as polyelectrolyte layer, by exploiting the ibuprofen negative charge (COO^-), able to electrostatically interact with the chitosan positive charge. Both the approaches did not significantly alter the morphology of the particles; compared to the corresponding bare samples, the bioactivity of the copper-containing MBG coated by following the first strategy (CAC samples) resulted delayed. This difference could be ascribed to the polyelectrolyte multi-layered coating, which acts as a barrier for the ionic exchange reaction, involved at the interface of the MBGs and the medium, essential to induce the HA formation. On the other hands, the bioactive behaviour of the copper-containing MBG coated by following the second strategy (CIC samples) resulted unaffected compared to the corresponding bare samples, probably due to the lower

steric hindrance of ibuprofen compared to alginate, leading to the formation of a more open network, which consequently allows faster ion exchange reactions, essential for HA deposition.

Both the investigated procedures allowed to modulate the release rate of both copper and ibuprofen. In fact, a significantly prolonged copper release profile up to 14 days has been observed, with a strong reduction of the burst release in the first hours of soaking. The release modulation can be associated to the long path length and the amount of time needed for the ions to diffuse into the polymer layers before reaching the medium. The polyelectrolyte multilayer, acting as a barrier, is able to hinder the contact between the ion and the release medium, thus delaying the release. The release of copper from the CAC samples resulted more sustained compared to the CIC samples, probably due to the denser polymer network obtained after the chitosan/alginate/chitosan deposition, which more hinders the contact between the particles and the medium. On contrary, the more open network of the chitosan/ibuprofen/chitosan coating is expected to allow easier the medium diffusion and thus the copper release. These results are in good agreement with the notified bioactive behaviour above mentioned, in which the polymer network is proved to play a key role in the delay of the ion exchange reactions between the surface particles and the medium.

Concerning the ibuprofen release, an evident sustained release profile up to 1 day of soaking has been reached for both the systems. In fact, both the multi-layered coatings demonstrated the ability to avoid the burst release notified for the bare samples, probably due to the strong ionic interactions between the amine groups of the chitosan and the carboxyl groups of the ibuprofen that could potentially hinder the diffusion pathways of ibuprofen among the layers, thus delaying the contact between the drug and the release medium, as already notified for the copper release.

The ability of these multilayer strategies to avoid the burst release observed for the bare samples confirms the feasibility of the use of the layer by layer deposition as promising technique to design a drug delivery system able to modulate the therapeutic agent release from the MBGs. In fact, the adopted LbL procedures have never been evaluated to modulate the release from mesoporous bioactive glasses and based on these obtained promising results, this technique could be considered a potential alternative approach to modulate the release of the therapeutic agents over a longer time scale. In addition, by tailoring the number of deposited layers, different drug delivery systems and release kinetics can be developed and investigated as a smart platform for bone tissue application.

As mentioned in the previous chapters, MBGs alone are not exploitable as long-term drug delivery systems for orthopaedic applications, due to the strong burst release of the therapeutic species (ions/drugs) once in contact with body fluids, and the difficulties related to their administration at the pathological site (*i.e.* bone fracture cavity) in the form of powder. To this purpose, their combination with polymers able to modulate the release kinetics and/or to act as a vehicle phase to the pathological site has been investigated as promising strategy to overcome their

drawbacks. In particular, MBGs have been incorporated into an injectable Poly(ether urethane) (PEU) based thermosensitive hydrogel developed by *Professor Ciardelli's group (DIMEAS, Politecnico di Torino, Italy).*

The resulting hybrid formulations have been evaluated in terms of ion/drug co-delivery kinetics, gelation behaviour and stability in aqueous environment. Cu-containing MBG particles were loaded with ibuprofen through incipient wetness technique and then embedded into the thermosensitive hydrogel. The incorporation of MBG particles within the sol-gel systems did not negatively affect their capability to undergo a temperature-driven sol-to-gel transition within few minutes. The progressive release of Cu^{2+} species was found to play a significant effect on the stability of the gels in aqueous environment catalysing the oxidation of PEU chains. The co-release of copper ions and ibuprofen from hybrid formulations turned out to be sustained and prolonged overtime up to more than one week, with a strongly reduced initial burst effect compared to MBG particles as such (2-4 % vs 7-14 % Cu^{2+} release and 6-9% vs 38-61% ibuprofen release from hybrid MBG-polyurethane formulations and free MBG particles, respectively). However, release profile of both copper species and ibuprofen resulted to be affected by the progressive occlusion of mesopores resulting from the dissolution of silica-based MBG framework and reprecipitation in the form of silica gel at the pore entrance. The high potentiality of the proposed strategy lies in the wide versatility of the proposed formulations. In fact, by tailoring the composition and cargo of MBGs, different ions and bioactive factors can be co-released based on the therapeutic effects required by the final targeted application. In addition, the use of a custom-made PEU hydrogel as vehicle phase of the MBGs provides the final system with a further degree of freedom. The characteristic LEGO-like chemical structure of PEUs allows a fine tuning of polymer properties by changing their constituting building blocks. This versatility opens the way to the design of stimuli-responsive hydrogels with an enhanced control over payload release and/or hydrogel dissolution/degradation, thus allowing a better tuning of the release properties compared to those observed for MBGs alone.

As far as the strontium-containing MBGs are concerned, as mentioned before, the two preparation methods allowed to obtain Sr-containing samples with different structural features in term of specific surface area, pore volume and pore size. Successively, the role of these aspects on the bioactivity and the biological response in terms of cytocompatibility and pro-osteogenic effect have been evaluated in collaboration with *Nobil Bio Ricerche Srl*. The *in vitro* biological assessment aimed to evaluate if the developed Sr-containing samples and their released products allow cell survival and can exhibit a therapeutic effect by stimulating pre-osteoblastic cells. In order to study this aspect and the role of both the particles size and the structural features on the induced biological response, the experiments described in Section 2.9.1, were carried out on MBG_Sr2%_SD and MBG_Sr2%_SG. Both type of Sr-containing MBGs were biocompatible, showed a reduced pro-inflammatory response and were able to stimulate the expression of pro-osteogenic genes

(COLL1A1, SPARC and OPG), confirming the potential of Sr^{2+} as therapeutic element for the stimulation of bone remodelling.

Based on the obtained results, Sr-containing MBGs could represent promising candidates for bone regenerative applications as such or in association with drugs as multifunctional carriers in combination with polymeric matrices. Since the release of strontium has been proved to induce bone formation, in order to further boost the therapeutic potential of the produced multifunctional device, N-Acetylcysteine (NAC) has been selected and loaded into the strontium-containing MBG mesopores based on a suggestion of the *Charitè,* a partner of MOZART project, which proved the beneficial role of NAC in supporting the bone regeneration process. To this purpose, N-Acetylcysteine was loaded into the Sr-containing MBGs by using the incipient wetness method as osteogenesis-enhancing molecule to be delivered into the bony defect where might improve bone regeneration and promote bone defect healing. Based on the results obtained with the ibuprofen loading, the incipient wetness method has been selected as loading procedure against the adsorption method, since allows to avoid the time-consuming filtration step and to control the amount of drug loaded into the carrier. In addition, the IW method has been proved to be the most suitable compared to the adsorption, in term of yield.

The particle morphology, size, structural features and strontium release kinetics did not result affected by the NAC loading.
In fact, FESEM observations evidenced that NAC loading does not significantly alter the morphological features of Sr-containing MBGs, which resulted very similar to those reported for not-loaded samples. A drastic reduction of the specific surface area, pore size and pore volume has been notified for all the evaluated NAC-loaded samples, as a consequence of drug incorporation.
DSC and X-ray powder diffraction (XRD) analysis were performed to assess the amorphous state of the drug and exclude the presence of large crystalline aggregates. Both the DSC thermograms and XRD analysis revealed the amorphous state of NAC into the mesopores, thus confirming that ri-crystallization did not occur inside the pores upon solvent evaporation during the incorporation process.
The release profile of both strontium and NAC was evaluated in aqueous medium. No changes were notified for the strontium release, confirming that the drug loading did not suppress or hinder the capability to release therapeutic ions through ion-exchange reactions. Concerning the NAC release, the total amount of loaded drug was released in the first hour of soaking in the medium. The burst release is then followed by a plateau till the end of the test.
After the characterization, NAC loaded Sr-containing MBG (SD) were incorporated into the PEU-based hydrogels produced by *Prof. Gianluca Ciardelli's group* with final particle concentration of 20 mg/mL.

The morphology and the stability in aqueous environment in the presence of a buffer solution at pH 7.4 at 37 °C of hybrid formulation, as well as the temperature-

dependent sol-to-gel transition of the developed systems was characterized by Prof. Gianluca Ciardelli's group (data not reported). Once assessed that the size of MBG particles embedded into the hydrogels was not significantly affected by the immersion into an aqueous medium and that the incorporation of the particles into the hydrogel does not affected the gelation potential of PEU-based hydrogels upon temperature increase, both the strontium ion and NAC release tests were performed. By the comparison of the kinetics within the first 24 hours of NAC release from free and hydrogel-containing MBG particles, the role exerted by the polymeric matrix in modulating the release profile of drug was clearly highlighted, with a significant reduction in the initial burst release upon incorporation within PEU hydrogel of about 40%.

Similarly, the incorporation of strontium-containing MBGs within the polymeric phase successfully decreased the undesirable initial burst release of Sr^{2+} species typically observed for particles as such. In fact, after 1 hour of incubation in similar releasing conditions, the strontium released from the hybrid formulation is approximately 80 % lower compared to the corresponding free MBG particles, further confirming the role exerted by the hydrogel in modulating the release rate of strontium, as already observed for the NAC release.

Based on these promising results, the ability of this hybrid formulation to exert a therapeutic effect *in vivo*, (without delaying the progression of bone healing) has been investigated.

The *in vivo* biological assessment was performed at the *Julius Wolff institute, Charitè – Universitätsmedizin Berlin,* during the three months that I spent in Berlin working as visiting researcher in the group led by Prof. Katharina Schmidt-Bleek, one of the academic partners involved in the MOZART project. The *in vivo* response induced by the PEU_MBG_Sr2%_SD_NAC was evaluated in a femoral osteotomy model of compromised healing in female rats, after creating a 2 mm defect in the femoral shaft. The healing progress was monitored radiologically by *in vivo* μCT analysis at two and four weeks, showing an increase in both, bone volume (BV) and tissue volume (TV).

After finalization at four weeks, the osteotomized bones were prepared for analysis by *ex vivo* μCT and histology. The reconstructed μCT images were used to study the bridging stage of the fracture gap (data not presented). The histological sections obtained after the decalcification and dehydration processes were stained with Safranin O staining, to detect the new cartilage development and MOVAT's pentachrome staining in order to evaluate the relative amount of mineralized bone, cartilage, connective tissue and bone marrow. The PEU_MBG_Sr2%_SD_NAC group showed a great amount of cartilage, evidencing the more advanced healing status compared to the empty and hydrogel groups. In addition, the PEU_MBG_Sr2%_Sr_NAC histological sections stained with MOVAT's pentachrome revealed a significantly higher amount of mineralized bone and cartilage tissue, further confirming the more advanced progression in healing process, compared to the empty and hydrogel group, as observed with the Safranin O staining. Based on these considerations, the beneficial effects on the bone healing outcome exerted by the multifunctional device allowed to validate the

strontium-containing MBGs loaded with NAC as a suitable carrier to be used for bone regeneration purposes for the delivery of therapeutic agents at the pathological site.

Finally, with the aim to achieve the second goal of this PhD project, *zwitterionization* has been identified as functionalization approach to further enrich the therapeutic potential of the MBGs, imparting anti-adhesive/anti-fouling features. In order to develop a different multifunctional biomedical device, able to synergistically combine the release of therapeutic ion/drug with anti-fouling/antibacterial properties, during this PhD work, strontium-containing MBGs have been produced and successively post-functionalized by co-grafting aminopropyl silanetriol (APST) and carboxyethylsilanetriol (CES) as organosilane agents. In details, Sr-containing MBGs have been produced in the form of nano- and micro-particles, to obtain materials with different morphological and textural features, and subjected to a co-grafting reaction to introduce almost the same amount of $-NH_3^+$/$-COO^-$ surface groups, which are expected to impart effective anti-adhesive properties.

TEM and FESEM observations evidenced that the functionalization process does not significantly alter the structural and morphological features of Sr-containing MBGs, which resulted very similar to those reported for not-loaded samples. A drastic reduction of the specific surface area, pore size and pore volume has been notified, as a consequence of functionalization.

Fourier Transform Infrared Spectroscopy (FTIR) analyses highlighted the successful grafting of $-NH_3^+$/$-COO^-$ groups and ζ-potential measurements confirmed the zwitterionic nature of the surface as a function of pH. In order to confirm that the post-functionalization did not inhibit the release property and bioactivity which is typical of bare strontium-containing MBGs, the *in vitro* release of strontium ions was studied in Tris-HCl at pH 7.4 for up to 14 days and *in vitro* bioactivity tests were performed in SBF to investigate the deposition of an apatite-like layer. The modification of the surface with zwitterionic pairs proved not to alter the ability to release strontium ions within concentrations which are able to promote early osteogenic differentiation and mineralized matrix deposition. In addition, the functionalization procedures did not interfere with the ion-exchange reactions which promote HA deposition, essential feature for promoting bone regeneration. *In vitro* biocompatibility assays in the presence of a mouse pre-osteoblastic cell line MC3T3-E1 were also performed to study the effect of post-grafted Sr-MBGs on the osteoblastic cell growth and differentiation, revealing no cytotoxic effect. Finally, to assess the anti-adhesive ability imparted by the surface *zwitterionization*, a reduced protein adsorption of serum proteins was evaluated by gel electrophoresis (SDS-PAGE) experiments using bovine serum albumin (BSA) and fibrinogen (Fib), respectively. *In vitro* non-specific protein adhesion assay demonstrated that the successful grafting of the *zwitterionic* pairs onto Sr-MBG surfaces reduced BSA and Fib adhesion up to ca. 85% and 70%, respectively. These very promising results could represent a springboard for the design of advanced biomaterials based on strontium-containing mesoporous

bioactive glasses boosted up with an anti-adhesive *zwitterionic* surface enable to promote bone regeneration and simultaneously inhibit non-specific biomolecule adsorption and, consequently, bacterial adhesion. In fact, the excellent results obtained by the protein adhesion assay could pave the way to further investigations, in order to demonstrate the anti-adhesive properties of the material also against bacteria attachment.

In conclusion, the possibility to tailor the composition of MBGs and their ability to incorporate and release a wide range of active agents make these nanocarriers very attracting candidates to develop personalized and multi-purpose devices able to stimulate the endogenous cascade healing underlying bone remodelling process. In addition, to make this system suitable for both hard and soft tissue applications and satisfy the requirement of resembling the extracellular matrix pattern of the tissues, the innovative biofabrication techniques such as electrospinning (ESP) and 3D printing, represent one of the most interesting fabrication routes to design specific scaffolds able to better mimic the natural tissue composition.

Furthermore, with the final aim to offer competitive added-value medical devices and allow their effective clinical translation, further investigations to exclude potential immunogenicity, associated to the component materials, and specific clinical studies are required.